

SPUTTER DEPOSITION OF ZNO THIN FILMS

By

LOREN WELLINGTON RIETH

A DISSERTATION PRESENTED TO THE GRADUATE SCHOOL
OF THE UNIVERSITY OF FLORIDA IN PARTIAL FULFILLMENT
OF THE REQUIREMENTS FOR THE DEGREE OF
DOCTOR OF PHILOSOPHY

UNIVERSITY OF FLORIDA

2001

Copyright 2001

by

Loren Wellington Rieth

Dedicated to my wife, Wendy; to my family, Herb Jr., Sheri, and Herb III; and the mother of us all.

ACKNOWLEDGMENTS

Dr. Holloway has been my mentor for the last seven years. His knowledge of science both humbles and enlightens me. His dedication to his profession and students is reflected in numerous awards, publications, and the common occupation of his car in the coveted parking spot directly in front of Rhines Hall. His patience and guidance have been invaluable.

My wife Wendy has been a source of so many things to me in the process of graduate school. Motivation, encouragement, strength, and love have all been given in excess. Her patience and support have helped ease the writing process and kept the basic necessities of life continuing as large portions of my time focused on completing this work.

It would be a travesty to call Ludie Harmon a secretary. So much of smooth day to day operation depends on her competence. More than this, she reminds us that we are people, and there are cares in the world which should be balanced with a career. Additionally, there is the candy jar and the weekly cookies that magically appear for which no amount of thanks is sufficient.

There are many people to thank in the Holloway group. In particular is Billie Abrams, whose interactions have enriched my graduate career and life. Dr. Mark Davidson and his unique talents in coaxing dead equipment to life and knowledge of scientific lore have been an asset to so many in our department including me. So much of what works does so because he works hard. My seven year tenure means I can

name a lot of names of people who have all helped in their ways, and include (in no particular order) Sushil, Craig, Heather, John, Troy, Big and Little Joe, Tracy, Brent, Eric, Lizandra, Jae-Hyun, Joon-Bo, Heesun, Sean, Jeff, Mike, Vaidy, Maggie, Scott, Jacque, Lisa, Nagraj, JP, Caroline, Huang, Billy, Alex, Suku, Serkan, Lei

Of course no acknowledgement would be complete without thanking my parents. To my mom, whose own graduate career I waylaid for 20 years, and my dad, who just managed to finish before there was me, I of course owe everything. They not only brought me into the world but have endeavored to help me through it.

TABLE OF CONTENTS

	<u>page</u>
LIST OF TABLES	ix
LIST OF FIGURES.....	x
ABSTRACT	xiv
1 INTRODUCTION AND MOTIVATION.....	1
2 LITERATURE REVIEW	5
2.1 Introduction	5
2.2 Photovoltaic Devices	5
2.2.1 History.....	5
2.2.2 Device Physics.....	8
2.2.3 Thin Film Solar Cells.....	12
2.2.4 Transparent Conducting Electrode (TCE)	17
2.3 Transparent Conducting Oxides.....	21
2.3.1 Background	21
2.3.2 Electrical Properties of TCOs.....	27
2.3.3 Optical Properties	39
2.4 Sputter Deposition	47
2.4.1 Background	47
2.4.2 Thin Film Coalescence.....	54
2.4.3 Negative Ion Resputtering.....	58
3 EXPERIMENTAL METHODS.....	63
3.1 Introduction.....	63
3.2 Thin Film Deposition.....	63
3.2.1 New Oxide Sputtering System	63
3.2.2 Description of the Sputtering System	67
3.2.3 Substrate Cleaning	68
3.3 Electrical Characterization.....	69
3.3.1 Hall Measurements	69
3.3.2 Four Point Probe.....	71
3.4 Structural Characterization	72
3.4.1 Profilometry.....	72
3.4.2 X-Ray Diffraction.....	72
3.4.3 Atomic Force Microscopy.....	73
3.4.4 Auger Electron Spectroscopy	75

3.4.5 X-ray Photoelectron Spectroscopy	76
3.4.6 Secondary Ion Mass Spectrometry	79
3.5 Optical Properties	80
3.5.1 Spectrophotometry.....	80
3.5.2 Fourier Transform Infrared Spectroscopy.....	80
3.6 Experimental Procedures	81
3.6.1 Affect of Annealing Ambient on the Properties of ZnO:Al.....	81
3.6.2 Development of Properties in Very Thin ZnO:Al Films	83
3.6.3 Negative Ion Resputtering in Sputter Deposition of ZnO:Al Films.....	84
4 AFFECT OF ANNEALING AMBIENT	89
4.1 Background	89
4.2 Results.....	90
4.2.1 Structural Characterization.....	90
4.2.2 Electrical Characterization	99
4.2.3 Optical Characterization	102
4.3 Discussion	108
4.3.1 Structural Properties	108
4.3.2 Electrical Properties.....	112
4.3.3 Optical Properties	120
4.4 Summary	122
5 DEVELOPMENT OF ELECTRICAL AND MICROSTRUCTURAL PROPERTIES IN VERY THIN ZNO:AL FILMS.....	124
5.1 Background	124
5.2 Results.....	125
5.2.1 Structural Characterization.....	125
5.2.1.1 Profilometry.....	125
5.2.1.2 Atomic force microscopy	126
5.2.1.3 Auger electron spectroscopy	131
5.2.2 Electrical Characterization	137
5.3 Discussion	141
5.3.1 Surface Morphology	141
5.3.2 Electrical Characterization	150
5.4 Summary	156
6 NEGATIVE ION RESPUTTERING	159
6.1 Background	159
6.2 Experiment Results.....	162
6.2.1 Profilometry.....	162
6.2.2 Electrical Characterization	165
6.2.3 Secondary Ion Mass Spectrometry Results	175
6.2.4 X-ray Photoelectron Spectroscopy Results	180
6.2.5 X-ray Diffraction Results.....	183

6.2.4 Atomic Force Microscopy Results	195
6.3 Discussion of RF Power Experiment.....	199
6.3.1 Model of the Effects of Negative Ion Resputtering on Electrical Properties.	199
6.3.2 Region I.....	207
6.3.2.1 Profilometry (Region I).....	207
6.3.2.2 Resistivity effects (Region I).....	210
6.3.2.3 Hall carrier concentration (Region I).....	212
6.3.2.4 Hall mobility (Region I).....	216
6.3.2.5 Secondary ion mass spectrometry.....	219
6.3.2.6 X-ray photoelectron spectroscopy	220
6.3.2.7 X-ray diffraction (Region I)	222
6.3.2.8 Atomic force microscopy (Region I)	229
6.3.3 Region II.....	230
6.3.3.1 Profilometry (Region II).....	230
6.3.3.2 Resistivity effects (Region II).....	231
6.3.3.3 Hall carrier concentration (Region II).....	233
6.3.3.4 Hall mobility (Region II).....	234
6.3.3.5 X-ray diffraction (Region II)	234
6.3.3.6 Atomic force microscopy (Region II)	236
6.3.4 Region III	236
6.3.4.1 Profilometry (Region III)	236
6.3.4.2 Resistivity effects (Region III)	237
6.3.4.3 Hall carrier concentration (Region III).....	237
6.3.4.4 Hall mobility (Region III)	239
6.3.4.5 X-ray diffraction (Region III).....	240
6.3.4.6 Atomic force microscopy (Region III).....	241
6.4 Summary	241
7 CONCLUSIONS.....	243
7.1 Negative Ion Resputtering	243
7.2 Chemisorbed Oxygen	247
7.3 Property Development in Thin ZnO:Al Thin Films	248
7.4 Future Work	250
LIST OF REFERENCES	253
BIOGRAPHICAL SKETCH.....	262

LIST OF TABLES

<u>Table</u>	<u>Page</u>
2-1. Materials parameters for chalcopyrite ternary compositions.	16
2-2. History of processes for making transparent conductors.	23
2-3. Compilation of electrical data for sputter deposited ZnO thin films with several different dopants.	25
3-1. Parameters used for Auger electron spectroscopy sputter depth profiles.....	77
3-2. Parameters used to collect XPS multiplex scans.	78
4-1. JCPDS powder XRD reference data for Wurtzite ZnO.	90
4-2. Quantified XRD data from (100) diffraction peak.....	97
4-3. Quantified XRD data from (002) diffraction peak.....	97
4-4. Resistivity data from before and after heat treatment measured by four point probe as a function of position and gas ambient used.	100
4-5. Changes in resistivity with 400°C one hour annealing.	102
4-6. Quantified optical band gap (E_g) data from before and after annealing at 400°C for one hour.....	108
5-1. Sample identification, deposition time, and film thickness.....	126
6-1. Atomic concentrations from XPS multiplex data for as deposited and sputter etched samples.....	181

LIST OF FIGURES

<u>Figure</u>	<u>Page</u>
1-1. Total and renewable energy consumption in the United States.....	2
2-1. Schematic cross sectional view of a typical CIS based thin film solar cell structure...	6
2-2. Progress in improving efficiency of solar cells	7
2-3. Irradiance of the solar spectrum.....	9
2-4. Theoretical plot of the I-V characteristics for a typical Si solar cell	10
2-5. Band diagram of a typical n-p homojunction solar cell	11
2-6. One unit cell of the CuInSe ₂ chalcopyrite crystal structure	16
2-7. Conduction and valence band alignments of a typically CIS based solar cell	18
2-8. Equivalent circuit diagram for a solar cell	19
2-9(a-b). Influence of a solar cell's series resistance	20
2-10. Decreasing resistivity of transparent conducting oxides	24
2-11. Schematic representation of the influence of grain boundaries.....	33
2-12. Illustration of the chemisorbed oxygen mechanism for solid state gas sensors	34
2-13(a-c). Theoretical plots of relationships between electrical and optical properties.....	43
2-14. Illustration of the Burstein-Moss shift	45
2-15. Generation of interference colors or Fabry-Perot oscillations.....	46
2-16. Plot of the power cosine distribution.....	49
2-17(a-b). Illustrations of planar sputter deposition sources	50
2-18(a-b). Illustration of the negative self bias formation during RF sputter deposition.....	54
2-19. Representation of the influences of surface forces on the morphology of a deposited film	55

2-20. A structural zone model showing changes in thin film morphology	56
2-21. The hexagonal wurtzite crystal structure for ZnO in the zincite phase.....	57
2-22. Schematic of the negative ion generation and acceleration process during sputter deposition of ZnO:Al thin films.	59
2-23. Theoretical plot of the mean free path of an Ar atom	60
3-1(a-d). Schematic diagram and pictures of the new oxide sputtering system	65
3-2. Cross-sectional view of the sputter deposition system known as “Rusty”	68
3-3. Positions on the 2.5 x 5 cm substrate where four point probe data were collected	82
3-4. Top-view of the deposition geometry used for the investigation of negative ion resputtering.....	85
4-1(a-b) X-ray diffraction spectra from before and after a ZnO:Al thin film is annealed in nitrogen	92
4-2(a-b) X-ray diffraction spectra from before and after a ZnO:Al thin film is annealed in forming gas.....	93
4-3(a-b) X-ray diffraction spectra from before and after a ZnO:Al thin film is annealed in stagnant air	94
4-4(a-b) X-ray diffraction spectra from before and after a ZnO:Al thin film is annealed in oxygen.....	95
4-5(a-b) X-ray diffraction spectra from before and after a ZnO:Al thin film used as a control sample	96
4-6(a-b). Transmission spectra of uncoated and ZnO:Al coated soda-lime glass substrates with data from before and after annealing of the coated sample.....	103
4-6(c-d). Transmission spectra of uncoated and ZnO:Al coated soda-lime glass substrates with data from before and after annealing of the coated sample.....	104
4-6(e). Transmission spectra of uncoated and ZnO:Al coated soda-lime glass substrates with no annealing of the coated sample for a control sample	105
4-7. Plots of the absorption squared (A^2) versus wavelength to determine changes in optical band gap of the ZnO:Al film with annealing	105
4-8. Fourier transform infrared spectra taken in reflection mode.....	109
5-1. Z range, “grain size”, and RMS roughness data for ZnO:Al thin films.....	127

5-2(a-d). AFM micrographs from a 0.5 x 0.5 μm area	129
5-2(e-h). AFM micrographs from a 0.5 x 0.5 μm area for ZnO:Al thin films	130
5-3(a-c). AES data from the 18 \AA thick ZnO:Al sample.....	132
5-4(a-c). AES data from the 105 \AA thick ZnO:Al sample.....	133
5-5(a-c). AES data from the 525 \AA thick ZnO:Al sample.....	134
5-6. Percentage of the soda-lime glass substrate covered by the sputter deposited ZnO:Al thin film.....	138
5-7(a-c). Electrical data for ZnO:Al thin films plotted as a function of film thickness.....	140
5-8. Schematic representation of the constant volume transformation.....	143
5-9(a-b). Relationships between surface coverage, film thickness (t in \AA), and nucleus radius (\AA).....	144
5-10. Illustration of carrier trajectories based on the Fuchs and Sondheimer model.....	153
5-11. Calculated plot of the resistivity ratio between the thin films.....	153
6-1. Cross-sectional view of the sputter deposition geometry.....	161
6-2. Measured thickness of the ZnO:Al thin film.....	163
6-3. Deposition rate of ZnO:Al.....	163
6-4. Deposited molecular flux of ZnO:Al	165
6-5. Deposition rate ratio between 250 W/1000 W and 500 W/1000 W conditions	166
6-6. Resistivity of ZnO:Al thin films	167
6-7. Resistivity of ZnO:Al thin films with 500 W data offset by 3.2 cm.....	167
6-8. Resistivity of the deposited ZnO:Al thin film plotted versus thickness.....	169
6-9(a-b). Carrier concentration of ZnO:Al thin films	171
6-10(a-b). Hall mobility of ZnO:Al thin films.....	174
6-11(a-b). SIMS depth profile data for ZnO:Al films deposited at 250 W	177
6-12(a-b). SIMS depth profile data for ZnO:Al films deposited at 500 W	178
6-13(a-b). SIMS depth profile data for ZnO:Al films deposited at 1000 W	179

6-14(a-b). XPS multiplex spectra of the O (1s) peak.....	182
6-15(a-b). XRD spectra from ZnO:Al thin films deposited at 250 W	184
6-16(a-b). XRD spectra from ZnO:Al thin films deposited at 500 W	185
6-17(a-b). XRD spectra from ZnO:Al thin films deposited at 1000 W	186
6-18(a-b). Maximum XRD peak intensity of the (002) peak for ZnO:Al thin films	189
6-19(a-b). Position of the ZnO:Al (002) peak in 2θ (degrees) plotted	191
6-20(a-b). FWHM of the (002) ZnO:Al XRD peak.....	193
6-21(a-c). Process used to quantify “grain size” from AFM micrographs.....	196
6-22(a-b). “Grain size” of the ZnO:Al thin films	198
6-23(a-b). RMS roughness of the ZnO:Al thin films.....	200
6-24. Resistivity of the ZnO:Al thin film	213
6-25(a-b). Corrected carrier concentration from Hall measurements for ZnO:Al thin films	214
6-26(a-b). Corrected Hall mobility for ZnO:Al thin films	217

Abstract of Dissertation Presented to the Graduate School
of the University of Florida in Partial Fulfillment of the
Requirements for the Degree of Doctor of Philosophy

SPUTTER DEPOSITION OF ZNO THIN FILMS

By

Loren Wellington Rieth

December 2001

Chairman: Paul H. Holloway
Major Department: Materials Science and Engineering

Sputter deposition and characterization of ZnO thin films for application as a transparent conducting electrode have been studied. The effects of gas ambient upon annealed film properties, evolution of structural and electrical properties of very thin ZnO films, and the influence of negative ion resputtering on the thin film properties were investigated.

For annealing sputter deposited ZnO thin films, the gas ambient in the quartz tube furnace was found to be a critical parameter for the resistivity of ZnO:Al thin films. Annealing films in forming gas (N₂/H₂ 90%/10%) at 400°C for 60 minutes was found to reduce the resistivity of the films by up to two orders of magnitude with a minimum value of $2 \times 10^{-3} \Omega \cdot \text{cm}$. Optical measurements indicate an increase in carrier concentration is responsible for the decreased resistivity.

The nucleation of ZnO:Al films on glass substrates occurs by the island (Volmer-Webber) mechanism. Films less than 1000 Å thick were found to have higher resistivity

due to decreased carrier concentration postulated to result from carrier depletion by chemisorbed oxygen. The minimum resistivity achieved was $4.3 \times 10^{-3} \Omega \cdot \text{cm}$ at a film thickness of 1580 Å.

The effects of negative ion resputtering on the structural and electrical properties of deposited ZnO:Al films were evaluated. A model incorporating system geometry, deposition conditions, negative ion resputtering, and film thickness was developed to explain the structural and electrical properties of the deposited films. The model defines Regions I, II, and III, with the resistivity in Region I between 4.3×10^{-3} to $1.2 \times 10^{-2} \Omega \cdot \text{cm}$, a carrier concentration of between 7.2×10^{19} to $3.2 \times 10^{20} \text{ cm}^{-3}$, and mobilities of approximately $7 \text{ cm}^2/\text{V} \cdot \text{s}$. In Region II, the resistivity decreases to $1.5 \times 10^{-3} \Omega \cdot \text{cm}$, due to increased carrier concentrations of $5 \times 10^{20} \text{ cm}^{-3}$, while mobility remains near $7 \text{ cm}^2/\text{V} \cdot \text{s}$. For Region III resistivity increases to greater than $10 \Omega \cdot \text{cm}$, due to carrier concentrations as low as $1.0 \times 10^{19} \text{ cm}^{-3}$, and mobilities as low as $1.5 \text{ cm}^2/\text{V} \cdot \text{s}$. Low carrier concentrations in Region I result from compensation by native defects created by negative ion resputtering, while low carrier concentrations in Region III result from chemisorbed oxygen species.

CHAPTER 1 INTRODUCTION AND MOTIVATION

The need for electrical power is the fundamental motivating force for the research presented in this work. Department of Energy statistics for total energy consumption in the US are presented in Figure 1-1, and show a steady increase with time since 1949. The vast majority of this energy is produced by fossil fuels and nuclear power as can be seen from the small fraction of the total energy consumption supplied by renewable energy sources. At current consumption rates, fossil and nuclear fuel supplies will last on the order of decades to centuries. Significant price increases will occur for energy produced from fossil and nuclear fuels as these resources are depleted. Additionally, use of fossil and nuclear fuels results in environmental degradation during procurement, consumption, and waste disposal. Therefore the long-term energy security of this country and the world at large is dependent on use of sustainable quantities of energy generated from renewable sources. Renewable energy sources currently under development and in use include hydroelectric, geothermal, wind, biomass, nuclear fusion, and solar (photovoltaic and thermal).

Photovoltaic cells, more commonly known as solar cells, are based on the ability of certain materials and structures to generate electrical power when exposed to light. Modern solar cells are based on semiconducting materials. Two classes of solar cells are bulk and thin cells, and are distinguished by the thickness of the material that absorbs the light to generate electricity. Bulk solar cells rely on semiconducting wafers on the order of half a millimeter in thickness. Thin film solar cells are fabricated by depositing layers

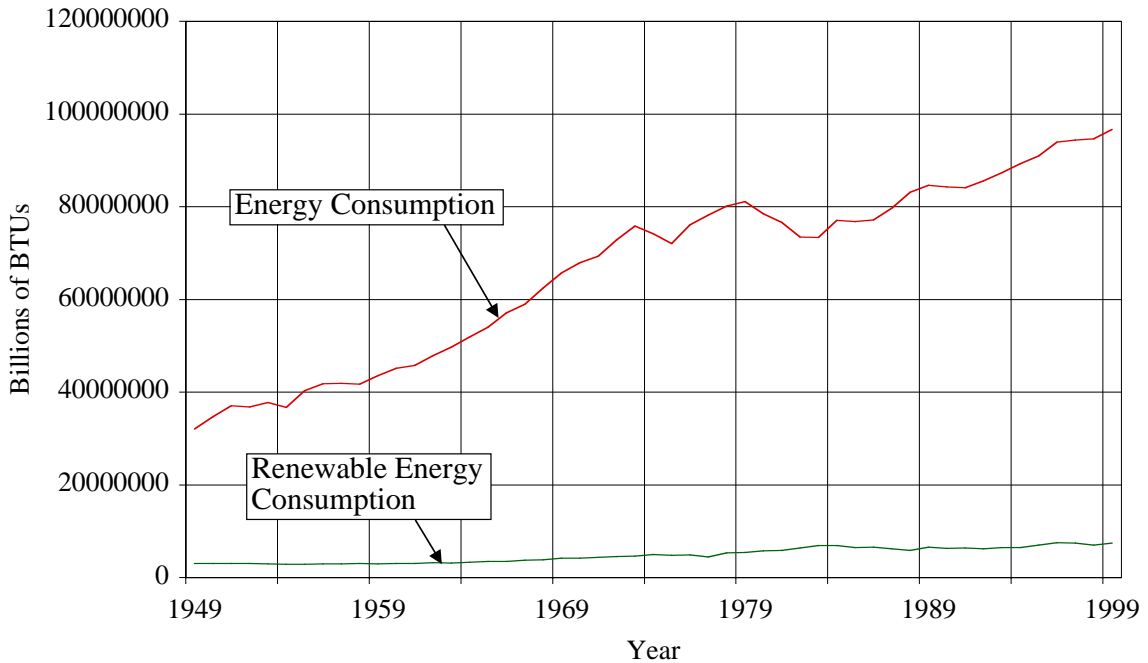


Figure 1-1. Total and renewable energy consumption in the United States of America in billions of BTU versus time in years [1].

of semiconducting materials of a thickness on the order of $1\ \mu\text{m}$ onto inexpensive substrates such as glass, plastic, or metal foils. Significantly lower production costs are possible due to 100 times smaller volume of semiconducting material used in thin film cells. It is the production cost per peak watt ($\$/\text{kW}_p$) that is a critical figure of merit. In order to be competitive with current power pricing, a rough threshold of $\$3/\text{kW}_p$ must be surpassed for areas serviced by the power “grid.” Current applications where solar cells are cost effective include remote locations and developing countries, where the power infrastructure is not established.

Thin film solar cells are based on a number of semiconducting materials, including copper chalcogenides, cadmium telluride, and amorphous silicon. Copper chalcogenides in the $\text{Cu}(\text{In,Ga})\text{Se}_2$ or CIGS system have demonstrated 18.8% conversion efficiency for research size cells [2]. Advantages of this materials system leading to high

efficiencies include a large optical absorbance ($\alpha \sim 10^5 \text{ cm}^{-1}$) from a direct band gap, ability to change the band gap by control of the stoichiometry, a large minority carrier lifetime, and compatibility with thin film deposition techniques [3,4].

Because semiconducting layer of thin film solar cells often have a high resistance, a front transparent conducting electrode (TCE) is critical to cell efficiency. Thin films of ZnO are almost exclusively used as the TCE for thin film solar cells based on CIGS. Further improvement of the properties of ZnO thin films is recognized as necessary for further improvement of large area production modules [5]. Use of ZnO as a TCE is attractive because of its match to the electrical properties of other layers in a CIGS device and the low price of zinc especially compared to the semiprecious metal indium. Zinc oxide is also compatible with large area thin film deposition techniques, Zn and O are isoelectronic with the CdS layer ZnO is deposited upon, and has optical and electrical properties that are competitive with other TCO materials.

The focus of this research is to improve the knowledge of the relationships between the thin film deposition process and the structure and properties of the resulting ZnO films. This knowledge can then be used to improve the properties of ZnO thin films, and decrease the effort needed to optimize film properties in the future. Based on production and performance considerations, sputter deposition of ZnO thin films has yielded the best results, and will therefore be the technique used in this work. Key issues investigated are the influence of sputtering process variables on the properties of the resulting films. The process variables for the sputtering process influence the microstructure of the deposited film, which in turn dictates the electrical and optical properties. A review of the literature is present in Chapter 2, and provides background

information on CIGS based thin film solar cells, ZnO window layers, and the sputtering process. The experimental method is discussed in Chapter 3, and relates the methods, conditions, and characterization tools used to determine the relationships between the deposition process and film properties. Results and discussion from an experiment designed to investigate the influence of annealing and the gas ambient used for annealing is presented in Chapter 4. Results and discussion presented in Chapter 5 cover an experiment designed to investigate the development of properties in very thin ZnO:Al thin films. The experiment discussed in Chapter 6 is designed to investigate negative ion resputtering and the mechanisms by which it influences the properties of deposited films, and film thickness effects on electrical properties in very thin films. The overall conclusions drawn from this work are communicated in Chapter 7.

As a final note, this work is primarily motivated by the application of thin film solar cells. It is worth noting that there are many applications for zinc oxide thin films. Several examples include gas sensors [6-9], surface acoustic wave devices [10], structural e-glass coatings [11,12], and with the advent of *p*-type ZnO wide band gap electronic structures [13].

CHAPTER 2 LITERATURE REVIEW

2.1 Introduction

The focus of this study is the relationships between the sputter deposition process and post deposition heat treatments to the structural, electrical, and optical properties of deposited ZnO:Al thin films. The objective is to improve properties of the ZnO:Al films with respect to application as a transparent conducting electrode (TCE) to CuInSe₂ (CIS) thin film solar cells. This chapter reviews background information and concepts including the basics of solar cells, transparent conducting oxides, and sputter deposition. The section on solar cells covers history, basic device physics, and influence of the TCE on solar cells. A cross-sectional view of a typical CIS based solar cell structure is presented in Figure 2-1. The transparent conducting oxide section reviews the history of transparent conductors and the principles of their electrical and optical properties. The topics covered in the sputter deposition section include the sputtering process in several important geometries, thin film coalescence, and negative ion resputtering. Specific information regarding ZnO will be worked into all of these themes.

2.2 Photovoltaic Devices

2.2.1 History

The photovoltaic or Dember Effect is defined as “providing a source of electric current under the influence of light or similar radiation.” [14] Becquerel discovered

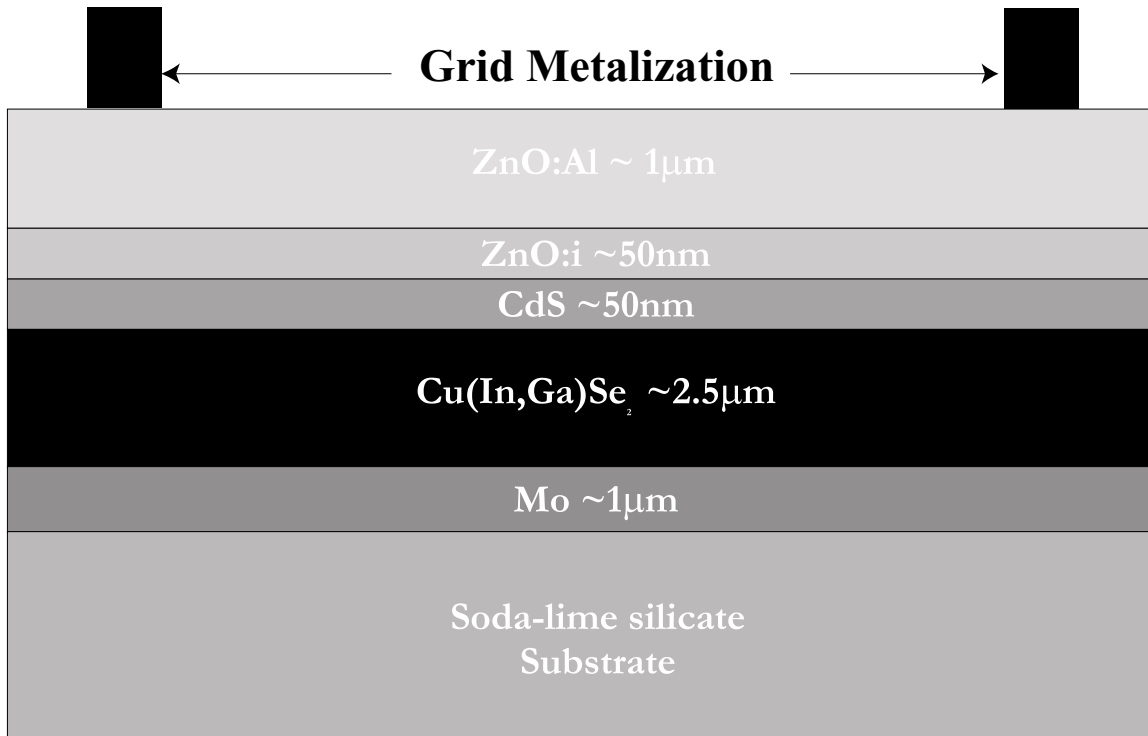


Figure 2-1. Schematic cross sectional view of a typical CIS based thin film solar cell structure.

this effect in 1839, when he noticed power generation from metal plates in electrolyte solutions. In 1876, power generation was reported from selenium, the first solid state photovoltaic device [4]. The first modern semiconductor solar cell was developed in 1954 by Chapin, Fuller, and Pearson, and was based on a *p-n* junction formed in silicon [15]. This quantum leap of technology in conjunction with the needs of the US space program formed the impetus for early research into solar cells. Due to the expense of these early cells, and the widespread availability of cheap “grid” power, solar cells for terrestrial applications received little attention until the 1970s. The energy crisis in the 1970s stimulated a tremendous amount of research into solar cells for terrestrial applications. The fruit of this effort can be seen in the rapid strides made in improving efficiency and lowering cost, and the large body of published literature generated in the

80s and 90s. In Figure 2-2 [3], solar cell efficiency is plotted versus material system and time, and excellent improvement in efficiency is noted for the beginning in the late 70s. Efficiency for CIS cells increases from ~4% to almost 10% from 1978 to 1981. Research and development have continued through the 90s and into 2000, yielding the large variety of commercial products available today [4].

Many semiconducting materials have been studied for photovoltaic applications. The structures of these materials include single crystalline, polycrystalline, and amorphous materials in bulk and thin film forms. Materials that have received substantial attention include Si, GaAs, InP, CdTe, and CuInSe₂ (CIS). Single crystal, polycrystalline, and amorphous silicon account for the vast majority of commercially available solar cells for terrestrial applications. Cells based on III-V chemistries (GaAs, InP) are used extensively for space applications due to their radiation hardness,

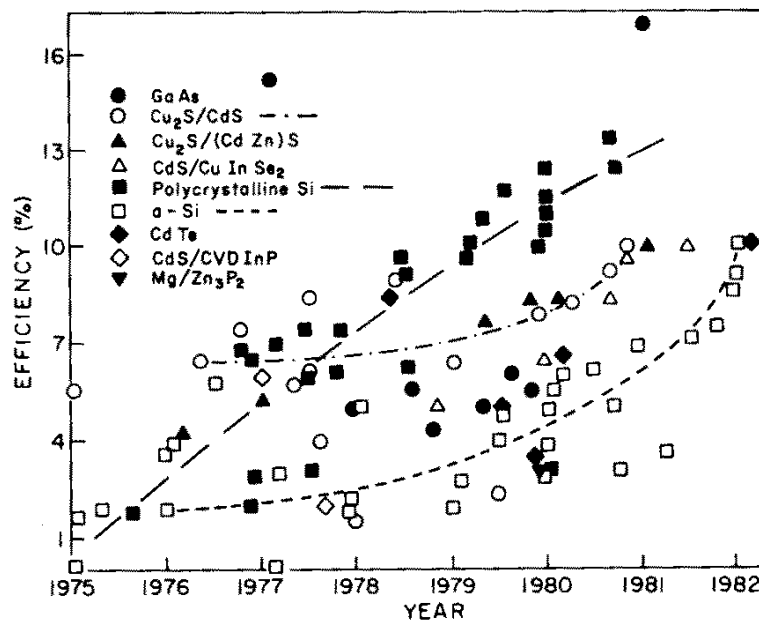


Figure 2-2. Progress in improving efficiency of solar cells based on several different materials as a function of time [3].

and high conversion efficiency, which translates to weight savings and longevity for satellite applications [4]. Thin film solar cells based on CIS have recently achieved 18.8% efficiency for laboratory sized cells, and have exceeded 10% for complete modules [2]. Panels based on CIS have recently entered the market as a commercial product for terrestrial applications, and are manufactured by Siemens Solar Industries [16]. Current applications for solar cells include power for remote locations, power generation in developing countries without a substantial power generation and distribution infrastructure, and the space industry.

Future research will continue to focus on improvements in conversion efficiency and lowering production costs. The basics of photovoltaic device physics and their relationship to efficiency will be treated in the next section, followed by a discussion of the benefits of thin film technology in lowering production costs.

2.2.2 Device Physics

At the simplest level, a solar cell is a device that converts absorbed light to electrical power. Most modern solar cells are based on *p-n* junction diode devices. In the cells, incoming sunlight generates electron-hole (e-h) pairs that are separated by an electrical field resulting from junction formation. The generate charge carriers must then flow through the various regions of the cell structure (i.e., grid metalization, TCE, etc.) to power the external load. A basic parameter used to evaluate all solar cells is the efficiency (η) of the conversion process, and is simply the ratio of the electrical power ($P=VI$) generated by the cell to the power of the light impinging on the cell, and is described in Equation 2.1 [17] where

$$\eta = \frac{V_m I_m}{P_{in}}. \quad (2.1)$$

For this equation, V_m and I_m are the voltage and current for maximum power (P_m), and P_{in} is the power of the incident light. The power of incident light is obviously extremely variable, and depends on the influences of the atmosphere, cloud cover, time of day, and many other factors. Typical incident powers for air mass conditions of 1 and 1.5 (AM1 and AM1.5) are 92.5 and 84.4 mW/cm^2 , respectively. The AM1.5 solar spectrum is presented in Figure 2-3 in terms of irradiance ($\text{W}/\text{m}^2 \cdot \mu\text{m}$) versus wavelength of light. The air mass conditions correspond to the spectrum of the sun at sea level for the sun at zenith (AM1) and 45° (AM1.5) above sea level [17]. Thus for CIS cells, it is essential that the TCE conduct electricity well to limit resistive power losses, and be highly transparent to light for wavelengths that have significant solar irradiance and that can be absorbed by the cell.

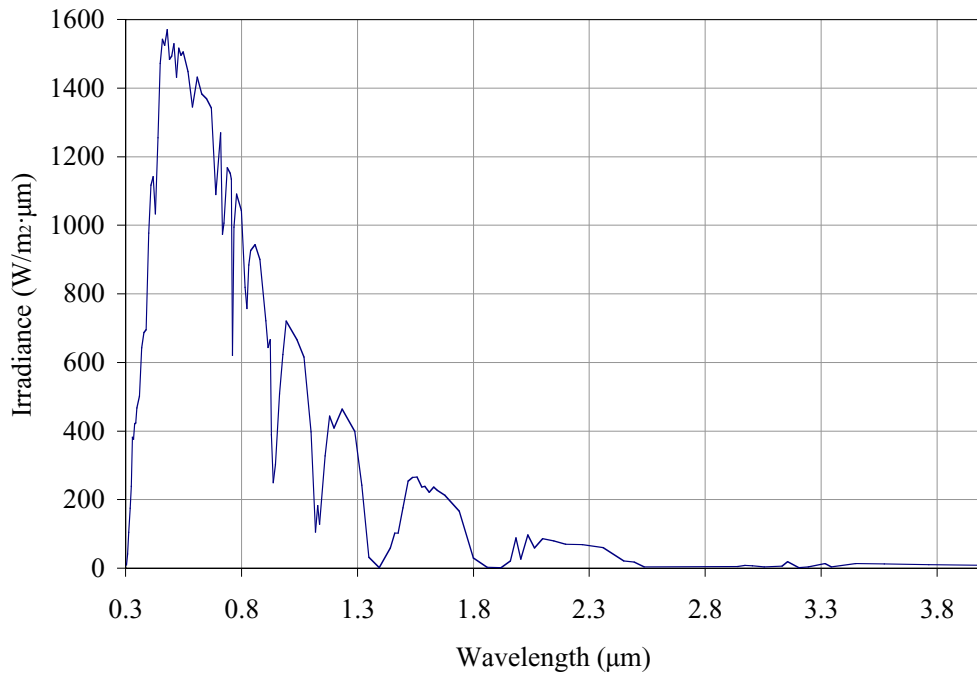


Figure 2-3. Irradiance of the solar spectrum as a function of wavelength for light filtered by the Earth's atmosphere to the air mass 1.5 global spectrum.

The maximum power delivered by the cell is determined by the fill factor (FF) for a solar cell. The fill factor is a measure of the squareness of the illuminated I-V curve, and like efficiency is used to characterize all types of solar cells. A plot of a typical I-V curve is presented in Figure 2-4 [18], where the hatched square represents the area of a square defined by the product of V_m and I_m , which equals P_m . The fill factor represents the ratio of the maximum power square to the power square defined by V_{oc} and I_{sc} , where V_{oc} is the open circuit voltage, and I_{sc} is the short circuit current. These relationships yield Equations 2.2 and 2.3 [17].

$$FF = \frac{V_m I_m}{V_{oc} I_{sc}} \quad (2.2)$$

$$\eta = \frac{FF \cdot V_{oc} I_{sc}}{P_{in}} \quad (2.3)$$

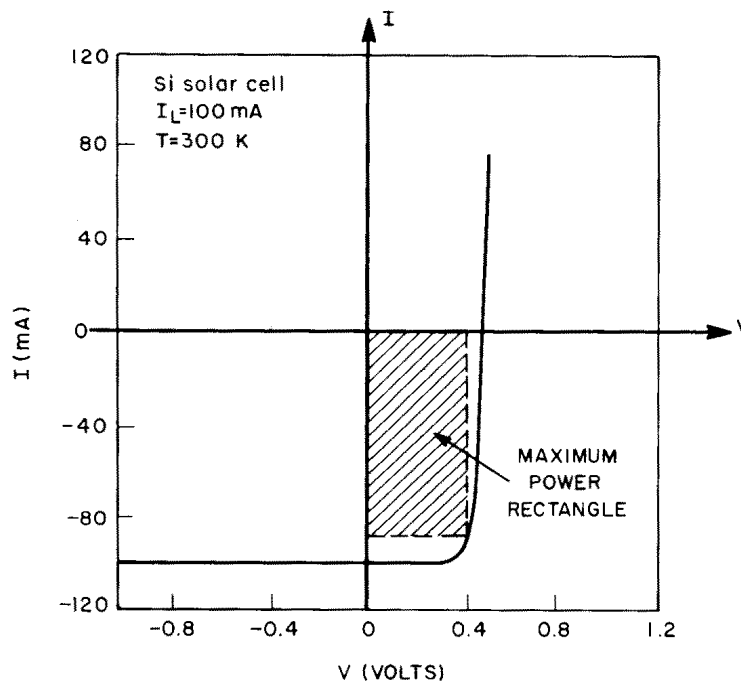


Figure 2-4. Theoretical plot of the I-V characteristics for a typical Si solar cell, with the maximum power rectangle highlighted [18].

The ZnO TCE primarily affects cell efficiency by influencing the FF and I_{sc} . The role of the TCE and the mechanisms for its influence on FF and I_{sc} are discussed in Section 2.2.4 below, after coverage of basic concepts is completed.

To understand device physics, start with the simplest case of a p - n homojunction diode formed near the surface of a bulk semiconductor wafer. A typical structure and band diagram is shown schematically in Figure 2-5. In this device, there is a n -type region on the surface, a depletion region containing the junction, and a p -type substrate. If a photon with energy ($E_{ph} = h\nu$) greater than the band gap (E_g) of the semiconductor is absorbed, a valence band electron is promoted to the conduction band yielding an electron-hole (e-h) pair. If this absorption process takes place in or within a diffusion distance from the space charge or depletion region, the carriers can be separated by the junction's built-in potential (V_{bi}). The built-in potential is a function of the band bending in the space charge region, and is therefore determined by the doping concentrations for a homojunction [17].

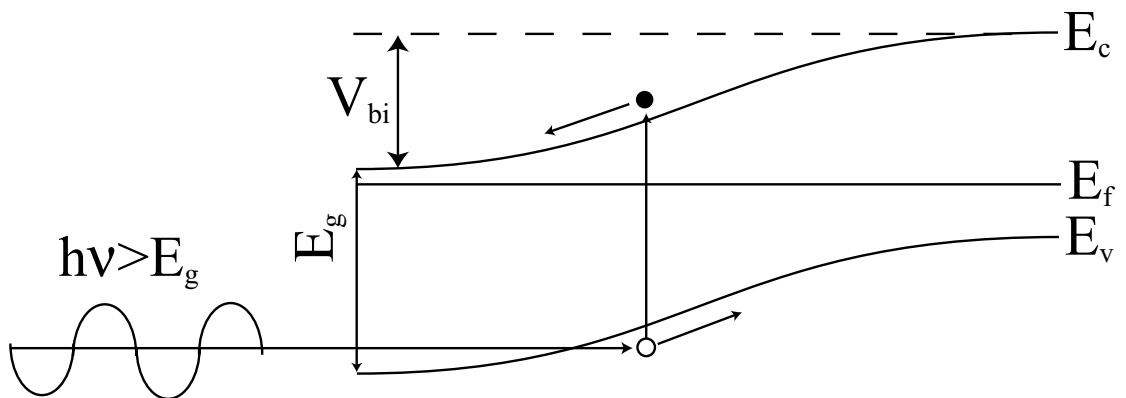


Figure 2-5. Band diagram of a typical n-p homojunction solar cell, illustrating generation of an electron-hole pair by absorption of a photon.

Since the width of the depletion region is small relative to the thickness of the cell, a significant portion of e-h pair generation occurs outside of the depletion region. This region has no built electric field; therefore current transport only occurs due to the diffusion field generated by the excess carriers. If these generated carriers reach the depletion region, they contribute to power generation. If the carriers recombine before reaching the depletion region, they do not contribute; therefore the minority carrier lifetime and diffusion distance are critical to device performance [17].

2.2.3 Thin Film Solar Cells

Thin film solar cells are solar cells based on deposited thin films of semiconductor materials, typically applied to inexpensive substrates (i.e., glass, polymer films, and metal foils). The principle of using a semiconductor junction is the same, but the structure and production of the cells are quite different. The device physics of thin film cells are significantly more complicated than the idealized conditions described above [3,4]. The solar cell structure presented in Figure 2-1 is a typical CIS based thin film solar cell, and is comprised of several layers, the functions of which will be discussed subsequently. Factors complicating the device physics arise from large defect concentrations in the deposited films, and the necessity of using multiple layers. Microstructural defects include point defects, dislocations, and extended defects such as grain boundaries. Macroscopic defects include porosity/voids, pinholes, delamination, and cracking. These defects lower the efficiency of the cell by degrading optical and electrical properties. Multiple layers can hamper performance due to interfacial recombination, potential barriers resulting from poor band alignment, and processing constraints imposed by the different materials. Thus, compared to ideal cells, which are

most closely approximated by bulk single crystal devices, thin film devices are less efficient.

Enthusiasm for thin film cells is maintained despite compromises in efficiency because of the potential for substantially reduced production costs [3]. Costs are lowered in source materials due to the relatively small volume of semiconductor material needed to form thin films in contrast to bulk cells where the entire structure is semiconducting material. This is an important advantage if a significant portion of the world's power is to be produced by solar cells. The area of cells needed to produce a significant fraction of the world's power demand is huge; therefore low material usage per unit area is absolutely critical. A second advantage results from lower processing costs associated with thin film devices versus bulk devices. As seen previously (Figure 2-2), tremendous strides have been made in improving the efficiency of thin film devices, but high volume production costs still need to be much lower to encourage widespread adoption of thin film solar cells. In all cases, production costs are lower than high efficiency single crystal devices, and compete with bulk poly-crystalline devices. Amorphous silicon (a-Si) is still the cheapest solar cell material to produce, but continues to suffer from low efficiency and lack of stability under long term illumination [4]. Amorphous silicon cells are widely used in consumer electronic applications where power consumption is minimal and low cost is critical (i.e., solar powered calculators).

The CIS material system has several advantages over other materials systems, one being a large absorbance ($\alpha \approx 10^5 \text{ cm}^{-1}$), which is larger than many other direct band gap semiconductors [3]. The absorbance describes the ability of a material to absorb light as expressed in Equation 2.4 where

$$I = I_0 e^{-\alpha x} . \quad (2.4)$$

The term I is the intensity of transmitted light, I_0 is incident light, α is the absorbance with units of cm^{-1} , and x is the distance traveled through the absorbing medium in units of cm. The high absorbance of CIS results in light being absorbed near the surface of the film, and therefore in close proximity to a shallow p - n junction region. This also means that the overall device can be thinner than a device based on a semiconductor with a lower α . Another benefit is the band gap of the device can be controlled by introducing Ga for In and S for Se, to match the band gap of the cell for most efficient utilization of the solar spectrum and to form graded gap structures. Turning to the individual layers of the CIS based solar cell in Figure 2-1, the substrate for thin film CIS solar cells is inexpensive soda-lime (window) glass. A $1 \mu\text{m}$ thick film of molybdenum is sputter deposited onto the glass substrate, and acts as a reflective back electrode to the solar cell. The primary purpose of the Mo contact is to efficiently conduct electricity generated in the CIS layer to the external circuit. The CIS layer is the semiconductor layer responsible for absorbing the light, and is known as the absorber layer. The CIS layer is typically $\sim 3 \mu\text{m}$ thick, and is deposited by a wide variety of techniques, of which co-evaporation has achieved the best results ($\eta=18.8\%$) [2]. Co-evaporation involves simultaneous evaporation of Cu, In, and Se from elemental sources, and therefore requires sophisticated flux controls to achieve proper stoichiometry. There is still considerable debate as to whether the semiconductor junction formed in CIS based solar cells is a homojunction within CIS, or a heterojunction formed with the subsequent CdS layer. From the illustration of the cell in Figure 2-1, the layer on top of CIS is a very thin (50 nm) layer of CdS known as the *buffer layer* that is deposited by chemical bath deposition

(CBD). The role of the buffer layer is still not well understood, but is critical to fabrication of the highest efficiency devices [19]. Resistive intrinsic ZnO (i-ZnO) and conductive doped ZnO form the transparent conducting electrode top contact, and are approximately 50 and 700 nm thick, respectively. This contact is typically deposited by sputter deposition, and will be discussed in the next section. The final two steps are the deposition of patterned metal electrodes to lower the series resistance (R_s), and a layer of MgF_2 to form an anti-reflection coating [2].

Again, the CIS layer has been deposited by many different methods including sputter deposition, thermal evaporation, electro-deposition, electrophoretic deposition, and many chemical processes with a variety of precursors. In each case, the α or chalcopyrite phase is desired. The chalcopyrite crystal structure is tetragonal, and is essentially two stacked zinc blende unit cells along the c-axis, and is shown schematically in Figure 2-6. Table 2-1 contains a list of some basic materials parameters for several copper chalcogenides [4]. The importance of this is that the band gap of the absorber can be tailored by adjusting compositions between the various ternaries, and that the minimum band gap of the cell structure is important for optimization of the TCO layer. The relationship between the band gap of the absorber and optical properties of the TCO will be discussed below. The explicit space group for CIS has been a subject of much interest, as knowing the space group can improve the accuracy of calculations concerning materials properties [20]. Thermodynamic assessments of the phase diagrams for CIS and CIGS have recently been reported, which have proven useful for optimization of processing conditions [20,21].

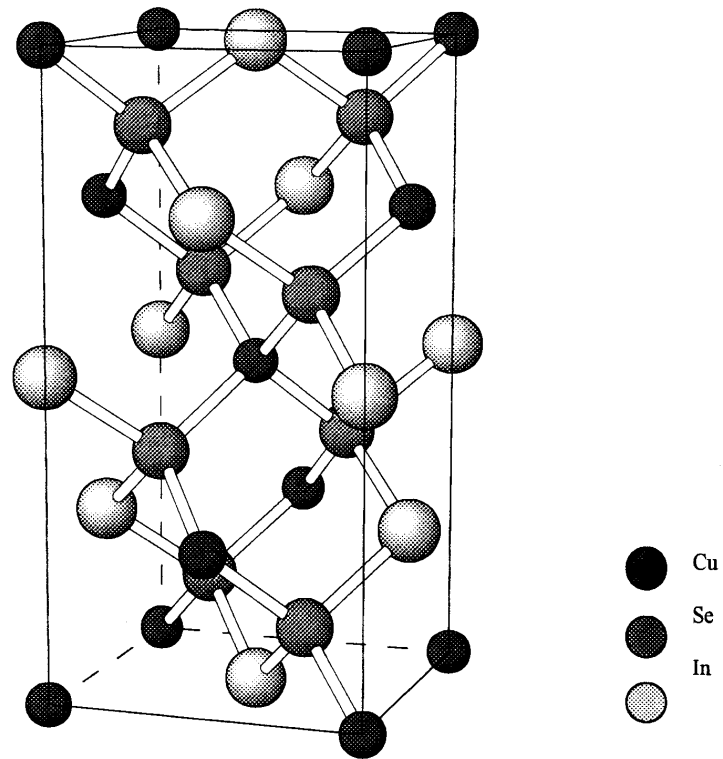


Figure 2-6. One unit cell of the CuInSe_2 chalcopyrite crystal structure [20].

Table 2-1. Materials parameters for chalcopyrite ternary compositions.

Compound	a (Å)	c/a	E_g (eV)
CuInSe_2	5.782	2.0097	1.04
CuGaSe_2	5.596	1.966	1.68
CuInS_2	5.52	2.016	1.43
CuGaS_2	5.35	1.959	2.43

The CdS buffer layer is still an active area of research. Research is focused on the role of the layer, since the most efficient devices have this layer. A large amount of effort has addressed how to replace the CdS layer because of the toxicity of cadmium [19]. The leading hypotheses regarding the role of the buffer layer are that it protects the absorber layer from ion bombardment during the sputter deposition of ZnO, that the CBD

chemistry treats the surface in such a way that the interfacial electrical properties are improved, and/or that it forms a high quality heterojunction. Some of the investigated alternatives include In(OH,S), CdZnS, ZnS, and ZnO [19,22].

2.2.4 Transparent Conducting Electrode (TCE)

For bulk single crystal *p-n* junction based solar cells, the top layer of the cell structure is typically a heavily doped *n*-type region. Therefore the resistivity of the absorber material is low, and it can effectively conduct power to the metal grid, which transfers the power to an external load. For the case of CIS based cells a fine grain size and an inability to achieve a highly doped *n*-type region on the surface dictate the need for an additional layer to efficiently conduct electricity. As this layer is on the top of the cell, it must also transmit the useful portion of the solar spectrum. These needs are well met by transparent conducting oxides (TCOs), of which ZnO has been found to be a particularly good match for CIS based cells. The two primary mechanisms by which the TCE affects the performance of the solar cell are through the fill factor (FF) and the short circuit current (I_{sc}).

There are several design constraints that make ZnO more attractive than other TCOs for application to CIS based solar cells. One of the most fundamental is the previously mentioned natural abundance and low cost of Zn. Also important is the thermal budget available for this processing step. It is generally accepted that for the current state of the art structures, processing above 200°C for any step after deposition of CdS results in severe degradation of the cell's performance [23]. Thus a high quality TCO must be deposited at or near room temperature. Transparent conductors based on ZnO have achieved resistivities in the low $10^{-4} \Omega \cdot \text{cm}$ by sputter deposition at room temperature. Films of ZnO can also have greater than 90% transmittance in the visible

spectrum, which is one of the best values for TCOs, while maintaining good electrical properties [24]. Also, as shown in Figure 2-7, the conduction band alignment between ZnO and the underlayers is good [25], which is important for transport of conduction band electrons generated in the absorber to the external load. In the presented schematic band alignment diagram, the conduction band for ZnO is 0.4 eV and 0.1 eV below the conduction bands of CdS and CIS, respectively. Additionally, ZnO is based on column II and VI elements from the periodic table, as is CdS; therefore Zn and O are isoelectronic in CdS.

As mentioned, the TCE influences the FF and I_{sc} of the cell. For the case of FF, the TCE can be a primary component of the series resistance (R_s), which can be seen in

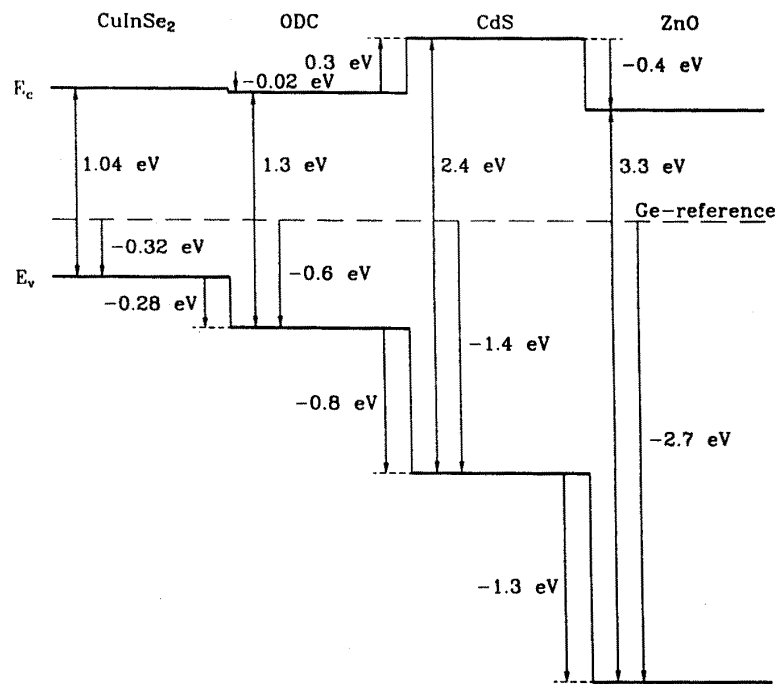


Figure 2-7. Conduction and valence band alignments of a typically CIS based solar cell between the different layers of the structure [25].

the schematic equivalent circuit shown in Figure 2-8 [17]. Equation 2.5 was developed to evaluate resistive effects in thin film solar cells [26].

$$FF = FF_0 - CI_{sc} \frac{R_s}{V_{oc}} - \frac{V_m}{V_{oc}} \frac{V_m}{I_{sc} R_{sh}} - \left\{ \frac{V_m}{V_{oc}} S_I \frac{[1 - F_2(V_m)/F_2(0)]}{S_I + \mu_2 F_2(V_m)} \right\} \quad (2.5)$$

The term FF_0 is the ideal diode fill factor and C is a parameter that is weakly dependent on V_{oc}/kT . The bracketed term on the right is a correction used for CdTe based solar cells, and is therefore not applicable to CIS based solar cells. As can be seen, a high series resistance and/or a low shunt resistance (R_{sh}) degrades the fill factor of the solar cell. Shunt resistance is a term for the internal resistance of the solar cell, and therefore controls the amount of power dissipated within the cell. A lower fill factor results in decreased conversion efficiency. This point is well illustrated in the plots shown in Figures 2-9(a-b) [18]. Figure 2-9a is a plot of four calculated I-V curves for an illuminated solar cell with the permutations of R_s values of 0 and 5 Ω and R_{sh} values of 100 and ∞ Ω . While shunt resistance (R_{sh}) has minimal impact on the I-V curves, higher series resistance (R_s) strongly decreases the cell's fill factor. Figure 2-9b plots the relative power generated versus R_s , and indicates the relative power (efficiency) drops

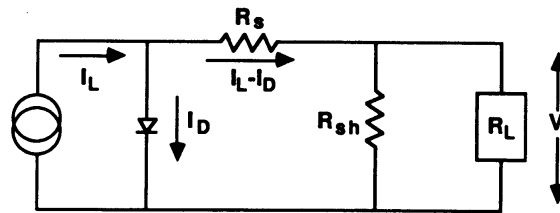
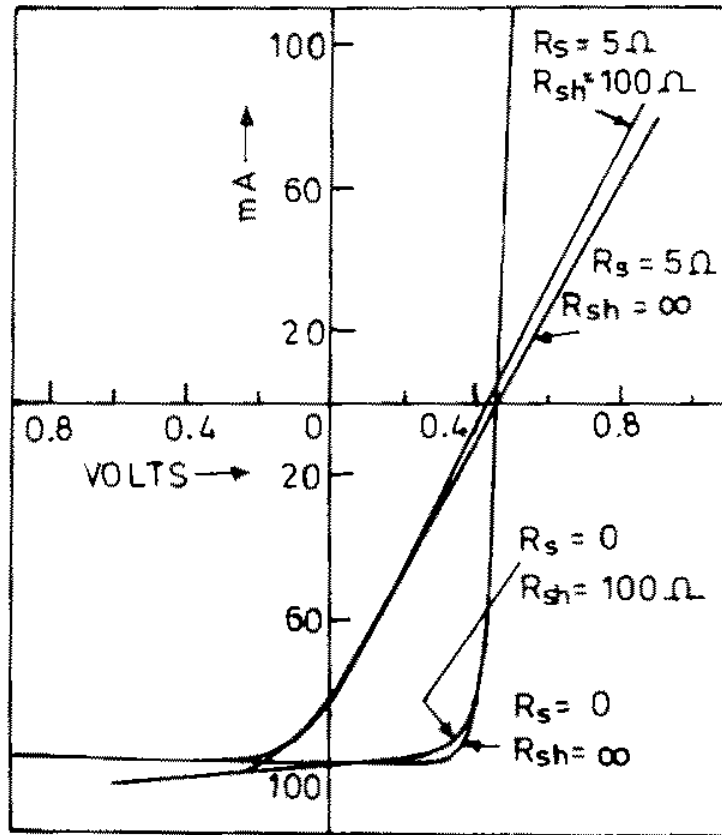
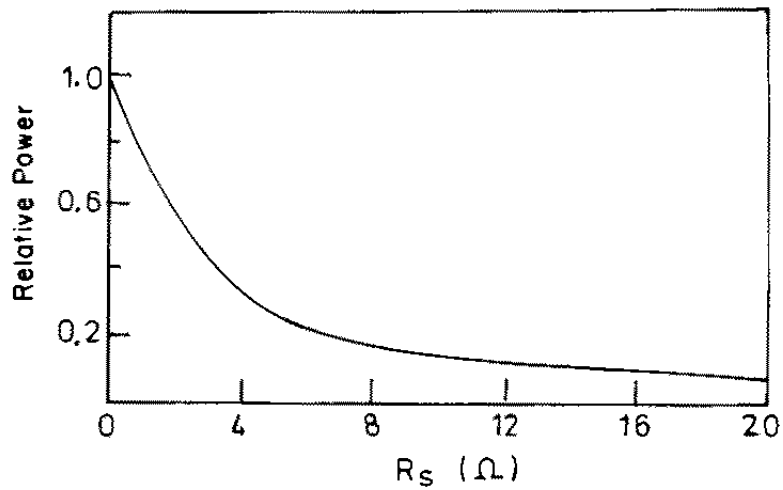


Figure 2-8. Equivalent circuit diagram for a solar cell, showing photocurrent (I_L), dark current (I_D), series resistance (R_s), shunt resistance (R_{sh}), and a load (R_L) [17].



(a)



(b)

Figures 2-9(a-b). Influence of a solar cell's series resistance on the (a) fill factor as shown by the squareness of the I-V curve and (b) relative power as a function of series resistance [18].

sharply with increasing R_s , particularly between 0 and 4 Ω . Series resistance for state of the art CIS based solar cells are $\sim 0.2 \Omega \cdot \text{cm}^2$ [2], and improvement of this value by decreasing the resistivity of the TCO layer will improve FF, and therefore efficiency of the cell.

The second mechanism by which ZnO influences CIS based solar cells is optical losses. This mechanism impacts the I_{sc} , since photons absorbed in the TCE do not generate photo-current. As will be detailed below, the optical properties and the electrical properties are fundamentally related by the plasma resonance and band gap energy, and are discussed in the section concerning optical properties of TCOs below. Optical absorption is a function of the film's thickness (x) and absorbance (α) as shown in Equation 2.4. The series resistance is a function of thickness as well as the resistivity. If the resistivity of ZnO is decreased, thinner films can be used resulting in less optical absorption. The effects of light absorption in the TCE can be investigated by spectrophotometry to characterize transmittance, and the spectral response of the cell, which characterizes the quantum efficiency (QE). Dips in the efficiency for particular wavelength regions of the spectrum can be correlated to spectrophotometry data from the TCE to assess its impact on the solar cell.

2.3 Transparent Conducting Oxides

2.3.1 Background

Transparent conducting oxides (TCOs) have been investigated since the 1950s for use in a variety of applications. Over these years, a large amount of research has been done to improve the optical and electrical properties, and there are several excellent reviews of the work that has been done on TCOs in general [11,12,27], and ZnO

specifically [28]. As a general class of materials, transparent conducting oxides (TCOs) are made of binary and more recently multi-component metal oxides. They are applied as thin films using various deposition techniques such as spray pyrolysis, sputter deposition, chemical vapor deposition, molecular beam epitaxy, and laser ablation [28-32]. The transparency is derived from a large band gap ($E_g > 3$ eV), which prevents absorption of visible wavelengths, and a lack of d-d transitions in the metal cations which could act as color centers. The d-d transitions cannot occur if the d orbitals of the metal cation are full, and therefore many TCOs incorporate this type of cations [13]. This yields a transmittance in the visible often greater than 90% ($T > 90\%$). The low electrical resistivity ($\rho \sim 10^{-3} - 10^{-4} \Omega \cdot \text{cm}$) of these materials is derived from extremely high carrier concentrations ($n \sim 10^{20} - 10^{21} \text{ cm}^{-3}$), since the carrier mobilities are low ($\mu \sim 5 - 50 \text{ cm}^2/\text{V} \cdot \text{s}$). The low mobility is a result of both the inherently low mobility of the oxide materials, and an array of scattering defects in the deposited films. Various figures of merit (FOMs) that incorporate optical absorption and electrical conductivity have been proposed, but no consensus has been reached on a universal FOM. Therefore FOMs are not commonly used in the literature. Until very recently, useful conductivities could only be achieved for *n*-type materials. This has changed with development of *p*-type TCO materials over the past few years [13].

The first oxide found to be transparent and conductive, CdO, was discovered by Badeker in 1907 [33]. The first TCO useful for practical applications was indium oxide doped with tin commonly known as indium tin oxide (ITO), which has a composition of ($\text{In}_2\text{O}_3:\text{SnO}_2$) (90wt%:10wt%). It was developed in the early 50s, and maintains some of the best performance characteristics for optical transparency and electrical conductivity

[11,24]. It has been the TCO of choice during the last 50 years for applications demanding the best conductivity with good optical properties in the visible regime. Currently half of the indium produced in the world finds application in ITO for flat panel display applications [34]. Other TCO materials that have received substantial attention include tin oxide (SnO_2) commonly doped with fluorine, and cadmium stannate (Cd_2SnO_4), which is intrinsically doped. Table 2-2 is a list of historically significant innovations in the TCO field with references compiled by Gordon [24].

Table 2-2. History of processes for making transparent conductors.

Material Process	Reference
Ag by chemical-bath deposition	Unknown Venetian
$\text{SnO}_2\text{:Sb}$ by spray pyrolysis	J. M. Mochel (Corning), 1947 [35]
$\text{SnO}_2\text{:Cl}$ by spray pyrolysis	H. A. McMaster (Libbey-Owens-Ford), 1947 [36]
$\text{SnO}_2\text{:F}$ by spray pyrolysis	W. O. Lytle and A. E. June (PPG), 1951 [37]
$\text{In}_2\text{O}_3\text{:Sn}$ by spray pyrolysis	J. M. Mochel (Corning), 1951 [38]
In_2O_3 : by Sputter Deposition	L. Holland and G. Siddall, 1955 [39]
$\text{SnO}_2\text{:Sb}$ by CVD	H. F. Dates and J. K. Davis (Corning), 1967 [40]
Cd_2SnO_4 by Sputter Deposition	A. J. Nozik (American Cyanamid), 1974 [41]
Cd_2SnO_4 by Spray Pyrolysis	A. J. Nozik (American Cyanamid), 1976 [42]
$\text{SnO}_2\text{:F}$ by CVD	R. G. Gordon (Harvard), 1979 [43]
TiN by CVD	S. R. Kurtz and R. G. Gordon (Harvard), 1986 [44]
ZnO:In by Spray Pyrolysis	S. Major <i>et al.</i> (Indian Inst. Tech), 1984 [45]
ZnO:Al by Sputter Deposition	T. Minami <i>et al.</i> (Kanazawa), 1984 [46]
ZnO:In by Sputtering	S. N. Qiu <i>et al.</i> (McGill), 1987 [47]
ZnO:B by CVD	P. S. Vijayakumar <i>et al.</i> (Arco Solar), 1988 [48]
ZnO:Ga by Sputter Deposition	B. H. Choi <i>et al.</i> (KAIST), 1990 [49]
ZnO:F by CVD	J. Hu and R. G. Gordon (Harvard), 1991 [50]
ZnO:Al by CVD	J. Hu and R. G. Gordon (Harvard), 1992 [51]
ZnO:Ga by CVD	J. Hu and R. G. Gordon (Harvard), 1992 [52]
ZnO:In by CVD	J. Hu and R. G. Gordon (Harvard), 1993 [53]
Zn_2SnO_4 by Sputter Deposition	H. Enoki <i>et al.</i> (Tohoku), 1992 [54]
ZnSnO_3 by Sputter Deposition	T. Minami <i>et al.</i> (Kanazawa), 1994 [55]
Cd_2SnO_4 by Pulsed Laser Dep.	J. M. McGraw <i>et al.</i> (CO. Sch. Mines & NREL), 1995 [56]

Focusing on development of ZnO as a TCO, research started in the late 1970s, with major contributions starting in the 80s. Research in the early 80s focused on intrinsically doped ZnO thin films [57,58], but the electrical properties of these films were found to be unstable above 150°C [59]. The stability issue was resolved by using extrinsically doped films. Figure 2-10 shows progress in decreasing the resistivity of several TCO materials including ZnO with time. Table 2-3 presents a compiled list of electrical properties for doped ZnO films deposited by magnetron sputter deposition. From the table the reader can note that while excellent electrical properties have been achieved, they involve either elevated substrate temperatures or positioning the substrate perpendicular to the source. Recall that elevated temperatures are incompatible with solar cell deposition process, and utilizing a substrate perpendicular to the source has issues with uniformity and feasibility particularly with large area substrates. The low

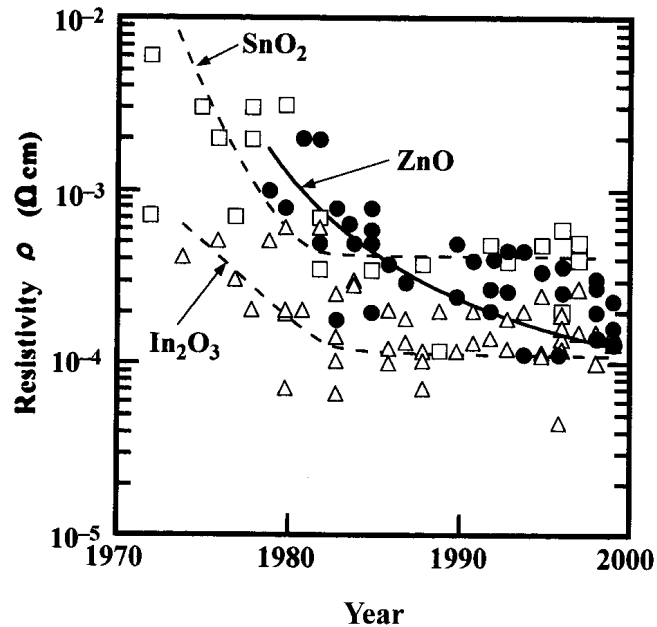


Figure 2-10. Decreasing resistivity of transparent conducting oxides indicating improved performance as a function of time [60].

resistivities achieved suggest that there is room for improvement for films deposited at room temperature with a parallel source and substrate geometry. Room temperature deposition with a parallel substrate and source is most compatible with volume production of CIS based solar cells, and therefore improving electrical properties achieved by this process is critical to improved efficiency in production devices.

Table 2-3. Compilation of electrical data for sputter deposited ZnO thin films with several different dopants.

Dopant	Target	ρ ($\times 10^{-4}$) ($\Omega \cdot \text{cm}$)	n ($\times 10^{20}$) (cm^{-3})	μ ($\text{cm}^2/\text{V} \cdot \text{s}$)	Reference
Al	Zn:Al	4.2	2.6	57	Jäger <i>et al.</i> [61]
Al	Zn:Al	4.0	4.9	32	Jäger <i>et al.</i> [61]
Al	ZnO:Al ₂ O ₃	7.7	4.2	19.5	Menner <i>et al.</i> [62]
Ga	ZnO:Ga ₂ O ₃	5.9	5.9	20	Menner <i>et al.</i> [62]
Al	ZnO:Al	6.5	6.5	15	Cebulla <i>et al.</i> [63]
Al	ZnO:Al	14	4.0	10	Cebulla <i>et al.</i> [63]
Al	ZnAl	2.7	8.4	28	Kluth <i>et al.</i> [64]
Al	ZnO:Al ₂ O ₃	1.9	11	30	Tominaga <i>et al.</i> [65]
Al	ZnO:Al ₂ O ₃	4.7	7.5	15	Park <i>et al.</i> [66]
Al	ZnO:Al ₂ O ₃	2.8	5.8	39	Löffl <i>et al.</i> [67]
Al	ZnO:Al	4.5	8.0	17	Ellmer <i>et al.</i> [68]
Al	ZnO:Al ₂ O ₃	3.6	5.6	37	Nakada <i>et al.</i> [69]
B	ZnO + B ₂ H ₆	4.0	2.6	60	Nakada <i>et al.</i> [69]
B and Al	ZnO:AlB ₁₂	6.5	2.4	40	Nakada <i>et al.</i> [69]
Al	ZnAl	2.7	4.3	53	Schäffler <i>et al.</i> [70]
Al	ZnO:Al	5.3	5.6	20	Konishi <i>et al.</i> [71]
Al	ZnAl	2.5	7.0	36	Mauch <i>et al.</i> [72]
Al	ZnAl	5.0			Harding <i>et al.</i> [72]
In	ZnIn	14			Igasaki <i>et al.</i> [73]
Al	ZnO:Al ₂ O ₃	1.4	13	34	Choi <i>et al.</i> [49]
Ga	ZnO:Ga ₂ O ₃	5.9	15	7	Jin <i>et al.</i> [74]
Al	ZnO:Al	5.4	4.5	26	Minami <i>et al.</i> [75]
Si	ZnO:SiO ₂	3.9			Minami <i>et al.</i> [75]
In	ZnO:In ₂ O ₃	3.0			Qiu <i>et al.</i> [47]
Al	ZnO:Al ₂ O ₃	1.9	15	22	Minami <i>et al.</i> [76]
B	ZnO:B ₂ O ₃	6.4	2.5	39	Minami <i>et al.</i> [76]
Ga	ZnO:Ga ₂ O ₃	5.1	4.4	28	Minami <i>et al.</i> [76]
In	ZnO:In ₂ O ₃	8.1	4.0	20	Minami <i>et al.</i> [76]
Defects	ZnO (Ar+H ₂)	20	2.0	16	Webb <i>et al.</i> [77]

Transparent conducting oxide thin films are used for a variety of applications, and depend on several different materials for optimum properties. The largest application is for heat reflecting, low emissivity coatings for architectural glass. This application does not require good electrical properties, only a high carrier concentration to achieve low emissivity in the infrared. Due to the huge area of coated material, it also depends on the use of an abundant and cheap material, which is easy to deposit. These criteria are best satisfied by fluorine doped tin oxide ($\text{SnO}_2:\text{F}$) deposited by spray pyrolysis or chemical vapor deposition [11,34]. Another large application is in visual displays. Modern cathode ray tube (CRT) displays use TCO films to dissipate static, and absorb magnetic radiation [34]. The flat panel display (FPD) industry uses TCO films as a transparent contact for displays based on LCD, electroluminescent, plasma, and other technologies. This application demands low resistivities ($1-3 \times 10^{-4} \Omega\text{-cm}$) and high transmittance ($T > 90\%$) in the visible, but the optical properties in the IR are not critical [34]. The high costs associated with FPDs make the expense associated with ITO justifiable for the performance needed.

The application of interest for this work is the use of ZnO films for CIS based solar cells. A solar cell TCE is a very demanding application, particularly for large area modules because current is transported over long distances. Both a low resistivity and high transmission in the visible and near infrared are critical to the efficiency of the device. Also, in the band diagram presented in Figure 2-7, the electron affinity match between ZnO and CIS is excellent, promoting good interfacial electrical properties. Zinc oxide based TCE layers are also used for all the highest efficiency cells, indicating good performance, and ZnO is inexpensive to produce due to the abundance of Zn, which is

critical to lowering production cost and enabling large volume production, respectively. Additionally, the highly resistive i-ZnO layer is critical to formation of high performance CIS based solar cells, and can be effectively deposited by adding oxygen to the sputtering gas ambient with deposition of ZnO:Al. Therefore, ZnO is very suitable for application as a TCE to CIS based solar cells.

2.3.2 Electrical Properties of TCOs

Improved electrical properties of deposited ZnO:Al thin films is one of the primary objectives of this work; therefore, electrical properties of TCO materials are reviewed and important concepts used to analyze results are presented. A majority of the published literature discusses the electrical properties of TCOs in terms of resistivity (ρ), which is the reciprocal of conductivity (σ), and has units of ohm·cm ($\Omega\cdot\text{cm}$). An early difficulty arises in whether to treat the electrical properties using a metallic free electron theory, or using semiconductor transport theory. Evidence that supports the case of metallic conduction include the lack of temperature dependence for the carrier concentration data down to very low temperatures (16K) [78]. This suggests that the doping density has exceeded the Mott critical density [79], and therefore has metallic like behavior. Above the Mott transition, the semiconductor is considered degenerate, meaning that the wave functions of the dopant atoms are interacting. Thus, to obey Pauli's exclusion principle the defect level generated by the dopant splits and an impurity band is formed. For the case of ZnO, at high doping levels, the impurity band moves into the conduction band, and results in the Fermi energy (E_F) being above the conduction band edge. Above the Mott transition, the dopant atoms are no longer ionized, as there

are no free states to be thermally ionized into. This is consistent with the lack of *carrier freeze out* behavior for low temperature Hall measurements [78].

The classical theory of conductivity in metals was developed by Drude at the turn of the century, and is based on equations of motion for electrons, with a term for drag to characterize the interaction of the medium with moving carriers. The conductivity, σ , or inverse of resistivity (ρ^{-1}) can be expressed as shown in Equation 2.6 [80,81].

$$\sigma = \frac{1}{\rho} = \frac{ne^2\tau}{m} \quad (2.6)$$

where n (cm^{-3}) is the density of free carriers, e (C) is the charge of the electron, τ (s^{-1}) is the relaxation time for the carrier which relates time between collisions, and m is the free electron mass. A relaxation time on the order of 10^{-15} seconds is typical for a TCO [82]. The term τ relates the motion of electrons to the applied electric field, as is shown in Equation 2.7 [83], where v_f is the final drift velocity for electrons and E is the electric field strength.

$$\tau = \frac{mv_f}{eE} \quad (2.7)$$

From this we can derive a mean free path (l) between carrier collisions, which is related to the carrier velocity (v) as shown in Equation 2.8 [83].

$$l = v\tau \quad (2.8)$$

Equation 2.8 is used in Chapters 5 and 6 to evaluate the mean free path for conduction electrons. The carrier velocity (v) used for these calculations is the thermal carrier velocity, which is $\sim 10^7$ cm/s [83]. The term τ describes the interaction between the electron and the material hosting conduction. The two fundamental mechanisms controlling the relaxation time are scattering events with the lattice (phonon scattering)

and defect scattering. Phonon scattering is a function of temperature, and tends to decrease with decreasing temperature. Defect scattering tends to be independent of temperature. Because the different scattering mechanisms are independent of energy and each other, the contributions of scattering by phonons, impurities, or defects can be summed using Mathiessen's rule as shown in Equation 2.9 [81].

$$\rho = \rho_{phonon} + \rho_{impurity} + \rho_{defect} \quad (2.9)$$

Metallic conductivity may also be described using quantum mechanics, with similar results. The primary distinctions made by quantum mechanical description of resistivity involves acknowledging that only electrons near the Fermi energy participate in conduction, and that the drift velocity of the electron in an electric field is small compared to the thermal velocity of the electrons at the Fermi energy. Therefore the velocity in Equation 2.7 becomes the Fermi velocity (v_F) instead of the drift velocity.

The vast majority of the literature treats TCOs as a degenerate semiconducting material, and use transport equations developed for semiconductors in analysis of the electrical properties. For this case, the relaxation time becomes a function of energy, and relaxation by different mechanisms are no longer necessarily independent of each other. For carrier concentration, it must be recognized that there are two types of carriers, electrons (n) and holes (p). For ZnO, the carrier type is electrons, and is therefore similar to metals with the exception that defects and/or impurities generate the carriers. The relaxation time becomes a mean relaxation time $\langle\tau\rangle$, and is replaced in the conductivity equations by a mobility (μ with units of $\text{cm}^2/\text{V}\cdot\text{s}$) as shown in the basic equation of conductivity for a semiconductor presented in Equation 2.10.

$$\sigma = \frac{1}{\rho} = (n e \mu_n + p e \mu_p) \quad (2.10)$$

where n is the concentration of electron carriers (cm^{-3}), p is the concentration of hole carriers (cm^{-3}), e is the charge of an electron, μ_n is the mobility of electrons ($\text{cm}^2/\text{V}\cdot\text{s}$), and μ_p is the mobility of holes ($\text{cm}^2/\text{V}\cdot\text{s}$). Mobility describes the interactions between carriers and the material through which they move. Carrier concentration is the density of mobile charge carriers available for conduction. The relationship between the mobility and the mean relaxation time is seen in Equation 2.11 [17],

$$\mu = \frac{e\langle\tau\rangle}{m^*} \quad (2.11)$$

where m^* is the effective mass, and $\langle\tau\rangle$ is the mean relaxation time. For metallic conduction, $\langle\tau\rangle$ simplifies to τ , and shows that the mobility can remain a useful indicator of carrier transport for metallic conduction [17]. Equation 2.11 is used to approximate the carrier relaxation time from the Hall mobility.

The effective mass of an electron appears in Equation 2.11, and is a concept that relates the influence of a material on the motions of electrons resulting from applied forces (electric field, magnetic field, etc). If the relaxation time (τ) is constant, then by Equation 2.11, a smaller effective mass will result in a larger mobility. As a general class of materials, TCOs have large effective masses, which for ZnO is reported to be $0.27m_0$, or 27% of the free electron mass [84].

Ideal ZnO, with perfect stoichiometry and no defects should be an insulator, with resistivity greater than $10^5 \Omega\cdot\text{cm}$. In reality, point defects are electrically active in ZnO, and in particular Zn interstitials and/or O vacancies are typically believed to generate conduction band electrons [85] which lower the resistivity to $\sim 10^{-4} \Omega\cdot\text{cm}$ [86]. To lower the resistivity to the $10^{-4} \Omega\cdot\text{cm}$ level desired for TCOs requires doping ZnO to carrier concentrations above 10^{20}cm^{-3} , while maintaining mobilities greater than $10 \text{cm}^2/\text{V}\cdot\text{s}$.

ZnO is almost exclusively *n*-type and this is the case treated here. As a side note, *p*-type ZnO has been recently reported, but has proven difficult to reproduce [13].

Doping can be accomplished by intrinsic and extrinsic dopants. Intrinsic dopants result from deviations in stoichiometry, and are the source for the native *n*-type conductivity that ZnO can have. In terms of Kröger-Vink notation, the native doping defects are Zn_i and V_O for zinc interstitials and oxygen vacancies, respectively. Intrinsic doping can achieve carrier concentrations of low 10^{20} cm^{-3} , and some of the best mobilities ($>50 \text{ cm}^2/\text{V}\cdot\text{s}$), with resistivities on the order of $10^{-3} \Omega\cdot\text{cm}$ [58]. The drawbacks of intrinsic doping are the susceptibility to decreased carrier concentration with increased temperature and oxygen potential of the gas ambient [59], inability to produce sufficiently high carrier concentrations ($n > 5 \times 10^{20} \text{ cm}^{-3}$), and difficulty in precisely controlling the stoichiometry to achieve the doping goals.

In the mid-80s, the use of extrinsic dopants was developed, allowing much of the progress in decreasing resistivity shown earlier in Figure 2-10. Some of the most commonly used dopants are group III elements, which substitute on the Zn lattice and act as electron donors [60]. The most commonly used dopant is Al, but B, Ga, and In have also been used. The group III element contributes one carrier per atom to the conduction band. Aluminum is abundant, easily incorporated, cheap, and non-toxic. A halogen atom on the oxygen also acts as a donor, contributing one electron to the conduction band. Fluorine (F_O) is the only halogen reported in the literature, and substitutes well for O because of their similar ionic radii [86]. Resistivity, carrier concentration, and Hall mobility of $4 \times 10^{-4} \Omega\cdot\text{cm}$, $5 \times 10^{20} \text{ cm}^{-3}$, and $40 \text{ cm}^2/\text{V}\cdot\text{s}$ have been reported [50]. The high mobility is hypothesized to result from F sitting on the O sublattice, where the ionized F^-

impurity scattering center introduced by the dopant primarily affects the valence band, and therefore does not as effectively scatter carriers in the conduction band [50]. On the other hand, group IV elements, and a variety of transition metals have been shown to exhibit poorer electrical and optical properties than the group III elements and F [60], presumably due to increased scattering. One difficulty in controlling carrier concentration is that intrinsic and extrinsic doping mechanisms can both be active. Recall that intrinsic doping results from deviations in stoichiometry in the form of Zn_i and V_O . Typically atomic densities are 5×10^{22} atoms/cm³, while typical doping levels are 10^{20} cm⁻³, indicating stoichiometric changes of ~0.1% can yield significant changes in carrier concentration. Additionally, the native defects of oxygen interstitials (O_i) and zinc vacancies (V_{Zn}) are reported to compensate conduction band electrons [85], and can therefore decrease carrier concentrations generated by intrinsic and/or extrinsic doping.

Grain boundaries add an additional layer of complexity to the investigation of electrical properties. Surface states and chemisorbed oxygen species both deplete carriers from the conduction band [9,78]. Surface states are states formed within the band gap resulting from the break in atomic bonding symmetry at the interface. Carriers enter the deep levels, and a space charge region occurs on each side of the grain boundary as shown in Figure 2-11 [3]. Similar to a *p-n* junction, the width of this depletion region is a function of the carrier concentration, and becomes smaller as the carrier concentration increases [78]. As the potential barrier becomes very narrow, tunneling transport supercedes thermionic associated with the Petritz model for grain boundary scattering [87]. The influence of grain boundaries on the electrical properties occurs through scattering, which is considered below.

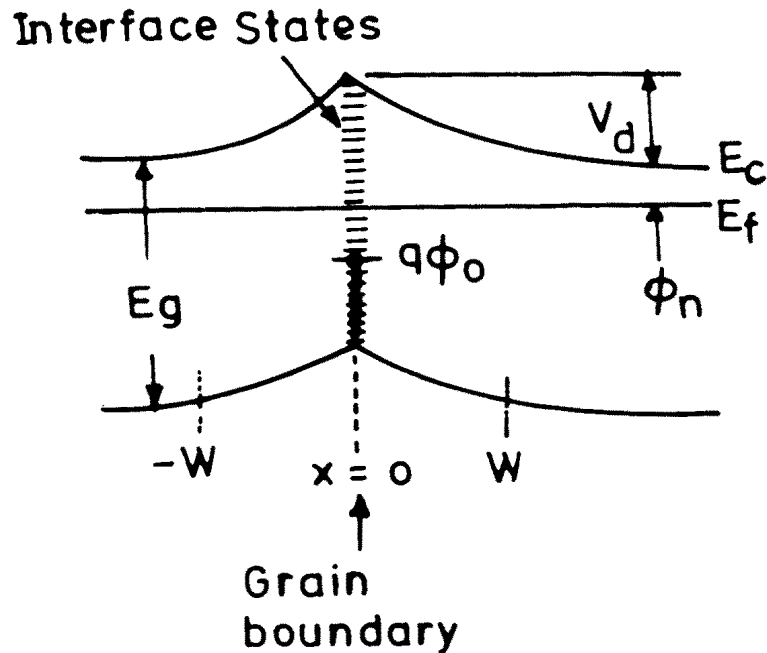


Figure 2-11. Schematic representation of the influence of grain boundaries and interface states on the band bending at the interface [3].

The issue of chemisorbed oxygen species at grain boundaries is important for applications of ZnO as a solid state gas sensor [6,9]. Changes between reducing and oxidizing ambients can be measured by changes in the resistivity of the material. In an oxidizing ambient, oxygen species, often attributed to O^- , bond to the surface by trapping a conduction band electron from ZnO. When the surface concentration of the species is high, and the grain size of ZnO is small, the grains can become depleted of carriers, and result in a significant increase in the resistivity. A schematic of the chemisorption process and its influence on band bending at the grain boundaries is presented in Figure 2-12 [9]. Though this illustration uses SnO_2 , ZnO follows the same process. It shows two grains of SnO_2 with chemisorbed oxygen. Below is a schematic of the potential across the grain boundary, and illustrates how the potential barrier is smaller when

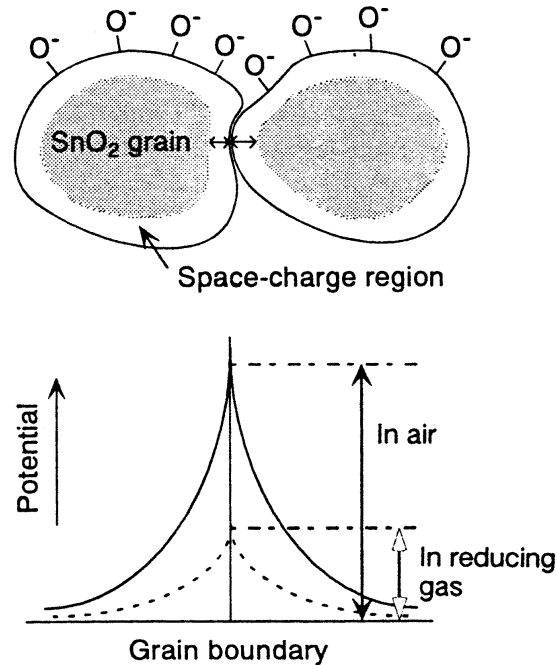


Figure 2-12. Illustration of the chemisorbed oxygen mechanism for solid state gas sensors, and the influence of chemisorbed oxygen on band bending at interfaces [9].

the sensor is in reducing environments, and higher in oxidizing environments. If a ZnO sensor is held at an appropriate temperature, and placed in a reducing gas, the concentration of the surface oxide species decreases, and the resistivity decreases. The decrease in carrier concentration resulting from the chemisorption process affects the electrical properties in two ways. The first is the lowering of the carrier concentration, which directly lowers the conductivity. Secondly, increased chemisorption results in a wider potential barrier, which more effectively scatters carriers, and therefore decreases carrier mobility [6].

A high carrier concentration is critical for a good TCO, but there are certain fundamental limits that must be addressed. The carrier concentration has a direct influence on the optical properties of the material. This relationship will be explored in the following section regarding the optical properties of TCOs. The end result is that a

very high carrier concentration compromises the optical properties of the material. These limits on high carrier concentrations result in carrier mobility being an important parameter for reducing the deposited film's resistivity. Increased mobility yields small improvements to optical properties in the infrared. Therefore to lower the resistivity, it is critical to increase the carrier mobility or identically lengthen the carrier relaxation time [11,82].

As was shown in Equation 2.11, the mobility is a function of the effective mass of the carriers, and the mean time between collisions. The effective mass is an intrinsic property of the material, which is $m^*=0.27$ for the case of pure ZnO. Therefore in order to increase the mobility, the mean time between carrier scattering events must be lengthened. Scattering involves the interaction of carriers with various aspects of the material, with important scattering mechanisms in TCOs including the crystalline lattice (μ_a), ionized impurities (μ_i), neutral impurities (μ_n), and grain boundaries (μ_g). Equation 2.12 is used to sum the effects of multiple scattering mechanisms.

$$\frac{1}{\mu} = \frac{1}{\mu_i} + \frac{1}{\mu_a} + \frac{1}{\mu_g} + \kappa \quad (2.12)$$

If one scattering mechanism is the culprit for a significantly lower mobility, then the overall mobility tends to be near the lowest value, and the scattering mechanism with the lowest mobility is considered the dominant scattering mechanism. If the carrier mobilities from more than one scattering mechanism are similar then the overall mobility will be lower than the individual components.

Lattice or phonon scattering occurs when charge carriers interact with lattice vibrations, which for a material with more than one atom per primitive basis has optical and acoustic phonon modes [17]. The only way to increase the mobility resulting from

phonon scattering is to decrease the temperature, which is not practical for TCO applications. Therefore, this scattering mechanism is relatively fundamental, as this form of scattering occurs even in a perfect crystal. The limiting value for mobility due to phonon scattering in lightly doped ($n \sim 10^{16} \text{ cm}^{-3}$) single crystalline ZnO is approximately $\mu_a = 250 \text{ cm}^2/\text{V}\cdot\text{s}$ [88] at room temperature. For both metallic and semiconductor conduction, phonon scattering is temperature dependent, with mobility increasing with decreasing temperature [80].

Ionized impurity scattering involves interactions and scattering of charge carriers by ions within the material through coulombic forces. This mechanism commonly dominates the mobility of highly doped silicon semiconductors used in today's integrated circuits. It is also commonly cited as the dominant scattering mechanism in TCO materials [60,78,89]. This mechanism, it is treated by a variety of different models and assumptions, typically with little or none of the derivation provided in accessible peer reviewed literature. Recall that the Mott transition describes the transition between insulating and metallic character with doping for a semiconductor. If heavily doped ZnO has made the transition to metallic character, then impurities are no longer ionized [79]. Temperature dependent Hall measurements taken from a variety of TCO materials including ZnO show a constant carrier concentration to low temperatures ($T < 20\text{K}$ or $kT < 2 \text{ meV}$), which suggest metallic character. Even if they are not ionized, dopant atoms could still yield scattering as neutral impurities, which will be discussed below.

Ionized impurity scattering is modeled as a coulombic potential between ionized atoms and charge carriers, and analyzed using quantum mechanic methods. The Brooks-Herring model adds a screening potential due to other carriers [90]. Higher

concentrations of ionized impurities yield more interactions, and therefore a lower mobility. For the non-degenerate case, the mobility due to ionized impurity scattering increases with temperature. Equation 2.13 gives the relationship between the mobility from ionized impurity scattering, temperature, and the ionized impurity density (N_i) [17].

$$\mu_i \propto \frac{T^{\frac{3}{2}}}{N_i} \quad (2.13)$$

This relationship is based on use of the Maxwell-Boltzmann distribution function, whereas the Fermi-Dirac distribution function should be used for a degenerately doped semiconductor. In a report by Zhang *et al.*, it is suggested that mobility from ionized impurity scattering loses its dependence on temperature when the Fermi-Dirac distribution function is used for the degenerate semiconductor case [78].

Neutral impurity scattering results from non-ionized point defects scattering charge carriers [17]. For the case of semiconductors, this scattering mechanism is typically only important at low temperatures when ionization of dopant atoms is *frozen out*. In contrast, neutral impurities are a common scattering mechanism in metallic conductivity. This is expected, as semiconductor materials tend to have exceptionally high purity with most foreign atoms being purposely introduced to ionize and dope the material. Neutral impurity scattering is not a function of temperature, but is found to vary with the density of neutral impurities [17]. Increasing concentrations of neutral impurities decrease the mobility. For the case of metallic conduction, neutral impurities are believed to scatter carriers by interrupting the periodicity of the lattice [80].

Two other sources of scattering are dislocations and extended defects such as grain boundaries. For metallic conduction, these defects cause scattering by introducing

perturbations in the periodicity of the crystal structure. Like neutral impurities, as the concentration of defects increases, more scattering occurs, which decreases the mobility. The effect of dislocations on carrier transport in semiconductors models the dislocation as a line charge in combination with a strain field [17]. This yields a mobility that is a function of the density of dislocations (n_d) and temperature, as shown in Equation 2.14 [17], where

$$\mu_d \propto \frac{1}{n_d T^{\frac{1}{2}}} . \quad (2.14)$$

The Petritz model is the most established theory for modeling carrier scattering at grain boundaries [87]. This model specifies that surface states at the boundary yield a depletion region around the boundary, and a potential barrier develops that must be surmounted for transport, and therefore relies on thermionic transport [78]. For the case of degenerately doped ZnO, the depletion region at the interface becomes very narrow, increasing the probability of carriers tunneling through the potential barrier, which decreases scattering [78]. This case is more analogous to metals, where grain boundary scattering tends to be a small effect at room temperature.

Chemisorption of oxygen species further complicates modeling electrical properties of grain boundaries. Recall that chemisorption of oxygen species trap conduction band electrons, and therefore can cause a depletion region at grain boundaries. The depletion region and the grain boundary can result in a potential barrier similar to the potential barrier generated by interface states considered above. The magnitude of changes in resistivity caused by chemisorption of oxygen species depends on the carrier concentration, surface area/grain boundary area to grain volume ratio, and concentration of chemisorbed oxygen species. For larger grain sizes in a heavily doped

material, the ratio of charge trapped in chemisorbed species to the quantity of carriers in the grain is small, therefore chemisorption does not significantly increase resistivity. For the case of very small grains or very thin films, chemisorption can trap a significant portion the free carriers, which decreases carrier concentration, and increase grain boundary scattering, and therefore increases resistivity. The sensitivity of resistivity for ZnO thin films to the oxygen potential of the annealing ambient, even at mild temperatures (300 – 400 °C) is widely attributed to this process [11,91,92]. It is difficult to measure the amount of chemisorbed oxygen in as deposited films due to contamination in the atmosphere for transfer of samples to characterization tools. If the quantity could be investigated and controlled, improved film electrical properties could result.

2.3.3 Optical Properties

The optical properties for deposited ZnO films are of critical importance towards application as a TCE, and are also useful for characterizing electrical properties of the films. The optical properties of TCOs arise from the interaction of light with electrons, and the physical structure of the film. The goal is to minimize these interactions, such that transmission of light is maximized. Processes involving electrons include band edge absorption [17], plasma resonance effects (absorption and reflection) [80-82], the Burstein-Moss shift [93], and defect absorption. Processes based on the physical structure of the film include thin film optical interference or Fabry-Perot oscillations [94], and light scattering [95]. Each of these effects will be discussed below, along with their influence on the optical properties of ZnO thin films.

Band edge absorption involves absorption of a photon to promote an electron from the valence band to the conduction band of a semiconductor. This absorption only occurs if the photon energy is greater than the band gap energy of the material. The band

gap of ZnO is direct and is about 3.2 eV for intrinsic material, which corresponds in energy to a photon with a wavelength of 388 nm. Equation 2.15 shows the relationship between absorbance (α), photon energy ($h\nu$), and the band gap energy (E_g) for allowed direct transitions [17].

$$\alpha = K(h\nu - E_g)^{\frac{1}{2}} \quad (2.15)$$

The term K is a material dependent constant, and is independent of the photon energy. This equation is useful for calculating the optical band gap of a material from spectrophotometry data. As we can see from the AM1.5 solar spectrum in Figure 2-3, a band gap of about ~3 eV ($\lambda \sim 400$ nm) is the minimum band gap for transmitting most of the solar spectrum.

The second optical effect that is critical for a TCO is plasma resonance effects. The term plasma refers to mobile charge carriers, in the case of *n*-ZnO, electrons in the conduction band. The carriers can be accelerated by the electric field component of electro-magnetic radiation, and their motion can be modeled as Lorentzian Oscillators [80,81]. The optical properties that result from these carriers were derived by Drude, and involve using a combination of the classical wave equation for motion of the carriers and Maxwell's equations to determine the complex permittivity that results. The real (ϵ_1) and imaginary (ϵ_2) components of the complex permittivity can be used to determine reflection, absorption, and transmission characteristics of the electron plasma [80,81]. The results for TCOs are similar to those of metals, and show that the carriers can resonate with the EM radiation at a particular frequency known as the plasma resonance frequency (ω_p). The plasma resonance frequency ω_p is a function of the carrier

concentration, the effective mass of the electron, and the dc (ϵ_0) and high frequency (ϵ_∞) dielectric constants as shown in Equation 2.16 [80-82].

$$\omega_p = \left(\frac{ne^2}{\epsilon_0 \epsilon_\infty m^*} \right)^{\frac{1}{2}} \quad (2.16)$$

This frequency is then used in equations for the complex permittivity, or complex dielectric constant, which has a real component (ϵ_1) and a complex component (ϵ_2).

Relationships between the frequency of an electric field, the plasma resonance frequency ω_p , and the dielectric constant are shown in Equations 2.17 and 2.18.

$$\epsilon_1 = \epsilon_\infty \left(1 - \frac{\omega_p^2}{\omega^2} \right) \quad (2.17)$$

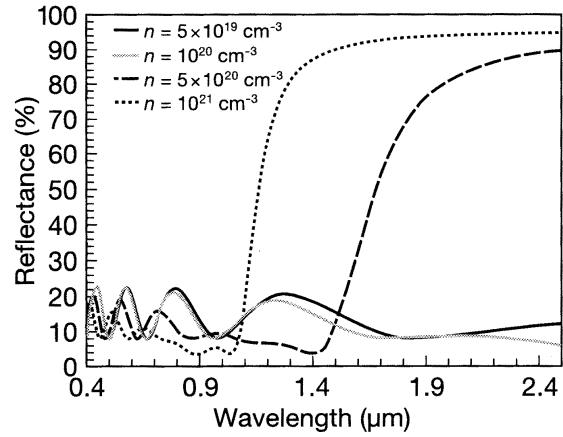
$$\epsilon_2 = \left(\frac{\epsilon_\infty \omega_p^2}{\omega^3 \tau} \right) \quad (2.18)$$

The term ω represents the angular frequency of the incident light, τ is the carrier relaxation time, and ϵ_∞ is the high frequency dielectric constant. The equations are based on the assumption that $1/\tau \ll \omega$ [82], indicating that the carriers are free. The results of these equations are that for $\omega < \omega_p$, $\epsilon_1 < 0$ and ϵ_2 is large which yields reflective behavior. For the region near $\omega = \omega_p$, $\epsilon_1 = 0$ and ϵ_2 is smaller, yielding a transition region from reflecting to absorbing character, which is seen in the plot of film reflectance versus wavelength in Figure 2-13a [82], where the wavelength at which the transition occurs changes with carrier concentration. Observe that higher carrier concentrations move the transition associated with the plasma resonance frequency ω_p to shorter wavelengths. In Figure 2-13b [82], absorptance is plotted versus wavelength, and shows the effects of carrier concentration on free carrier absorption. The absorptance relates the percentage of the incident light that is absorbed by the film, and care should be taken not to confuse

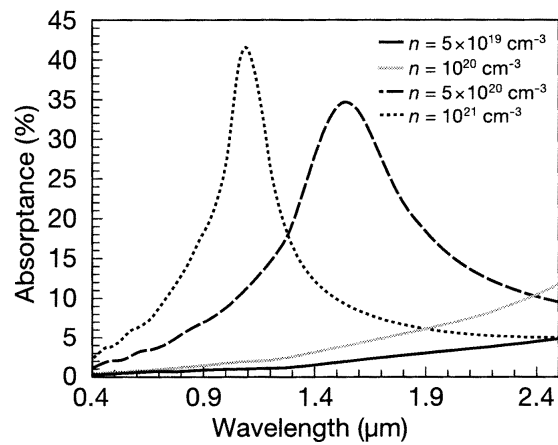
it with absorbance (α) the intrinsic property of a material that defines its ability to absorb light. The other term used in this work is absorption or optical absorption, which is the product of the absorbance and the distance light travels through the medium ($\alpha \cdot x$), and is a unitless number. Figure 2-13c [82] also plots absorptance versus wavelength, and shows changes in absorptance with mobility. Notice that high carrier concentrations increase absorptance, and moves the peak in absorptance to shorter wavelengths, while increasing mobility decreases absorptance, but does not influence the wavelength of the peak. As ω increases, $\omega > \omega_p$, ϵ_1 approaches ϵ_∞ , and ϵ_2 approaches 0, yielding classic dielectric behavior, which indicates EM radiation propagates through the material. This behavior is seen in each of the above plots as the region where neither reflection nor absorption occurs indicating light is transmitted.

The wavelength at which free carrier optical effects are significant are controlled predominantly by the carrier concentration and carrier effective mass. For the case of ZnO on a CIS based solar cell, the band gap of CIS is 1.04 eV, which corresponds to a wavelength of ~ 1200 nm. ZnO with an effective mass $m^* = 0.27$ and a carrier concentration of $5 \times 10^{20} \text{ cm}^{-3}$ has a plasma resonance frequency ω_p which corresponds to a wavelength of 1200 nm. Therefore the optical properties for samples with carrier concentrations on the order of $5 \times 10^{20} \text{ cm}^{-3}$ and above must be measured to determine the impact on the solar cell performance.

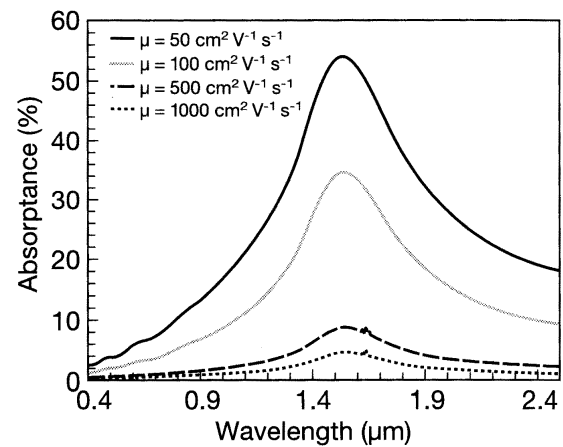
In contrast to carrier concentration, which if values are too large will result in the deposited film reflecting or absorbing light needed by the cell, higher carrier mobilities do not change the plasma resonance frequency. Recall that increasing mobility in fact helps decrease the absorptance resulting from free carrier absorption. This indicates that



(a)



(b)



(c)

Figures 2-13(a-c). Theoretical plots of relationships between electrical and optical properties for (a) reflectance versus carrier concentration, (b) absorbance versus carrier concentration, and (c) absorbance versus carrier mobility [82].

the mobility can be increased, which decreases resistivity, without compromising infrared transmittance. Thus, decreasing the resistivity of ZnO for solar cell applications is best accomplished by improving the mobility, while maintaining the maximum carrier concentration not degrading infrared transmittance for wavelengths needed by the solar cell.

The Burstein-Moss shift is a band gap widening process that can occur in degenerately doped material [93]. As the carrier concentration increases, the Fermi energy moves above the conduction band edge, resulting in complete occupation of states at the bottom of the conduction band. Therefore, optically stimulated transitions to these states cannot occur, and the optical band gap of the material increases. This process is illustrated schematically in Figure 2-14. The vertical area shows the allowed transition from the valence band to an energy in the conduction band above the Fermi energy. The amount of the shift is a function of the doping concentration, and the density-of-states effective mass (m_{cv}^*) as shown in Equation 2.19 [11].

$$\Delta E_g = \frac{h^2}{8m_{cv}^*} \left(\frac{3n}{\pi} \right)^{\frac{2}{3}} \quad (2.19)$$

The density-of-states effective mass reflects the fact that the effective mass of a conduction band electron can be a function of conduction band density-of-states in some situations [96]. For the particular case of ZnO, the band gap is already large enough that the useful solar spectrum is transmitted effectively, so an increase in the band gap is not required.

Defect absorption for TCOs can take two forms, absorption of light that promotes an electron to a defect level, and absorption by metallic particles in the TCO. These

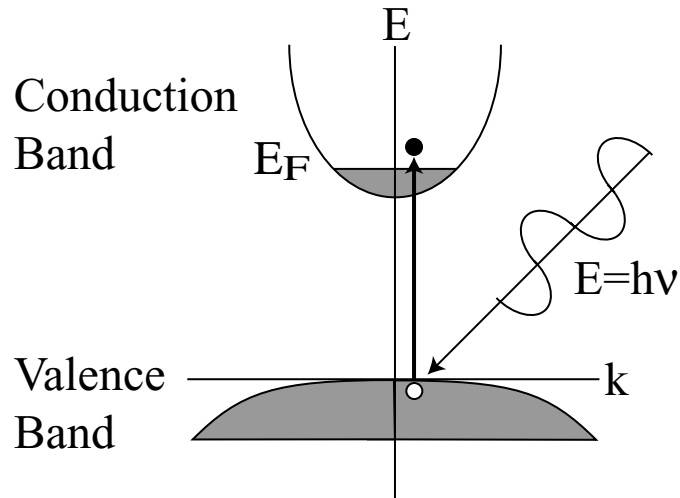


Figure 2-14. Illustration of the Burstein-Moss shift, which increases the optical band gap due to occupancy of states in the conduction band.

processes will be discussed qualitatively. The first process involves an impurity or defect of some form which generates a state within the band gap. A photon with the correct energy can promote an electron from the valence band or another defect state into the defect state, with the photon being absorbed. The second process arises because many TCOs are intentionally or unintentionally off stoichiometry towards the oxygen deficient side. If the material is far enough off stoichiometry, then highly reflective scattering precipitates can form. This more often occurs in films deposited by reactive sputter deposition, as seen by the transition from opaque to transparent films with increasing oxygen partial pressure in the sputtering gas [97]. Poor transparency across the visible spectrum is often attributed to defect absorption, but typically no mechanism for the absorption is given.

The next two effects are based on the structure of the film and the fact that the index of refraction (n) for pure ZnO is $n=2.1$ [94], which is different than glass ($n=1.4$) and air ($n=1.0$). The result for films with a thickness on the order of the wavelength of

light is that multiple internal reflections can occur, and depending on the wavelength of light, angle of incidence, and indices of refraction for the substrate and thin films, interference effects can result. Interference effects are found in spectrophotometry data for ZnO:Al films on glass in this work. The reflectance at an interface results from differences in the index of refraction, and follows the relationship expressed in Equation 2.20 with n as the index of refraction, and k as the extinction coefficient.

$$R = \frac{(n-1)^2 + k^2}{(n+1)^2 + k^2} \quad (2.20)$$

Figure 2-15 is a schematic of multiple reflections occurring within a thin film, with a series of terms r and t when the illustrated light rays intersect a surface. The term r describes the component of light reflected from the interface, and the term t describes the light transmitted through the interface. The subscripts relate from which interface the reflection or transmission has occurred, and the superscripts relate how many times the

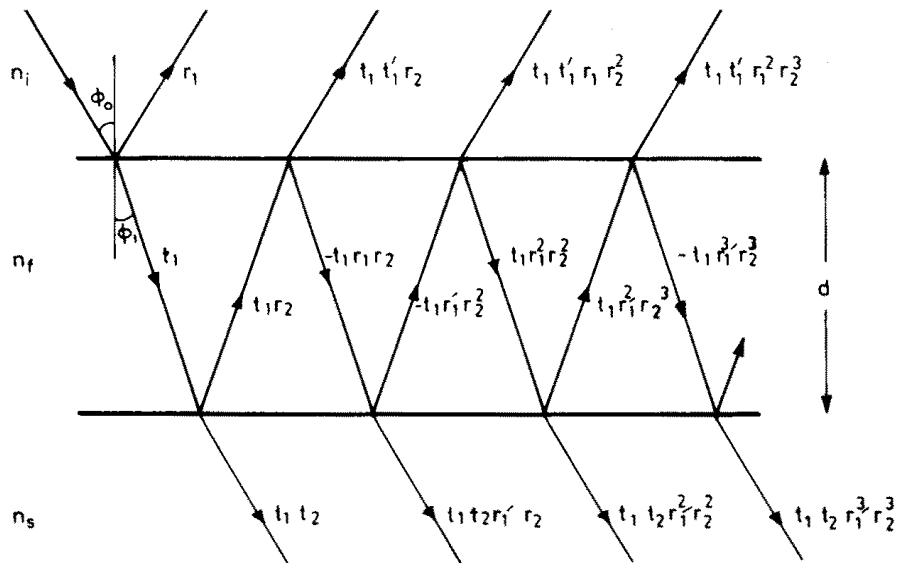


Figure 2-15. Generation of interference colors or Fabry-Perot oscillations due the optical paths in a thin film on a substrate in air [3].

light ray has been transmitted or reflected from the interface. For the case of solar cells, an anti-reflective coating (typically $1/4\lambda$ thick MgF_2) is applied to the surface, which prevents initial reflections from the ZnO. The Fabry-Perot oscillations result in an oscillatory behavior in the transmittance and reflectance spectra, and can be seen clearly in most of the collected spectrophotometry data.

The final effect to consider is scattering of light. Scattering can occur at the film's surface, which typically results from roughness, or from within the bulk of the film. Scattering from within the film results from inhomogeneity in the index of refraction, which can result from extended defects such as grain boundaries, inclusions, voids, cracks, and others [94]. The films produced in this work are highly transparent to the eye, and specular reflection from the film's surface is observed, suggesting that minimal scattering is occurring from the surface or "bulk" of the film.

2.4 Sputter Deposition

2.4.1 Background

The primary focus of this work is on improving the properties of sputter deposited ZnO:Al thin films. It is therefore critical to present some background knowledge about sputter deposition, influences the various process parameters exert on the plasma, and their relationship to properties of the deposited film. The sputtering process was first reported in 1852 by Grove [98]. It has evolved significantly since then to the point that in the last 50 years it has been used to deposit films on architectural glass, integrated circuits, hard drive platters, and a plethora of other applications. The sputtering process is a glow discharge or a plasma process, which uses ionized gas atoms/molecules accelerate in an electric field to erode material from a source (target), which then

condense from the gas phase on a work piece (substrate). A strong negative field is applied to the target to attract positive ions, hence a sputter deposition source is referred to as the cathode. If a thin film with the same chemistry as the target is desired, a noble gas (e.g. Ar) ambient is typically used.

The erosion of the target is a momentum transfer process [99], the efficiency of which is termed the sputter yield (S atoms/ion). Liberating a deposited flux involves transferring energy to surface atoms of the target material, and the atoms of the surface acquiring enough energy to escape the target. The maximum energy transferred between two colliding particles is determined by the difference in their mass as shown in Equation 2.21 [94].

$$\frac{E_2}{E_1} = \frac{4M_1M_2}{(M_1 + M_2)^2} \cos^2 \theta \quad (2.21)$$

The terms E_1 and E_2 refer to the energy of the separate particles in a binary collision, M_1 and M_2 are the masses of the particles, and θ is the angle of the collision. Equation 2.21 represents the maximum energy that can be transferred from the energetic gas atom impinging on the target to a surface atom on the target. The energy needed to liberate an atom from the target is related to its surface binding energy (E_b), and therefore this minimum quantity of energy must be supplied by the ions to sputter the material. Equation 2.22 [94,100] expresses the relationship between sputter yield (S) and energy transfer from Equation 2.21, surface binding energy (E_b), kinetic energy of the ions (E_1), and a term describing the efficiency of transferred momentum between ions and surface atoms (α).

$$S = \frac{3\alpha}{4\pi^2} \frac{4M_1M_2}{(M_1 + M_2)^2} \frac{E_1}{E_b} \quad (2.22)$$

Equation 2.22 is valid for ion energies $E_1 < 1000$ eV, and one mass is taken to be the sputtering ion and the other being the sputtered atoms mass. Sputtering yield is also influenced by the incident angle of the ions, as this influences the collision cascade the ion undergoes within the target [101]. A factor that has been found to be critical in this research is the distribution angle of the flux leaving the target. For each point on the target that generates a deposited flux, the flux leaving that point source is a function of the angle relative to the target's normal axis. This is known as the cosine or power cosine distribution, and is shown schematically in Figure 2-16 [102]. In Figure 2-16, as the angle departs from the target's normal, the flux decreases following either a $\cos\phi$ or $\cos^n\phi$ relationship [102]. For sputter deposition, n is typically $0.5 < n < 2.0$ [101]. The deposition rate is a function of the sputter yield, the flux of ions impinging on the target, transport of the deposited flux to the substrate, and sticking of that material to the substrate [94]. The characteristics of the resulting film depend on the material, its mobility on the surface, the geometry of the incoming flux, and the amount of energy imparted by species bombarding the substrate.

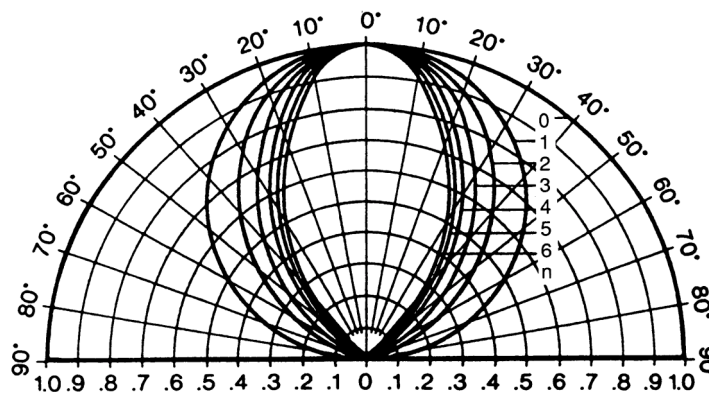


Figure 2-16. Plot of the power cosine distribution, which controls the flux distribution as a function of angle relative to the target's normal [94].

For the case of DC sputter deposition, there are several source geometries in use, one of which is the planar sputter deposition source. Two common varieties of planar sources are diode and magnetron, and are illustrated in Figures 2-17a and 2-17b, respectively. The name diode sputtering comes from the I-V characteristics of the plasma which are similar to that of a diode, i.e. more current flows with *forward* bias versus very little current flow with *reverse* bias. To achieve a sustainable plasma, the vacuum chamber is initially evacuated to a pressure typically on the order of 10^{-8} - 10^{-6} Torr, to achieve an ambient that will not contaminate the deposited film. Then the chamber is back filled with the working gas to a pressure on the order of 1-200 mTorr, the range needed to sustain the plasma. The sputtering pressure is an important parameter, since it influences the resistance of the plasma, and therefore the I-V characteristics of the plasma. As the pressure increases, the plasma becomes effectively less resistive, the

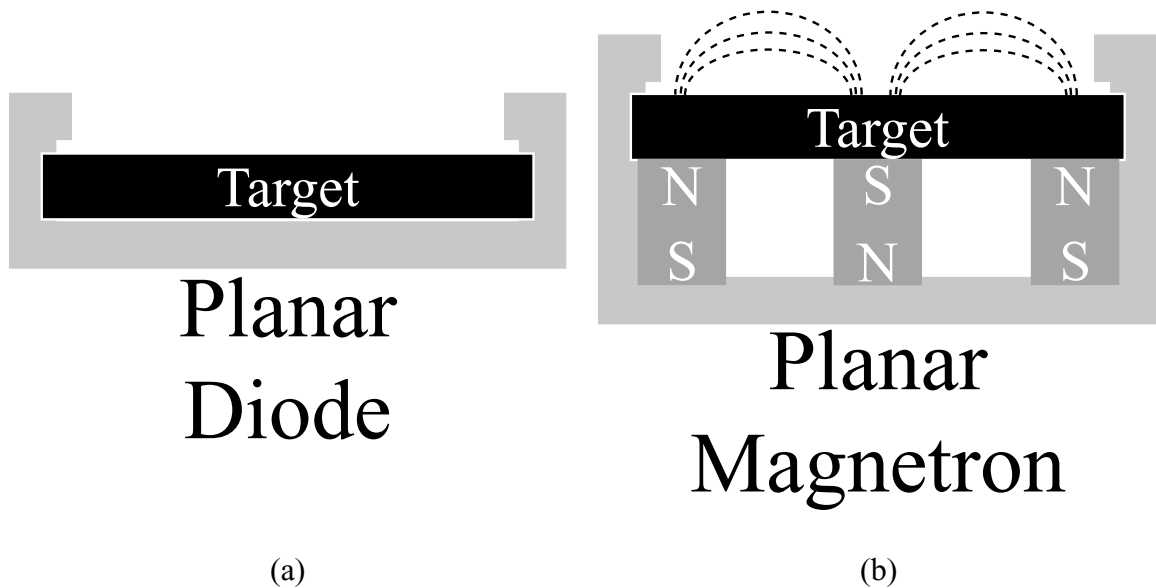


Figure 2-17(a-b). Illustrations of planar sputter deposition sources in the (a) diode configuration and (b) magnetron configuration.

voltage drops and the current increases. The current is related to the ion flux impinging on the target, and the voltage is the bias of the target, which controls the velocity of the impinging ions. The target geometry also influences the I-V characteristics of the plasma. Increasing the target area yields a higher ion current for the same ion flux ($\text{ions}/\text{cm}^2\cdot\text{s}$), effectively lowering the resistance of the plasma. Modern DC power supplies can control the power, voltage, or the current of the discharge depending on needs. The deposition rate typically scales linearly with deposition power [101].

One of the benefits of sputtering can be the relative high energy of the deposited material [94,101] with values of 5 eV of kinetic energy compared to ~ 100 meV for thermal deposition sources. The higher energy increases surface mobility of adatoms, therefore allowing more rearrangement of atoms on the surface, typically yielding improved film properties. By the kinetic theory of gases, an atom is more likely to be inelastically scattered at higher gas pressures. This advantage is lost if the deposited material loses energy in gas phase collisions during transport to the substrate. Scattering in the gas phase also influences the flux of reflected neutrals that impinge on the substrate. Reflected neutrals are ionized atoms/molecules that are accelerated towards the target, and then neutralized and reflected from the target with a significant portion of their incident energy. Their impact on the substrate can affect the microstructure and residual stress in the deposited thin films. The substrate to target distance can also affect the degree of gas phase scattering that occurs. As the distance the sputtered atoms travel through the process ambient gas increases, more scattering occurs. Additionally, as the target to substrate distance increases, the angular distribution of the flux causes the flux to spread out in space, and therefore increasing distance decreases the deposition rate.

Another important parameter is the substrate temperature. This parameter is important to adatom mobility, desorption processes, and thermodynamic driving forces which affects phase stability and nucleation and growth phenomena. Thus the deposition rate and microstructure of the developing film can be influenced by substrate temperature. The influence of substrate temperature on the microstructure of deposited film will be discussed more thoroughly in Section 2.4.2

Magnetron sputtering involves placing magnets behind the sputtering target. The resulting magnetic field extends into the gas ambient in front of the source, and influences the trajectories of moving charge particles by the Lorentz force [94]. The result of this is confinement of electrons near the sputtering target, which increases the amount of ionization in the working gas. Ions are not confined here because the charge to mass ratio is much smaller, and therefore ion trajectories are not as strongly influence by the magnetic field. The higher degree of ionization in the plasma effective lowers its resistance, increasing the ion flux (current) relative to the target bias (voltage), and effective increases the sputtering rate and broadens the operating pressure range. This is desirable for a high rate process, which is useful for decreasing manufacturing costs. Also, high deposition rates limit the exposure time of the growing film to the vacuum ambient, and therefore helps lower the incorporation of gas phase contaminants into the films [94].

The other major class of sputtering apparatus is radio frequency (RF) sputtering. Similar to DC, RF sources can be diode or magnetron based. The planar target geometry will be considered. Sputter deposition using RF power can be used to deposit material from insulating targets. Power from a RF generator typically operating at 13.56 MHz is

transmitted to a matching network via a 50 Ω coaxial cable. The matching network consists of a variable capacitor and inductor, and is needed to match the impedance of the capacitive discharge plasma to the 50 Ω output impedance of the generator. The applied RF field would normally tend to just oscillate charged particles, and therefore not generate any sputter deposition. However, due to the large difference in mass between ions and electrons, oscillations of the electrons are large enough that a significant portion impinges on the target and the chamber, whereas the ions are basically static. Because the chamber walls are grounded, and the target is electrically floated on capacitors, the target tends to build up a negative charge over time, i.e. develops a negative bias. As the negative bias increases, positive ions in the plasma become more strongly attracted to the cathode and acts to increase the positive ion current. A steady state bias is achieved when net current transported by positive ions and electrons in each full oscillation of the electric field is zero. At these steady state conditions, a negative bias on the order of 100 to 1000 of Volts exists on the cathode, and is known as the cathode self bias. This bias is sensitive to many parameters, including those mentioned above for the case of the I-V characteristics of a DC discharge. Additionally, the bias is sensitive to the ratio of capacitance for the target structure to the surrounding system. In practice this translates to a target bias that can be highly sensitive to the system geometry [99]. Figure 2-18(a) depicts what occurs when the RF power is initially applied to the target. Figure 2-18(b) is for steady state the condition, and depicts the developed negative bias or target self bias as seen by the voltage offset of the RF signal [103].

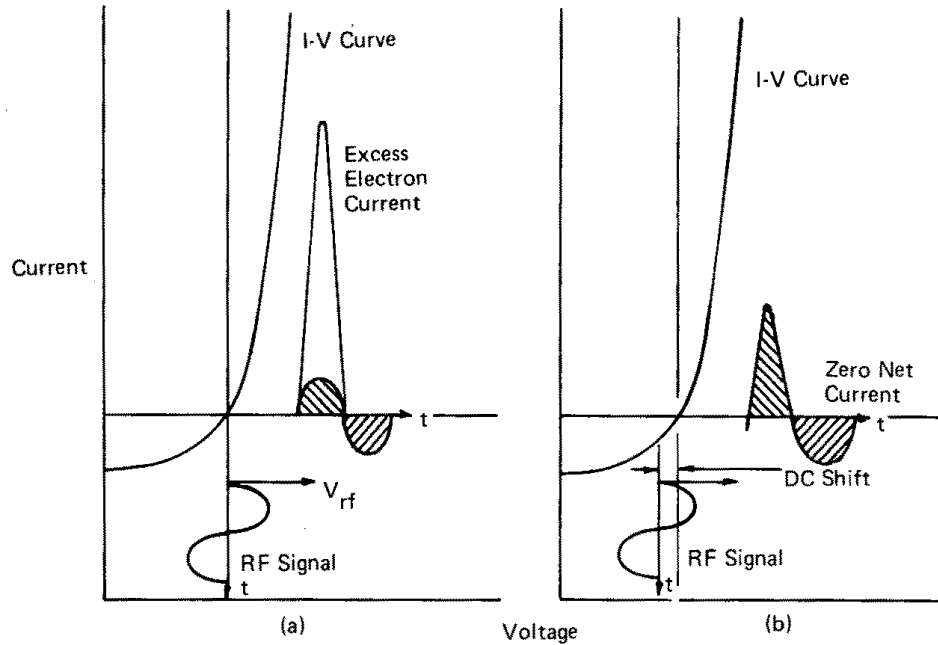


Figure 2-18(a-b). Illustration of the negative self bias formation during RF sputter deposition with (a) power initially applied and a large excess electron current and (b) at steady state where the electron current equals the positive ion current [99].

2.4.2 Thin Film Coalescence

Processes occurring at the substrate can also have a large influence on the structure and properties of the sputter deposited films, and are therefore critical to investigating relationships between the deposition process and resulting film properties. Nucleation and growth of the deposited film will be discussed using capillarity theory [94]. The processes involved are adsorption and desorption of material from the substrate, and motions and reactions on the surface. Capillarity theory uses a combination of bulk and surface free energies (surface tension) to assess the driving forces participating in the nucleation and growth process. Figure 2-19 shows the balance of surface tension forces involved with a nucleus on a substrate. The terms γ_{sv} , γ_{vf} , and γ_{fs} represent surface tensions between surface-vapor, vapor-film, and film-surface,

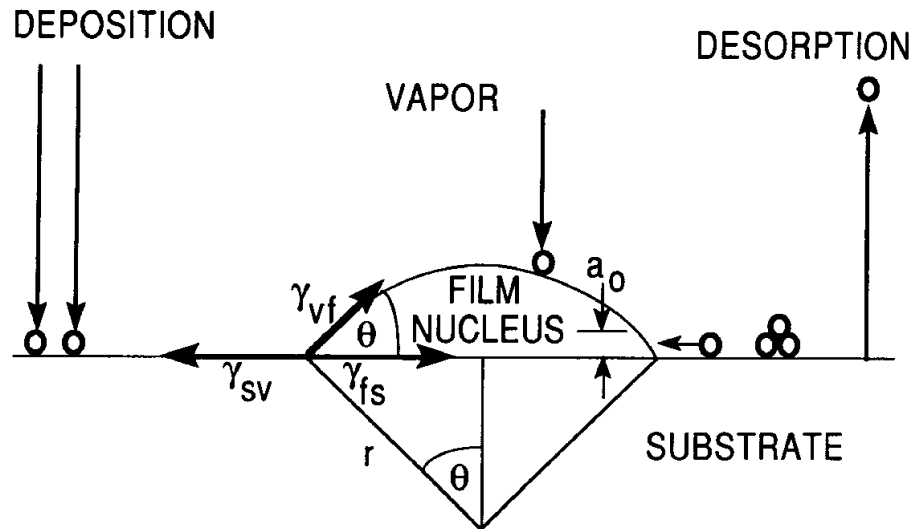


Figure 2-19. Representation of the influences of surface forces on the morphology of a deposited film during nucleation based on the capillarity theory [94].

respectively, while θ is the contact angle between the substrate and the nucleus. The angle θ changes to balance the surface tensions present. The degree to which the adatoms respond to the forces exerted is related to their ability to move on the surface. This surface mobility is related to the kinetic energy of the arriving adatom, energy available to move the adatom (e.g. heat, ion bombardment), and the surface diffusivity of the adatom [101]. The most common method to increase the mobility of adatoms is to heat the substrate, but there are often constraints and trade-offs, which limit temperatures in practice. For sputter deposition, recall that impingement of hyper-thermal atoms (atoms with kinetic energy greater than kT) can increase motions of surface atoms, and thereby influence the microstructure of the developing film.

For sputter deposition the working pressure and substrate temperature most strongly influence the adatom mobility. Thornton developed a structural model relating substrate pressure and temperature to the morphology of the film, and is known as a

Structural Zone Model (SZM). Figure 2-20 is a diagram of the SZM that Thornton developed empirically by microstructural characterization of sputter deposited metal films [104]. The four basic zones are 1, T, 2, and 3, with zone 1 occurring at higher pressures and lower temperatures. Zone 1 is characterized by a columnar grain structure with significant porosity between the grains, and large defect concentrations within the grains. Films with a Zone T microstructure are formed as the pressure decreases and/or the temperature of the substrate increases. The porosity between the fine columnar grains diminishes, which increases film density. Higher temperatures are needed to achieve Zone 2, which has a larger grain columnar structure, possibly a faceted surface, and properties are nearly those of bulk materials. A Zone 3 morphology occurs for temperatures near the melting temperature of the deposited material and has large equiaxed grains due to recrystallization processes. Mechanical and electrical properties are similar to bulk values.

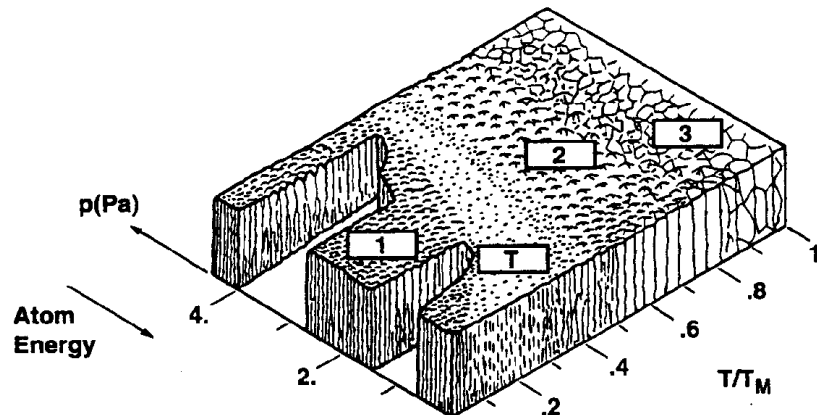


Figure 2-20. A structural zone model showing changes in thin film morphology as a function of pressure and substrate temperature used to sputter deposit the films [104].

Another common occurrence in the microstructure of deposited films is crystallographic texture, which is when grains share similar crystallographic orientations. Note that the crystal structure of ZnO is the wurtzite crystal structure, which is basically two interpenetrating hexagonal close packed lattices, one with zinc and one with oxygen [105]. This structure is shown in Figure 2-21, and has lattice constants of $a=3.25 \text{ \AA}$ and $c=5.207 \text{ \AA}$. For thin films, the most common texturing observed is for one crystal plane to be parallel to the substrate's surface, with this plane being the preferred growth plane [101]. For sputter deposited ZnO thin films on glass, a strong basal or (002) plane texture is widely reported in the literature from X-ray diffraction (XRD) θ - 2θ data [28,65,106-109]. In these data, a strong (002) ZnO peak is found, while no peaks for other crystal planes are observed. For thin films, XRD θ - 2θ data gives information about crystal planes parallel to the substrate surface, and therefore the ZnO data indicates the texture

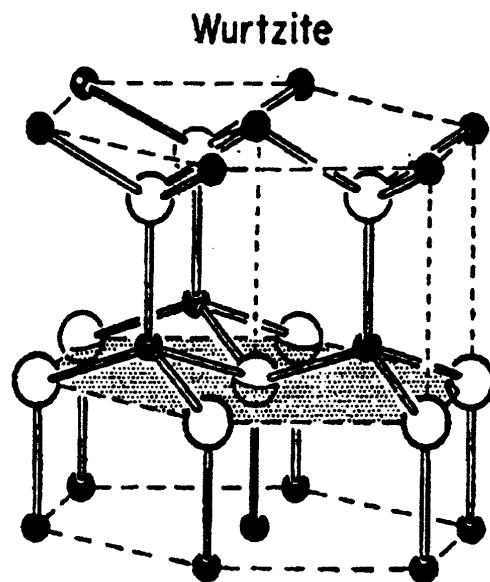


Figure 2-21. The hexagonal wurtzite crystal structure for ZnO in the zincite phase.

has (002) planes preferentially aligned parallel to the surface [110]. This phenomenon occurs if a particular crystal plane has low free energy, and can therefore grow faster and dominate the film. A sufficient degree of adatom mobility is needed for development of texture, such that atoms can move to lower their free energy by joining a lower energy crystal face.

For textured thin films with a crystal plane parallel to the substrates surface, XRD θ - 2θ data will show a single strong peak for the crystal plane parallel to the substrate surface versus a series of peaks with different intensities that is characteristic of powder samples. This occurs because XRD measures spacing between crystal planes parallel to the surface. In contrast to powder samples, which have randomly oriented grains, resulting in some diffraction from many crystal planes, grains in a textured film are aligned so that one crystal plane is most commonly parallel to the substrate's surface. Therefore, diffraction always occurs from the crystal plane parallel to the substrate surface, yielding a single peak [101].

2.4.3 Negative Ion Resputtering

Several reports in the literature and experiments performed in this work suggest negative ion resputtering (NIR) involving negative oxygen ions is a critical factor in deposition of ZnO films for TCO applications [76,111-113]. The NIR effect is reported to have a strong influence on electrical and structural properties of deposited films. Investigation of the NIR effect and the mechanisms for its influence on the electrical properties of deposited ZnO films is one of the foci of this work. The process for NIR is illustrated schematically in Figure 2-22. The mechanism for generation of negative ions is not well understood. In work by Cuomo *et al.*, an empirical relationship was found between the ionization potential and the electron affinity and presence of the negative ion

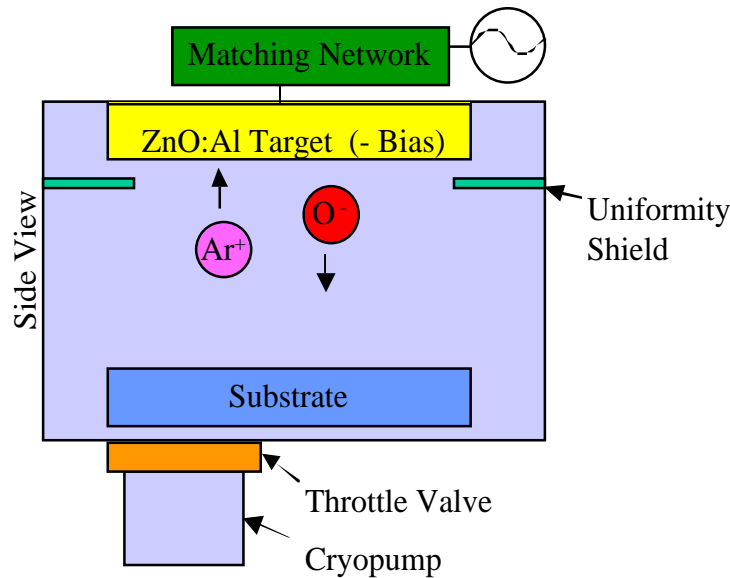


Figure 2-22. Schematic of the negative ion generation and acceleration process during sputter deposition of ZnO:Al thin films.

resputtering effect [114]. From this relationship, they developed a model about generation of negative ions during sputter deposition that is discussed below. The generated negative ions are accelerated rapidly in the cathode fall towards the substrate. It is generally believed that the ions are neutralized while traversing the plasma, mostly likely by electron detachment through impact with an electron in the plasma. Thus it is typically energetic neutrals that impinge on the substrate, with energies on the order of the target bias. Note that though the negative ions are neutralized before impinging on the substrate, they will continue to be referred to as negative ions to identify their source. Cuomo *et al.* postulated that negative ions would reach the target with energies near those of the target bias due lack of gas phase scattering. As the velocity of a gas atom changes, its collision cross section (σ in units of cm^2) with other gas atoms in the vacuum also changes. Change in collision cross section with increasing kinetic energy has been calculated for an Ar atom in an Ar ambient, and the cross section is found to decrease

with increasing kinetic energy. Therefore, energetic negative ions have a longer mean free path through the gas ambient than atoms with thermal energy [115]. A plot of the mean free path versus kinetic energy of an Ar atom in a 30 mTorr Ar ambient is presented in Figure 2-23 [115]. The mean free path of a thermal Ar atom is indicated in the lower left corner of the graph, and the mean free path of the argon is observed to increase significantly with increasing kinetic energy. The increase in mean free path of negative oxygen ions compared to a thermal oxygen atom has been verified experimentally by Tominaga *et al.*, using a time of flight apparatus [116].

The NIR effect has been observed during deposition of many materials other than ZnO. It was first investigated by Cuomo *et al.* who observed actual erosion of the substrate instead of film deposition while trying to deposit various gold rare earth metal alloys [114]. They developed an empirical model to predict the occurrence of NIR

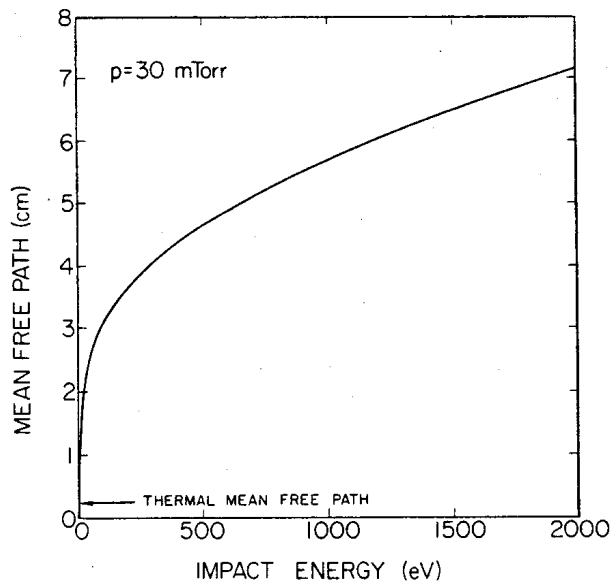


Figure 2-23. Theoretical plot of the mean free path of an Ar atom as a function of kinetic energy in a 30 mTorr Ar ambient.

based on the difference between the ionization potential of one atom and the electron affinity of the atom that forms the negative ion. This model is based on charge transfer between the different elements in the target. The process involves the element with lower electron affinity receiving energy greater than the ionization potential, liberating an electron. The electron then lowers its energy by attaching to an atom with higher electron affinity, followed by the atom leaving the target as a negative ion. They determined if the difference between ionization potential of the former and electron affinity of the latter atoms were less than approximately 3.4 eV, then significant NIR would occur. The ionization potential of Zn is 9.4 eV, and the electron affinity of O is 1.46 eV, giving a difference of almost 8 eV [101]. Thus, in contrast to experimental evidence, resputtering is not predicted for ZnO by this rule. Many ionic materials generate NIR through a process that is thought to result from liberating the constituent ions from the solid [101]. Because ZnO is an ionic solid, this qualitative rule would suggest that NIR would occur.

Kester *et al.* investigated resputtering for BaTiO₃, and the effect of process parameters on its magnitude [117,118]. They found the flux ratio $J(j_i/j_n)$ of the negative ion flux (j_i) versus the deposited neutral flux (j_n) was a critical parameter, with higher ratios causing more damage. They found the ratio to be higher for higher RF deposition power. Increasing the working pressure was also found to increase the ratio, as the neutral flux was more frequently scattered due to its lower velocity as compared to the high velocity negative ions. This suggests suppression of NIR only occurs for high pressures and long substrate to target distances. Unfortunately, film's deposited at these conditions tend to form a Zone 1 microstructure on Thornton's diagram. Recall that Zone 1 films are generally porous with poor properties, including high resistivities [101].

Several modifications to traditional sputtering systems have been studied in the effort to reduce damage from negative ions. Minami *et al.* have tried the “substrate perpendicular to the target” geometry and magnetic fields to improve the TCO properties of ZnO [76,109]. The two geometric modifications utilize the difference in flux distribution of the negative ions versus deposited neutrals. Neutral species leave the target in the typical cosine distribution [102], whereas negative ions are accelerated into a strongly collimated beam by the electric field normal to the target surface [117]. Thus the perpendicular substrates receive a much lower $J(j_i/j_n)$ than a facing substrate. As predicted by the flux ratio rule mentioned above, the substrates out of the direct path of the negative ion flux tend to show marked improvement in properties, as was confirmed by several researchers [76,111,112]. These processes generally result in severe non-uniformity in film thickness and/or low deposition rates and are therefore difficult to use for large area samples and high volume production. Minami *et al.* also tried magnetic fields normal to the target to influence the trajectory of the negative ions so they would not impinge on the substrate. While resistivities on the order of $10^{-4} \Omega\cdot\text{cm}$ were achieved, a substrate temperature of 250°C , which is beyond the limits of the thermal budget for CIS cells, is needed to achieve the low resistivities [109]. Tominaga *et al.* and Minami *et al.* both found that negative ion bombardment affected the electrical properties predominantly by changing the carrier concentrations [109,112,119]. The reported mechanism involve knocking dopant atoms off lattice sites, and prevention of their ionization, but no evidence was presented to support this model [112]. Therefore, determination of the mechanisms for the influence of NIR on the electrical properties of sputter deposited ZnO thin films is one of the foci of this work.

CHAPTER 3 EXPERIMENTAL METHODS

3.1 Introduction

This chapter will describe the tools, techniques, and procedures used to conduct the research presented in this dissertation. The first sections will describe the systems used to deposit the thin films, and the procedures used to prepare the glass substrates. The following section will cover the techniques used to measure the electrical properties of the deposited thin films. Hall and four point probe measurements were used to determine the carrier concentration (n), Hall mobility (μ), and resistivity (ρ). The next section will describe the methods used to characterize the structural and compositional properties of the thin films. These techniques include profilometry, X-ray diffraction (XRD), atomic force microscopy (AFM), Auger electron spectroscopy (AES), X-ray photoelectron spectroscopy (XPS), and secondary ion mass spectrometry (SIMS). Typical properties of interest include film stoichiometry, crystal structure, texture, surface morphology, “grain size”, and chemical bonding states. Optical properties were measured by spectrophotometry and Fourier transform infrared spectroscopy (FT-IR).

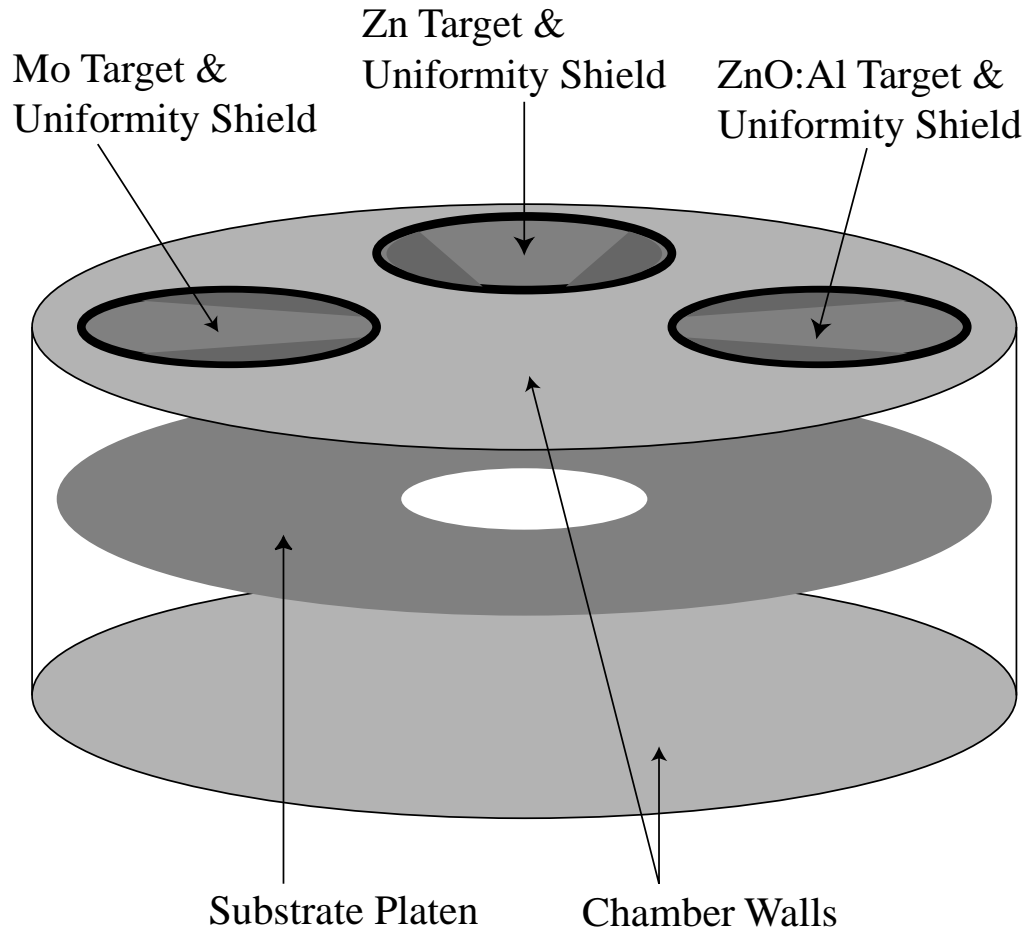
3.2 Thin Film Deposition

3.2.1 New Oxide Sputtering System

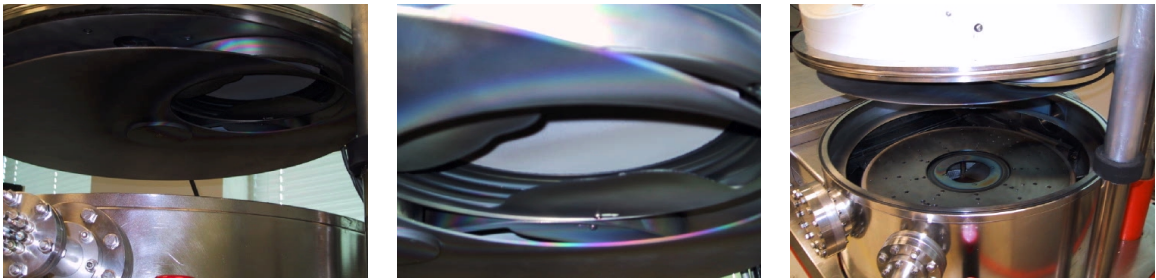
The new oxide sputtering system (NOSS) is a recently acquired used Perkin-Elmer model 4400 sputter deposition system. It has three RF planar diode sources, each handling a 20 cm target in a sputter down geometry. Targets currently mounted in these

sources are Mo, Zn, and ZnO:Al₂O₃ (98wt%:2wt%). The RF power is supplied by a Randex 2 kW RF generator operating at a frequency of 13.56 MHz with an output impedance of 50 Ω. The RF output passes through a power meter, through a transmission line, and into a manually controlled impedance matching network. The manual controls are load and tune which control a variable inductor and capacitor, respectively. The impedance matching network allows coupling of the RF energy into the capacitive plasma discharge which has a complex impedance on the order of $\sim 2\Omega - j45$ [120]. The 2 Ω component signifies a real resistance, while the negative imaginary (j) component of $-j45$ indicates the load is capacitive. The system has a single RF generator with switching to route the power to the appropriate source or the substrate table (when sputter etching is used to clean or modify the substrate). Uniformity shields are integrated into the source, and are 1.6 cm below the target. These shields modify the geometry of the source flux to account for the higher angular velocity for increasing radial distance on the substrate platen, and thus generate a uniform film when the platen is rotated. The overall geometry and pictures of the deposition system are shown in Figure 3-1.

The sources and the substrate table are cooled by chilled water. The substrate table has rotary motion capabilities, allowing deposition of uniform films on up to fourteen (14) substrates (up to 10 cm diameter) in a single batch process. The motion system for the substrate table has been upgraded with a stepping motor, which allows more sophisticated and repeatable control of the substrate motion. Full rotation at precise speeds and accelerations, oscillations about a region below the deposition source, and



(a)



(b)

(c)

(d)

Figures 3-1(a-d). Schematic diagram and pictures of the new oxide sputtering system, with the (a) sputtering chamber, (b) sputtering source, deposition shield, and uniformity shutter, (c) close up of source geometry, and (d) water cooled substrate support table.

accurately positioning substrates below the sources are the primary uses for the motion system. The *throw* or substrate to target distance is set at 9 cm.

A stainless steel, load-locked vacuum system is used to generate the vacuum required for sputter deposition. A CTI 8 cryopump and a Leybold Trivac 60cfm rotary vane pump provide the high vacuum and rough pumping, respectively. A throttle valve between the cryopump and the deposition chamber reduces the pump's effective pumping speed by up to a factor of 50 when engaged. Two mass flow controllers (MFCs) are used to regulate introduction of Ar and O₂ gas, and are used in conjunction with the throttling valve to generate a controlled gas ambient over the pressure range of 2-150 mTorr, a range typical for sputter deposition. Both MFCs have a range of 0-100 standard cubic centimeters per minute (SCCM), and control gases from ultrahigh purity gas bottles. The system operates at a typical base pressure of 1.5×10^{-7} Torr. Vacuum gauging is provided by an array of two Bayard-Alpert ionization gauges, two Convectron gauges, three thermocouple gauges, and one MKS Baratron capacitance manometer. The Bayard-Alpert gauges are used for measurements at high vacuum conditions ($<10^{-5}$ Torr), and are therefore used to determine the base pressure of the system. The base pressure is a critical factor in controlling contamination in the growing film. The other critical gauge is the MKS Baratron gauge, which gives accurate, precise, fast, and direct measurement of the pressure for the range of 10^{-5} to 1 Torr, and therefore spans the pressure range used for sputter deposition. A direct gauge refers to the fact that the gauge is sensitive directly to gas pressure, and its calibration is therefore independent of the gas being measured. This is critical for generating ambients with controlled partial pressures of a multiple gas species.

3.2.2 Description of the Sputtering System

Thin films for several early experiments were deposited in a home built sputtering system, which is affectionately known as Rusty. An illustration of the system's bell jar and geometry of the sources and substrate holder are shown in Figure 3-2. This system has two RF and two DC planar magnetron sources configured in a sputter up geometry. Each source is manufactured by US Guns Inc, is designed for a 5 cm target diameter, and has a separate power supply. The RF supplies include a RF Plasma Products model RF-5 generator with an automatic impedance matching network, and a Plasma-Therm generator with a manual matching network. These sources are referred to as RF1 and RF2, respectively. The DC power supplies are a US MDX-1k and US DC-1000, and are referred to as DC1 and DC2, respectively. The sources have power ratings of 600, 500, 1000, and 1000 watts, respectively. The substrate support has integrated temperature control utilizing resistive Watlow cartridge heating elements, a K-type thermocouple, and control provided by an Omega 7700 Mircomega auto-tune PID temperature controller. The temperature control system is used to maintain accurate elevated temperatures for the substrate during deposition.

The vacuum necessary for sputtering is generated inside a Pyrex bell jar and base plate style chamber. A Varian 6 diffusion pump and Sargent-Welch model 1397 rotary vane pump provide the high vacuum and rough pumping, respectively. A liquid nitrogen cooled cryo-trap and a throttle valve are between the system and the diffusion pump. This system has two MFCs for Ar and O₂, which are used to introduce UHP gas into the system. Vacuum gauging consists of one Bayard-Alpert ionization gauge, two thermocouple gauges, and one MKS Baratron gauge.

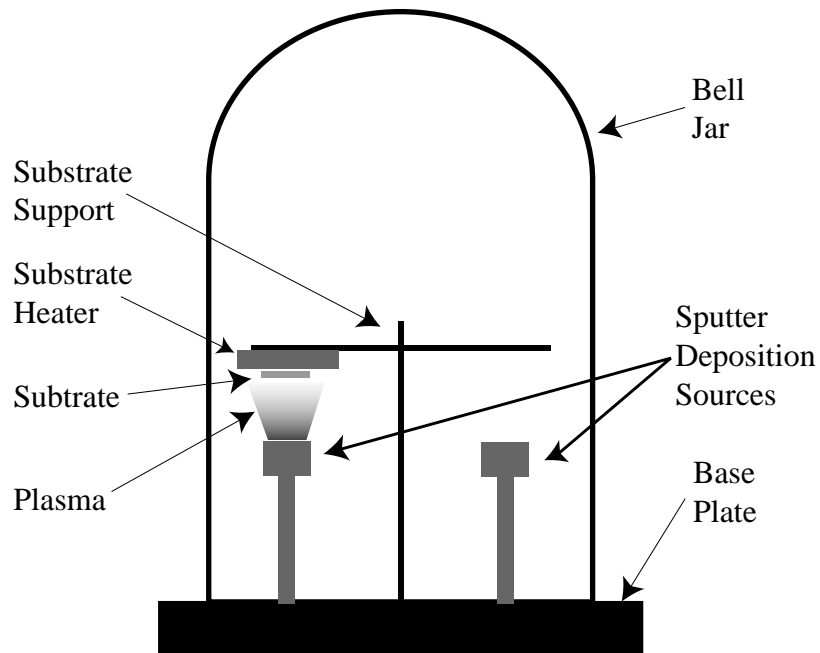


Figure 3-2. Cross-sectional view of the sputter deposition system known as “Rusty”.

3.2.3 Substrate Cleaning

Soda-lime float glass was used as the substrate for the deposited films. The glass substrates were purchased from US Precision glass, and were 5 x 5 cm square pieces seam-ripped from larger sheets. The glass was very dirty, therefore a cleaning procedure which involved a physical scrubbing was developed. The first step of the procedure was to clean a 2L beaker and pyrex casserole dish with Alkonox detergent and deionized water (DI). Then roughly 2L of water and ~30 grams of Alkonox were heated in the beaker with a hot plate until steaming. When warm, roughly half the detergent solution was poured into the pyrex dish, and two folded polypropylene clean room wipes were placed on the bottom of the dish. The substrates were scrubbed on the wipes in a manner similar to polishing a specimen. The substrates were rinsed in a spray of DI water, followed by a scrub on both sides plus the edges with a clean brush. The substrates were rinsed again in

a spray of DI water, and placed in a Fluoroware wet process holder in the first tank of a cascade rinser from Bold Technologies. When the holder was full (12 substrates), it was run through the whole cascade rinser with N₂ bubble agitation. When the substrates were thoroughly rinsed, they were blown dry individually with a filtered dry N₂ gun and placed in a storage box.

The substrates were stored in a box from Fluoroware designed to hold photographic plates of the same size. Previous to use, the substrates were cut to the appropriate size for the experiment (typically 2.5 x 5 cm), and then clean again by a strong nitrogen blow.

3.3 Electrical Characterization

3.3.1 Hall Measurements

Hall measurements were used to characterize the resistivity (ρ with units of $\Omega\cdot\text{cm}$), carrier type, carrier concentration (n with units of cm^{-3}), and mobility (μ with units of $\text{cm}^2/\text{V}\cdot\text{s}$). The measurements were taken by the van der Pauw method [121], with ohmic contacts provided by electron beam deposited Al contacts patterned using a shadow mask in intimate contact with the sample. The maximum sample size was 7 x 7 mm, with samples being cut from larger samples by a scribe and fracture procedure. The contacts formed a 4 x 4 mm square, and each dot was approximately 0.5 mm in diameter. The samples were mounted in a custom made shadow mask holder, placed in the electron beam evaporation system, and the stainless steel bell jar was pumped down to $\sim 5 \times 10^{-7}$ Torr using a cryo-trapped diffusion pump backed by a rotary vane pump. The charge of Al in the pocket of the Telemark electron beam deposition source was evaporated at a rate of $\sim 15 \text{ \AA}/\text{s}$ to generate a film thickness of $\sim 3300 \text{ \AA}$ as measured on a Quartz Crystal

microbalance. A vacuum cowling covers the Hall measurement probe head to prevent condensation during low temperature measurements, therefore Hall measurements were performed in the dark.

The Hall system was assembled from off the shelf components. A Fieldial Field Regulated Magnet Power Supply model V-FR2503 supplied current to a Varian Associates large field electromagnet, which was set to an 8,000 gauss field strength. A Keithley model 220 supplied a constant current, with a Keitley model 197 Microvolt Digital Multimeter (DMM) used to measure the resulting voltages. A HP model 3488A switching network connected the appropriate sample contacts to the appropriate electrical components for the various probing geometries specified by the van der Pauw method. A Tektronix model 177 curve tracer was integrated into the system to determine if the contacts were ohmic by looking for the characteristic linear I-V curve. A PC controlled all the components, and acquired and processed the data. The data reported by the system included carrier concentration (n), mobility (μ), resistivity (ρ), carrier type, Hall coefficient (R_H), and error analysis. In operation, the system first determines the appropriate current for the measurement. The system was programmed to supply the current need to generate a voltage of 5 mV. For this measurement, the current was passed through the contacts on one side of the square, and the voltage drop was measured across the contacts on the opposite side of the square.

It is important to understand the quality of information reported by Hall measurements, and the underlying assumptions and pitfalls associated with it. For the case of degenerately doped ZnO:Al there are several issues which should be identified, and some limits that need to be articulated. First is the Hall factor (γ_H), which is

generally assumed to be 1. This is a fair approximation for many semiconductors, but for the highest possible accuracy, the value should be determined. The fact that the material is degenerately doped can generate impurity bands, and affect the electron distribution function ($f(e)$). The magnitude of the Hall voltage is another difficult issue. For samples with low Hall mobility, the difference between the Hall voltage with and without a magnetic field will be small, making accurate measurement of the field derived Hall voltage difficult. This required that care be taken in analyzing the data to make sure the changes measured due to the Hall voltage were appropriate and consistent for the magnetic field polarity and contact geometry. These measurements are primarily used to compare samples relative to each other. Because the same parameters are used for the Hall system, and the films are consistently the same material, comparisons of data between samples has the needed accuracy. Comparison with literature values for other research in ZnO should also be reasonable since the materials parameters should be similar. Parameters used in Hall measurements are often not reported, therefore while comparisons with the literature are useful, they must be examined with a critical eye.

3.3.2 Four Point Probe

The measurements were taken on an Alessi four point probe. A probe head with tungsten carbide tips with a point radius of 0.002", a probe spacing of 0.05", and a probe pressure of 70 to 180 grams was used for all measurements. Current was supplied by a Crytronics model 120 current source with a range of applied currents between 1 μ A to 100 mA. Voltages were measured by a Keithley model 181 nanovolt electrometer with an input impedance of greater than 1 giga-ohm. Equation 3.1 and 3.2 were used to determine sheet resistance (R_s in units of Ω /sq.) and resistivity (ρ in units of Ω ·cm), respectively.

$$R_s = \frac{4.532 \cdot V}{I} \quad (3.1)$$

$$\rho = \frac{4.532 \cdot V \cdot t}{I} \quad (3.2)$$

Based on the dimensions of the sample and probe head, no geometrical correction factors were applied. The term t is film thickness (cm), and V is the voltage measured at the supplied current (I).

3.4 Structural Characterization

3.4.1 Profilometry

To measure thickness of the deposited films, a portion of the substrate was masked with a permanent marker. After the deposition, the mark was removed with acetone and a swab, which effectively removed the deposited film on top, yielding a well defined trench step. A Tencor Alphastep stylus profilometer was used to measure the depth of the trench, and therefore the film thickness.

3.4.2 X-Ray Diffraction

X-ray diffraction spectra were collected on a Philips APD 3720 powder diffractometer using Cu K α radiation ($\lambda=1.54056 \text{ \AA}$). The standard settings for the X-ray generator were 40 kV at 20 mA. Three types of $\theta/2\theta$ spectra were collected for this research, and will be designated as *survey*, *high resolution*, and *line profile*. Conditions for a survey scan were a continuous scan, a 2θ range of 10° to 80° , a stepsize of 0.020° , and a step time of 0.5 seconds. High resolution spectra were continuous scans with a 2θ range of 30° to 40° , a step size of 0.010° , and a step time of 1.0 seconds. Line Profile Analysis was performed on data collected with a step scan over a 2θ range of 32° to 38° , a step size of 0.010° , and a step time of 2.5 seconds.

Quantification of peak full width at half maximum (FWHM) was performed using the Philips *Line Profile Analysis* [122] software package. The “Approximate Analysis” function is used, which fits a single peak with a Voight function. Broadening of the peaks FWHM is attributed to strain and crystallite size, but the relative contribution of each cannot be explicitly determined. Therefore only the FWHM is taken from this technique. The software package *MacDiff* was used to quantify peak intensity, FWHM, area, and 2θ peak position. For all measurements, the background was subtracted before quantification was performed.

3.4.3 Atomic Force Microscopy

Atomic Force Microscopy (AFM) micrographs were taken with a Digital Instruments NanoScope III. Samples roughly 7 x 7 mm were attached to a steel sample mount with double stick tape, and placed on the magnetic holder in the instrument. The small scanner (Scanner E) with a range of 12.5 μm in the x-y directions, and 2.5 μm in the z direction was used to acquire all the images. The micrographs were taken in the tapping mode with Si_3N_4 tips manufactured by Digital Instruments. Often more than one image was taken from neighboring areas to make certain the images were representative of the local area. Height and tip amplitude data were taken for each micrograph. All the images and data were taken from height information. The amplitude information was used to identify trouble spots due to the high sensitivity of this data to interactions between the tip and the sample. The contrast in the amplitude image is based on changes in the amplitude of the vibrating cantilever tip. This often gives stronger contrast than height imaging when tip interacts differently with the surface (greater or lesser interaction forces).

An automatic “Plane Fit” in the x and y directions and a “Flatten” command were applied to the images before any analysis was performed. For the plane fit command, a third order plane fit was used. In this procedure, the computer used a least squares algorithm to calculate a third order polynomial for the x or y plane data, and then subtracts this from the image data. This function serves to not only level the image, but to reduce bowing and curvature that results from drift during data collection. The flatten command performs a similar procedure, but applies it to each scan line. A first order polynomial is calculated by a least squares technique, and was subtracted from each line. This command served to line up adjacent scan lines, and reduces slope associated with measurement drift along a scan line.

Typical data taken from AFM height images includes root mean square surface roughness (RMS roughness), surface area difference (%), and grain size. The RMS roughness will simply be referred to as roughness, and was measured by an algorithm in the Digital Instruments software. The surface area difference is also quantified by the software, and describes additional surface area of the sample relative to a flat plane with the same x and y dimensions as the image. The grain size is determined by measuring the grain boundary intercepts, a standard stereological technique [123]. For the data presented, a series of eight lines 400 nm in length, and at random orientation are laid on the image. The topography of the line is displayed in cross section. Intercepts are determined by using low points on the cross section plot, and careful observation and comparison with full image. This is done for each of the eight lines, and an average is calculated. The grain size is determined by dividing the length of the line by the average number of intercepts. This stereological technique is based on the assumption that the

sample has equiaxed grains typical of bulk samples for which this technique was developed. In addition to the caveat in the previous statement, the number of intercepts is based on interpretation of low features between hillocks as grain boundaries, therefore the grain size must be used carefully for analyses.

3.4.4 Auger Electron Spectroscopy

Auger electron spectroscopy (AES) measurements were taken on a PHI model 660 Scanning Auger Microprobe (SAM). This system utilizes a LaB₆ thermionic emission electron source with a co-axial Cylindrical Mirror Analyzer (CMA) to measure the kinetic energy of Auger electrons, these energies being characteristic of the elements generating them. A thorough description of the Auger analysis is beyond the scope of this work, but is covered in depth in several books [124,125]. AES is considered a surface analysis technique because the detected Auger electrons can only escape from within the first several monolayers below the sample surface. The CMA is sensitive to distance between itself and the sample, and is therefore calibrated using the standard elastic peak technique. The system has an Ar ion beam source, which is used to sputter etch the sample's surface. It was used to clean contaminants from the surface, remove surface layers to get compositional information more representative of the film's "bulk", and to perform depth profiles. The parameters used for the ion beam source are an accelerating potential of 3 kV, a beam current of ~90 nA, and a spot area of approximately 1 mm². The rate and area of the etch are influenced by the rastering conditions applied to the beam, with a 3 x 3 mm raster pattern at the specimen being the standard setting. The system was maintained at a base pressure on the order of 10⁻¹⁰ Torr, and typically operated at 10⁻⁸ Torr while the Ar ion source was in use.

The two types of AES data presented in the work are survey spectra and depth profiles as a function of sputter etching time. For all spectra, a primary beam energy of 5 kV was used. Ten replicates of the spectrum of counted electrons at an energy ($n(E)$) versus kinetic energy (KE) are summed over the energy range of 50 to 2050 eV. This data is taken with an energy step size of 1.0 eV, and a dwell time of 30ms at each energy. This spectrum is then numerically differentiated by an algorithm from the computer acquisition system's software to yield the spectrum in terms of $d(n(E))/d(E)$ versus KE. The differentiated spectrum is then used to accurately determine kinetic energy of the Auger electron peaks, which in turn is used to determine the elements present on the sample's surface. The differentiation algorithm also has a smoothing function, which can operate across a user determined cell size. It was left at the standard setting of 9 for all data presented in this dissertation. To account for charge shifting, peak energies were referenced to adventitious carbon (272 eV) if possible.

Depth profile data was taken using the window method, which involves alternating between sputter etching the sample and collecting small windows of Auger spectra focused on the peaks for elements of interest. This signal from each Auger window is then differentiated, using the same algorithm as the survey spectra. The peak-to-peak heights of the differentiated spectra are plotted as a function of element and sputter etching time. Parameters used for collecting depth profiles are presented in Table 3-1.

3.4.5 X-ray Photoelectron Spectroscopy

X-ray photoelectron spectroscopy (XPS) is also known as Electron spectroscopy for chemical analysis (ESCA). XPS spectra were taken on a PHI model 5100 ESCA system. A non-monochromated Mg $K\alpha$ X-ray source, producing characteristic radiation

Table 3-1. Parameters used for Auger electron spectroscopy sputter depth profiles.

Element	Oxygen	Zinc	Silicon
Peak Energy (eV)	506.0	984.5	1601.0
Window Boundary – Low (eV)	475.0	946.0	1585.0
Window Boundary – High (eV)	525.0	1025.0	1615.0
Dwell Time (ms)	50	50	50
Number of Sweeps	10	10	10

with a peak photon energy at 1253.6 eV was used for all spectra. The X-ray generator was operated at 15 kV and 300 watts (20 mA). Photoelectrons liberated from the sample are collected, retarded, and analyzed in a hemispherical analyzer. The analyzer acts as a band pass filter, allowing only electrons with a particular kinetic energy through to the Channeltron detector. The kinetic energy is converted into binding energy through use of Equation 3.3:

$$BE = h\nu - KE - \phi_D \quad (3.3)$$

where BE is the binding energy of the detected electron, h is Planck's constant, ν is the frequency of X-ray probe beam, KE is the kinetic energy of the photoelectron, and ϕ_D (4.7 eV) is the work function of the detector (hemispherical analyzer). Spectra are traditionally presented starting with the highest binding energy to the lowest on the abscissa.

The based pressure of the system is on the order of 10^{-10} Torr, and typically operates at 10^{-8} Torr if the Ar ion gun is being used for sputter etching. Similar to AES, XPS is also a surface analysis techniques due to the limited escape depth of measured photoelectrons. Argon ion etching was used to remove surface contaminants and to erode into the thin films to gather information from a region that can reasonably be considered the "bulk" of the thin film. The conditions used for the ion source were an accelerating potential of 4 kV and a beam raster area of 4 x 7 mm at the specimen's surface.

The two types of XPS data taken include survey spectra and multiplex spectra. Survey spectra had binding energies from 1100 to 0 eV, and were taken with an energy resolution of 0.5 eV per step, a dwell time of 30ms, a pass energy of 89.45 eV, and a take off angle of 45°. The measured peaks were correlated to tabulated energies and spectra for the elements to determine the elements present at the sample surface.

Multiplex scans take data across a series of small energy ranges (windows) in order to gather more accurate data on peaks of interest found in survey scans. Parameters used to collect the multiplex scans are presented in Table 3-2. Qualitative atomic concentrations of elements on the surface were determined from the area of the elemental peaks in conjunction with sensitivity factors. The multiplex data were also used during peak deconvolution. The deconvolution process involves choosing a peak from a Multiplex window, subtracting the background and fitting the peak with one or more component Gaussian-Lorentzian functions. The variables for these functions included peak energy, height, full width at half maximum (FWHM), and percentage Gaussian. All peaks were fitted by a combination of manual and automatic fitting. This technique was used to accurately determine the character of the peak for investigating of the chemical bonding.

Table 3-2. Parameters used to collect XPS multiplex scans.

Element	Oxygen	Carbon	Zinc
Window Boundary – High (eV)	536.0	292.0	1032.0
Window Width (eV)	10.0	15.0	20.0
eV/Step	0.1	0.1	0.1
Time/Step (ms)	50	50	50
Pass Energy (eV)	35.75	35.75	35.75
Sweeps	10	10	10

3.4.6 Secondary Ion Mass Spectrometry

Secondary Ion Mass Spectrometry (SIMS) was used to measure the composition of the deposited films, with particular interest in concentrations of electrically active dopants and contaminants. The SIMS spectra were collected on a Perkin-Elmer PHI 6600. Data were acquired using an oxygen primary ion beam from a duoplasmatron source and positive secondary ion acquisition. The primary beam energy was 6 keV with a beam current of 209 nA. The primary beam was rastered over either a 400 x 400 μm or 500 x 500 μm area, and used a gating of 65%. A quadrupole mass filter was used to pass secondary ions with a specific charge to mass ratio to the secondary ion detector. The detected signal was intensity, or counts per second, for the secondary ions as a function of the charge to mass ratio being passed by the mass filter. The systems neutralizer was utilized to avoid sample charging during collection of the spectra.

The two types of SIMS data collected include survey spectra from the as deposited surface, and depth profiles. Survey spectra were used to determine the elements present on the surface, with secondary ion intensity plotted versus the mass to charge ratios over the range 1 to 110. Depth profiles measure the signal from the mass to charge ratio for elements of interest as a function of sputtering time. This is used to characterize changes in composition through the thickness of the film. Elements of interest that were profiled include C(12), Na(23), Mg(25), Al(27), Si(28), Ca(40), Al(54) and Zn(66). The number in parenthesis specifies the particular isotope followed during the depth profile, with the exception for Al(54), which is the dimer of Al(27).

3.5 Optical Properties

3.5.1 Spectrophotometry

Optical spectrophotometry measurements were taken on a Perkin-Elmer Lambda 9 system from the UV region into the Near IR region in order to obtain spectral features associated with the band edge and plasma resonance phenomena. Transmission spectra were collected at normal incidence, using a double beam geometry with a sampling and a reference beam. For all measurements, the reference path was left open. The glass background spectrum was removed by collecting and averaging a series of 4 spectra from bare glass, and dividing measurements taken from the sample by the averaged glass spectrum. The optical beam size on the sample was roughly 3 x 0.3 cm. The diffraction grating is changed at 860 nm, and yields a small discontinuity in the collected spectra. A tungsten lamp source provides the light for the measurements.

3.5.2 Fourier Transform Infrared Spectroscopy

Fourier transform infrared (FT-IR) spectra were collected using a Nicolet model 510p spectrophotometer in reflection mode. The measurements were made using a variable angle reflectance stage, and measurements were typically taken at 30° and 60°. Data were collected at two angles to gauge the influence of measurements above and below the Brewster angle [126], and to have two spectra for more accurate comparison to spectra generated by a model. Calibration to remove the background was performed using a gold mirror standard. Measurements were then made on both sides of the substrate (glass and film) at both angles of incidence. These spectra were compared to spectra generated by a model developed by George Alameddin. Film thickness, carrier concentration, infrared damping coefficient, and optical constants for the film and substrate were the parameters entered into the model. By changing the parameters, the

calculated spectra were matched to the measured ones. Thus, values for the modeled parameters could be determined from the FT-IR spectra. The infrared damping coefficient is inversely related to mobility, thus carrier concentration and mobility can be estimated.

3.6 Experimental Procedures

3.6.1 Affect of Annealing Ambient on the Properties of ZnO:Al

The objective of this experiment was to determine the sensitivity of ZnO:Al thin films to modest heat treatments, and to determine if the gas ambient in the furnace had a strong influence on the results of the heat treatment. The films for this experiment were deposited in Rusty with cleaned 2.5 x 5 cm pieces of glass used as substrates. The parameters held constant for deposition of the thin films are as follows:

- Target: ZnO:Al₂O₃ (98wt%:2wt%) hot pressed
- Base Pressure: 8×10^{-7} Torr
- Substrate to Target distance: 4 cm
- Process Pressure: 5 mTorr Ar (UHP)
- Ar Flow Rate: 7 sccm
- RF Power: 100 watts forward, <2 watts reflected
- Substrate Temperature: Unheated

The as deposited samples were characterized by stylus profilometry, spectrophotometry, FT-IR, XRD, and four point probe measurements. Profilometry measurements were made by the standard procedures previously outlined.

Spectrophotometry measurements were taken on a Perkin-Elmer Lambda 9 over the range of 300 to 2000 nm using the previously outlined standard procedures. FT-IR

measurements were taken in reflection mode, with a 60° incident angle from the surface normal using standard procedures. XRD diffraction measurements were taken by loading the sample directly into the diffractometers chuck, resulting in data taken roughly from the center of the sample. Both survey and high resolution spectra were collected, and each high resolution measurement was repeated after removing and remounting the sample in the diffractometer. The replicate data were used to judge the repeatability of the measurements. Four point probe data were taken from three different positions, one near each end, and one from the middle, and is illustrated in Figure 3-3.

Four of the samples heat treated in a quartz tube furnace with ambients of N_2 , forming gas (N_2/H_2 90%:10%), stagnant air, and O_2 . The fifth sample was used as a control, and was therefore not heat treated. To heat treat the samples, the furnaces were warmed up to $400^\circ C$ and purged with the appropriate gas for at least one hour, with the sample in the furnace, but out of the hot zone. The samples were then pushed with a small push rod into the hot zone of the furnace, and remained there for 1hr and 15minutes. The samples where then pulled out with the push rod, cooled in the area



Figure 3-3. Positions on the 2.5 x 5 cm substrate where four point probe data were collected.

outside the hot zone but still within the controlled ambient of the furnace. When cooled to approximately 75°C, the samples were removed from the furnace and rapidly quenched to room temperature. The samples were then recharacterized by the same procedures used before the heat treatment.

3.6.2 Development of Properties in Very Thin ZnO:Al Films

The objective of this experiment was to investigate the development of structural and electrical properties of ZnO:Al thin films, and relate those characteristics to thickness dependent effects in the electrical properties. The thin films were deposited in Rusty onto cleaned 2.5 x 2.5 cm glass substrates. Standard permanent marker stripes were made before each run for profilometry measurements. Also, the substrate's surface was cleaned with a strong N₂ blow just prior to introduction into the deposition system. The deposition parameters held constant are as follows:

- Target: ZnO:Al₂O₃ (98wt%:2wt%) hot pressed
- Base Pressure: 8×10^{-7} Torr
- Substrate to Target distance: 5 cm
- Process Pressure: 5 mTorr Ar (UHP)
- Ar Flow Rate: 7 sccm
- RF Power: 100 watts forward, <2 watts reflected
- Substrate Temperature: 150°C
- Substrate Geometry: Substrates were positioned off axis (not directly above the source)

The parameter varied during this experiment was the deposition time, which was used to control film thickness. Deposition times of 10, 20, 30, 60, 180, 300, 420, and 900 seconds were used. The deposition rate at the conditions used was measured by

profilometry to be 1.75 Å/s. The thickness was determined by multiplying the deposition rate by the deposition time. Additionally, the films were characterized by four point probe, Hall measurements, AFM, and AES. Four point probe and Hall measurements were used to characterize ρ , n , and μ . The 7 x 7 mm samples for Hall Measurements were cleaved from the substrates edge closest to the deposition source. Four point probe measurements were taken from the edge closest to the source, middle of the substrate, and the edge farthest from the source.

Analysis of AFM micrographs was used to determine the surface morphology of the thin films. The technique of AES was used to look for contaminants, and to investigate surface coverage of the sample. Two survey spectra were collected using the standard parameters, with a sample tilt of 45° and a sample beam current of ~50 nA, one before and one after a depth profile. The profile was collected using window scans, using the parameters specified previously. The Auger data from the window scans were differentiated, and peak-to-peak heights were used to evaluate changes in the surface composition. To determine the surface fraction covered by the film, atomic concentrations were taken from an as deposited survey spectrum using the standard procedures in the instrument's software. These were compared to atomic concentration measured for a pure ZnO:Al and pure glass surfaces. The atomic concentrations measured on the as deposited surface were evaluated relative to the pure surface standards, and from this a fractional surface coverage for the film was estimated.

3.6.3 Negative Ion Resputtering in Sputter Deposition of ZnO:Al Films

The objective of this experiment was to determine the role of negative ion resputtering (NIR) during sputter deposition of ZnO:Al thin film, and the influence of RF power on the magnitude of the NIR effect. The films for this experiment were deposited

in NOSS. All thin films were deposited onto soda-lime glass substrates cleaned by the procedures given above.

The substrate consisted of 2.5 x 5 cm pieces of glass, with three pieces of glass placed end to end to effectively make one 2.5 x 15 cm substrate. One end of the substrate was placed under the center of the sputter deposition source, and was arranged perpendicularly to the edge of the uniformity shield to minimize film thickness gradients across the 2.5 cm dimension of the substrate. A side view of the system was presented in Figure 2-22, and schematically showed the generation and acceleration of negative ions away from the deposition source. The top view illustrates the position of the substrate relative to the deposition source and is presented in Figure 3-4.

The sample deposited at 500 watts is an important exception to this substrate geometry. For this sample, instead of the end of the substrate coming to the center of the

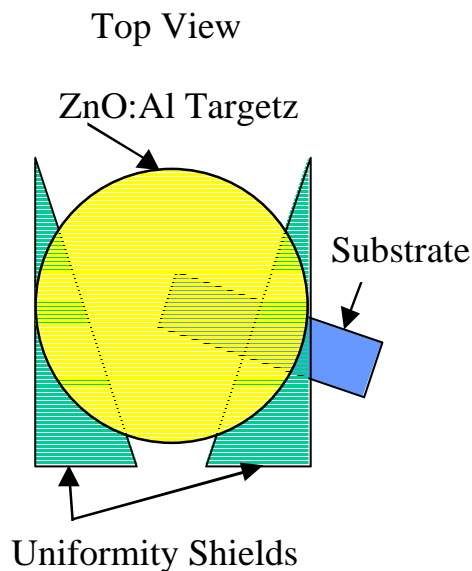


Figure 3-4. Top-view of the deposition geometry used for the investigation of negative ion resputtering, with the substrate extending from the center to the edge of the source.

source, it was translated away in the radial direction (the direction along the long axis of the substrate) approximately 3.2 cm based on trends in the data. Before the substrates were placed in the system, a stripe was made down the long axis of the substrate near the edge with a fine point permanent marker for standard profilometry measurements.

The order of the depositions was 500 watts, 250 watts, and 1000 watts. The 500 watt sample was deposited by itself, while the 250 and 1000 watt samples were both loaded on opposite ends of the substrate platen and done as a single run. After the 250 watt sample was deposited, the stepper motor was used to rotate the platen such that the substrate for the 1000 watt deposition was in position. The deposition shutter was closed during substrate rotation and retuning of the source for 1000 watts. The conditions held constant for the depositions are as follows:

- Base Pressure: 1.5×10^{-7} Torr
- Substrate to Target distance: 9 cm
- Process Pressure: 5 mTorr Ar (UHP)
- Ar Flow Rate: 3.2 sccm
- Presputtering: 10 minute at 250 W with deposition shutter closed
- Substrate temperature: room temperature (by chilled water)

The power, deposition time, and position on the substrate were treated as variables. The position on the substrate was measured along the edge near the profilometry mark, with the end of the substrate under the source as the origin. A list of the varied deposition parameters follows. The deposition time was changed in order to keep the thickness of the deposited films within the same order between conditions,

thereby minimizing the influence of variable thickness between the different deposition conditions.

- 250 watts for 60 minutes
- 500 watts for 60 minutes
- 1000 watts for 20 minutes

After deposition, a series of small marks were scribed on the samples every 0.6 cm near the stripe used for profilometry measurements. Using the optical camera in the profilometer, these marks could be found, allowing thickness measurements to be made at precise locations. The marks were also used for positioning four point probe measurements, which were taken with the geometry of the four points arrayed orthogonally to the long axis of the substrate. Since the film thickness is the same across the short axis of the substrate, the thickness data can be used in Equation 3.2 to calculate film resistivity accurately as a function of position along the long axis of the substrate.

In order to get XRD data from particular positions, the substrate was cleaved into three equal sections (2.5 x 1.7 cm) perpendicular to the long axis. These samples were mounted to microscope slides with double-sided tape. In order to assure the film surface was positioned correctly, a dummy piece of glass of the same type used for a substrate was also attached to the microscope slide, such that it was in the sample chuck and the film was on the sampling plane. For this experiment, both survey and line profile spectra were collected.

Hall and AFM measurements require samples significantly smaller than those used for the XRD measurements, therefore each XRD sample was further subdivided to yield two roughly 7 x 7 mm samples. The sample for Hall measurements had Al dot

contacts deposited as previously described, and measurements were made using the standard procedures. After Hall measurements, SIMS was used to characterize the composition of the Hall samples using the previously described conditions. An oxygen primary beam was used for positive SIMS, because the concentration of electropositive elements is the focus of this characterization. In particular, the ratio of Zn to Al, and Zn to the alkali metals were pursued because they dope and compensate ZnO, respectively. The AFM sample was then characterized. The information used for this experiment included grain size, RMS roughness, surface area difference, and surface morphology.

X-ray photoelectron spectroscopy was used to characterize the composition and chemical bonding for the surface of the deposited film. Standard survey scans using the previously mentioned conditions were first collected. Multiplex scans were then performed for O, C, and Zn using the conditions specified above. Sputter etching of the film using the ion source at standard conditions for six minutes was performed to remove surface contaminants from the ambient, and was followed by survey and multiplex scans using the same conditions as those used prior to sputter etching.

CHAPTER 4 AFFECT OF ANNEALING AMBIENT

4.1 Background

The resistivity of ZnO:Al films deposited in early experiments were typically very high ($\rho > 10^{-2} \Omega \cdot \text{cm}$), and varied by orders of magnitude with small changes in position on the sample's surface. Best results were achieved for small areas of some films with values on the order of 10^{-3} to $10^{-2} \Omega \cdot \text{cm}$. Numerous reports in the literature [11,91,92,127] indicate that modest heat treatments in reducing ambients could yield large decreases in resistivity for ZnO:Al thin films. Reported heat treatments were typically performed at temperatures between 300 and 400°C, for durations of between half an hour and several hours and in reducing gas ambients based on combinations of hydrogen and inert gas. Heat treatments at these temperatures are not compatible with the thermal budget imposed for ZnO:Al films as part of a solar cell structure. Thus, while not practical in the context of fabricating a device, characterization of effects resulting from heat treatments provides data regarding potential of deposited films to achieve better properties, and helps define the cause of high resistivity.

Preliminary experiments indicate that annealing in a high purity forming gas ambient can significantly reduce resistivity of deposited films. From this experiment, annealing conditions of 400°C for one hour is chosen, with flowing gas for all gas ambients except stagnant air. The control sample is not annealed and instead was used to assess aging effects and experimental error. Goals of the experiment were to learn the

minimum resistivity achievable, and mechanism(s) causing increased resistivity of deposited films. To determine the mechanism, effects of annealing in different gas ambients at a consistent temperature and time were studied. The film properties were characterized by XRD, four point probe, spectrophotometry, and FT-IR to measure the structural, electrical, and optical properties. Characterization was performed before and after annealing using consistent conditions. The results of the characterization and discussion of the implications of the data are presented in the following sections.

4.2 Results

4.2.1 Structural Characterization

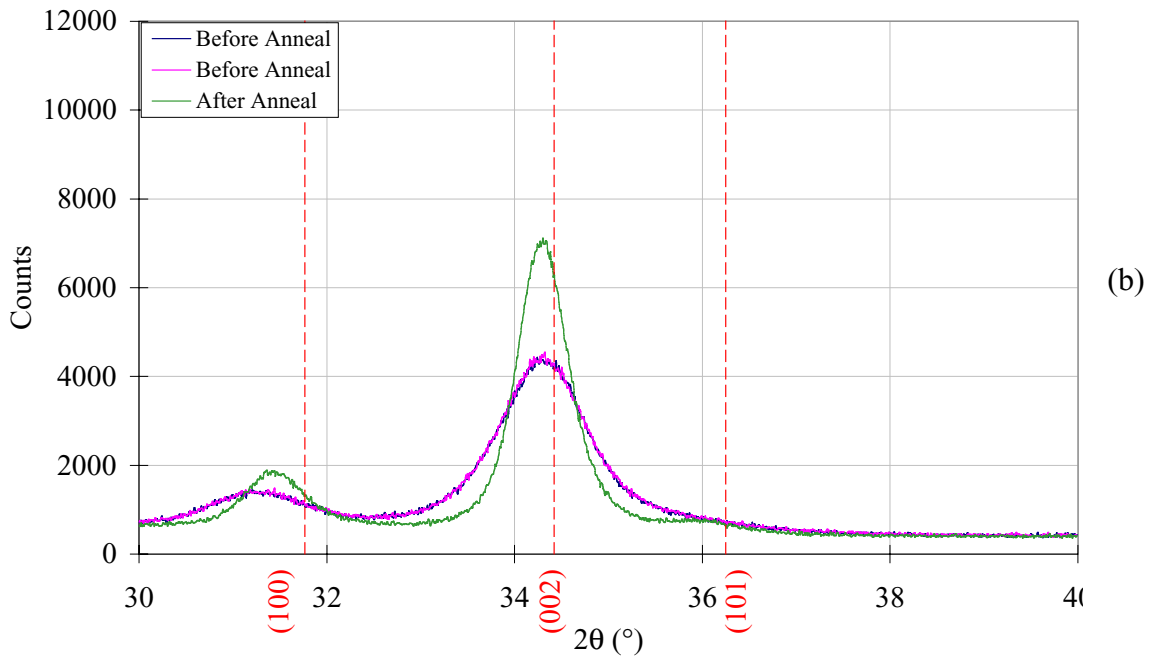
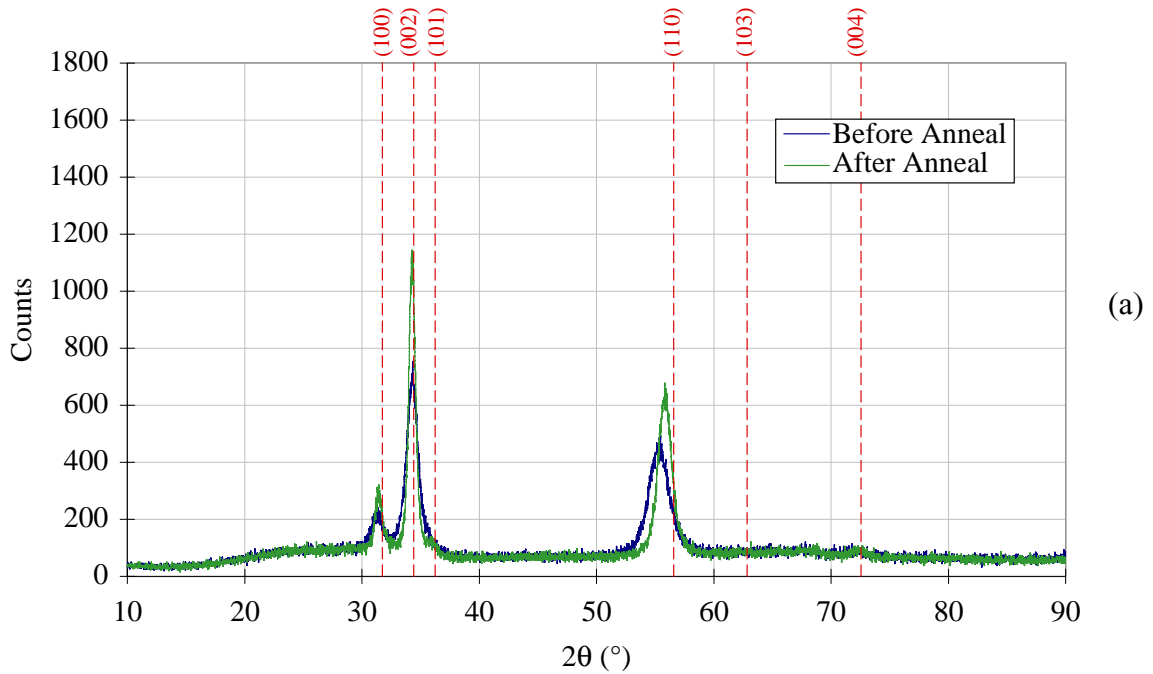
The methods and conditions used to take XRD data for this particular experiment are presented in Sections 3.4.2 and 3.6.1, respectively. The X-ray sampling area is centered on the sample's center, which corresponds to Position 1. Recall that the locations of positions 1, 2, and 3 on the 2.5 x 5 cm sample are schematically illustrated in Figure 3-3. Selected Miller indices for the crystal planes of neat (pure) ZnO, their 2θ values, d-spacings, and relative intensities from the JCPDS are presented in Table 4-1.

Table 4-1. JCPDS powder XRD reference data for Wurtzite ZnO.

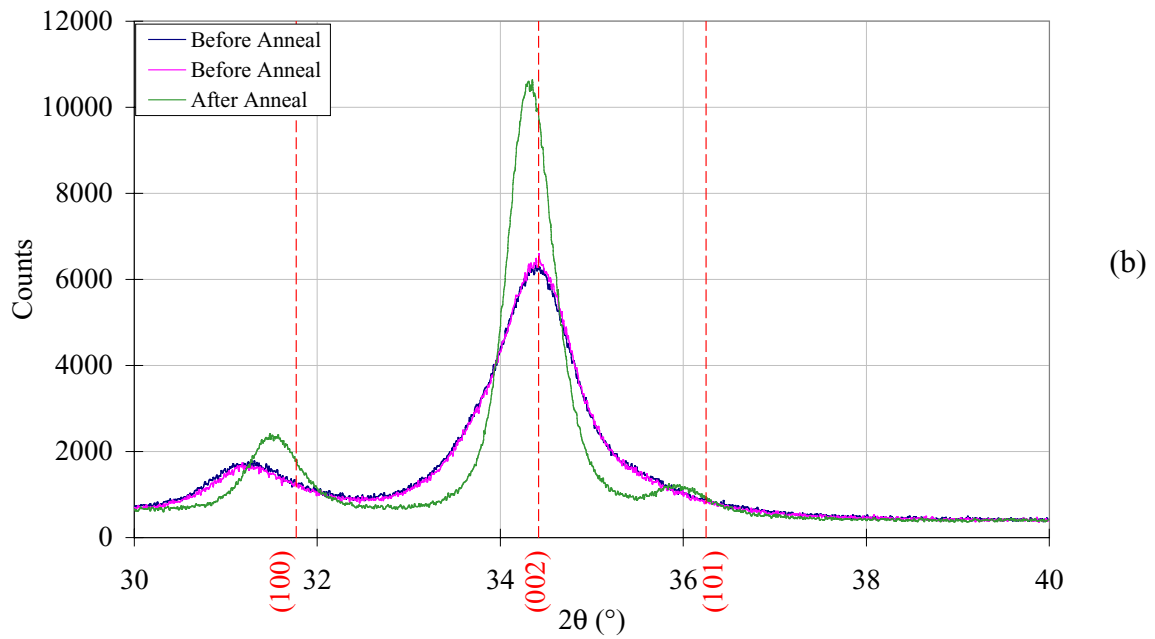
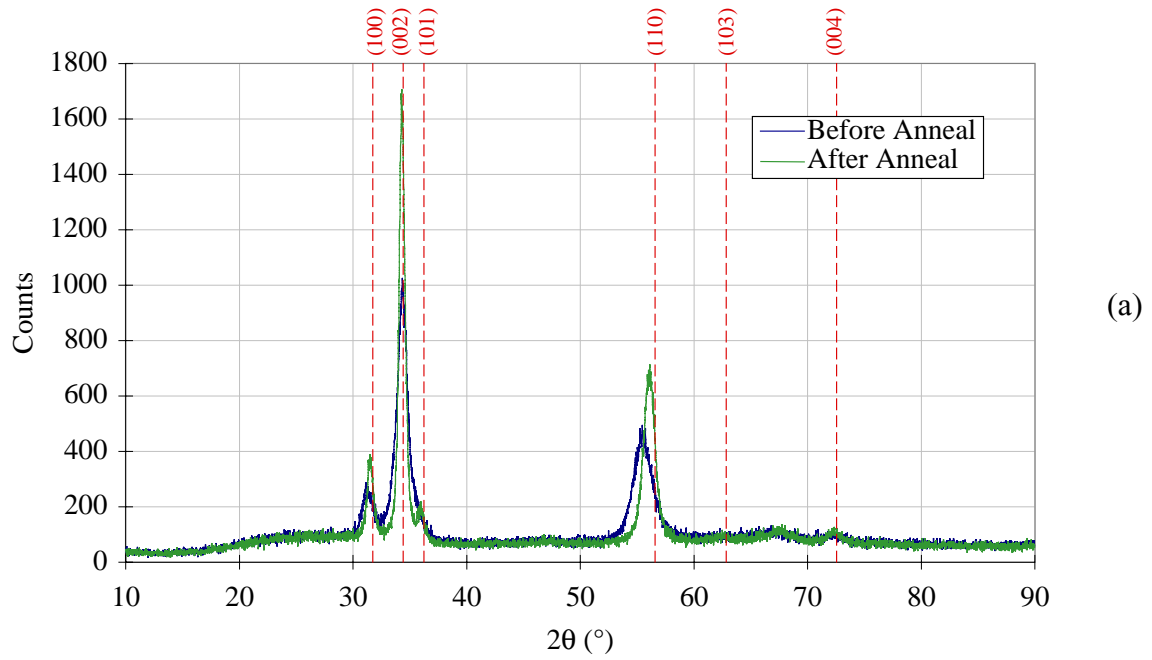
Plane (hkl)	d-Spacing (Å)	2θ (°)	Normalized Intensity
(100)	2.81430	31.770	57
(002)	2.60332	34.422	44
(101)	2.47592	36.253	100
(110)	1.62472	56.603	32
(103)	1.47712	62.864	29
(004)	1.30174	72.562	2

The XRD spectra are presented in Figures 4-1(a-b) to 4-5(a-b), with survey spectra ($10^\circ < 2\theta < 90^\circ$) shown in (a) and high resolution spectra ($30^\circ < 2\theta < 40^\circ$) shown in (b). The labeled red dashed vertical lines on all XRD spectra mark the JCPDS listed 2θ positions for peak from Table 4-1. The plot for each gas ambient shows the results from before and after the heat treatment in the specified gas ambient. For high resolution data, two traces are plotted for data taken before heat treatment (blue and pink) for each gas ambient used, which are replicate spectra. The excellent overlap of replicate data indicates measurement precision is high.

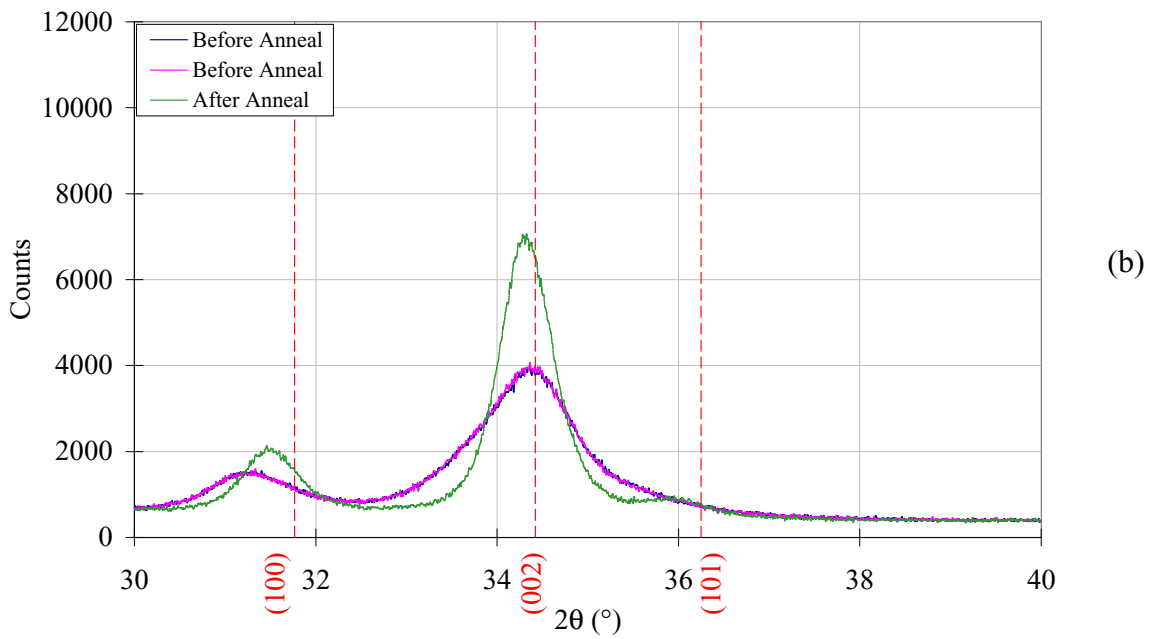
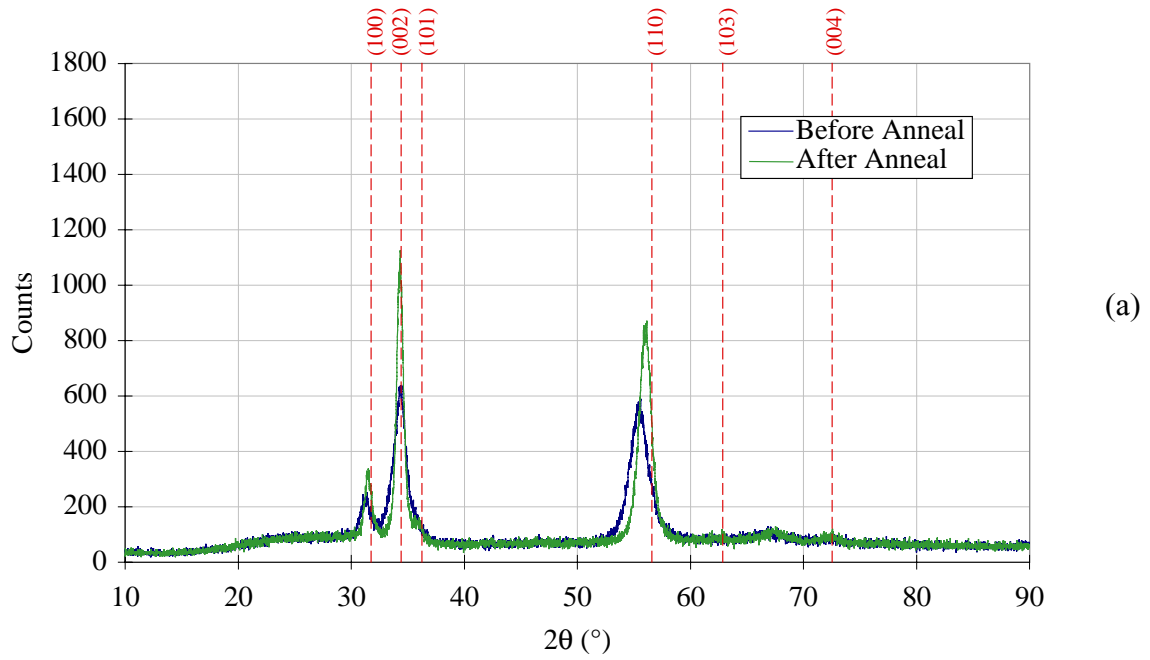
Survey spectra show three dominant peaks corresponding to (100), (002), and (110) ZnO crystal planes. A weak but recognizable peak for the (101) plane can be appreciated in data from annealed samples. Diffraction peaks from several JCPDS listed crystal planes are missing, and intensities from detected peaks do not match the listed normalized intensities. Also, run-to-run variations in peak intensities for the three dominant peaks, as well as variations in the relative intensities between the three peaks for a particular sample occur in the spectra. The presence of changes with heat treatment in peak position, intensity, and FWHM can be appreciated in high resolution and survey spectra for all gas ambients. Intensities increase and breadths decrease for all peaks with heat treatment, while both increases and decreases occur in 2θ peak positions. To investigate these variations, peak position (degrees), intensity (counts), peak area, and full width at half maximum (FWHM in degrees) data are quantified from (100) and (002) peaks from before and after annealed conditions using the *MacDiff* [128] software package. Data are not quantified from the (110) peak, which is the third dominant peak, because this peak does not fall within the 2θ range for high resolution data. Data are



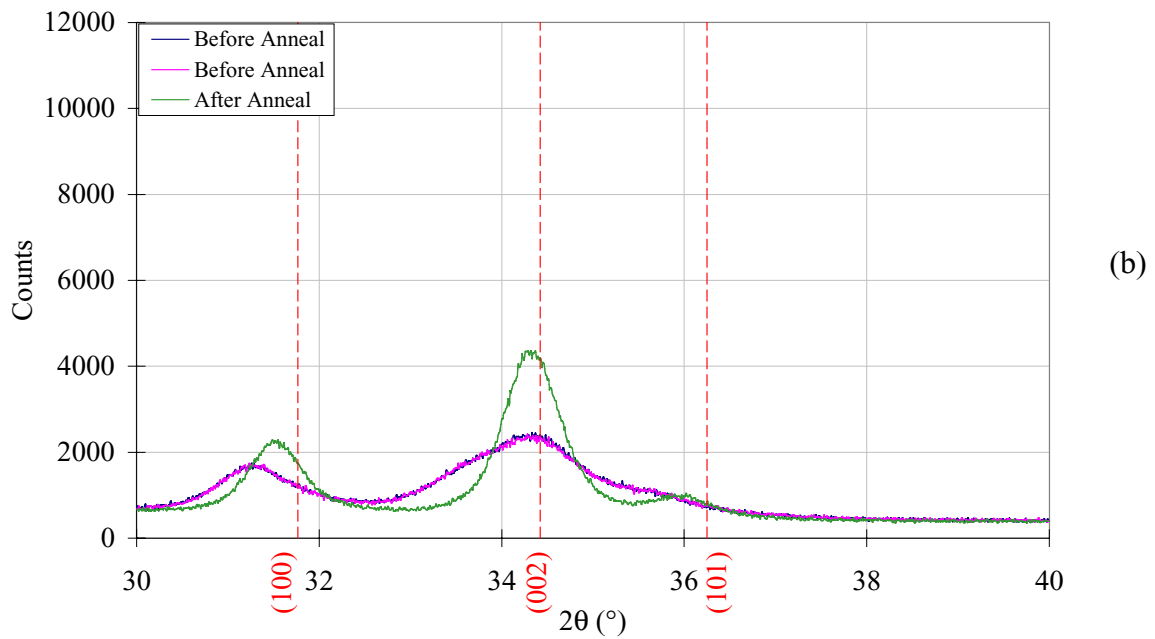
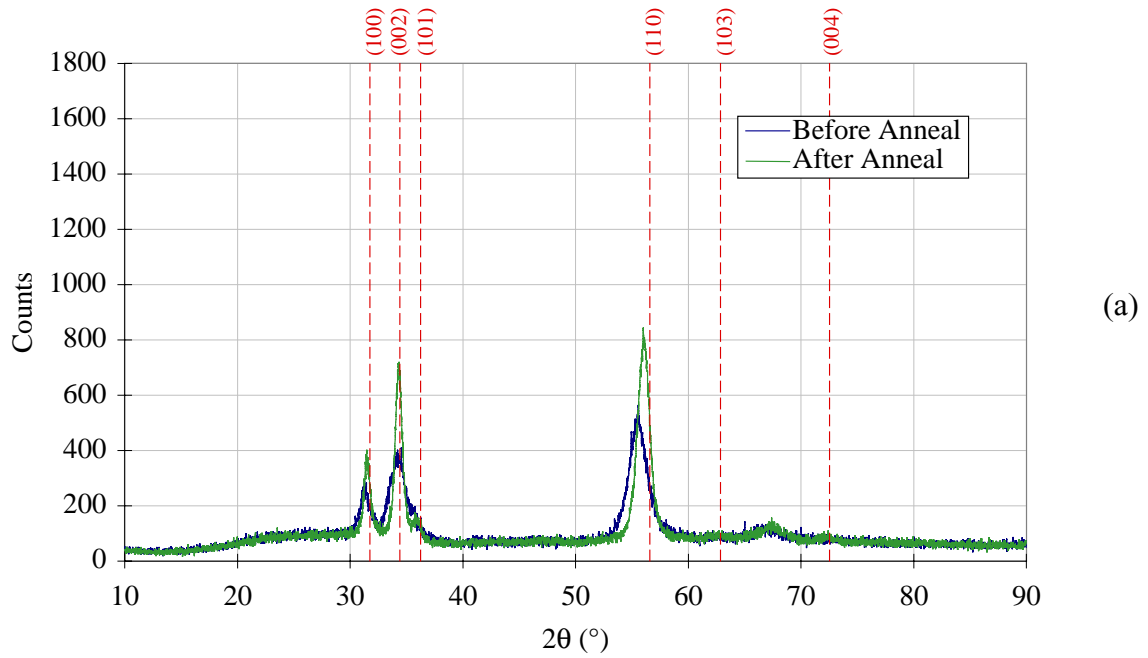
Figures 4-1(a-b) X-ray diffraction spectra from before and after a ZnO:Al thin film is annealed in nitrogen with (a) survey spectra and (b) high resolution spectra focusing on the (002) peak.



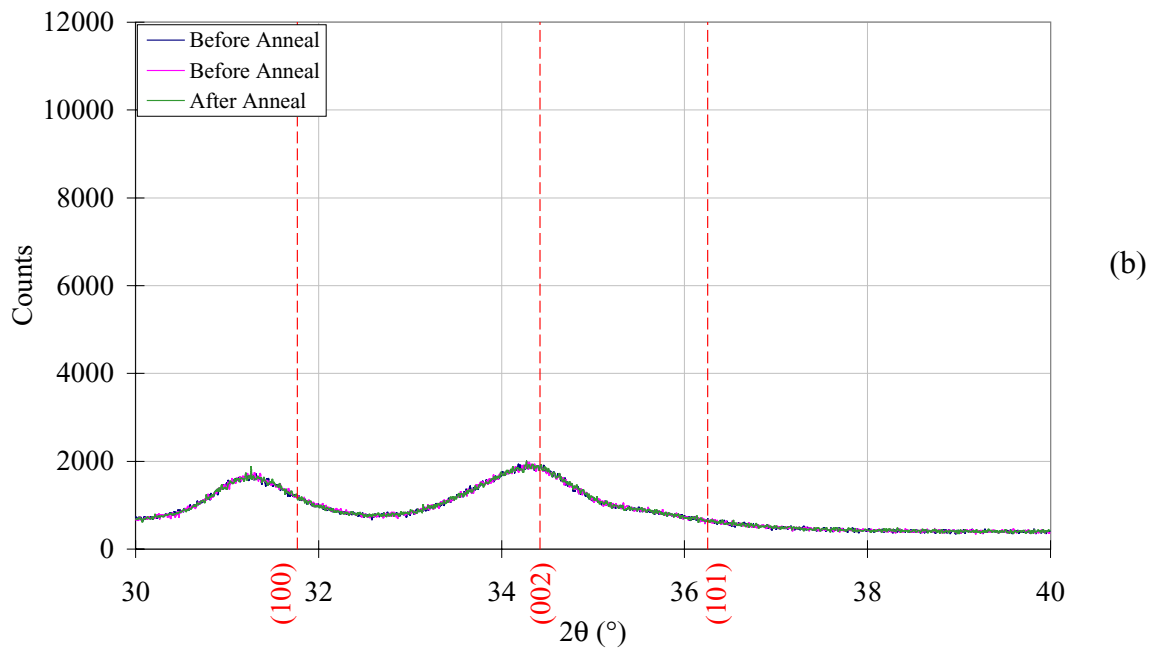
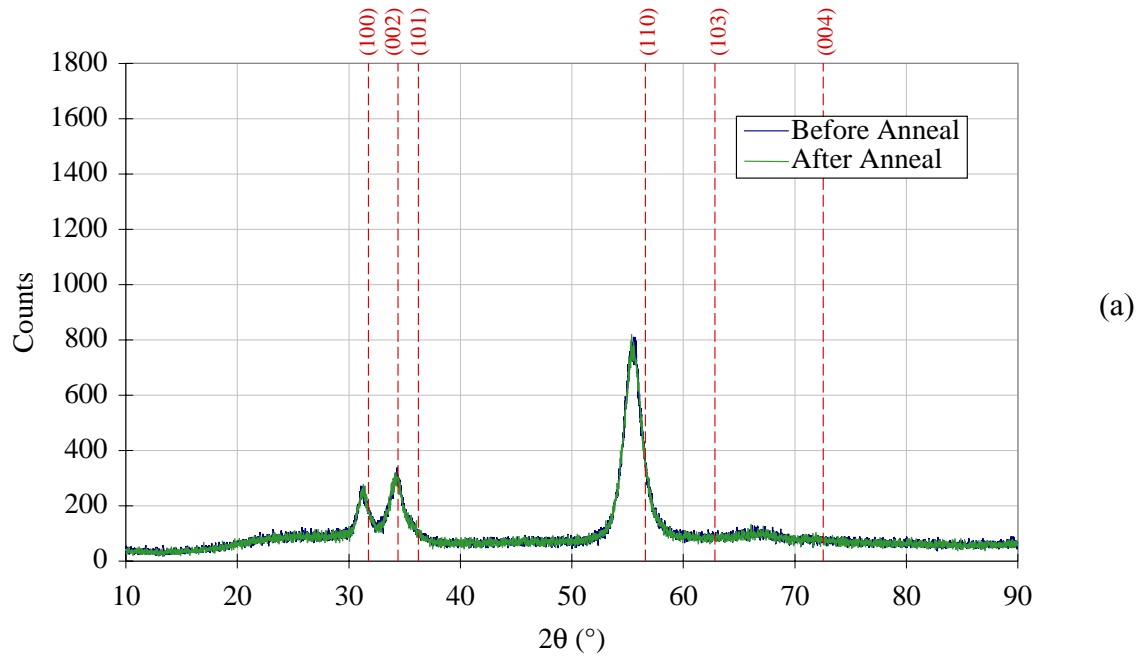
Figures 4-2(a-b) X-ray diffraction spectra from before and after a ZnO:Al thin film is annealed in forming gas with (a) survey spectra and (b) high resolution spectra focusing on the (002) peak.



Figures 4-3(a-b) X-ray diffraction spectra from before and after a ZnO:Al thin film is annealed in stagnant air with (a) survey spectra and (b) high resolution spectra focusing on the (002) peak.



Figures 4-4(a-b) X-ray diffraction spectra from before and after a ZnO:Al thin film is annealed in oxygen with (a) survey spectra and (b) high resolution spectra focusing on the (002) peak.



Figures 4-5(a-b) X-ray diffraction spectra from before and after a ZnO:Al thin film used as a control sample (a) survey spectra and (b) high resolution spectra focusing on the (002) peak.

taken from peaks with the background subtracted and the peak fitted with an approximated Voight function. Quantified data from (100) and (002) peaks from before and after heat treatment are presented in Tables 4-2 and 4-3, respectively.

Changes of less than 5% occur in all data between before and after annealing as compared to the control sample, indicating good measurement precision. This fact plus the good agreement between replicate spectra taken prior to annealing indicates good precision for both measurement and quantification of the data. For (100) data, all 2θ peak positions were smaller than the JCPDS value of 31.770° . The 2θ peak positions

Table 4-2. Quantified XRD data from (100) diffraction peak.

(100) Peak	2 θ position ($^\circ$)		Intensity (Counts)		Peak Area		FWHM ($^\circ$)	
	Before	After	Before	After	Before	After	Before	After
Ambient								
Nitrogen	31.20	31.41	578	1125	61427	87095	0.986	0.688
Forming Gas	31.19	31.50	850	1629	82154	113826	0.883	0.624
Stagnant Air	31.22	31.47	702	1329	67061	99022	0.871	0.662
Oxygen	31.23	31.50	839	1514	76569	110177	0.827	0.644
Control	31.21	31.20	837	875	82984	84470	0.901	0.875
Run-to-Run Variation	0.18%	0.28%	36%	36%	30%	26%	18%	10%

Table 4-3. Quantified XRD data from (002) diffraction peak.

(002) Peak	2 θ position ($^\circ$)		Intensity (Counts)		Peak Area		FWHM ($^\circ$)	
	Before	After	Before	After	Before	After	Before	After
Ambient								
Nitrogen	34.30	34.29	3547	6393	427798	471969	1.038	0.632
Forming Gas	34.40	34.32	5256	9845	631750	688551	0.988	0.597
Stagnant Air	34.37	34.31	3019	6273	409778	492042	1.148	0.679
Oxygen	34.30	34.32	1546	3695	231186	303162	1.357	0.713
Control	34.28	34.31	1137	1134	147445	150687	1.158	1.194
Run-to-Run Variation	0.34%	0.09%	128%	90%	124%	78%	30%	18%

shift 0.2 to 0.3° higher with annealing for all gas ambients, bringing them closer to the JCPDS value. The peak intensity from the (100) plane is consistently the lowest of the three dominant peaks. Intensity relative to background increases by 80 to 95% with annealing. The (100) peak area is consistently much less than the (002) peak. Peak area increases between 39% and 48% with annealing, which is substantially smaller than the increase in peak intensity. Before heat treatment, the (002) FWHM values are consistently larger than for (100) values, while after heat treatment (002) FWHM values are consistently smaller than for the (100) peak. For all cases, the FWHM decreases with heat treatment at 400°C for 60 minutes. The (100) FWHM decreases by 22 to 30% with heat treatment. Significant run-to-run variation is found from samples with and without heat treatment in the data for intensity, peak area, and FWHM, while little variation outside experimental error occurs for 2θ peak position. Run-to-run variation in peak intensity and peak area is significantly higher than variation in FWHM.

For the (002) peak, the 2θ peak position is always lower than the JCPDS listed value of 34.422°. Peak position decreases for samples annealed in forming gas and stagnant air, but does not change outside of experimental error for nitrogen or flowing oxygen anneals. Intensity of the (002) peak is typically highest except for the control sample for which the (110) peak is most intense. Intensity increases by 80%, 87%, 108%, and 139% with heat treatment in nitrogen, forming gas, stagnant air, and oxygen, respectively. Peak area also increases by 10%, 9%, 20%, and 31% with annealing in nitrogen, forming gas, stagnant air, and oxygen, respectively. This increase is much smaller than those measured for peak intensity. The FWHM decreases by 39%, 40%, 41%, and 47% with annealing in nitrogen, forming gas, stagnant air, and oxygen,

respectively. All FWHM values are significantly higher than the lowest values reported from experiments in Chapter 6, which are approximately 0.3° . Run-to-run variations are large and have similar values both before and after heat treatment for peak intensity and peak area. The FWHM shows less variation, but the 30% and 18% variation that occurs for data from before and after heat treatment are still significant. Run-to-run variation in 2θ peak position is very small, and for data taken after heat treatment, no variation outside of experimental error occurs.

4.2.2 Electrical Characterization

Four point probe measurements are taken as discussed in the experimental methods section (3.3.2). The current and voltage data were combined with the thickness ($\sim 0.5 \mu\text{m}$) to determine the film's resistivity. Resistivity as a function of before and after the 400°C one hour heat treatment, gas ambient, and position on the substrate appear in Table 4-4. As shown in Figure 3-3, positions 1,2, and 3 correspond to center, left side, and right side of the $2.5 \times 5 \text{ cm}$ sample, respectively. The term NC in Table 4-4 refers to "no compliance", which occurs when the current source is unable to drive the selected current. This occurs when the sample's resistance is too high, and typically occurs for ZnO:Al films with resistivities $\geq 10^2 \Omega\cdot\text{cm}$ for film thicknesses in this experiment.

Measurable resistivities vary by more than five orders of magnitude, and no compliance results suggest higher resistivities are present. Four classes of variations are found in the data and include positional, run-to-run, heat treatment, and heat treatment ambient. With position, maximum variations of greater than four orders of magnitude and three orders of magnitude occur for data taken before and after annealing, respectively. The smallest variations with position are approximately a factor of 3 and 2

Table 4-4. Resistivity data from before and after heat treatment measured by four point probe as a function of position and gas ambient used.

Ambient	Position 1 ($\Omega\cdot\text{cm}$)		Position 2 ($\Omega\cdot\text{cm}$)		Position 3 ($\Omega\cdot\text{cm}$)	
	Before	After	Before	After	Before	After
Nitrogen	560	1.69	194	5.83	3.44×10^{-2}	1.30×10^{-2}
Forming Gas	0.665	4.65×10^{-3}	9.63×10^{-2}	3.13×10^{-3}	1.42×10^{-2}	1.71×10^{-3}
Stagnant Air	NC	41.8	1.01	0.256	4.74×10^{-2}	4.21×10^{-2}
Oxygen	NC	109	4.42×10^{-2}	2.35	1.66	11.3
Control (No Anneal)	NC	NC	1.68×10^{-2}	1.30×10^{-2}	34.6	29.8

for before and after annealing, respectively. Also, as deposited resistivities are consistently highest for position 1, corresponding to the sample's center. Many resistivities are too high to be measure prior to annealing, as shown by the NC values which are only found at position 1. After annealing, position 1 resistivities are highest for samples annealed in forming gas, stagnant air, and oxygen, but position 2 has the highest resistivity for the sample annealed in nitrogen.

Run-to-run variations in resistivity occur in data from both before and after heat treatment. Comparison of resistivities from the same position on the sample must be used to assess run-to-run variations due to the large effect position has on resistivity. Run-to-run variations in resistivity for annealed films are confounded by effects of different ambients used, therefore the data will be highlighted subsequently. Prior to annealing, resistivities range from 0.67 to $>560 \Omega\cdot\text{cm}$, 1.7×10^{-2} to $190 \Omega\cdot\text{cm}$, and 1.4×10^{-2} to $35 \Omega\cdot\text{cm}$ for data taken from positions 1, 2, and 3, respectively. Data from as deposited films indicates that despite care to use consistent deposition and characterization conditions, more than three orders of magnitude in variation occurs for resistivity data. This indicates that large variations occur for all three measurement positions. The relatively small variation between repeated measurements from the

control sample of 26% and 15% for positions 2 and 3, respectively, suggest measurement variation is not responsible for the large run-to-run differences.

The 400°C, one hour anneal typically changes the sample's resistivity, but the magnitude of the changes show significant variation. Annealing typically decrease the resistivity, except for the oxygen ambient case where resistivities increase for some positions. Differences in the response of resistivity to gas ambient used in annealing will be presented subsequently. Because results change with gas ambient, variations in response to the heat treatment must be investigated by looking at positional variations on samples annealed in the same ambient. To facilitate investigation of changes in resistivity with heat treatment, Table 4-5 presents the magnitudes of changes in resistivity with annealing. The ? signifies the resistivity values both before and after annealing are too high to be measured.

The largest resistance changes are found for position 1, which also had the highest initial resistivity. Changes in resistivity for position 2 are consistently larger than changes for position 3 despite similar initial resistivities. Focusing on resistivity changes for particular gas ambients, annealing in nitrogen lead to the largest change with a 331 times reduction in resistivity for position 1. For position 3, a 2.6 time reduction in resistivity occurs. The larger change occurs with a higher initial value. The lowest resistivity of $1.30 \times 10^{-2} \Omega \cdot \text{cm}$ is not significantly lower than several as deposited values. For forming gas, large decreases in resistivity occur for all positions. Also, all resulting resistivities are significantly lower than any as deposited resistivities from this experiment. The variation in resistivity with position is the smallest found for this experiment. The as deposited resistivities for this sample are also among the lower as

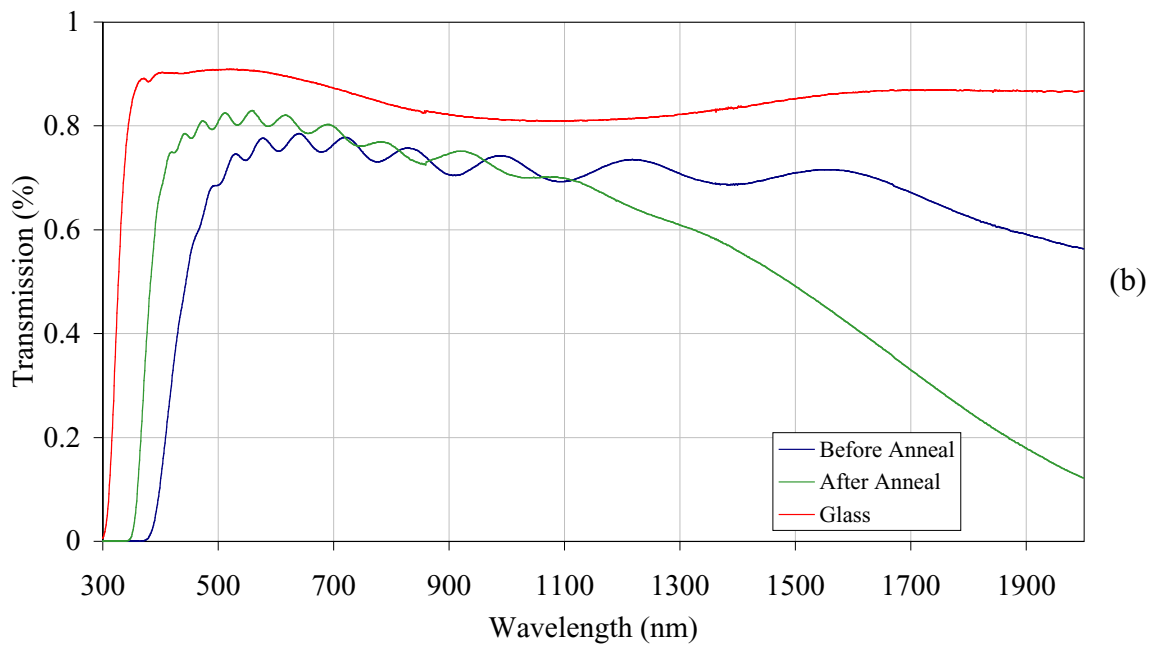
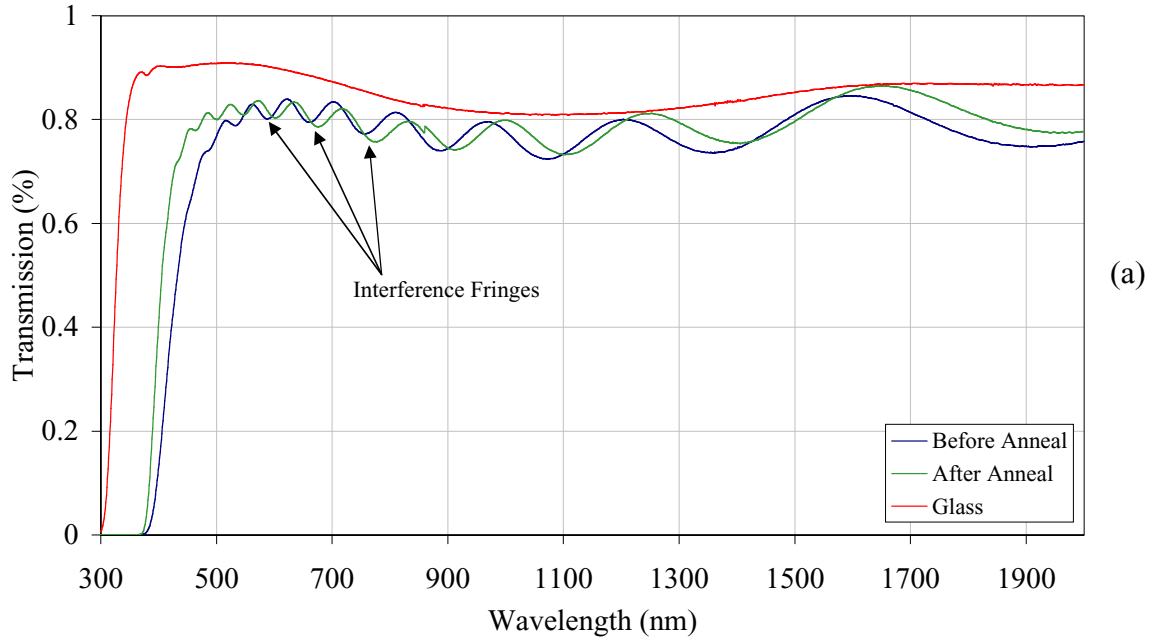
Table 4-5. Changes in resistivity with 400°C one hour annealing.

Ambient	Position 1 $\Delta\rho$	Position 2 $\Delta\rho$	Position 3 $\Delta\rho$
Nitrogen	-331x	-33x	-2.6x
Forming Gas	-143x	-31x	-8.3x
Stagnant Air	>-10x	-3.9x	-1.1x
Oxygen	>-5x	+53x	+6.6x
Control (No Anneal)	?	-1.3x	-1.2x

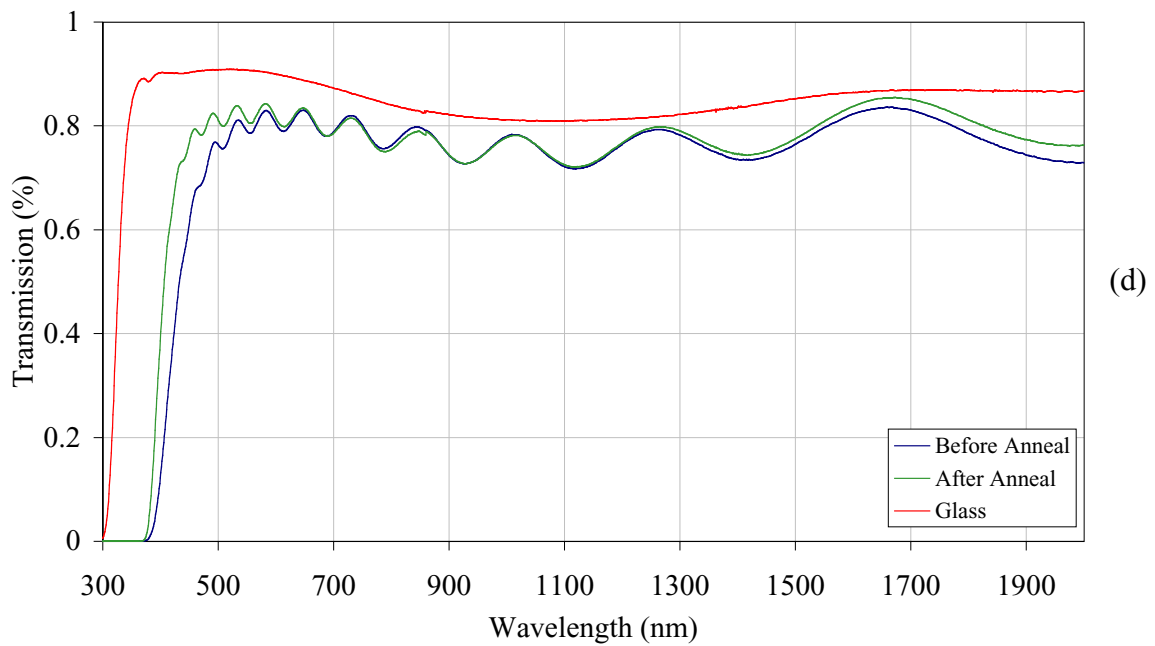
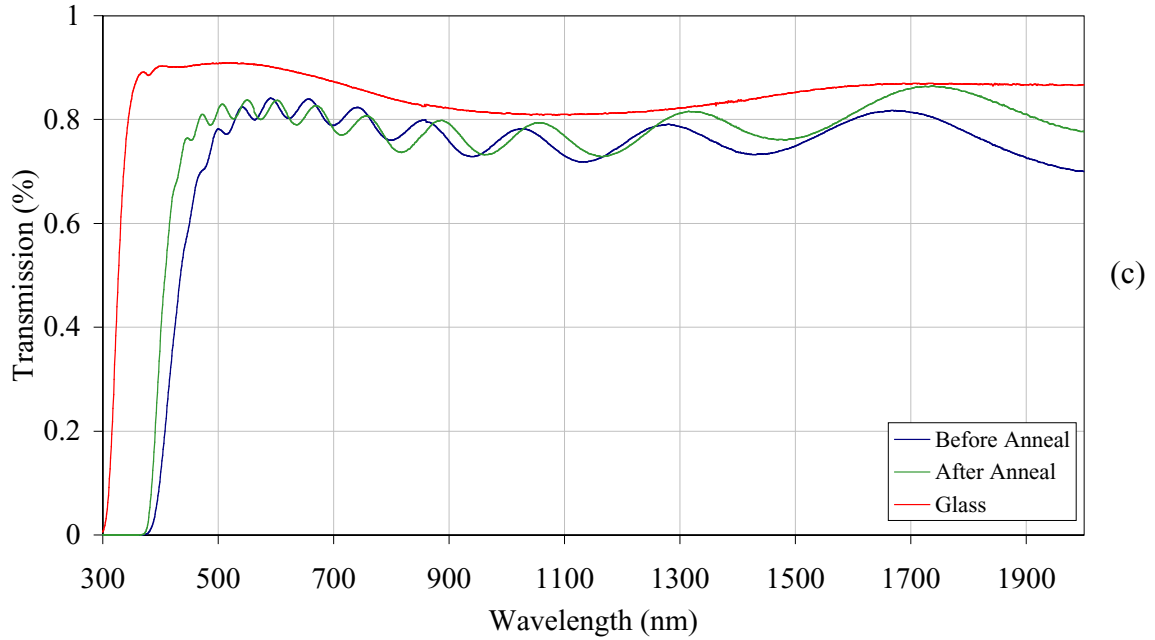
deposited resistivities, particularly for position 1. For stagnant air, little change occurs for position 2, and no change outside of experimental error occurs for position 3. The initial resistivity for position 2 is higher than position 3. More than an order of magnitude change occurs for position 1 when it is considered that the NC value is greater than $5 \times 10^2 \Omega \cdot \text{cm}$, but the magnitude of the change is not known. For oxygen, at least a factor of 5 decrease in resistivity occurs. In contrast, a factor of 53 and 7 increase in resistivity occur for positions 2 and 3, respectively. The initial value for position 1 is much higher than the initial values for either position 2 or 3.

4.2.3 Optical Characterization

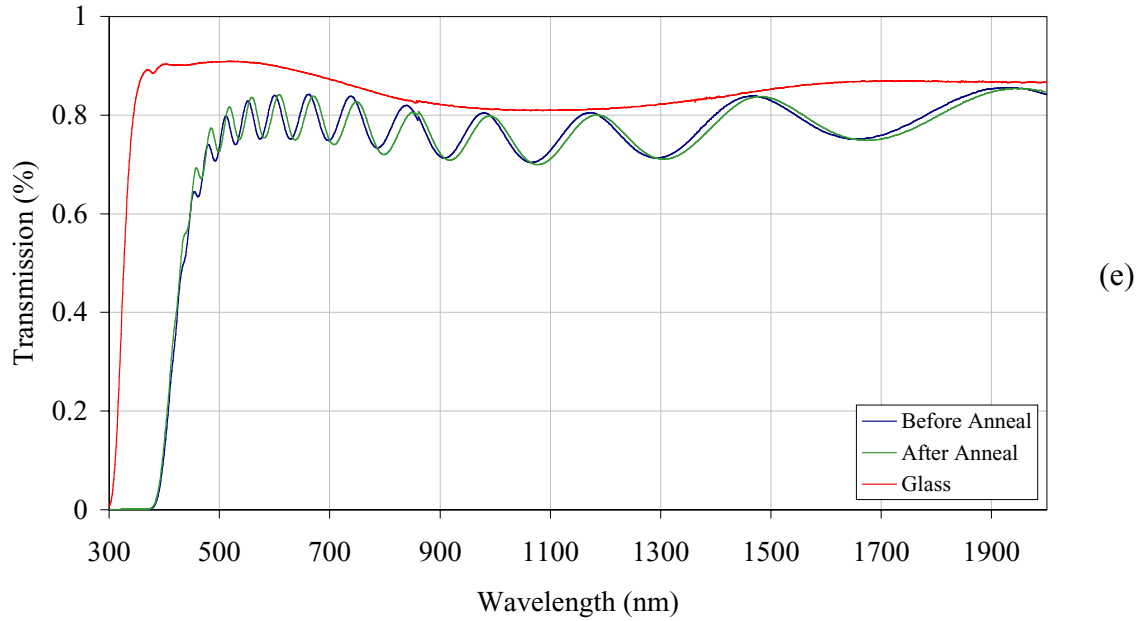
Optical spectrophotometry in transmission and Fourier transform infrared spectroscopy measurements in reflection are collected for this experiment. All measurements are taken from the film's center, corresponding to position 1. Transmission is measured over the wavelength range of $300 < \lambda < 2000$ nm and are presented in Figure 4-6 (a-e). Each plot contains a spectrum from the bare glass substrate, and the glass substrate coated with as deposited films, and films annealed at 400°C for one hour in flowing nitrogen, flowing forming gas, stagnant air, flowing oxygen, and the unannealed control sample. Thin film optical interference fringes are observed as oscillations in the transmittance for data from coated substrates. Reported



Figures 4-6(a-b). Transmission spectra of uncoated and ZnO:Al coated soda-lime glass substrates with data from before and after annealing of the coated sample in (a) nitrogen ambient, and (b) forming gas ambient.



Figures 4-6(c-d). Transmission spectra of uncoated and ZnO:Al coated soda-lime glass substrates with data from before and after annealing of the coated sample in (c) stagnant air ambient, and (d) oxygen ambient.



Figures 4-6(e). Transmission spectra of uncoated and ZnO:Al coated soda-lime glass substrates with no annealing of the coated sample for a control sample.

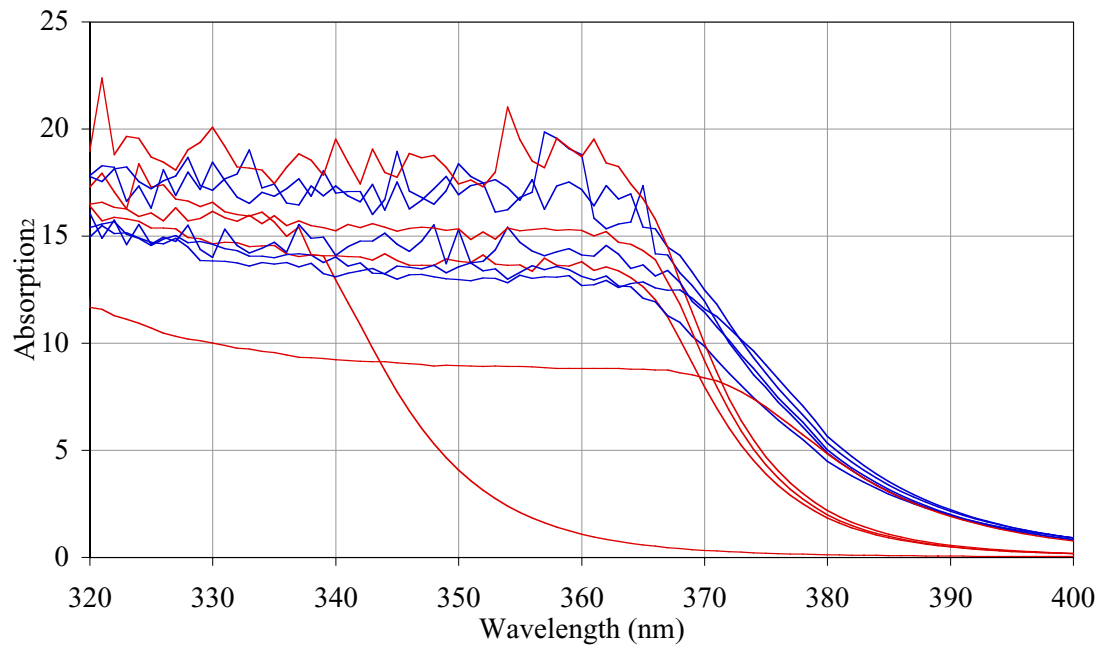


Figure 4-7. Plots of the absorption squared (A^2) versus wavelength to determine changes in optical band gap of the ZnO:Al film with annealing. The blue lines represent before annealing, and the red line represent after annealing.

transmittance data are taken from the midpoint of the oscillations. Figure 4-7 (previous page) presents the same data with units of absorption (A) and has been squared (A^2), and spectra from all gas ambients presented on one plot. Recall that absorption (A) is the product of the absorbance (α) and the film thickness (x). Blue and red traces designate before and after 400°C, 1 hour heat treatment, respectively. By plotting spectra of the absorption squared from the bare glass substrate, and extrapolating the linear part of the band edge curve to zero absorption, the band gap of glass is found to be $E_g=3.95$ eV (314 nm). Transmission between 80 and 90% is found for wavelengths greater than 345 nm, with no sharp features. With the ZnO:Al coating, transmittance is 10% lower than the bare glass spectrum with the exception for unannealed and annealed samples in forming gas. This indicates the deposited ZnO:Al films, except for forming gas samples, have $T\sim 90\%$ for $500<\lambda<2000$ nm. The unannealed forming gas sample has a $\sim 12\%$ lower transmittance than bare glass indicating $T\sim 88\%$ for $500<\lambda<1500$ nm, and declines slowly between $1500<\lambda<2000$ nm. The annealed forming gas sample is similar to the unannealed sample between $600<\lambda<1200$ nm, but decreases markedly between $1200<\lambda<2000$ nm. Classical thin film interference fringes are observed over the transparent regions of the ZnO spectra. The average transmittance cited above are based on a smoothed response through the interference fringes. The phase of the oscillations is different for some cases between unannealed and annealed conditions.

Another important feature is band edge absorption, which is observed as the sharp decrease in transmittance for ZnO films near 400 nm. Absorption data are mathematically transformed transmittance data, with the relationship described by

Equations 4.1 and 4.2. The term I is intensity of light which passes through the sample, I_0 is the intensity of light incident on the sample, and A is the absorption.

$$\frac{I}{I_0} = T = e^{-A} \quad 4.1$$

$$\ln\left(\frac{I}{I_0}\right) = -A \quad 4.2$$

Squared absorption data is plotted in Figure 4-7 over the wavelength range $320 < \lambda < 400$ nm, and is used to quantify the optical band gap and changes in the optical band gap with annealing. Quantified band gap information is presented in Table 4-6, and is given in units of eV.

All band gaps except for the sample annealed in forming gas are consistent with the 3.2 to 3.4 eV values typically reported in the literature. The shifts in band edge with annealing can be observed as shifts of the sharply decreasing portion of the red traces (after) compared to the blue traces (before) to smaller wavelengths in the optical absorption spectra (Figure 4-7). One red trace does not shift, but stays consistent with the blue traces, and is the unannealed control sample. The three tightly group red traces are shifted a small amount to shorter wavelengths compared to blue traces, and correspond to samples annealed in nitrogen, stagnant air, and oxygen annealing ambients. The tight grouping of these three spectra corroborates the similar band gap shifts measured with these ambients. The red trace shifted are large amount to smaller wavelengths corresponds to the sample annealed in forming gas, and is consistent with the large quantified shift in band edge with annealing. The small degree of changes in the control sample suggests good measurement precision.

Table 4-6. Quantified optical band gap (E_g) data from before and after annealing at 400°C for one hour.

Ambient	E_g (eV) Before	E_g (eV) After	Shift (ΔeV)
Nitrogen	3.20	3.27	0.07
Forming Gas	3.19	3.50	0.31
Stagnant Air	3.20	3.28	0.08
Oxygen	3.20	3.28	0.08
Control (No Anneal)	3.19	3.17	-0.02

Fourier transform infrared spectroscopy (FT-IR) reflectance measurements over wavenumbers ranging from 400 cm^{-1} -4000 cm^{-1} ($25 > \lambda > 2.5 \mu\text{m}$), and are shown in Figure 4-8. Infrared (IR) spectra were also taken both before and after heat treatment.

Unfortunately, spectra from annealed samples were lost to a computer malfunction, but they were found to be identical to unannealed spectra except for the sample annealed in forming gas. A very high reflectivity was observed across the spectrum for the sample annealed in forming gas. Five FT-IR spectra taken from samples before heat treatment are presented in Figure 4-8.

The primary features in these FT-IR data are two peaks of increased reflectance (65% and 55%) at 450 and 1230 cm^{-1} , respectively. These peaks are from silica phonon modes from the glass substrate. These phonon modes are identified in the FT-IR spectra. The lack of features from ZnO indicates that the films are highly transparent in the mid to far IR region, with the exception of the sample annealed in forming gas.

4.3 Discussion

4.3.1 Structural Properties

The peaks in the collected spectra match the positions listed in JCPDS entries for pure ZnO. Most peaks listed in the JCPDS database, which are taken from a randomly

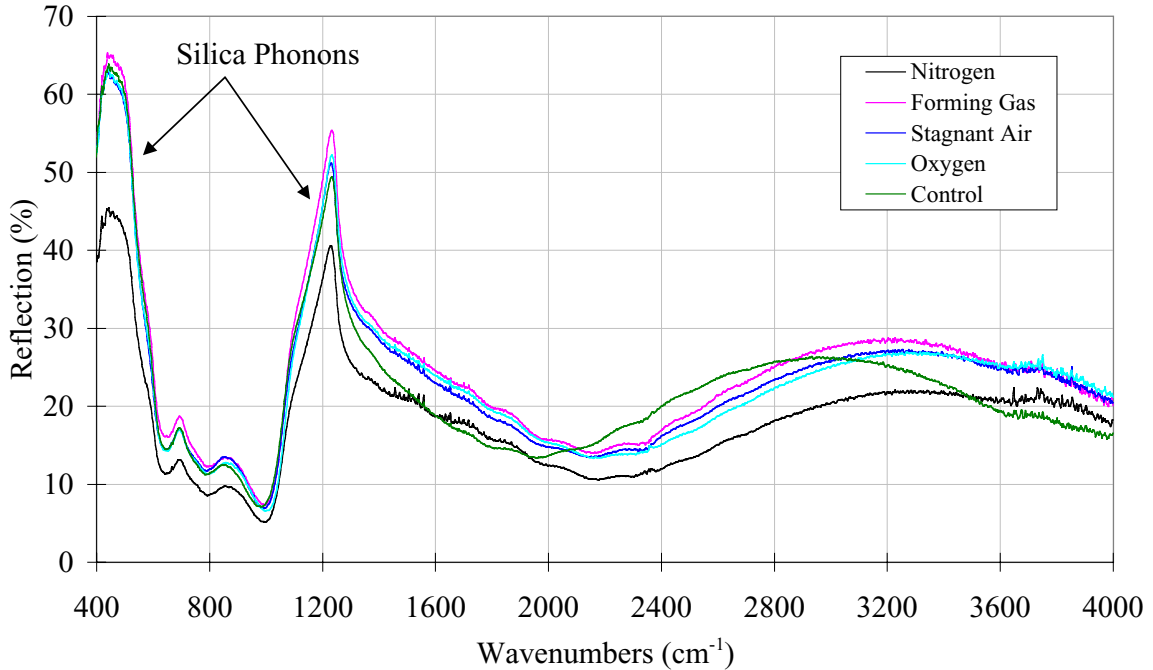


Figure 4-8. Fourier transform infrared spectra taken in reflection mode at an incident angle of 60° for as deposited ZnO:Al thin films on soda-lime glass substrates. Reflectance is plotted versus wavenumbers of the optical radiation.

oriented polycrystalline sample, do not appear in XRD data from ZnO thin films.

Normalized intensities of observed peaks are also very different from those listed in the JCPDS database. This indicates the film's grain structure is not randomly oriented, but is textured as discussed in section 2.4.2. The three strongly diffracting crystal orientations are the (100), basal (002), and (110) planes. This is in contrast with much of the literature, in which a very strong (002) texture is present for substrate temperatures ranging from room temperature to above 300°C [28] on a variety of substrate materials. The relative intensities of these peaks change for different samples suggesting a run-to-run variation in the processes controlling film texture. The formation of texture suggests that adatoms have a certain degree of mobility on the surface to allow the low energy planes to preferentially form parallel to the glass substrate's surface. Dominance of the

(002) peak in XRD spectra reported in the literature and seen in experimental results below (Chapter 6) suggest that the (002) basal plane has the lowest free energy.

Observation of (100) and (110) peaks indicate some process is interfering with formation of a strong basal texture.

One possible mechanism for changes in texture is negative ion resputtering. For experiments reported in Chapter 6, fluxes of high energy oxygen atoms from the sputtering source are postulated to strongly affect the properties of the growing film. A negative ion flux is found to strongly degrade electrical properties of deposited films. The large variation in electrical properties with position supports the case that negative ion resputtering is active during deposition. If negative ion resputtering is responsible for both increased resistivity and degradation of texture and crystal quality of deposited films, then a correlation should exist between higher resistivity and lower (002) texture in the films. As XRD results are collected from position 1, electrical results from this position must be compared. For as deposited films, FWHM is lowest and intensity is highest for the forming gas sample, which also has the lowest as deposited resistivity. The nitrogen sample has the second lowest FWHM and second highest intensity, and has the second lowest resistivity. All other as deposited films have too high a resistivity to measure, larger FWHM values, and lower intensities. Thus a correlation is found between degradation in basal texture and increased resistivity, consistent with negative ion resputtering. The mechanism for this texture could be that ions impinging on the substrate which induce damage that prevents the formation of the typical film texture. Run-to-run variations in relative intensities for all three peaks indicate the deposited films have different degrees of texture.

To investigate effects of the 400°C one hour anneal on structural properties of the deposited films, changes in XRD spectra are evaluated. Survey spectra indicate that the intensity of existing peaks is enhanced by heat treatments for all ambients. This indicates that texture does not change with heat treatment. Quantified data from high resolution spectra give a clearer indication of changes in the peak shapes and show a decided improvement in the intensity and decrease in breadth for both (100) and (002) peaks. This is attributed to improvement in the crystal quality, because the FWHM is related to crystallite or domain size. For thin films in general, accurate determination of grain size from FWHM data is not possible, but relative changes for similar films can be used to gauge relative crystal quality or crystallinity. Lattice strain can influence FWHM, but also influences 2θ peak position. While FWHM consistently decreases, there is no consistent change in 2θ peak position, which suggests that decreased FWHM results from improved crystallinity instead of changes in lattice strain. Quantified data from Table 4-3 indicates intensity consistently increases by approximately 100% for both (100) and (002) for all gas ambients. Peak area consistently increases with annealing, but to a much smaller extent than increased intensity. The increased measured intensity increases peak area and decrease in measured FWHM decreases peak area. The nearly constant peak area across annealing suggests changes in intensity and FWHM almost balance each other out. The small increase in quantified peak areas suggests that volume fractions of each orientation are staying nearly constant. Thus growth of particularly oriented grains is not occurring at the expense of others, which suggests Ostwald ripening [94] is not occurring.

The spectra also reveal that small changes in 2θ peak positions resulted from the anneal. The (100) and (110) peaks moved to higher 2θ values while the (002) moved to lower 2θ values. The shifts in 2θ values and the corresponding changes in the d-spacing were all less than 1%. The lack of a uniform direction of shift indicates a change in the film instead of a change in 2θ calibration of the diffractometer. The fact that the 2θ peak positions of the (100) and (110) planes are independent of the basal lattice spacing, while the (002) peak depends exclusively on this parameter suggests anisotropic changes in the plane spacing. The offset to lower values indicates a consistent increase in d-spacing, which is indicative of residual tensile stress in the out of the film plane direction. The consistency of the decrease in FWHM, increase in intensity, and changes in peak position indicate that the gas ambient used in the anneal does not have a large influence on crystallographic changes resulting from the anneal. This is in stark contrast to the large differences the annealing ambient cause in resistivity. It suggests the mechanism for changes in resistivity occur by a process to which XRD is not sensitive.

4.3.2 Electrical Properties

Large variations in resistivity are noted in the data, and separate into four categories including variations with position, run-to-run, annealing, and annealing ambient. For positional changes prior to annealing, the film's center (position 1) always has the highest resistivity, often one or more orders of magnitude larger than values from positions 2 and 3 (left and right side, respectively, in Figure 3-3). The mechanism for positional variation is postulated to be negative ion resputtering. This effect is the focus of Chapter 6, and is postulated to be responsible for carrier concentrations much lower than the sputter target doping level. This is consistent with optical characterization data

to be discussed subsequently, which indicates carrier concentration is low for all samples both before and after annealing, except for the sample annealed in forming gas. Also, the strong variations in resistivity with position are similar to variations that occur in resistivity data presented in Chapter 6. The films were deposited from a two inch diameter planar magnetron source. Tominaga *et al.* found that the negative ion resputtering is focused to an area on the substrate directly opposite the high erosion *racetrack* zone formed on the planar magnetron target [112].

A model for positional changes in film properties based on work by Messier *et al.* is presented in Chapter 6, and focuses on the ratio of negative ions to deposited neutrals incident on the substrate, and the energy to which the negative ions are accelerated. Large ratios of negative ions to deposited neutrals result in more bombardment damage. Changes in ion energy change the results of the ion-sample interactions, and therefore yields more complex changes in the results of bombardment. For the sputter deposition conditions used, target bias and therefore negative ion energy is not expected to change. For a magnetron source, a majority of the deposited flux is generated in the *racetrack* zone, and by the cosine distribution described in the literature review, leave the target with a variety of different angles. The negative ion flux is also primarily generated at the *racetrack* zone, but is postulated to have a much smaller distribution of departure angles from the sputtering source with most leaving perpendicular to the source. Thus, negative ion flux opposite the *racetrack* is relatively large, but because the deposited neutral flux leaves the target with the cosine distribution of angles, the ratio of negative ions to deposited neutrals is higher directly towards the position opposite the *racetrack* than other areas. Preliminary experiments for Chapter 5 found that resistivities are

substantially lower off-axis of the source, which is a position that should receive little negative ion flux. This is consistent with the lower resistivities found for positions 2 and 3 at the substrate's edges. The mechanism for negative ion resputtering effects on electrical properties is discussed in Chapter 6.

Large run-to-run variations in resistivity are attributed to small variations in substrate placement above the sputtering source. This is supported by the fact that one resistivity at either position 2 or 3 is always on the order of $10^{-2} \Omega\cdot\text{cm}$, while the other is higher. This is consistent with a substrate being slightly offset from the source, resulting in different magnitudes of negative ion resputtering for the two opposite edges. An offset substrate is also consistent with run-to-run variations at position 1, as different substrate offsets can have a large effect on film resistivity due to the close proximity of the *racetrack* zone to the substrate's center. This proximity means the ratio of negative ions to deposited neutrals can change dramatically over short distances, similar to large changes in resistivity over small distance found in experiments reported in Chapter 6.

For annealing, all ambients are found to improve crystallinity of deposited films, but for resistivity, annealing ambient strongly affects results. It can be seen that the resistivity decreased after the heat treatment for all samples with the exception of the sample annealed in oxygen. The resistivity was measurable for all of the annealed films, though the resistivity was not always lower. For oxygen anneals, resistivity decrease for position 1 and increased for positions 2 and 3. The resistivity at position 1 is too high to measure, while resistivities prior to annealing of 4.42×10^{-2} and $1.66 \Omega\cdot\text{cm}$ occur for positions 2 and 3, respectively. With annealing, resistivities change to 109, 2.35, and $11.3 \Omega\cdot\text{cm}$ for positions 1, 2, and 3, respectively. Thus low resistivity values at positions

2 and 3 become higher, while the very high resistivity for position 1 decreases. The decrease in position 1 resistivity is consistent with the increased carrier concentration indicated by optical characterization as discussed subsequently. The difference in sign of the resistivity change for position 1 versus positions 2 and 3 suggests that the initial resistivity influences the results of this anneal. It is speculated that this results from competition between processes that increase and decrease resistivity. Resistivity decreases in position 1 because the initial state is more damaged by negative ion resputtering than positions 2 and 3. Thus, improved carrier concentration occurs with improved crystallinity resulting from heat treatment despite a competing mechanism that increases resistivity. It is speculated that increased resistivity for positions 2 and 3 result from chemisorption of oxygen species following the mechanism outlined for gas sensors in the literature review. This mechanism will be discussed in more detail subsequently for samples annealed in forming gas. The scatter in oxygen annealed samples is $\sim 50x$, whereas before the anneal it varied by $\sim 2500x$. Thus annealing reduced the scatter in resistivity by a factor of 50.

Annealing in stagnant air yields little change in resistivity for positions 2 and 3 with changes from 1.01 to 0.256 $\Omega\cdot\text{cm}$ and 4.74×10^{-2} to 4.21×10^{-2} $\Omega\cdot\text{cm}$, respectively. At least an order of magnitude decrease occurs for position 1, where resistivity changes from too high to measure ($\rho > 10^2$ $\Omega\cdot\text{cm}$) to 41.8 $\Omega\cdot\text{cm}$. Therefore, there is a large degree of scatter in the resistivity both before and after the heat treatment. Nitrogen annealing consistently lowered the resistivity with decreases for positions 1 and 2 (both of which started with high resistivities) by factors of 330x and 33x, respectively. The resistivity at position 3 was low before the anneal, and decreased by 2.6x with annealing. The lack of

changes for positions 2 and 3 suggests that competition between mechanisms for increasing and decreasing resistivity are in balance. Position 1 is similar to the oxygen case where the damage from negative ion resputtering is heavy, and because it is farther from equilibrium is more easily improved by the heat treatment.

The sample annealed in forming gas is by far of the most interest as it exhibited the lowest resistivity for annealed samples and the lowest resistivities measured by an order of magnitude. Also positional variations in resistivity for this sample is the smallest for any sample, with less than a factor of three separating the values. Decreased resistivity by annealing in a reducing ambient is consistent with reports in the literature. Decreased resistivity and improved uniformity while maintaining excellent optical properties are very important improvements towards production of a large area transparent conducting contact to solar cell structures. The data indicates the gas ambient during annealing is a critical parameter to the resistivity but not texture or crystallinity of the deposited film.

The two most commonly cited mechanisms for decreasing resistivity by a hydrogen containing reducing ambient are a decrease in chemisorbed oxygen species, and changes in the stoichiometry by formation of oxygen vacancies and/zinc interstitials [11,91,92,127]. Recall from the discussion of gas sensors in the literature review (Chapter 2) that chemisorbed oxygen acts as an electron trap, which reduces the free carrier concentration. Therefore changes in amount of chemisorbed oxygen can influence carrier concentration. For stoichiometric changes, a reducing ambient increases the carrier concentration by reducing oxygen levels to slightly less than stoichiometric values, causing formation of zinc interstitials and/or oxygen vacancies, which act as

shallow donors. The chemisorption postulate is supported by the low temperature (400°C) and short duration (60 minutes) of the anneal, as this surface process does not require bulk diffusion. This phenomenon is well established in the use of ZnO as a gas sensor [6,8,9] as discussed in section 2.3.2. The sensitivity (S) is a primary performance criteria for measuring the electrical response of a solid state gas sensors to a particular gas. It relates the magnitude of the change in resistance achievable with a gas. The sensitivity of ZnO to reducing ambients is very high for temperatures similar to those used in the anneals performed in this experiment. The reported mechanism is changes in the surface coverage of the grains with the chemisorbed oxygen species. In reducing ambients containing hydrogen, it is found that the hydrogen reacts with the chemisorbed oxygen species, and the products of these reactions are removed from the film. The higher the oxygen partial pressure, and the higher the surface coverage of chemisorbed species, the higher the resistivity.

Change in carrier concentration due to changes in the intrinsic donor concentration is another possible mechanism for the decreasing resistivity. The intrinsic doping effect in ZnO is well established, and was discussed in section 2.3.2. The concentration of zinc interstitials and oxygen vacancies in thermodynamic equilibrium depends on the temperature and vapor pressures of oxygen and zinc. The vapor pressure of zinc in the tube furnace is assumed to be zero, and therefore any effects of the gas ambient result from changes in the partial pressure of oxygen. As the oxygen partial pressure is reduced, the concentrations of zinc interstitials and/or oxygen vacancies should increase, thereby increasing the carrier concentration of the film and decreasing the resistivity (assuming a constant mobility).

Two other possible mechanisms by which resistivity is decreased with increasing carrier concentration are activation of the extrinsic Al dopant atoms, and reduction of compensating effects. Activation of extrinsic dopants traditionally involves enhancing dopant substitution for the appropriate host atom. For ZnO:Al, this involves enhanced substitution of Al on Zn sites, and all anneals would be expected to yield similar results independent of the gas ambient. XRD indicates that structurally all films responded favorably to the heat treatments. The resistivity in the area measured by the diffractometer (position 1) also improved in each case, but the amount of the decrease in the resistivity varied significantly with the gas ambient used. This suggests that even if this mechanism were active, it does not dominate the changes in electrical properties.

Changes in compensation could result from changes in the stoichiometry of the film. Zinc vacancies or oxygen interstitials have both been proposed as compensating mechanisms for conduction band electrons, and would be sensitive to the oxygen potential of the gas ambient. This is the mechanism postulated in Chapter 6, and is also compatible with the data in this experiment. Negative ion resputtering exposes the growing film to energetic atomic oxygen, which is a very reactive form of oxygen. As detailed in Chapter 6, if the energy of negative oxygen ions are sufficient, they can be implanted and come to rest on lattice or interstitial sites. Excess oxygen on lattice sites could drive the stoichiometry to oxygen rich, resulting in zinc vacancy formation and the consumption of conduction band electrons. Oxygen interstitials have also been postulated to consume conduction band electrons. Therefore both forms of excess oxygen can cause compensation of conduction band electrons generated by Al doping. Because this model involves non-equilibrium excess concentrations of oxygen, reduction

in compensation would be expected for annealing in reducing or low oxygen partial pressure ambients (i.e. pure nitrogen). This is consistent with decreased resistivity and increased carrier concentration found by electrical and optical characterization.

Therefore the two most likely mechanisms for decreased resistivity with increased carrier concentration for samples annealed in forming gas are decreases in concentration of chemisorbed oxygen species and decreases in compensation by excess oxygen. The fact that crystallographic damage is occurring with negative oxygen bombardment suggests the ions have greater than 100 eV of kinetic energy, which is consistent with the typical target self bias during sputtering. This is more consistent with changing the oxygen content of the film instead of changes in surface fractions of chemisorbed oxygen. To roughly gauge the degree of compensation achievable by chemisorbed oxygen, a calculation to determine compensation of a spherical grain is performed. The surface site density for chemisorption is set at 10^{15} cm^{-2} , a typically surface site density. The doping within the grain is set to $6.5 \times 10^{20} \text{ cm}^{-3}$, which assumes 100% activation. Assuming each oxygen consumes 1 electron, when the number of chemisorbed oxygen atoms equals the quantity of dopant within the grain, the grain will be fully depleted. Surface site density times area of a sphere is set equal to carrier concentration times volume of a sphere. The solution for radius $r \sim 50 \text{ nm}$, based on reports in literature and evidence found in future experiments is similar to grain sizes in the deposited films. Thus all grain boundaries in the film would need to be nearly saturated with chemisorbed oxygen to achieve compensation levels found in the film. This degree of oxygen chemisorption seems unlikely even with the availability of atomic oxygen. Therefore in agreement with results in Chapter 6, it is postulated that increased resistivity results from

low carrier concentration which results in a large part from compensation by greater than stoichiometric levels of oxygen causing oxygen interstitials or zinc vacancies.

4.3.3 Optical Properties

Spectrophotometry measurements show excellent transmittance across the visible and near infrared regions indicating that the films are close to stoichiometric, and do not have active major defect absorption mechanisms. It is difficult to give a quantitative value for the transmittance because of the interference oscillations in the spectra, but in general the transmittance below the band gap is greater than 90% when absorption from the glass substrate is considered. The exception to this is the film that became strongly absorbing in the IR region after annealing in forming gas. The strong absorption is the result of free carrier absorption [80,82]. This indicates that the plasma resonance frequency has shifted to higher frequencies (shorter wavelengths), and thus by Drude's model presented in section 2.3.3, the carrier concentration in the film has increased substantially. This is consistent with greatly improved resistivities for all positions with forming gas annealing. Absorption at wavelengths of $\sim 2 \mu\text{m}$ is consistent with a carrier concentration on the order of 10^{20} cm^{-3} . A large increase in carrier concentration is corroborated by a relatively large shift in band gap energy (0.3eV) for forming gas annealed samples. Hall data presented in future chapters will show that a carrier concentration on the order of 10^{20} cm^{-3} is typical for a resistivity on the order of $10^{-3} \Omega\cdot\text{cm}$. Band gap energy shifted by ~ 0.07 to 0.08 eV with annealing in nitrogen, oxygen, and stagnant air. As will be discussed in the next paragraph, this shift is associated with increased carrier concentration, which is consistent with decreases in resistivity found for the film's center (position 1) with annealing, which is where the transmission spectrophotometry data was taken from.

The shift in band gap energy is the result of the Burstein-Moss shift (described in the literature review) [93]. For this experiment, the band edge absorption of every film shifted to higher energies after being annealed. This indicates an increase in carrier concentration because the Fermi energy moves higher into the conduction band with increased carrier concentration, and results in occupation of all states to higher energies. Thus photons must have higher energy to promote a valance band electron to above the Fermi energy, which is above the conduction band edge. This pushes the optical band edge to higher energies. The magnitude of this change reflects the magnitude of the carrier concentration effect, and the conduction band curvature. The conduction band curvature is not known. It is also not known if the as deposited samples are degenerately doped prior to annealing or not, therefore it is not known if the band gap of as deposited films has been shifted by the Burstein-Moss effect. If the as deposited samples were not degenerately doped, then carrier concentration can increase until the film is degenerately doped without yielding any Burstein-Moss shift in the optical band gap. Therefore, it is impossible to determine the magnitude of carrier concentration change from the Burstein-Moss shift. It is clear that the shift for the sample annealed in forming gas is larger than those annealed in N₂ or O₂, indicating that its carrier concentration is significantly higher than the other films.

The FT-IR spectra from as deposited films do not show any effects from the ZnO thin film on the glass suggesting the deposited film is transparent across the wavenumber range of the spectra. By the Drude model, if the carrier concentration exceeds approximately 10^{19} cm^{-3} then the IR reflectance of the film will change in the wavenumber range (400 to 4000 cm^{-1}). Only the sample annealed in forming gas

demonstrated strongly increased IR reflectance, indicating that a change of greater than an order of magnitude in carrier concentration (from $<10^{19}$ to $>10^{20}$ cm^{-3}) occurred. For the samples annealed in other ambients, the Burstein-Moss shift indicates that the carrier concentration has increased, but FT-IR measurements indicate carrier concentration is still less than approximately 10^{19} cm^{-3} . The low carrier concentration for the samples annealed in other ambients is consistent with relatively poor position 1 resistivities measured for all films except those annealed in forming gas. If all the Al incorporated into the target (2 wt% Al_2O_3 in 98 wt% ZnO) were active, the carrier concentration in the deposited film would be 6.5×10^{20} cm^{-3} . As previously discussed, the resistivity and FT-IR spectra are consistent with a carrier concentration of less than 10^{19} cm^{-3} , therefore activation of the dopant atoms from the target is extremely poor in all of the as deposited films, and all of the annealed films with the exception of those annealed in forming gas. As previously discussed, decreased carrier concentration is attributed to compensation of conduction band carriers generated by Al doping by excess oxygen. Annealing, particularly in forming gas acts to transport the excess oxygen from the film, yielding a reduction in compensation, and thereby the increased carrier concentration observed.

4.4 Summary

The interpretation of results for this experiment was made difficult by the severe non-uniformity in the electrical properties of the films. This non-uniformity is consistent with evidence of negative ion resputtering found both in the literature and experiments reported below in Chapter 6. Both the strong variation in resistivity, and the low free carrier concentration are consistent with negative ion resputtering. All deduced carrier concentration data are based on observed Burstein-Moss shifts and free carrier effects in

optical data taken from the film's center (position 1), which is the region consistently found to have the consistently worst electrical properties. Annealing in forming gas was found to yield resistivities much lower than any other ambient. This is consistent with a relatively large Burstein-Moss shift of 0.3 eV and the shortest wavelength for plasma resonance, both of which indicate larger increases in carrier concentration than for other annealing ambients. The Burstein-Moss shift seen in spectrophotometry data from all annealed samples suggests carrier concentration increased with all annealing ambients. This is consistent with the decrease in electrical resistivity that occurred at position 1 for all annealed films. No optical measurements were performed for positions 2 or 3, so changes in carrier concentration for these positions cannot be evaluated. The decreased resistivities found for annealing in forming gas and nitrogen would be consistent with reduction of compensation by removal of oxygen. Oxygen annealing increases resistivities in positions 2 and 3. It is speculated that this increase is dominated by decreased carrier concentration, as the case for heat treatment resulting in a decrease in carrier mobility seems implausible. Again, excess oxygen stoichiometry and chemisorbed oxygen can both compensate conduction band electrons, therefore increased resistivity is attributed to a combination of these two processes. The XRD results were also taken from the center of the film, and also indicate modest improvements in the film quality for all heat treatments. Because the changes in resistivity with different ambient in this position were a strong function of gas ambient, while changes in the XRD spectra were not, it is concluded that changes in crystallinity are not the dominant mechanism for the decrease in resistivity.

CHAPTER 5
DEVELOPMENT OF ELECTRICAL AND MICROSTRUCTURAL PROPERTIES IN
VERY THIN ZnO:Al FILMS

5.1 Background

The objective of this experiment is to investigate development of structural and electrical properties for sputter deposited ZnO:Al thin films. The importance of this issue is motivated by production of thinner films to decrease optical loss, to better understand the electrical transport properties, and for the particular application of CIS based solar cells to investigate electrical transport in the near substrate interfacial region (NSIR). For optical loss, the intensity of transmitted light is exponentially dependent on the absorbance (α with units cm^{-1}) multiplied by distance the light travels in the medium (x with units of cm) as presented in Section 2.3.3. Thus thinner films with equivalent optical properties will absorb less light. To maintain a low series resistance for the solar cell, the resistivity of ZnO:Al must decrease with decreasing film thickness.

Typically, structural properties of thin films are relatively poor in very thin films during the early stages of deposition. They improve as film thickness increases. Factors contributing to poor microstructure include small grain size, porosity, and high concentrations of point and line defects. Investigation of relationships between structural and electrical properties for very thin films is therefore important for solar cell applications. Use of thinner TCO layers to increase optical transmission results in less cross-sectional area available in the ZnO:Al layer for lateral current transport to the grid metallization. Thus as the TCO layer becomes thinner, the more defective material near

the film substrate interface becomes a larger percentage of the current carrying cross-sectional area, and plays an increasing significant role in current transport. For the case of CIS based solar cells, there is also the issue of carrier transport across this region. The photo-current generated in the absorber layer must cross the relatively defective region during transport to the metallization. Optimization of TCO electrical properties typically employs four point probe and Hall measurements of films with a thickness used for the application. These data therefore characterize lateral transport through the “bulk” of the thin film. To investigate electrical properties during early stages of film growth, 20 Å to 1580 Å thin films are deposited, and their structural and electrical properties are characterized by atomic force microscopy (AFM), Auger electron spectroscopy (AES), Hall measurements, and four point probe. Surface analysis techniques are required to investigate the film’s structure because some of the deposited films are very thin.

5.2 Results

5.2.1 Structural Characterization

5.2.1.1 Profilometry

Profilometry measurements of thickness are difficult for films less than 100 Å, therefore film thickness is controlled by variation of deposition time with a known deposition rate. Deposition rate is measured by depositing a ZnO:Al thin film on a glass substrate with a masked area. After deposition, the mask is removed, leaving a step feature, the height of which is measured by stylus profilometry. A deposition rate of 1.75 Å/s is measured for sputter deposition conditions of 100 W RF power, 2.5 x 2.5 cm glass substrate held off-axis from the source, a substrate to target distance of 5 cm, an Ar pressure of 5 mTorr, and a deposition time of 900 s. Except for deposition time, all films

are deposited using the same conditions, and also include a 600 s presputter performed with the deposition shutter closed. Presputtering stabilizes the source so that the deposition rate is constant for all deposition times. Table 5-1 identifies the samples, their deposition time, and calculated thickness. Sample 14 is used to determine deposition rate, and therefore its thickness is measured. For the remainder of this chapter, samples will be referred to by their film thickness, as this is the primary experimental variable.

Table 5-1. Sample identification, deposition time, and film thickness.

Sample ID	Deposition Time (s)	Thickness (Å)
14	900	1580 (measured)
16	10	18
17	20	36
18	60	105
19	30	54
20	180	315
21	300	525
22	420	735

5.2.1.2 Atomic force microscopy

AFM measurements are taken from small 7 x 7 mm samples cleaved from substrate's edge nearest the source, and used to measure the Z range, Root Mean Square (RMS) roughness, "grain size", and surface morphology. The Z range is the height difference between the lowest and highest features on the sample. RMS roughness represents the standard deviation between the height of topographic features and the mean feature height. "Grain size" is determined by the stereological techniques described in the Chapter 3. As was stated previously, this measurement is not expected to give an actual grain size, but describes the diameter of distinctive granular surface features, which may or may not reflect grain size. Figure 5-1 is a plot of the Z range,

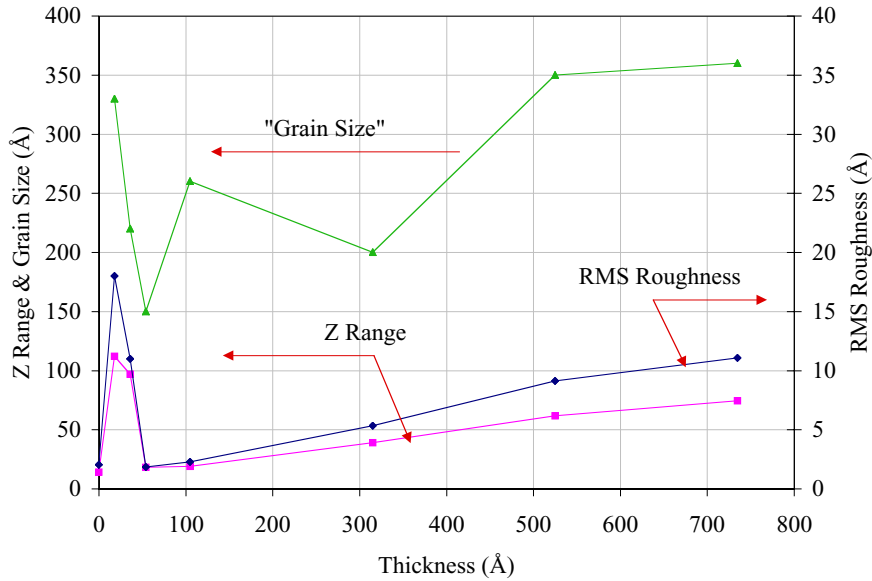


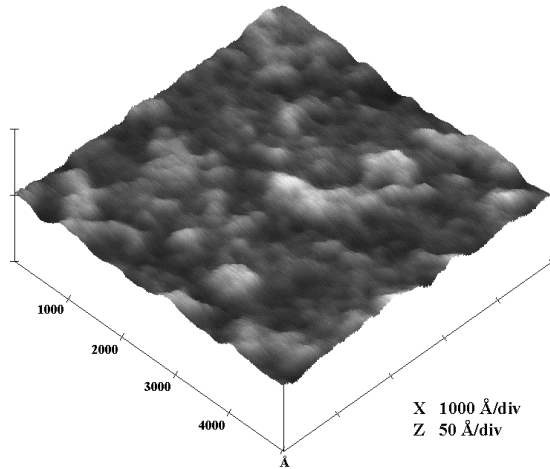
Figure 5-1. Z range, “grain size”, and RMS roughness data for ZnO:Al thin films derived from AFM measurements and plotted versus film thickness.

“grain size”, and RMS roughness derived from AFM measurements versus the film thickness. Z range and “grain size” data use the left ordinate axis, while RMS roughness uses the right ordinate axis. RMS roughness and Z range data from the bare glass substrate are presented at a thickness of 0 nm.

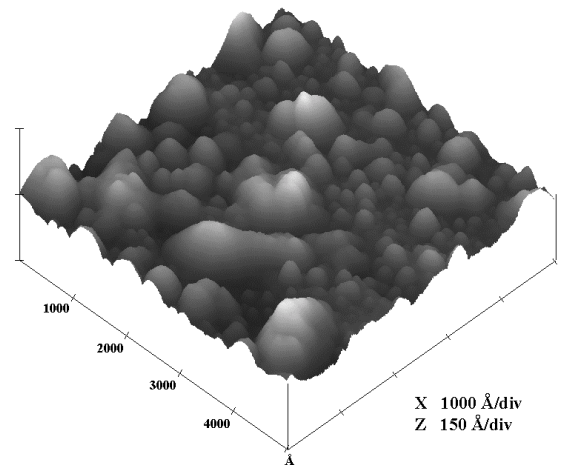
Trends in Z range and RMS roughness data with film thickness correspond very well. The Z range and RMS roughness are 112 and 18 Å, respectively, at a thickness of 18 Å, and decrease to 18 and 2 Å, respectively at 54 Å, then slowly and monotonically increase to 74 and 11 Å, respectively, for the 735 Å sample. The Z range data from 18 Å and 36 Å films are remarkably higher than the calculated film thickness. Grain size data follows similar trends to Z range and RMS roughness, but scatter in the data is larger, with values changing from larger (330 Å) to smaller (150 Å) to larger (360 Å) for film thicknesses of 18 Å, 54 Å, and 735 Å, respectively. Variability in “grain size” data results from difficulty in taking micrographs for films less than 105 Å in thickness.

Difficulty in getting good micrographs for the thinnest films in turn causes inaccuracies in determining the number of intersections between the line of known length and the grain boundaries. The grain boundary intercept method [123] used to quantify “grain size” specifies that the number of intersections with grain boundaries is inversely proportional to grain size, therefore difficulty in measuring the number of intersections causes a larger error in grain sizes for thinner films. In all cases, the films are very smooth with RMS roughness less than 20 Å, and appear to be fine grained with averaged grain sizes significantly less than 500 Å. In order to appreciate the changes that occur in surface morphology, Figures 5-2(a-h) present the AFM micrographs used to derive quantified surface morphology data.

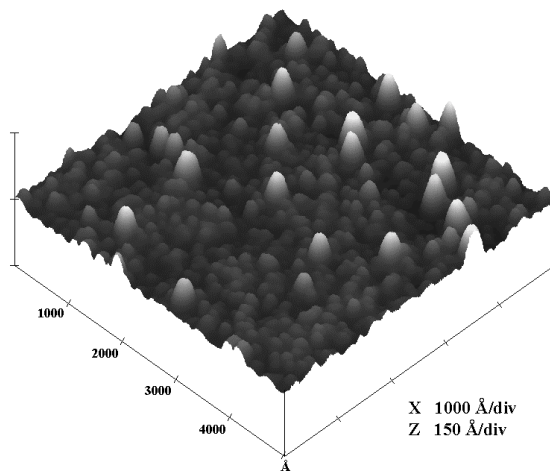
Care should be used when examining the micrographs, as different z axis sensitivities (50 to 150 Å/division) were used in the plots. The selected z axis sensitivities were a compromise between consistency (for ease of comparison), and different scales to accentuate the morphology. A marked difference in surface morphology can be seen between the bare substrate (Figure 5-2a) and samples with deposited films (Figures 5-2 (b-h)). The glass substrate has an irregular rolling hillock surface morphology, which changes to a more defined and taller hillock surface morphology even with the shortest deposition time. The diameter of the hillock features associated with a deposited film change with film thickness and are what is described by the “grain size”. For the thinnest samples (18 Å and 36 Å thick) there appears to be two different sizes of surface features, one set with a larger height of (110 Å and 97 Å, respectively) relatively to the smaller heights (70 Å and 50 Å, respectively). For the 18 Å sample, the taller features are also typically larger in diameter ($d \sim 1000$ Å) than the



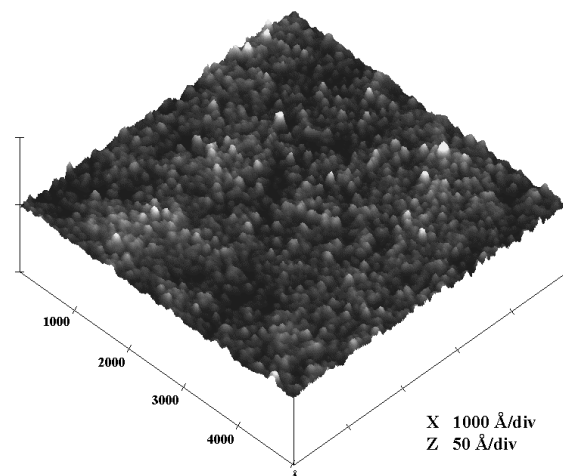
(a) Bare Substrate



(b) 18Å Film

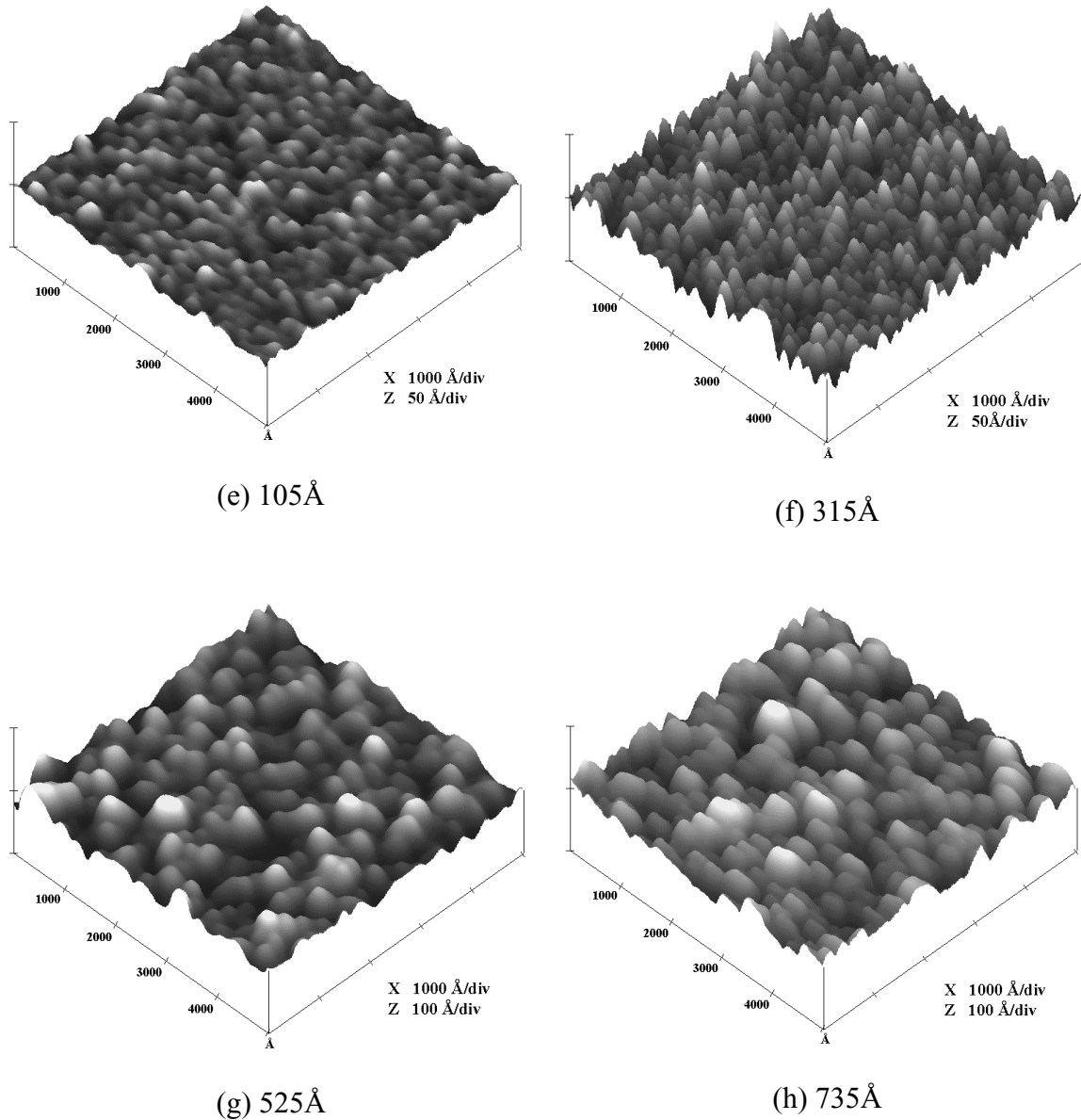


(c) 36Å Film



(d) 54Å Film

Figures 5-2(a-d). AFM micrographs from a $0.5 \times 0.5 \mu\text{m}$ area for (a) the bare soda-lime glass substrate and (b-d) increasing thicker films of ZnO:Al.



Figures 5-2(e-h). AFM micrographs from a $0.5 \times 0.5 \mu\text{m}$ area for ZnO:Al thin films with (e-h) increasing thickness.

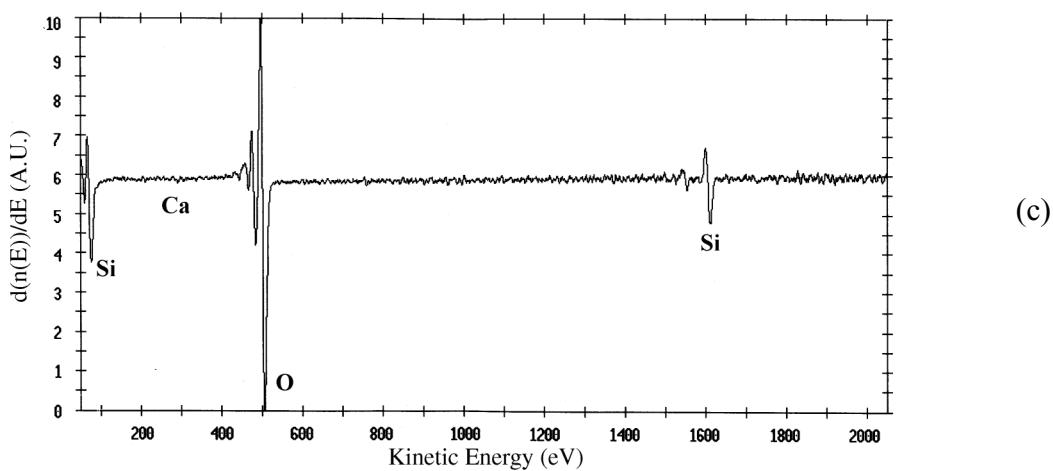
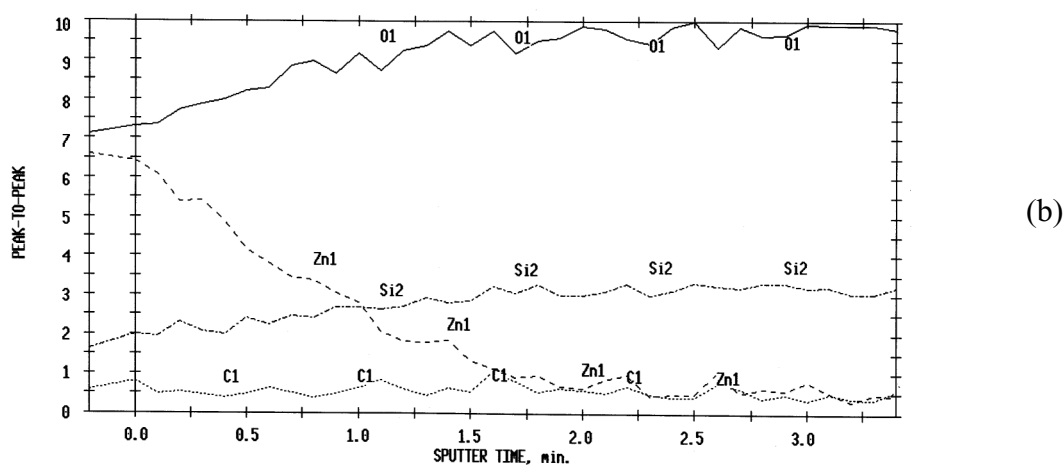
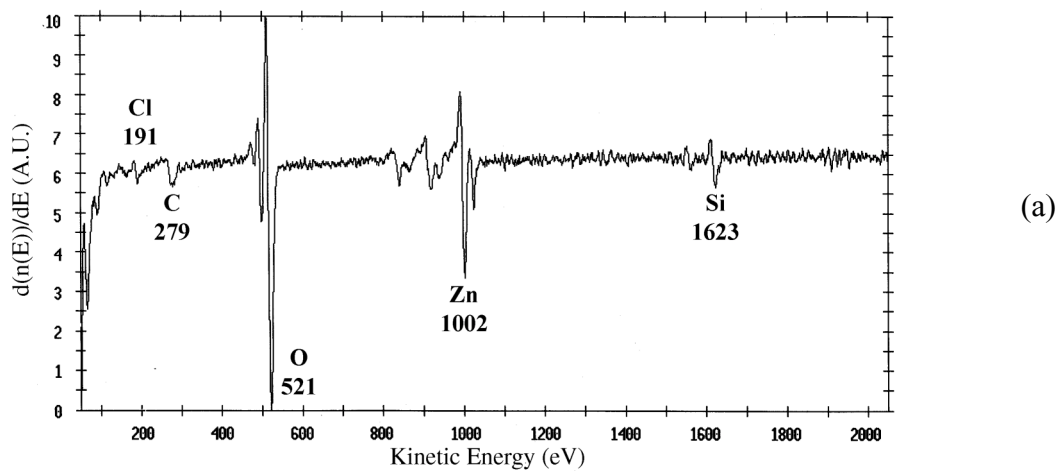
shorter features ($d \sim 100 \text{ \AA}$). For the 36 \AA sample, the taller features have diameters approximately twice ($\sim 440 \text{ \AA}$) those of the shorter ones ($\sim 220 \text{ \AA}$). Average grain sizes measured by the grain boundary intercept method are 330 \AA and 220 \AA for 18 \AA and 36 \AA thick samples, respectively. For the 54 \AA sample, the surface features are more consistently the same height, but have decreased markedly in diameter to $\sim 150 \text{ \AA}$

uniformly, and subsequently increase in diameter with increasing film thickness to a diameter of 360 Å for a 735 Å film.

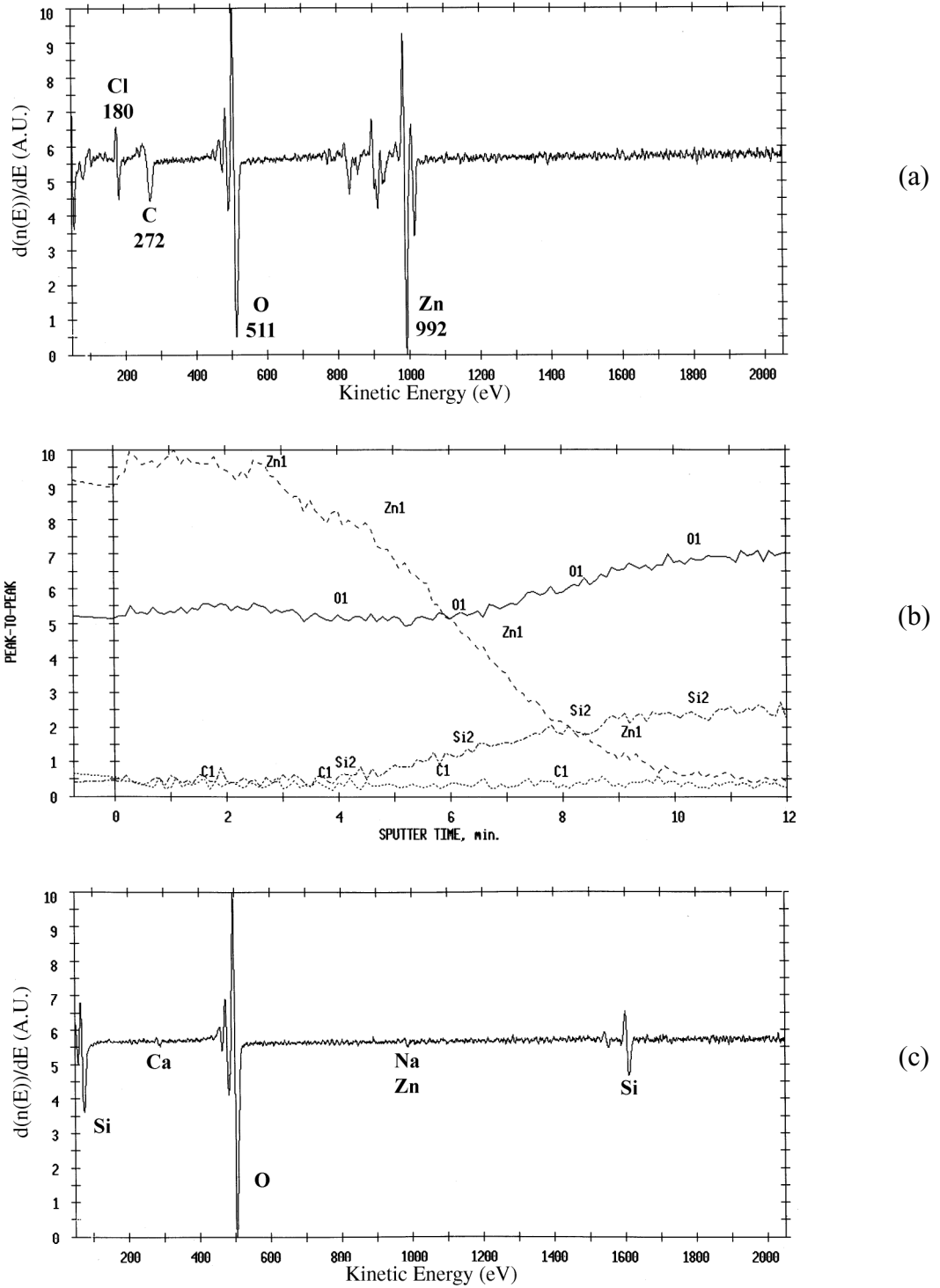
5.2.1.3 Auger electron spectroscopy

Auger Electron Spectroscopy (AES) is used to characterize the surface composition of the ZnO:Al film, changes in composition with depth into the sample by sputter depth profiling, and composition of the substrate. From this compositional data, stoichiometry, impurities, and percentage of the surface covered by the film are measured. Approximate composition for soda-lime float glass is 71% silica, 16% soda, 9% lime, 3% magnesia, and 1% alumina [129]. Composition of the ZnO:Al target is 98wt% ZnO and 2wt% Al₂O₃, which corresponds to atomic concentrations of 48.4%, 1.6%, and 50% for Zn, Al, and O, respectively. For each sample, a survey spectrum is collected from the as deposited sample, a sputter depth profile is continued until the Zn signal stabilizes at the noise level, and then a final survey spectrum is collected from the exposed glass substrate. As deposited survey spectra, sputter depth profiles, and post depth profile survey spectra from 18 Å (thin), 105 Å (intermediate), and 525 Å (thicker) samples are presented in Figures 5-3(a-c), 5-4(a-c), and 5-5(a-c), respectively, and illustrate trends in the Auger data. All survey spectra are collected over the energy range of 50 to 2050 eV. Depth profiles are plots of peak-to-peak height of differentiated signals for selected elements as a function of Ar sputtering time.

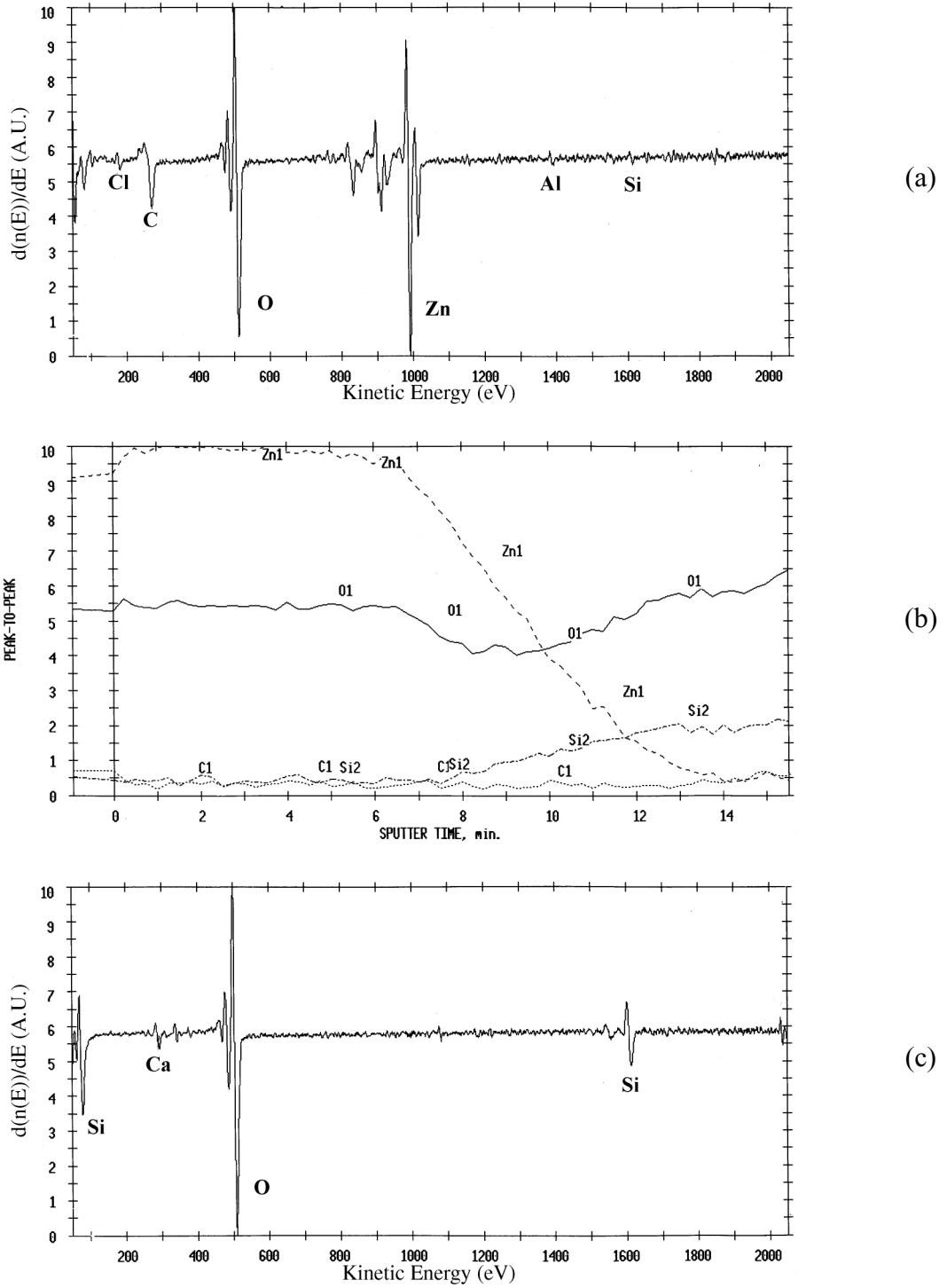
Peaks consistent with adventitious carbon (272 eV), chlorine (179 eV), zinc (992 eV), oxygen (510 eV), aluminum (1393 eV), and silicon (1617 eV) are found in survey spectra of as deposited samples. Adventitious carbon and chlorine show significant variations in peak-to-peak height from sample to sample. For all samples, the carbon signal drops off to the noise level almost immediately with sputter depth profiling



Figures 5-3(a-c). AES data from the 18 Å thick ZnO:Al sample with a (a) as deposited survey spectrum, (b) sputter depth profile, and (c) after profile survey spectrum.



Figures 5-4(a-c). AES data from the 105 Å thick ZnO:Al sample with a (a) as deposited survey spectrum, (b) sputter depth profile, and (c) after profile survey spectrum.



Figures 5-5(a-c). AES data from the 525 Å thick ZnO:Al sample with a (a) as deposited survey spectrum, (b) sputter depth profile, and (c) after profile survey spectrum.

suggesting it is a surface contaminant. A significant silicon peak is found in as deposited survey spectra for 18 Å, 36 Å, and 54 Å samples. For these samples, silicon peak intensity decreases with increasing film thickness. No silicon signal is found for 105 Å samples, but a very small Si signal is found for 315 Å and 525 Å samples. The small Si peak for 315 Å and 525 Å samples is unexpected, and will be discussed subsequently. Large Zn and O peaks are found in all as deposited survey spectra. The Zn peak is roughly half as intense as the oxygen peak for the 18 Å sample, and increases until it is similar in intensity to the oxygen peak for samples 105 Å and greater in thickness. The Al peak is extremely weak for some samples, and in others cannot be distinguished from the noise level.

Sputter depth profiles of O, C, Zn, and Si signals are collected for each sample. As indicated above, the carbon signal drops to the noise level within seconds of sputter depth profiling. Both the deposited film and substrate contain oxygen, therefore contributions to this signal come from the film and/or substrate. In contrast to as deposited survey spectra from completely coalesced films ($t > 105$ Å) where the Zn and O peak-to-peak height is roughly equal, initially Zn peak-to-peak height is nearly two times as intense as O in sputter depth profiles. The difference in relative peak to peak height between Zn and O is an artifact resulting from a combination of the differentiation algorithm and the energy step size used to collect the data. Energy step sizes of 1.0 eV and 0.5 eV are used to collect survey and depth profile data, respectively. In each depth profile, there is a region where the Zn signal is decreasing and Si signal is increasing, which corresponds to the transition between taking data from the film and substrate, and will be referred to subsequently as the transition region. For 315 Å and 525 Å films, the

Ar ion beam is focused on a smaller 2 x 2 mm area, as compared to a 3 x 3 mm area used for thinner samples. Decreasing the sputtered area increases the sputtering rate such that depth profiles can be collected over a shorter period of time. When corrected for changes in sputtering rate, longer sputter depth profiling is needed to reach the transition region in thicker samples. For samples 54 Å or less in thickness, which have incomplete surface coverage, the intensity ratio of Zn to O is 1.7, 1.6, and 0.9 for 54 Å, 36 Å, and 18 Å films, respectively. This is consistent with incomplete surface coverage suggested by the presence of a Si peak in the as deposited survey spectra. Also, the Zn signal begins to decrease and Si begins to increase immediately with sputter depth profiling. For all the profiles, the double y-axis on the left side of the plots indicates that the first two data points are taken from surfaces that have not been sputtered. Depth profiles are continued until a short time after the Zn signal stabilizes at the noise level, to ensure the surface is characteristic of substrate's bulk. Shifts in peak kinetic energy up to ± 10 eV from reference values are found in some AES spectra, though smaller shifts of ± 3 eV are more typical. All peaks for the as deposited survey of 18 Å are shift approximately 10 eV higher in energy, and this is attributed to negative charging induced by the electron beam. A strong shift to lower kinetic energies is found with increasing sputter depth profiling time for the 105 Å sample, but peak energies have returned to the handbook values for the post profile survey spectra. This suggests shifts to lower kinetic energy result from positive charging of the sample which would retard the escaping electrons.

Survey spectra taken after depth profiling generally have very few features; the three primary peaks are two silicon peaks at 82 eV (LMM) and 1609 eV (KLL), and an oxygen peak at 510 eV (KLL) [130]. A weak peak consistent with Ca (291 eV) is found

in many survey spectra after profiling, and is consistent with the glass additive of lime. A very weak peak consistent with Mg (1183 eV) is discernable in half of the after profile survey spectra and is consistent with magnesia added to the float glass. For the 105 Å sample, a small peak at 990 eV after profiling is consistent with either Na or Zn, as reference values for these peaks are within 3 eV of each other, and the peak is too weak to extract shape information. No peak consistent with Na is found in any other case. To approximately quantify surface coverage, the method presented in Section 3.6.2 is applied. This method relies on the surface compositional sensitivity of AES to determine the fraction of the surface covered by SiO₂. The method takes the ratio of Si atomic concentrations between the as deposited film and bare glass surface, which yields the fraction of surface area which is glass. The fraction of bare substrate is subtracted from 100% to give the fraction of surface covered by ZnO:Al. Figure 5-6 plots percentage of the surface covered by the film versus film thickness. Surface coverage is initially 60% for an 18 Å, and rapidly increases to 100% coverage for film thickness greater than 100 Å. This procedure does not account for information volume from which the AES signal is collected. The depth from which Auger electrons can escape while maintaining their characteristic energies is based on the inelastic mean free path of the electron in a material. The implications of the escape depth on the estimation of surface coverage will be considered in the discussion.

5.2.2 Electrical Characterization

Hall and four point probe measurements are used to evaluate electrical properties of the deposited films. Four point probe resistivity data is used to check Hall resistivity data and investigate variations in resistivity with position on the sample. Hall

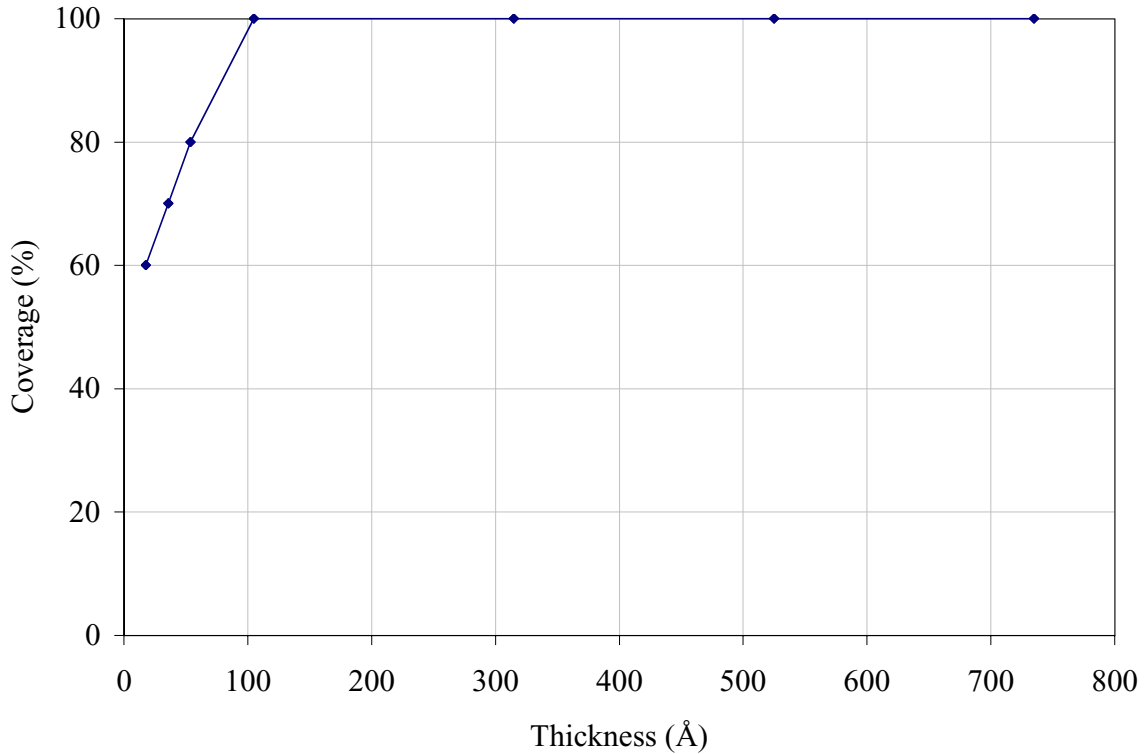
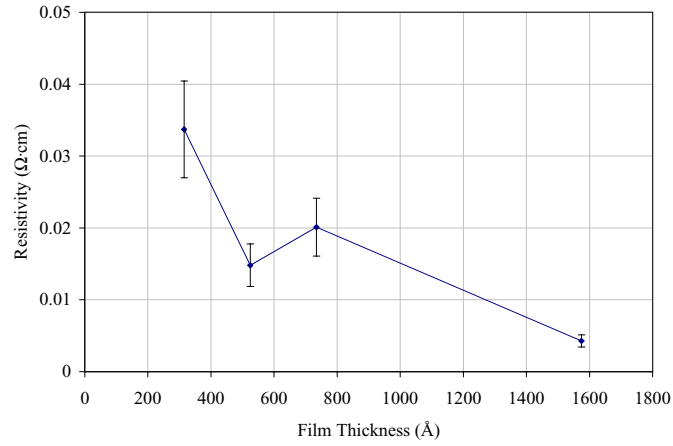


Figure 5-6. Percentage of the soda-lime glass substrate covered by the sputter deposited ZnO:Al thin film, as derived from AES data.

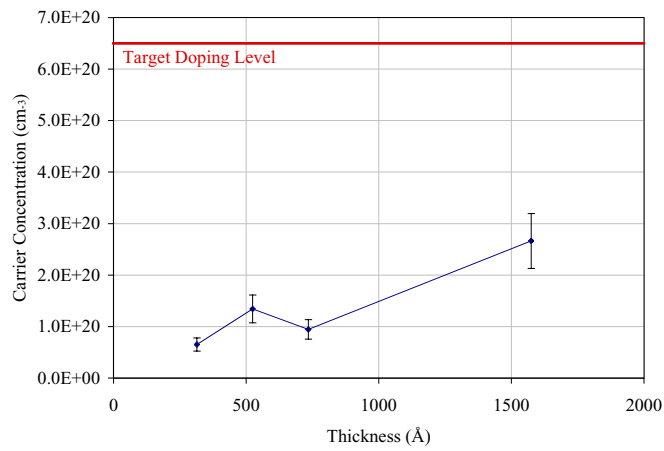
measurements are used to characterize resistivity, carrier concentration, and Hall mobility for the deposited films. Small 7 x 7 mm samples are cleaved from the substrate's edge closest to the sputtering source for Hall measurements. Samples with thicknesses between 18 Å and 105 Å are too resistive to measure with either technique, which is consistent with the lack of film coalescence measured by AES data. Based on the minimum current and maximum voltage specifications for the instruments, 1 $\Omega\cdot\text{cm}$ is the highest measurable resistivity for a 100 Å film. This resistivity limit decreases linearly with film thickness. Resistivity, carrier concentration, and Hall mobility data from 315 to 725 Å samples, and the 1575 Å sample used to determine the deposition rate are plotted as a function of film thickness in Figures 5-7 (a-c).

In Figure 5-7a, resistivity starts high at $3.4 \times 10^{-2} \Omega \cdot \text{cm}$ for the 315 Å film, and decreases by nearly an order of magnitude to $4.3 \times 10^{-3} \Omega \cdot \text{cm}$ at a thickness of 1575 Å. This minimum resistivity is a factor of 2 lower than the best as deposited resistivity reported in Chapter 4. The resistivity for the 100 Å film is greater than $1 \Omega \cdot \text{cm}$, and is therefore at least an order of magnitude more resistive than the 315 Å sample. Carrier concentrations plotted in Figure 5-7b increases by a factor of four from 6.5×10^{19} to $2.7 \times 10^{20} \text{ cm}^{-3}$ between film thicknesses of 325 Å and 1575 Å, respectively. The Al concentration in the target is $6.5 \times 10^{20} \text{ cm}^{-3}$, therefore measured carrier concentrations are between 10 and 50% of the target's extrinsic doping concentration. Hall mobility data are plotted in Figure 5-7c, and show values between 2.9 and $5.7 \text{ cm}^2/\text{V} \cdot \text{s}$ for thicknesses of 315 Å and 1575 Å, respectively. There is significant scatter in the data, and no trends of increasing or decreasing Hall mobility with film thickness can be identified. Therefore Hall mobility is considered to remain essentially constant with film thickness for this experiment.

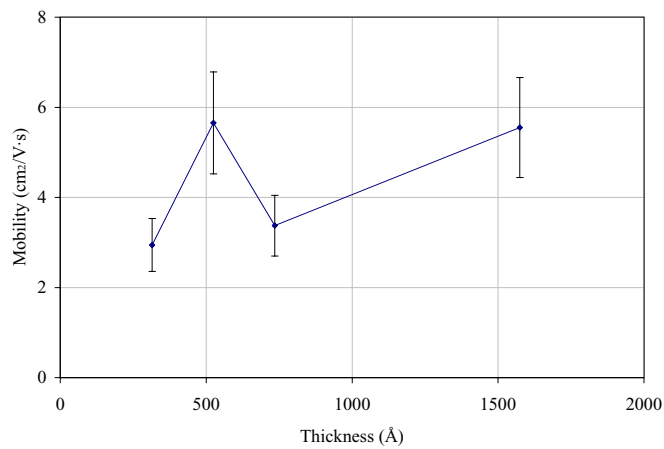
A variation of up to a factor of five in resistivity with position is measured by the four point probe technique. Resistivity is lowest at the substrate's edge closest to the source, which is directly above the source's outside edge. Resistivity increases towards the substrate's edge that is furthest from the source. This variation is significantly less than the position to position variations reported in Chapter 4. Hall resistivities are within the range of values measured by four point probe, suggesting a reasonable precision in measurements.



(a)



(b)



(c)

Figure 5-7(a-c). Electrical data for ZnO:Al thin films plotted as a function of film thickness including (a) resistivity, (b) carrier concentration, and (c) Hall mobility.

5.3 Discussion

5.3.1 Surface Morphology

The Z range data from AFM measurements for 18 and 36 Å samples is significantly larger than the calculated film thickness. For the 18Å sample, the Z range is 112Å, approximately a factor of 6 larger than the estimated film thickness. For the 36 Å sample, the Z range is 97 Å, approximately three times larger than the film thickness. This is explained in part with hypothesis that the deposited film forms by island (Volmer-Webber) nucleation [94]. This hypothesis is supported by the distinct change in surface morphology between the bare glass substrate and coated substrate, and the presence of a significant Si and Zn peaks even for a 54 Å film. Further evidence for this is the distinct change in surface morphology in AFM micrographs and the presence of a strong Zn peak in AES data for even the thinnest films, suggests a ZnO film is nucleating and changing the surface properties significantly. The presence of a discernable Si peak indicates a portion of the bare substrate is also exposed.

An island (Volmer-Webber) growth mode describes a film that does not grow smoothly across the substrate's surface, but instead develops small islands of deposited material that grow both normal and parallel to the surface. Islands form because deposited material tends to agglomerate in order to minimize the free energy of the substrate/film/vapor system. From the capillarity theory of nucleation, which was presented in Section 2.4.2, nucleus morphology is based on the relative surface energies between the substrate (s), film (f), and vapor phases (v). The balance of the surface forces is shown in Figure 2-19, and the relationship between surface tensions that yields island growth is given in Equation 5-1 where

$$\gamma_{sv} < \gamma_{fs} + \gamma_{vf} . \quad (5-1)$$

The term γ is surface tension, with subscripts describing which interface the surface tension is associated with. If Equation 5-1 is satisfied, then the contact angle θ , illustrated in Figure 2-19, will be greater than zero, and three dimensional or island growth will occur. Deposited flux impinges across the whole substrate, therefore island growth requires movement of adatoms on the surface until they join with other deposited material to form nuclei and/or desorb as non-agglomerated material.

To determine if feature height as measured by Z range from AFM data is consistent with island nucleation, a model involving transformation of a smooth layer to an island layer while maintaining constant volume is calculated based on nuclei that are modeled as half a sphere resting on the surface. An illustration of this transformation between a smooth layer and a discontinuous layer of hemispherical nuclei is presented in Figure 5-8. The measured deposition rate is for a film with much larger thickness than roughness, yielding an effectively planar film. Thus the deposition rate used to calculate film thickness assumes that a planar film results for all deposition times. The transformation takes a 1 x 1 cm area on the substrate, with different film thicknesses deposited on it. Film volume (V_f), from the product of area and film thickness, is set equal to the number of nuclei (N) times nucleus volume which is a function of the hemispheres radius (r). This relationship is expressed in Equation 5-2, and assumes nuclei are perfect non-overlapping hemispheres of uniform size with radius r and has the form

$$V_f = N \cdot \frac{2}{3} \pi r^3 . \quad (5-2)$$

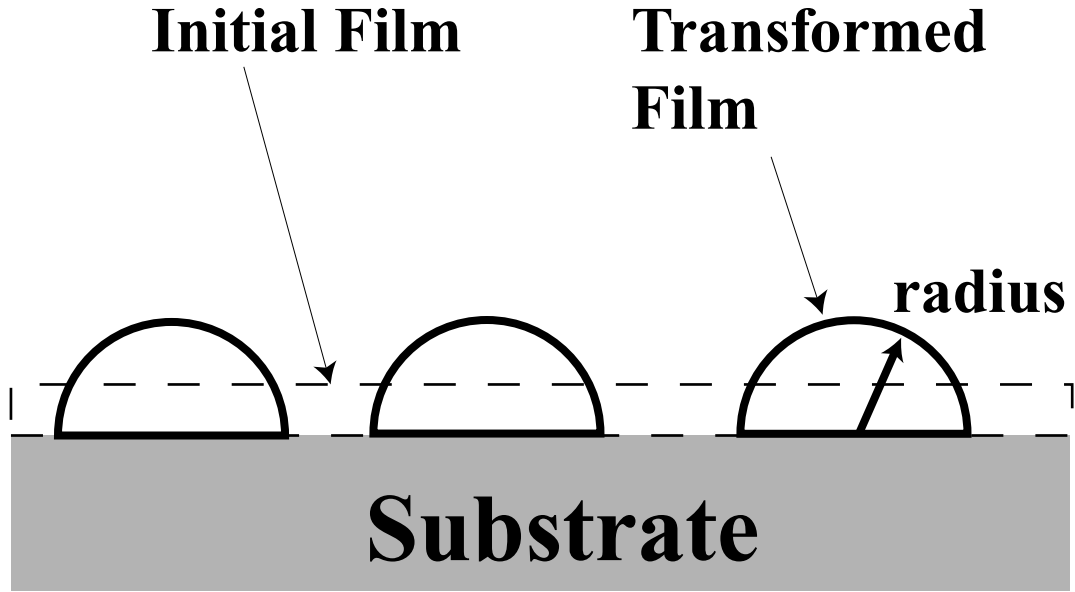


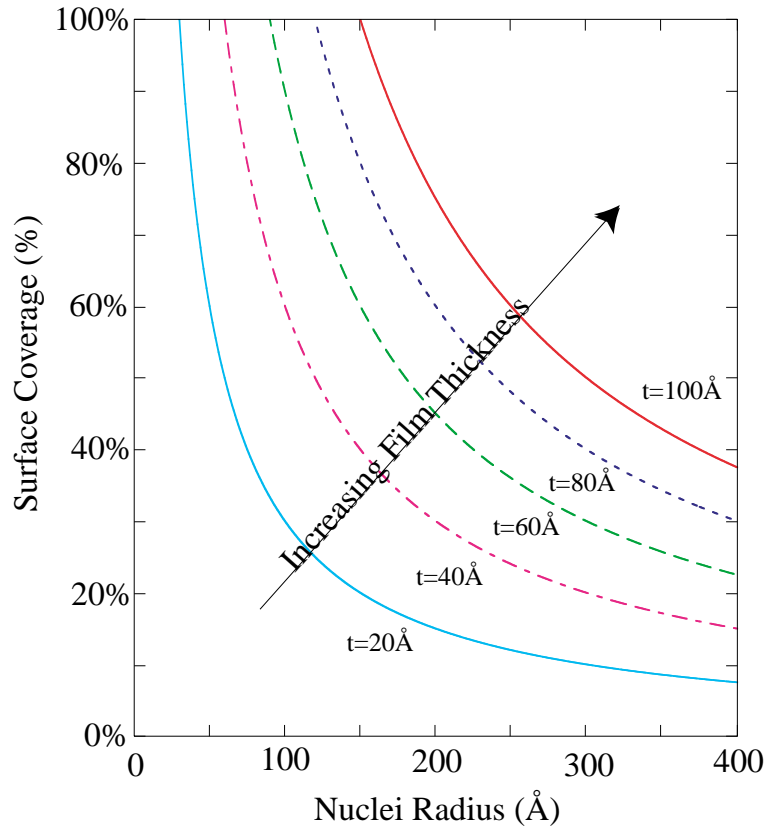
Figure 5-8. Schematic representation of the constant volume transformation between a smooth layer and hemispherical nuclei.

Additionally, N hemispherical nuclei will cover a surface area of S_f , which is described by the relationship in Equation 5-3 where

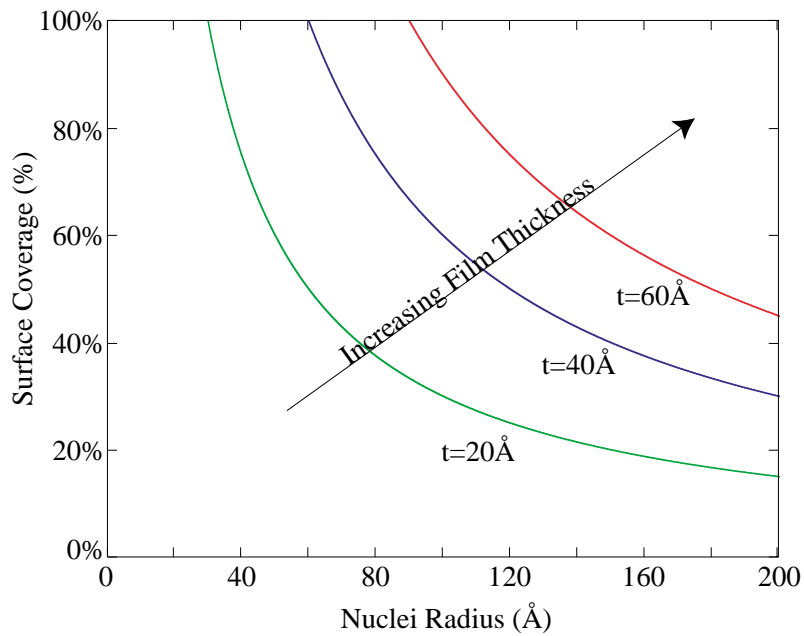
$$S_f = N \cdot \pi r^2. \quad (5-3)$$

MathCAD is used to evaluate these two formulas for a series of film thicknesses, which changes the film volume, and for each film thickness, a series of different nucleus radii are evaluated [131]. The results are plotted as percentage of the 1cm x 1cm surface covered by nuclei versus the nuclei radius. The colored lines represent contours of equal film thickness, and show changes in covered surface area for different nucleus radii.

Figure 5-9a is a plot of percentage surface area covered versus nucleus radii for films between 20 and 100 Å, and radii between 1 and 400 Å. Figure 5-9b is a similar plot, but concentrates on films between 20 and 60 Å in thickness, and nucleus radii between 1 and 200 Å.



(a)



(b)

Figures 5-9(a-b). Relationships between surface coverage, film thickness (t in Å), and nucleus radius (Å) for a constant volume transformation over two different ranges.

The AES results suggest surface coverage is 60% for an 18 Å film. Looking at the contour for a 20 Å film in Figure 5-9b, 60% coverage corresponds to a nuclei radius of 50 Å, and a grain diameter of 100 Å. If the RMS roughness and Z range calculations are restricted to an area where only smaller surface features are present, the Z range and RMS roughness are 70 Å and 11.72 Å, respectively, and “grain size” is approximately 100 Å. Thus predicted feature sizes for an island layer are consistent with the smaller features found for this sample. But the larger features which have a Z range of 112 Å and grain size ~ 1000 Å are not consistent with this model. Interpretation of the larger features will be discussed below. The AES results suggest surface coverage for a 36 Å film is 70%. The model suggests a nucleus radius of 70 Å will result in 70% coverage for a 36 Å film. The Z range is 97 Å and 50 Å and “grain size” is 440 Å and 220 Å for large and small features, respectively. Thus the 36 Å film is similar to the 18 Å film in that the smaller features are consistent with feature sizes predicted by the island model, whereas the large features are larger than predicted. This suggests that the measured Z ranges that are larger than the film thickness for 18 Å and 36 Å samples are due to island formation during the initial stages of film deposition. For both cases, the heights of hemispherical nuclei can be two to three times the height of a smooth layer with the same volume.

Explanation of the larger surface features is more challenging. While the constant volume morphology transformation gives results that are consistent with small surface features, large surface features are still too large. Two possible explanations for the large features are that they are simply large nuclei, possibly formed by two or more nuclei coming together, or that these features are really exposed glass substrate. Evidence

against the large features being combined nuclei includes the large difference between measured and modeled feature size, the difference in morphology between large and small nuclei, and the lack of recognizable exposed free substrate suggested by AES measurements. The other possibility is the large features are really exposed glass surfaces. This is possible if the AFM tip experiences a larger repulsive force from the exposed glass surface than the ZnO:Al film. The presence of static electricity of the same polarity on exposed glass surfaces and the AFM tip would cause them to repel each other and produce an image with artificially large features for area corresponding to bare glass. Static charge would be mobile in the ZnO due to its relatively low resistivity, and therefore it is possible that the glass substrate and ZnO film interact differently with the AFM tip.

Even if only the smaller features are considered for 18 and 36 Å samples, these features are large compared to the minimum in Z range and RMS roughness that occurs for the 54 Å sample, which are 18 Å and 1.8 Å, respectively. AFM and AES results from 54 Å and thinner samples suggest that very early in deposition, roughness increases dramatically as the deposited film forms 3D island nuclei. As deposition time increases, nucleus density and size increases as more nuclei form and grow under the continued flux. The additional nucleation increases coverage of the bare glass surface, and therefore has a smoothing effect on the film morphology. As the film approaches coalescence, the roughness approaches values measured for the bare glass substrate.

Films greater than 54 Å in thickness slowly increase in roughness, but even the thickest film is slightly less rough than the 18 Å film. The film becomes physically continuous at between 54 Å and 105 Å in thickness, as indicated by the lack of detected

silicon for 105 Å films. The 54 Å and 105 Å samples are also nearly as smooth as the substrate, though surface morphology is still distinctly more similar to ZnO films. At this thickness the substrate surface effectively becomes ZnO, which marks completion of nucleation and, and is followed by film growth and development of the film's structure [101]. Thus the initial high but steep decreasing roughness for films between 18 Å and 54 Å results from nucleation, and with coalescence at 105 Å and for increasing thicker films, microstructural development involves slow increasing Z range and RMS roughness.

The low but slowly increasing roughness for films thicker than 54 Å suggests that with coalescence, further film growth involves slowly increasing feature sizes. The process of expanding grain size in thin films results as some grains grow more quickly than others. Slower growing grains get crowded out as faster growing grains get larger, and start growing together. Also, large grains impede the deposited flux from reaching small grains by a shadowing process. If a particular crystal face has a lower free energy, this plane typically grows more quickly. This process is often responsible for crystallographic texturing, and is describe in Section 2.4.2 in the literature review. Preliminary samples prepared to optimize deposition conditions for best electrical properties showed a strong basal (002) texture in XRD spectra, therefore it is likely that samples for this experiment deposited using the same deposition conditions also have a strong basal texture. This mechanism for grain evolution is consistent with the slowly increasing Z range and roughness that occurs after film coalescence. The postulated microstructural development process for ZnO:Al films will be incorporated into the discussion of electrical properties.

In discussion of AES results, it is important to remember that this techniques has very different sensitivities to different elements. AES survey spectra and depth profiles are presented and interpreted in terms of the peak to peak height for elemental signals present. The sensitivity factors are used to turn the raw peak to peak height of the differentiated Auger peak into an atomic concentration. Most measurements involve comparisons between samples, and therefore calculating atomic concentrations is unnecessary, but it is useful to know the sensitivities for interpreting the data. For the elements of interest, the sensitivity factors are: Zn(997 eV)=0.190, O(510 eV)=0.400, Si(1609 eV)=0.038, C(272 eV)=0.140, and Al(1396 eV)=0.070 [130]. The relatively low sensitivity for silicon inhibits the ability to measure small concentrations on the surface. As previously mentioned, quantification of atomic concentrations is used for estimation of surface coverage. Another important issue is that elemental signals never go completely to zero for depth profiles. This is an artifact of the data collection process used by the computer, and results from noise in the energy window. The non-zero noise level is seen in depth profile data, but does not represent a true Auger peak height.

For Auger Electron Spectroscopy, compositional analysis and estimation of surface coverage are both of interest. The as deposited survey spectrum for the 525 Å sample suggests a continuous layer of ZnO, with some carbon and chlorine surface contamination. Both contaminants are common, and mostly likely result from atmospheric interaction and perspiration. The carbon signal quickly decays to the noise level with depth profiling, confirming that it results from surface contamination, i.e. adventitious carbon. There is also an extremely weak Si signal present for the as deposited film. Because no Si peak is present in the 105 Å as deposited survey spectrum,

the weak Si peak from 525 and 735 Å samples is considered to result from glass dust from the scribe and cleave procedure used to make Hall measurement and AFM samples. Depth profile data indicates Zn and O peak to peak height are constant between 0.5 to 6 minutes of sputter depth profiling, with no C or Si beyond the noise level. Lack of C suggests the films are free of contamination, and lack of Si indicates this region of the depth profile represents the “bulk” of the film. After 6 minutes, the Zn signal decreases and Si signal increases indicating the substrate is being exposed. The breadth of the transition region between the ZnO:Al film and glass substrate is discussed below. Spectra for all film thicknesses taken after sputter depth profiling exhibit peaks consistent with soda-lime glass, which always includes Si and O peaks, and sometimes includes Ca and/or Mg peaks. The presence of Na should be detected based on the sensitivity of AES to Na, and typical concentrations used for soda-lime glass (16wt% Na₂O). Depletion of soda at the glass surface could occur through dissolution in water during the wet cleaning process used on the glass substrate, as soda in glass is known to be water soluble [129]. Alternatively, sodium is often a mobile species in materials, and can be pushed by the Ar ions used for depth profiling. Positive Ar ions used for sputter depth profiling would repel positive Na ions in the material, potentially driving them deeper in the glass substrate where they are not detected [132].

For the 105 Å sample, results are very similar to the 525 Å sample. Again, the as deposited sample shows surface contamination by C and Cl. The carbon signal drops immediately to the noise level with depth profiling, indicating it is a surface contaminant. In sputter depth profile data for the 105 Å film, the Zn and O signals remain constant between 0.5 and 3 minutes of sputter, followed by decreasing Zn signal and an increasing

Si signal, signifying penetration of the film such that data comes from both the film and glass substrate. The as deposited survey spectrum from the 18 Å sample has Zn, O, C, and Cl peaks, but also has a significant silicon peak from the glass substrate. Depth profile data from before the first sputtering step show the Zn to O peak ratio is lower than for 105 Å and 525 Å films, and the Si peak is larger. Also, the Zn signal intensity dropping immediately towards the noise level with sputtering, and the lack of a constant large Zn signal are both consistent with incomplete surface coverage. Thus for all films, only surface contamination is present as suggested by survey spectra from as deposited films and depth profiles. The Si signal in as deposited survey spectra for 18 Å, 36 Å, and 54 Å films is consistent with incomplete surface coverage.

The decrease in Zn intensity and rise in Si intensity takes place over a significant portion of the total depth profile time for all films. Because the deposition process is performed at low temperatures, reactions and diffusion between substrate and film is not anticipated. Therefore the breadth of the film substrate interface in the depth profile data is the result of film roughness. Both the as deposited roughness and roughness induced by sputter erosion will broaden this region, following processes that are well described in the literature [124,125].

5.3.2 Electrical Characterization

The best as deposited resistivity measured in this experiment is $4.3 \times 10^{-3} \Omega \cdot \text{cm}$, which is roughly a factor of 3 lower than the best as deposited resistivity reported in Chapter 4. This improvement in as deposited resistivity is attributed to holding the substrate off-axis of the source, which prevents negative ion resputtering of the deposited film. It was postulated that the consistently larger resistivities reported for Position 1 in Chapter 4 resulted from negative ion resputtering. Optical data indicated that the high

resistivity resulted from very low carrier concentrations ($n < 10^{19} \text{ cm}^{-3}$). The lowest carrier concentration measured for this experiment is $6.5 \times 10^{19} \text{ cm}^{-3}$, which suggests negative ion resputtering increases resistivity by decreasing carrier concentration. This agrees with results reported below in Chapter 6, which is a more detailed investigation of negative ion resputtering.

Hall data show some interesting and non-intuitive trends with film thickness. As a first approximation for predicting the changes in electrical properties for very thin films, the ZnO:Al film can be considered metal-like. Two of the leading theories treating the electrical properties of thin continuous metal films were developed by Fuchs and Sondheimer [133,134], and Mayadas and Shatzkes [135]. A simple expression for resistivity (ρ) in the very thin film regime is given in Equation 5-4 [136] where

$$\frac{\rho_F}{\rho_B} = 1 + \left(\frac{3}{8}\right) \frac{l}{t} (1 - p). \quad (5-4)$$

The subscripts on the resistivity indicate bulk (B) and film (F), respectively. The term p describes interactions between carriers and the free surfaces, is a unitless variable, and has values from 0 to 1. If $p=1$ then carriers are specularly reflected from the interfaces, and therefore they do not influence resistivity. If $p=0$, carriers interacting with free surfaces are diffusely scattered, and therefore free surface interfaces decrease carrier mean free path and increase resistivity. The term (l/t) is the ratio of the film thickness to the mean free path of the carriers. This term indicates that for surface scattering to be important, the film thickness must be equal to or thinner than the length of the carriers scattering mean free path. A schematic illustration of this model is presented in Figure 5-10. The first (1) arrow indicates the “bulk” mean free path of the carrier (l). The second (2) arrow illustrates a carrier that is specularly reflected from the film surface, and

therefore maintains the same direction and mean free path. The third (3) arrow illustrates a diffuse scattering event where the carriers mean free path is significantly shortened. A plot of the theoretically predicted trends in the ratio of ρ_F to ρ_B with different p values is shown in Figure 5-11 [137]. This plot shows a similar trend to the resistivities measure in the deposited ZnO:Al films. As the film thickness increases, the resistivity decreases exponentially towards a minimum value (Figure 5-7a). This model implicitly assumes that resistivity changes in very thin films result from increased carrier scattering. Therefore this model predicts as thickness decreases, scattering and therefore resistivity increases.

The Hall data presented in Figure 5-7c reveal a disagreement with the Fuchs and Sondheimer model. Resistivity does decrease in a manner consistent with this model, but the mechanism causing this decrease is reduced carrier concentration, not reduced mean free path or mobility (Figures 5-7 b and c). No trends for increasing or decreasing mobility with film thickness is observed. Carrier concentration is observed to decrease by a factor of 4 from 2.7×10^{20} to $6.5 \times 10^{19} \text{ cm}^{-3}$ with decreasing film thickness from 1575 Å to 325 Å. Decreasing carrier concentration correlates with increasing resistivity for decreasing thickness, with resistivity increasing by a factor of 8 from 4.3×10^{-3} to $3.4 \times 10^{-2} \text{ } \Omega \cdot \text{cm}$ from 1575 Å to 325 Å. This suggests increasing resistivity with decreasing film thickness is dominated by decreasing carrier concentration.

Indirect evidence suggests resistivity continues to increase with decreasing film thickness. The AES data suggests that the 105 Å sample is a completely coalesced film. Based on the measurement range of the Hall and four point probe instruments, the maximum measurable resistivity for a 105 Å sample is $\sim 1 \text{ } \Omega \cdot \text{cm}$. Therefore the 105 Å

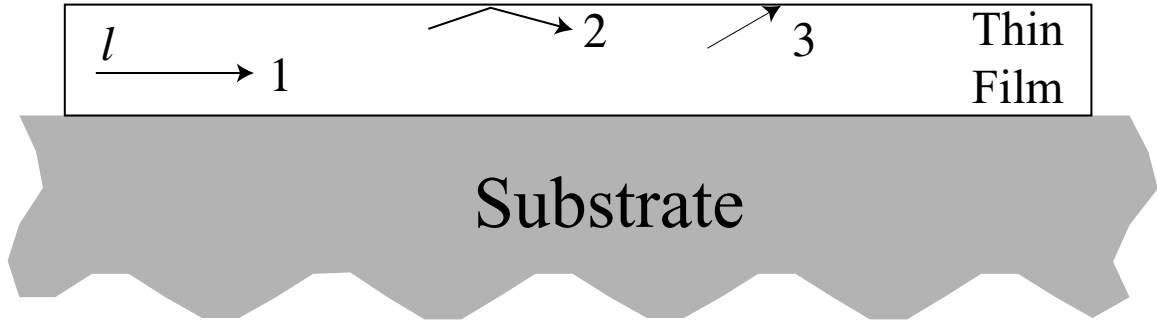


Figure 5-10. Illustration of carrier trajectories based on the Fuchs and Sondheimer model with (1) bulk transport, (2) specular reflection from the interface, and (3) carrier scattering at the interface.

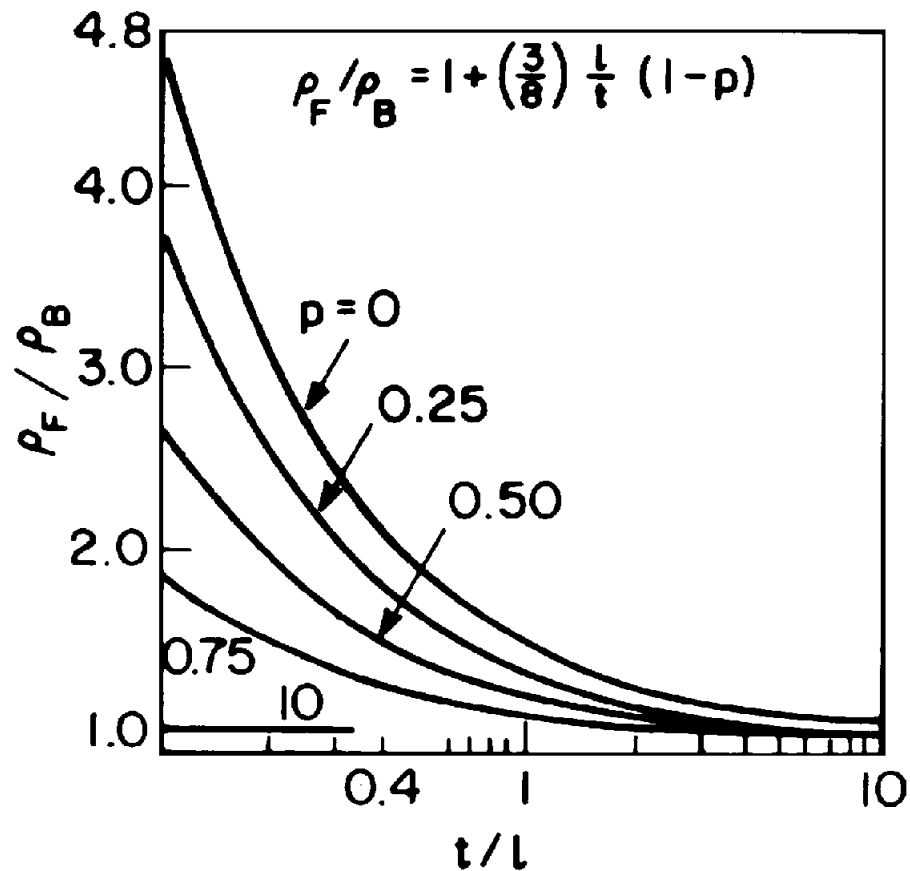


Figure 5-11. Calculated plot of the resistivity ratio between the thin films with interface scattering and bulk films as a function of mean free path (l), film thickness (t), and interface character (p), with larger numbers being more specular in carrier reflection.

sample's resistivity is some value greater than $1 \text{ } \Omega \cdot \text{cm}$, which is at least 30 times larger than the value of $3.4 \times 10^{-2} \text{ } \Omega \cdot \text{cm}$ found for $315 \text{ } \text{Å}$. The AFM and AES data suggest $54 \text{ } \text{Å}$ and thinner films are not coalesced and are increasing in roughness with decreasing thickness. The mechanism of conduction in a noncoalesced film is fundamentally different, but the percolation mechanism is beyond the scope of interest for this experiment.

An alternate mechanism to explain the increased resistance in thin films is postulated. In this mechanism, chemisorbed oxygen species decrease the carrier concentration with decreasing film thickness in coalesced films. While metals fundamentally have free mobile electrons due to metallic bonding, ZnO:Al depends on donor states generated by defects to achieve free electron carriers. The Al doping level of the target is $6.5 \times 10^{20} \text{ cm}^{-3}$, which indicates that even with 100% incorporation, the free electron concentration of these films are roughly two orders of magnitude lower than a typical metal. This lower carrier concentration leaves very thin films vulnerable to compensation by trapping of conduction band electrons on chemisorbed oxygen. Mechanisms for oxygen chemisorption and its effect on carrier concentration for ZnO are presented in the literature review section discussing ZnO as a thin film sensor for particular gases (section 2.3.2). To evaluate the potential of chemisorbed oxygen to decrease carrier concentration, some simple modeling is performed. For the $325 \text{ } \text{Å}$ film, the carrier concentration is only 10% of the Al dopant concentration in the target, which suggests that enough oxygen must be chemisorbed to remove up to 90% of the free carriers in the film. To further simplify the calculation, the quantity of carriers in the film, which is the product of the carrier concentration ($n=6.5 \times 10^{20} \text{ cm}^{-3}$) and the film

thickness (t), is set equal to the density of available surface sites (S) (typically $\sim 10^{15}$ cm^{-2}). Assuming a planar surface saturated with chemisorbed oxygen, a film up to 150 Å would be completely compensated. This is in reasonably agreement with the level of depletion found for the 325 Å film, and is consistent with the rapidly decreasing carrier concentration with decreasing thickness. The presence of grain boundaries in the polycrystalline film, the interface with the substrate, and surface roughness provide additional area for chemisorption, which increases the possible fraction of compensation. The likelihood of a surface saturated with chemisorbed oxygen species is small, which lowers predicted compensation. This mechanism is also consistent with decreasing carrier concentration with film thickness found in experimental data reported in Chapter 6, which will be discussed using a similar model.

This model can also explain variations in resistivity found by four point probe data across the surface. The entire 2.5 x 2.5 cm substrate is positioned off the targets normal axis. Lowest resistivities are found for areas closest to the sputter source, which are positioned above the outside edge of the source. Resistivities increase with position towards the edge of the substrate furthest from the source's center. The non-uniform flux distribution will result in decreasing film thickness on the substrate further from the source's center. For very thin films, decreasing film thickness with position on the substrate further from the deposition source results in increased compensation and therefore increased resistivity. Also, film thickness was measured near the substrate's edge closest to the source's center, therefore the film is thinner than measured for areas farther from the source's center. Measured thickness is entered into Equation 3.2, which is used to calculate resistivity from measured current, voltage, and film thickness. If the

actual film thickness is less than the measured film thickness, then the derived resistivity is higher than the actual value. A combination of both effects is considered responsible for variations in resistivity across the substrate.

5.4 Summary

Both the microstructural and electrical properties of sputter deposited ZnO:Al thin films are found to evolve significantly with increasing thickness. The microstructural evolution consisted of changes in surface morphology, Z range, RMS roughness, “grain size”, and surface coverage as measured by AFM and AES. The thinnest films (0 to 40 Å) are found to be discontinuous, and had a remarkably high Z range and RMS roughness compared to the substrate. Features of two different sizes appear in the micrographs. For the 18Å and 36Å films, the smaller features have a 70Å and 50Å Z range, respectively, which is still significantly larger than film thickness. A simple model to predict the effects of islands on feature height suggests that the smaller features are three dimensional nuclei. The large features are much too large to be predicted by the island model. These features are attributed to static electric interactions between the glass substrate and the AFM tip. AES data indicates 54 Å films are still not continuous, but surface coverage has increased to approximately 80%. The Z range and roughness also decreased significantly, approaching the values for the glass substrate. Films become continuous at thicknesses between 50 Å to 100 Å, and a steady trend of increasing roughness, decreasing resistivity, and increasing carrier concentration is observed with increasing thickness. The “grain size” is used to quantify the diameter of surface features, which might or might not represent individual grains of the polycrystalline film. The “grain size” follows similar trends as Z range and RMS Roughness, albeit with more

scatter in the data. AFM and AES data are consistent with island (Volmer-Webber) nucleation and growth. The slow increase in “grain size” with film thickness for coalesced films ($t > 100 \text{ \AA}$) is attributed to differences in grain growth rates due to shadowing and free energy of the growth surface. XRD spectra from preliminary samples used for optimization of electrical properties indicate (002) texturing occurs in samples deposited by the sputter deposition process used.

The electrical properties also change significantly in this film thickness regime. The resistivity decreases sharply as the film thickness increases. Measured values range over an order of magnitude, with a minimum resistivity of $4.3 \times 10^{-3} \text{ } \Omega \cdot \text{cm}$ for as deposited films. This improved resistivity as compared to as deposited samples in Chapter 4 is attributed to lack of negative ion resputtering, due to use of the off-axis deposition geometry. Films which are discontinuous ($18 \text{ \AA} < t < 54 \text{ \AA}$) have resistivities too high to measure. The AES data suggest that the 105 \AA film is continuous, but the resistivity remains too high to be measured. As film thickness increases, the resistivity decreases in a manner consistent with the Fuchs and Sondheimer model for conduction in very thin metallic films, which specifies that resistivity increases with decreasing film thickness due to increased scattering from interfaces. Carrier concentration and Hall mobility data indicate that the mechanism responsible is different than the Fuchs and Sondheimer model, as carrier concentration is responsible for a majority of the change in resistivity. The carrier concentration decreases by a factor of 4 from 2.7×10^{20} to $6.5 \times 10^{19} \text{ cm}^{-3}$ with decreasing thickness from 1575 \AA to 315 \AA , and is therefore primarily responsible for the increase in resistivity. The proposed mechanism for decreasing carrier concentration with film thickness is postulated to be increasing compensation due to chemisorbed

oxygen species. This mechanism is supported by a simple model which indicates that for very thin films, the quantity of free carriers becomes similar to the number of sites available for oxygen chemisorption. Therefore, as film thickness decreases with a concomitant decrease in the total number of conduction band electrons, the quantity of chemisorbed oxygen remains roughly the same due to equivalent free surface and grain boundary area in the film. This results in an increasing fraction of the available electrons being consumed by chemisorption of oxygen species, reducing the film's carrier concentration.

CHAPTER 6 NEGATIVE ION RESPUTTERING

6.1 Background

Negative ion resputtering (NIR) has been postulated to have a strong influence on the electrical properties of sputter deposited ZnO:Al thin films from earlier experiments within this work and from reports in the literature [101,109,112,113,116]. Despite the strong influence, there is a lack of detailed information regarding this process and its effects on developing films. The experiment presented in this chapter investigates the magnitude of NIR effect on structural and electrical properties, how RF power influences this process, and mechanisms by which the electrical and structural properties of the films are affected. The relative magnitude of the effect is evaluated by characterization of electrical and physical properties of the deposited films. This introduction is followed by presentation of results from electrical and physical characterization, discussion of the results, and a summary of critical findings.

The process of negative ion resputtering (NIR) is described in section 2.4.3 of this work. The process involves generation of a negative ion in close proximity to the sputtering source (cathode), with the ion being accelerated away from the source by the same electric field that attracts positive Ar ions towards the target for the sputtering process. Negative oxygen ions (O^-) are responsible for NIR during sputter deposition of ZnO, and are accelerated to a significant portion of the cathode potential which varies between -300 to -1000 V DC with RF power used in this study. Thus, the negative

oxygen ions are accelerated to similar energies as the Ar^+ in the sputtering process, and can therefore cause damage and resputtering to the deposited film. Previous unreported experiments from this work, and reports in the literature [76,111,112] suggest the negative ion flux is highly directional, with the ions being accelerated perpendicularly away from the target's surface. For magnetron sources, the negative ion flux is found to be most intense in areas directly opposed to the *racetrack* erosion region of the target. Experimental evidence for this is seen in the strongly position sensitive electrical properties of deposited films discussed in Chapter 4. Often the best film properties are obtained for substrates supported off-axis from the target's normal axis in the manner used for experiments in Chapter 5 and/or with the substrate perpendicular instead of parallel to the sputtering target. This is consistent with decreased minimum resistivity for as deposited samples from Chapter 5 compared to Chapter 4, and several reports in the literature which also find off-axis deposition geometry to improve electrical properties [76,111].

Process parameters that influence the NIR must be determined to investigate this effect. Based on the postulate that the NIR effect is very position dependent, the properties of a film deposited across a large substrate are measured in an initial experiment. Strong variations of the resistivity with position on the substrate were measured, in a pattern consistent with NIR. Therefore, variations in properties with position can be used to evaluate the NIR effect. The influence of RF power is the process variable investigated in this way.

Parameters held constant across these experiments include use of the same sputter deposition system and target. The substrate and its position are also held constant. Three

2.5 x 5 cm glass substrates side by side effectively formed a 2.5 x 15 cm substrate. This substrate was 9 cm below the target, with one edge below the target's center, which is defined as 0 cm. This geometry is detailed in the experimental methods section, and is schematically represented in Figure 6-1. One exception to this geometry is the 500 W sample, which was deposited in a preliminary experiment. This substrate is positioned away from the target's center towards the target's edge. Based on trends in the data and memory of placing the sample in the system, it is estimated that the substrate was translated ~ 3.2 cm radially away from the center of the target. As reported in the experimental methods, there is a uniformity shield positioned below the deposition source, which influences deposition rate and variations in properties induced by NIR. The deposition parameters varied for this experiment are the RF power and deposition time.

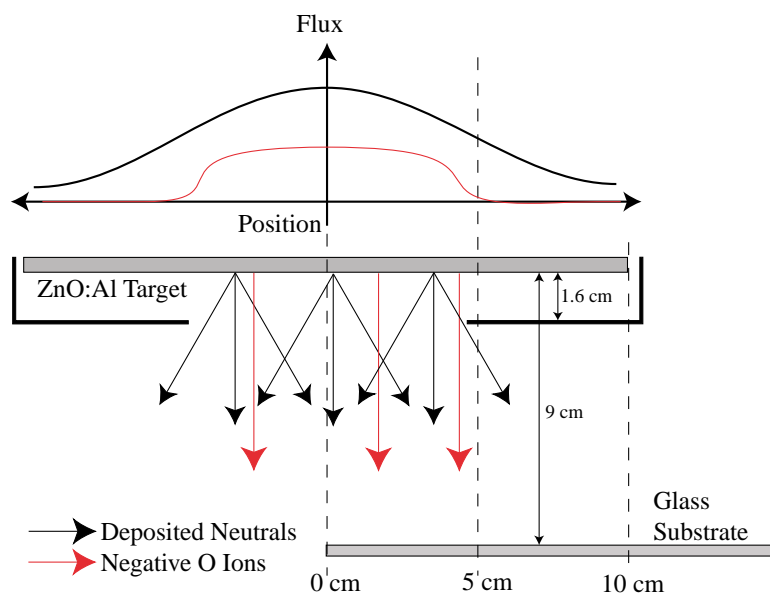


Figure 6-1. Cross-sectional view of the sputter deposition geometry, and a schematic representation of the changes in deposited neutral and negative ion flux as a function of position.

6.2 Experiment Results

6.2.1 Profilometry

Profilometry across a shadowed step feature is used to measure the film thickness at seven equally spaced points along the 5 cm dimension of the 2.5 x 5 cm substrates. These measurements are used to characterize variations in film thickness versus position relative to the center of the sputter deposition source. To investigate the influence of RF power, the conditions used to deposit the samples are 250 W and 500 W for 60 minutes, and 1000 W for 20 minutes. The thickness and deposition rate as a function of position on the substrate for the three RF powers are presented as in Figures 6-2 and 6-3, respectively. In each of these plots, there are two curves associated with the 500 W deposition condition. The dashed line represents data mathematically offset by adding 3.2 cm to the positional index to make zero consistently the center of the source for all three RF power conditions. Data with the position index manipulated in this way will be referred to as offset data, and an offset of 3.2 cm will be used consistently. As a reminder of the offset, 500 W data plotted versus position will always be plotted with a dashed line. The solid line represents the actual data, with the positional index relative to the end of the substrate, and not the center of the sputter deposition source. The offset 500 W data is used in the following results and discussion sections. Any reference to data without the offset will be referred to explicitly as non-offset data. The red dashed vertical markers designating positions of the regions apply to the offset data for samples deposited at 500 W, and the data for samples deposited at 250 W and 1000 W.

The thickness and deposition rate of the deposited films span more than an order of magnitude between the ends of each substrate. The thinnest measured films are approximately 100 Å thick. This limit is imposed by the lack of optical contrast needed

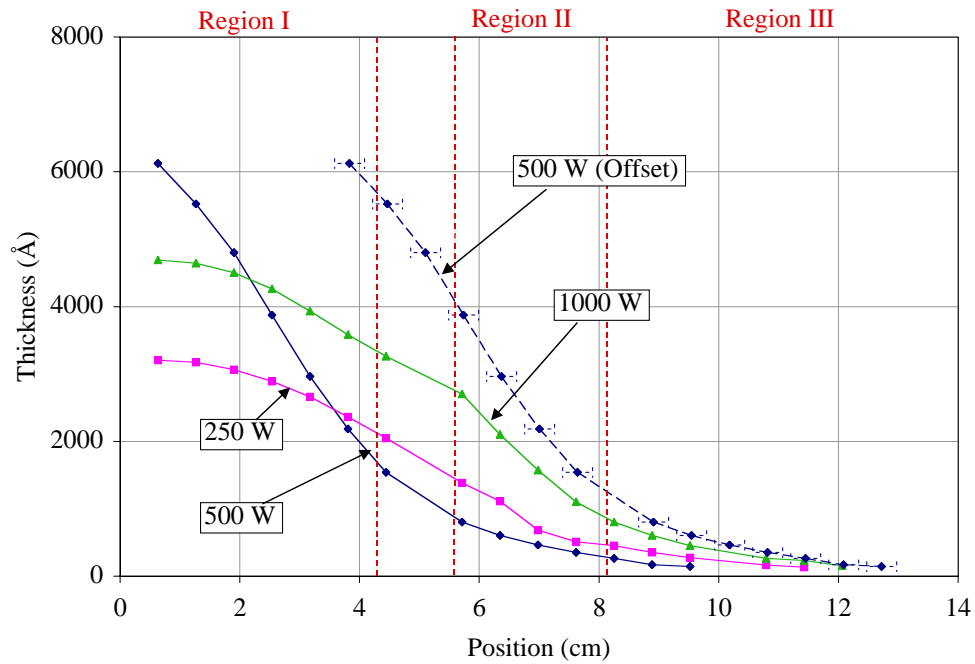


Figure 6-2. Measured thickness of the ZnO:Al thin film as a function of position on the substrate and RF power used to deposit the film.

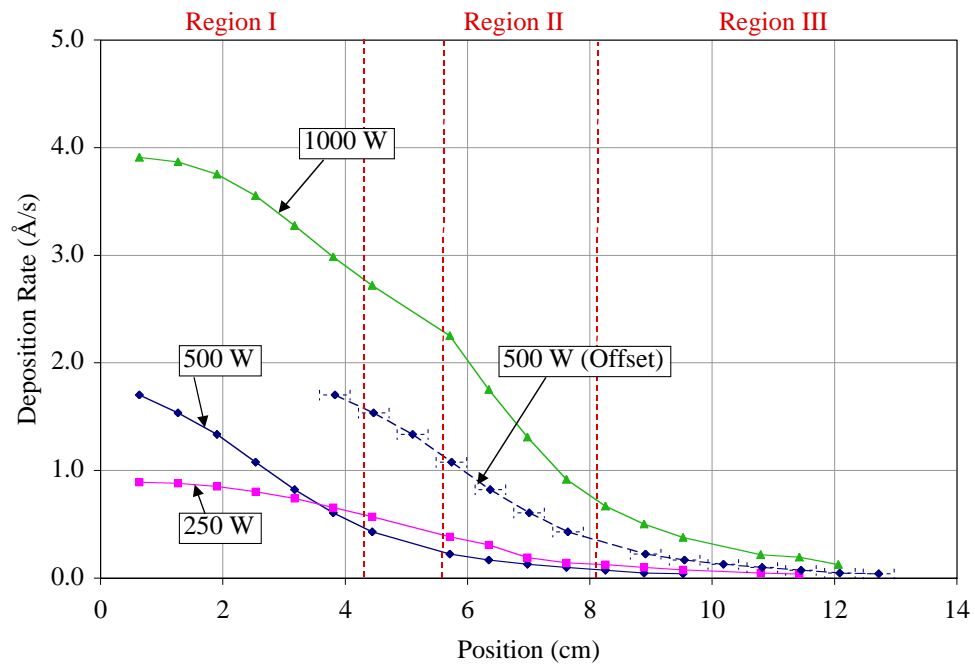


Figure 6-3. Deposition rate of ZnO:Al as a function of position on the substrate and RF power used to deposit the film.

to find the step feature and lack of measurement accuracy for films thinner than 100 Å. The second of the three side-by-side substrates ends at 10 cm for the 250 W and 1000 W cases, and 13.2 cm for the 500 W case. Only two and three data points from the 250 W and 1000 W conditions, respectively, are taken from the third substrate, and all values indicate very thin films. The curves for thickness and deposition rate from each power condition show similar though offset decaying functions with increasing position. Note the lack of intersections between the curves for different RF power conditions for either film thickness or deposition rate. Note also that neither the thickness nor deposition rate curves are completely smooth. Particularly strong deviations occur in the 250 W and 1000 W data around the position of 6 cm.

The molecular deposition flux, or the flux of material that contributes to the film thickness, is calculated from the deposition rate of the film, the density of ZnO, and its molecular weight. The flux is presented in Figure 6-4, and ranges in values between 1.5×10^{13} to 1.6×10^{15} molecules/cm²·s as a function of the RF power used to deposit the film, and the position on the substrate. The trends in the flux data are identical to those in the data for the deposition rate because the flux is calculated using a linear relationship to the deposition rate.

One difference between the thickness and deposition rate plots is the vertical order of the curves. The thickness of films deposited at 500 W is greater than for 1000 W, and least for 250 W. For the deposition rate, the order is 1000 W, 500 W, and 250 W for highest to lowest, respectively. As a rule of thumb, deposition rate increases linearly with power, all else being equal. To determine if this rule of obeyed, the ratio of the deposition rates for the 250 W and 500 W conditions to the 1000 W condition are plotted

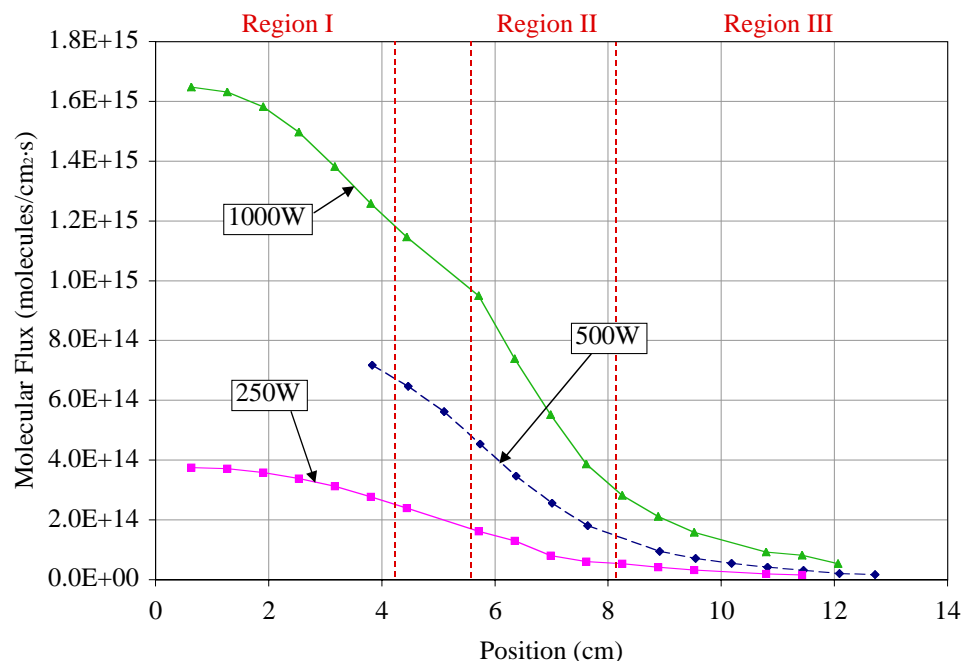


Figure 6-4. Deposited molecular flux of ZnO:Al plotted as a function of position on the substrate and RF power.

versus position in Figure 6-5. For positions less than 4 cm, the 250 W/1000 W data has a value of ~ 0.23 , which is very close to the expected value of 0.25. Deviations to lower values occur between the positions of 4 and 8 cm, with the lowest value being 0.14. The 500 W/1000 W data start with value of ~ 0.57 around the position of 4 cm, and decrease to values near 0.45 from ~ 6 to 10 cm. The final two data points are near 0.37.

6.2.2 Electrical Characterization

Electrical measurements are made using a four point probe and Hall measurement system. The four point probe measurements are made while the substrate is still whole. The probe head is brought down on accurately measured locations in the manner described in section 3.3.2. Data are collected every 0.6 cm, yielding a series of 14-18 measurements from each substrate. Hall measurements are taken by the van der Pauw method from the Hall system described in section 3.3.1, which accepts a maximum

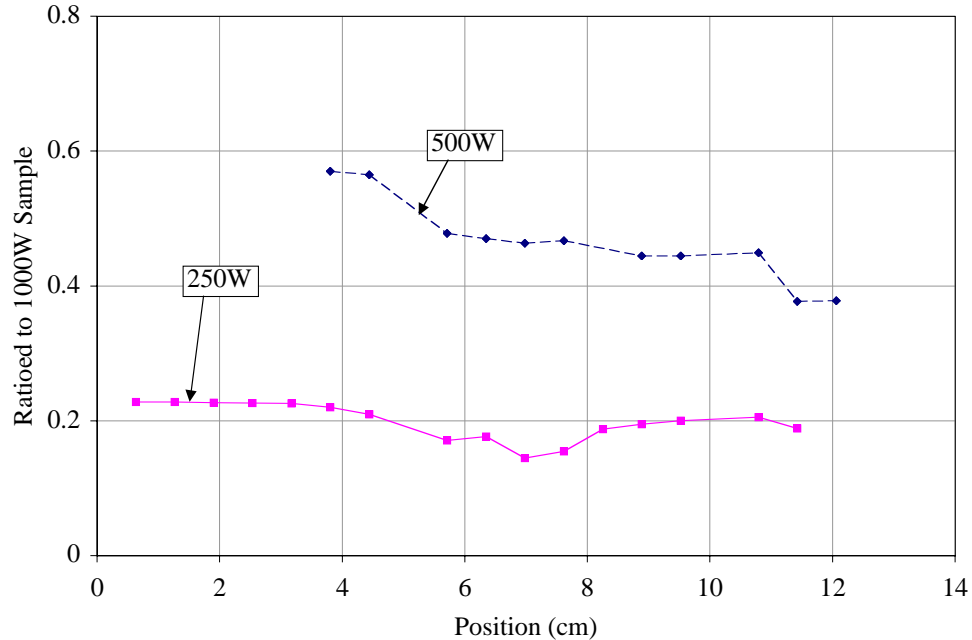


Figure 6-5. Deposition rate ratio between 250 W/1000 W and 500 W/1000 W conditions versus position on the substrate.

sample size of 7 x 7 mm [121]. Both Hall and AFM samples were cleaved from XRD specimens after spectra are collected. Because exact positions of Hall and AFM samples are unknown and film thickness changes with position, there is uncertainty in the thickness used to derive resistivity from Hall data. Inaccuracies in position are indicated by ordinate error bars, while abscissa error bars indicate estimated error in the measured values.

All resistivity data are plotted on semi-log axes. The resistivity as a function of position measured by both four point probe and Hall is presented in Figure 6-6. The mathematical offset has not been applied to the 500 W data in this plot. The solid and dashed traces of the same color indicate four point probe and Hall data, respectively. Resistivity data from four point probe are replotted in Figure 6-7, with the position offset applied to 500 W data. There is good agreement between trends in resistivity for all

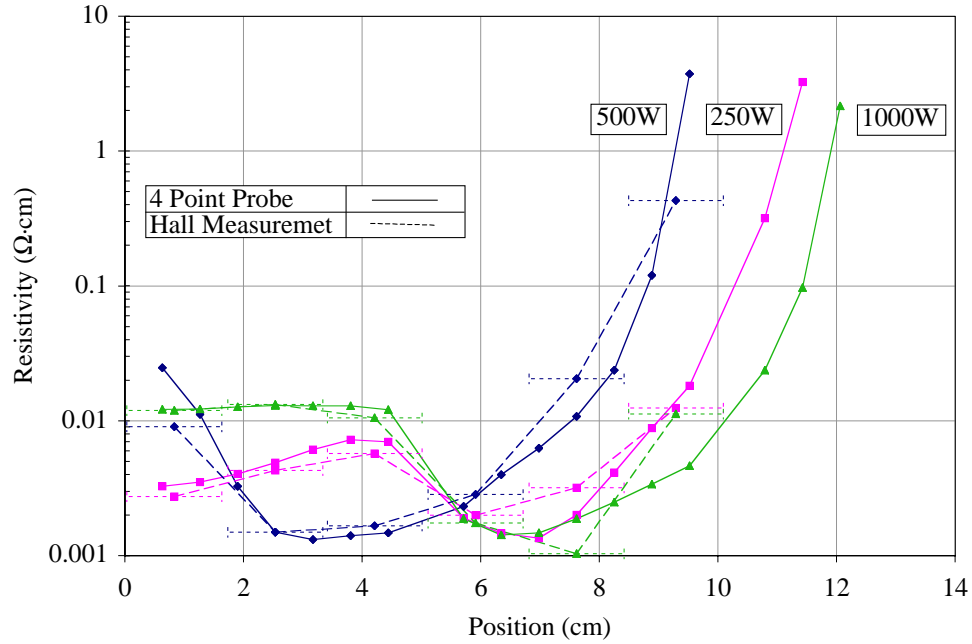


Figure 6-6. Resistivity of ZnO:Al thin films collected by four point probe (solid) and Hall measurements (dashed) versus position on the substrate and RF power.

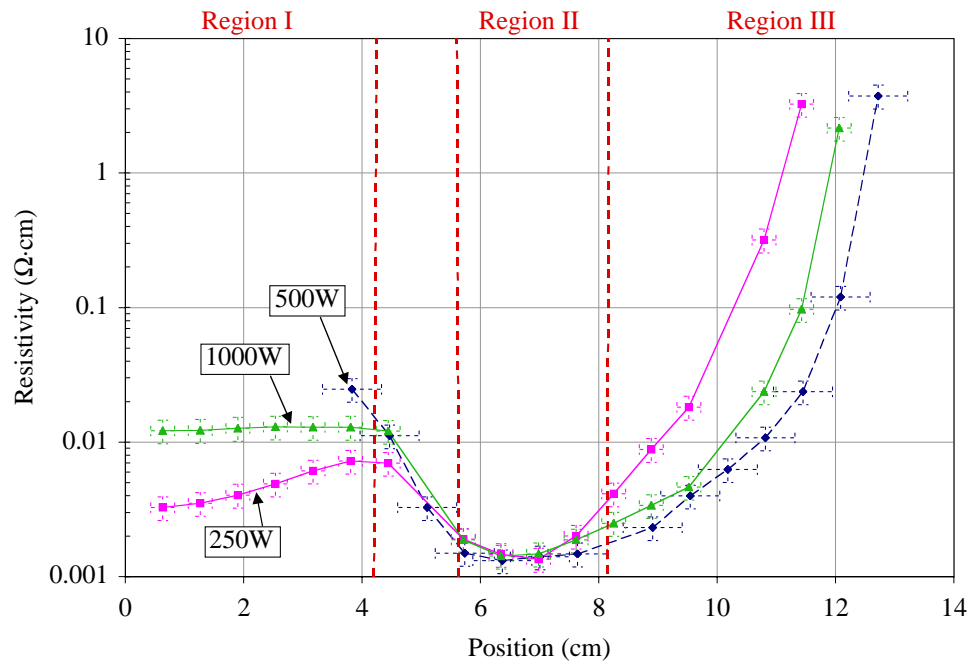


Figure 6-7. Resistivity of ZnO:Al thin films with 500 W data offset by 3.2 cm as a function of position on the substrate and RF power from four point probe.

samples, and therefore remaining data will be plotted by default with the position offset applied.

Resistivities span ~ 3.5 orders of magnitude for all power conditions. The general trends for all three RF powers indicates that there are three distinct regions in the resistivity, defined as Regions I, II, and III. Region I occurs for positions less than 4.5 cm, and has an intermediate resistivities between $\rho \sim 5 \times 10^{-3}$ and $\sim 10^{-1}$ $\Omega \cdot \text{cm}$. Resistivities for 250 W samples trend from 3.3×10^{-3} up to 7.0×10^{-3} $\Omega \cdot \text{cm}$ between positions of 0.6 to 4.5 cm. For 1000 W samples, resistivities in Region I consistently have a value near 1.3×10^{-2} $\Omega \cdot \text{cm}$. Thus the 1000 W samples are between 2.5 and 5 time higher in resistivity than 250 W samples. Note that the first datum point for the 500 W sample is 3.8 cm, which is near the edge of this region. Resistivities for these samples are 2.5×10^{-2} and 1.1×10^{-2} $\Omega \cdot \text{cm}$ at positions of 3.8 and 4.5 cm, respectively. Resistivity sharply decreases by between $\sim 4x$ and $8x$ with increasing positions from 4.5 to 5.7 cm for all RF powers, and marks the transition between Regions I and II.

Region II spans ~ 5.7 to ~ 8 cm, and has the lowest resistivity, which is consistently $\rho \sim 1.5 \times 10^{-3}$ $\Omega \cdot \text{cm}$ and is independent of RF power. This resistivity is between a factor of $\sim 5x$ and $20x$ lower than the highest resistivities from Region I. At the 8.2 cm position, resistivities increase, and significant differences between power conditions are found, with values of 4.1×10^{-3} , $\sim 2.0 \times 10^{-3}$, and 2.5×10^{-3} $\Omega \cdot \text{cm}$ for 250 W, 500 W, and 1000 W samples, respectively. This area is the transition between Regions II and III. The end of Region II is defined as where the resistivity starts to increase, which occurs at the position of ~ 8 cm for the different RF powers. The transition between Region II and III is not well defined in position because Region III is defined in terms of

film thickness, therefore its location can vary in position based on sputter deposition conditions.

Region III corresponds to areas less than 500 Å in thickness, and has resistivities that increase sharply with increasing position from low values of $\sim 5 \times 10^{-3} \Omega \cdot \text{cm}$ to the highest resistivities measured in this experiment of greater than $10^0 \Omega \cdot \text{cm}$ (the maximum measurable resistivity). Figure 6-8 is a plot of resistivity as a function of film thickness, and shows an almost direct overlap of resistivities for samples thinner than 500 Å indicating independence from RF power. Note that while Region III corresponds to films less than 500 Å thick, the transition from Region I to II varies from 1000 Å to 2000 Å to 4000 Å for films deposited at 250 W, 1000 W, and 500 W, respectively. This is consistent with the lack of correlation in resistivity plotted as a function of thickness for Region I and the transition into Region II. Because Region III is defined in terms of film

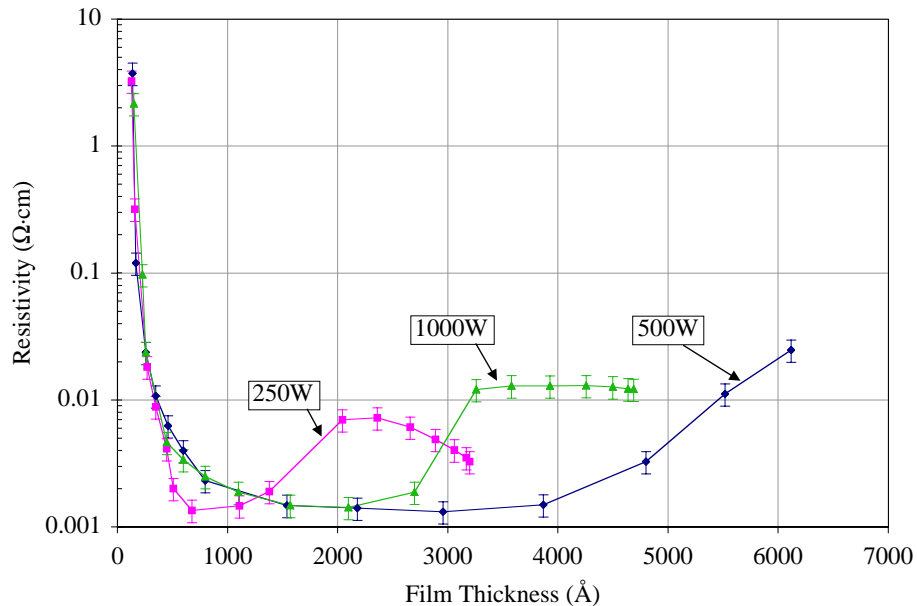


Figure 6-8. Resistivity of the deposited ZnO:Al thin film plotted versus thickness and RF power used to deposit the film.

thickness, its position on the substrate depends on deposition conditions i.e. deposition time and RF power. Samples with a thickness of 500 Å (the beginning of Region III) occur at 8.3, 10.2, and 8.9 cm for 250 W, 500 W, and 1000 W samples, respectively, and all have resistivities near $5 \times 10^{-3} \Omega \cdot \text{cm}$.

Hall data are used to determine majority carrier type, carrier concentration, and Hall mobility. All films are *n*-type, with carrier concentrations presented as functions of position and film thickness in Figures 6-9(a and b), respectively. Carrier concentrations on the order of 10^{20} cm^{-3} are needed for a TCO with a resistivity near $10^{-4} \Omega \cdot \text{cm}$ while maintaining greater than 85% transmittance, which are requirements for high efficiency solar cells [11,82]. This condition is met by a majority of samples with some notable exceptions presented below. General trends in carrier concentration are low values for Region I which increase abruptly to the highest measured values in Region II, and decrease sharply across Region III. These trends are consistent with trends in reported resistivity data. In Region I carrier concentrations range from 7.2×10^{19} to $3.3 \times 10^{20} \text{ cm}^{-3}$, and have a strong dependence on RF power. The 250 W samples consistently have the highest carrier concentrations for Region I, with values that decrease in carrier concentration from 3.3×10^{20} to $1.8 \times 10^{20} \text{ cm}^{-3}$ between positions of 0.8 and 4.2 cm. Carrier concentration for the 1000 W samples increases from 7.2×10^{19} to $1.4 \times 10^{20} \text{ cm}^{-3}$ between 0.8 and 4.2 cm. The singular datum point for the 500 W sample in Region I has a carrier concentration of $8.2 \times 10^{19} \text{ cm}^{-3}$ at a position of 4.0 cm. Note that carrier concentrations less than 10^{20} cm^{-3} are found for the 500 W sample at a position of 4.0 cm, and for 1000 W samples at positions of 0.8 and 2.4 cm.

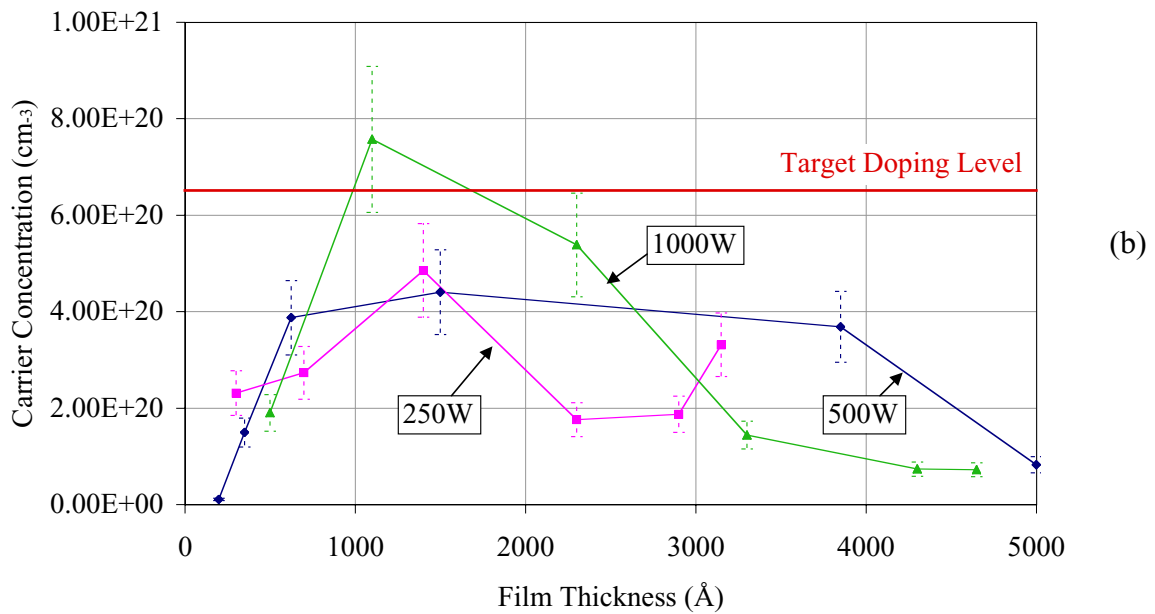
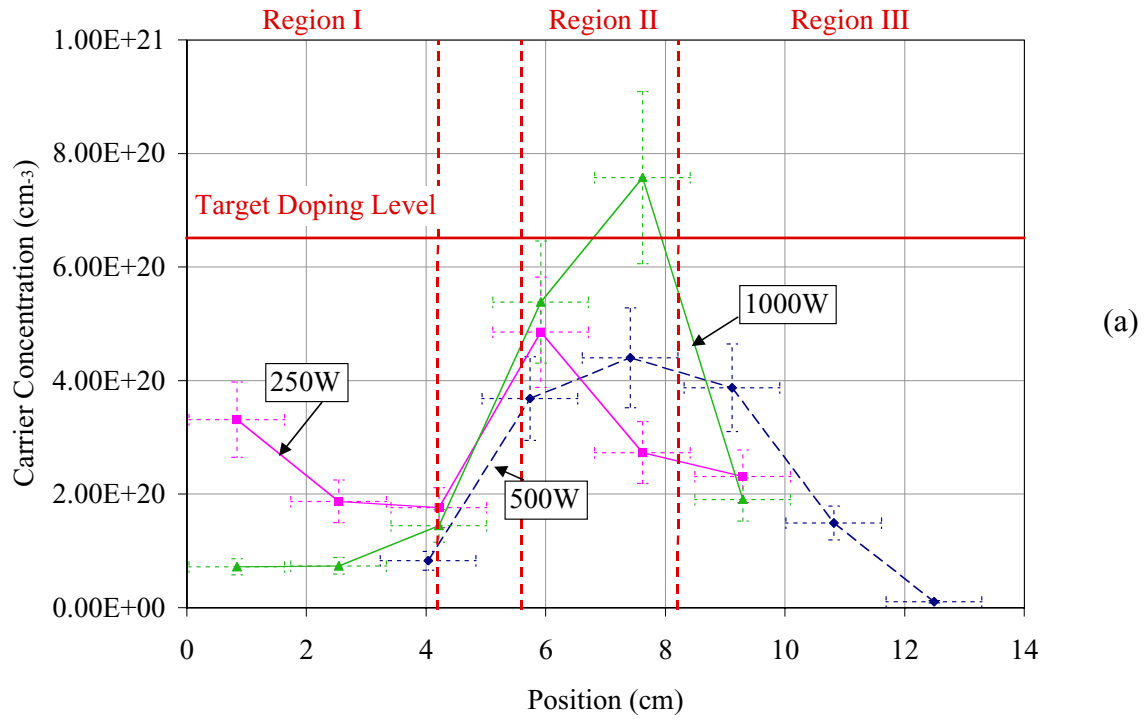


Figure 6-9(a-b). Carrier concentration of ZnO:Al thin films from Hall measurements and plotted versus (a) position on the substrate and (b) film thickness.

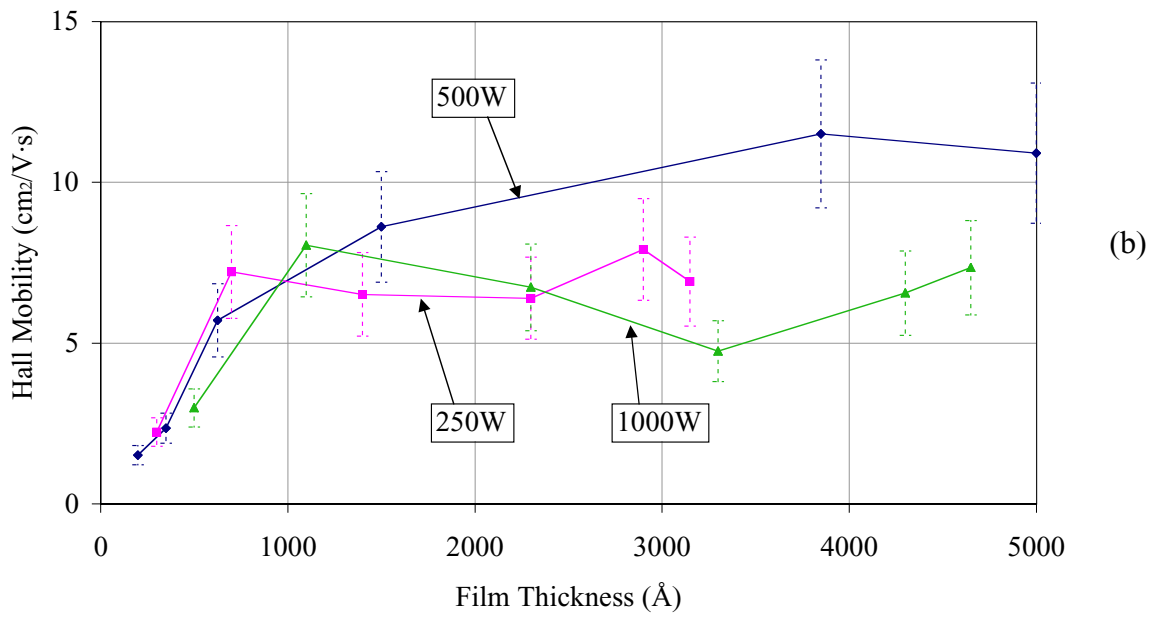
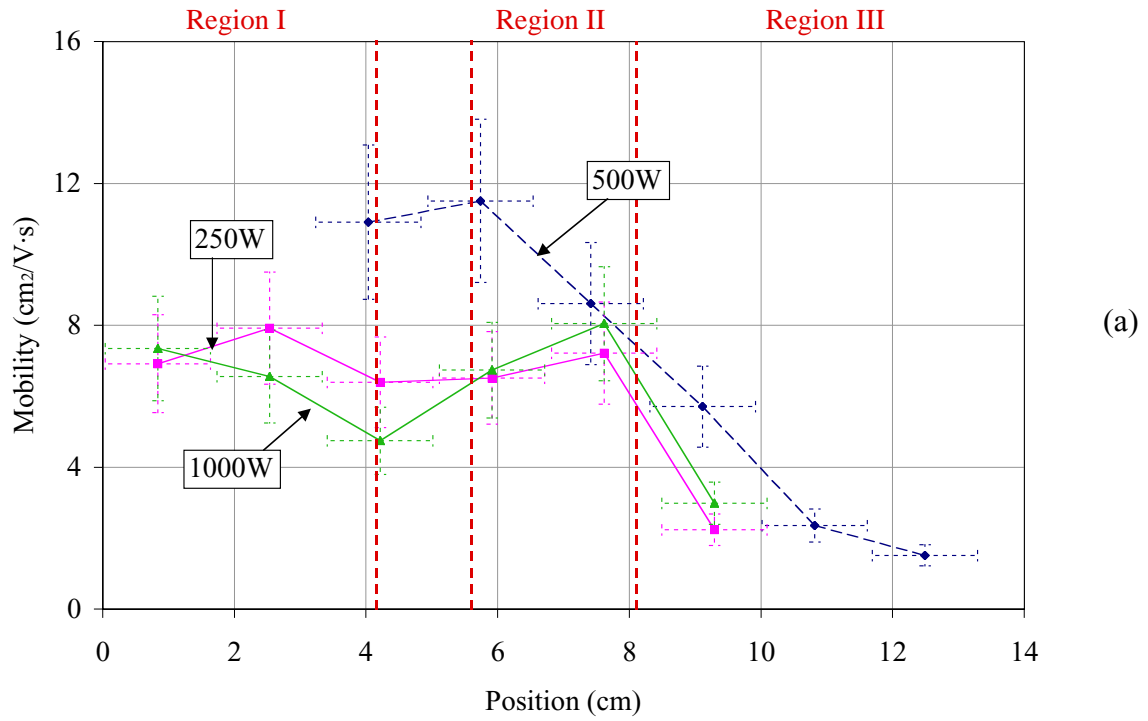
Carrier concentrations increase sharply (2 to 4x) for the transition between Regions I and II at positions from 4 and 6 cm, and reach maximum into Region II where all values are greater than 10^{20} cm^{-3} . For 250 W samples, carrier concentration decreases across Region II from 4.9×10^{20} to $2.7 \times 10^{20} \text{ cm}^{-3}$ at positions of 5.9 to 7.6 cm. The 500 W samples exhibit consistent values near $4.0 \times 10^{20} \text{ cm}^{-3}$ across Region II from positions of 5.7 to 9.1 cm. For 1000 W samples, carrier concentration increases across Region II from 5.4×10^{20} to $7.6 \times 10^{20} \text{ cm}^{-3}$ at positions of 5.8 and 7.6 cm.

The plot of carrier concentration versus position indicates that carrier concentrations are lower in Region III than Region II. Looking at carrier concentration as a function of film thickness, it is important to note that for 250 W and 1000 W data there is only one datum point from Region III, therefore there are no trends in data within this region. Also note that no abscissa error bars are present for data plotted as a function of thickness. This is because errors are estimated in terms of position, and position is not linear when plotted as a function of thickness. For the 250 W sample, carrier concentration is $2.3 \times 10^{20} \text{ cm}^{-3}$ for a film thickness of 300 Å at a position of 9.3 cm. The carrier concentration is within experimental error of value taken from the position of 7.6 cm from Region II. For 500 W samples, a decrease of more than an order of magnitude in carrier concentration occurs with thickness from 1.5×10^{20} to $1.0 \times 10^{19} \text{ cm}^{-3}$ with film thicknesses from 350 Å and 200 Å, respectively. For the singular 1000 W data point in Region III, the carrier concentration is $1.9 \times 10^{20} \text{ cm}^{-3}$ for a film thickness of 500 Å and a position of 9.3 cm. Carrier concentration is ~4 times lower than the adjacent value from position 7.6 cm from Region II. Note that the carrier concentration for 500 W sample with a thickness of 200 Å has a carrier concentration an order of magnitude lower that

10^{20} cm^{-3} . Additionally, all positions with carrier concentrations less than 10^{20} cm^{-3} are also marked with red data markers in quantified XRD results. The meaning of the red data markers will be presented in the XRD results section, and implications of this correlation will be discussed below.

With the exception of one datum point (1000 W at 7.6 cm), all carrier concentrations are below the Al doping concentration of the target ($6.5 \times 10^{20} \text{ cm}^{-3}$). The highest carrier concentrations for the 250 W, 500 W, and 1000 W samples are 4.9×10^{20} , 4.4×10^{20} , and $7.6 \times 10^{20} \text{ cm}^{-3}$, respectively. These carrier concentrations are 69%, 75%, and 116%, respectively, of the target's extrinsic doping concentration. While these carrier concentrations are good, they are the highest values measured. The worst dopant activation percentages measured from Region I for the 250 W, 500 W, and 1000 W cases are 28%, 13%, and 11% respectively. Note that the 500 W sample also shows an exceptionally low carrier concentration of $1.04 \times 10^{19} \text{ cm}^{-3}$ at 12.5 cm in Region III, which translates to less than 2% activation.

Hall mobility is plotted as a function of position and film thickness in Figures 6-10(a-b). The highest mobility is $< 12 \text{ cm}^2/\text{V}\cdot\text{s}$, which is approximately half the value of a high quality ZnO TCO ($\mu > 25 \text{ cm}^2/\text{V}\cdot\text{s}$) [28]. There is not a strong correlation between Hall mobility and position or deposition power. The Hall mobility data will be discussed versus RF power instead of by position. For 250 W samples, there is a 25% increase between the worst ($6.4 \text{ cm}^2/\text{V}\cdot\text{s}$) and best ($7.9 \text{ cm}^2/\text{V}\cdot\text{s}$) Hall mobility in Regions I and II (positions $< 8 \text{ cm}$), which is about the precision of the measurement. For 1000 W samples, there is a 55% increase in mobility between the worst ($4.7 \text{ cm}^2/\text{V}\cdot\text{s}$) and best ($8.0 \text{ cm}^2/\text{V}\cdot\text{s}$) mobility in Regions I and II, which indicates at least a small variation



Figures 6-10(a-b). Hall mobility of ZnO:Al thin films plotted versus (a) position on the substrate and (b) film thickness.

beyond the uncertainty of the measurement. The trends in data decrease from 7.3 to 4.7 $\text{cm}^2/\text{V}\cdot\text{s}$ between 0.8 and 4.2 cm across Region I. It then increases across Region II to a value of 8.4 $\text{cm}^2/\text{V}\cdot\text{s}$ at 7.6 cm. The mobility of both 250 W and 1000 W samples decrease sharply at 9.3 cm in Region III with values of 2.2 and 3.0 $\text{cm}^2/\text{V}\cdot\text{s}$, respectively.

The 500 W samples show the largest variation in mobility with an 87% decrease from best (12 $\text{cm}^2/\text{V}\cdot\text{s}$) to worst (1.5 $\text{cm}^2/\text{V}\cdot\text{s}$) at positions of 5.7 and 12.5 cm, respectively. Between Region I and II (4.0 and 5.7 cm), the change is less than the uncertainty of the measurement. From 5.7 cm (highest mobility) to 12.5 cm (lowest mobility), the data decreases monotonically and the change is greater than the measurement error.

No systematic correlation between mobility and film thickness is found for the different RF powers for films thicker than 1000 Å. Below approximately 600 Å, the mobility of all samples decreases with fairly consistent slope and similar magnitudes. This indicates a correlation between thickness and mobility that is independent of the deposition power in Region III.

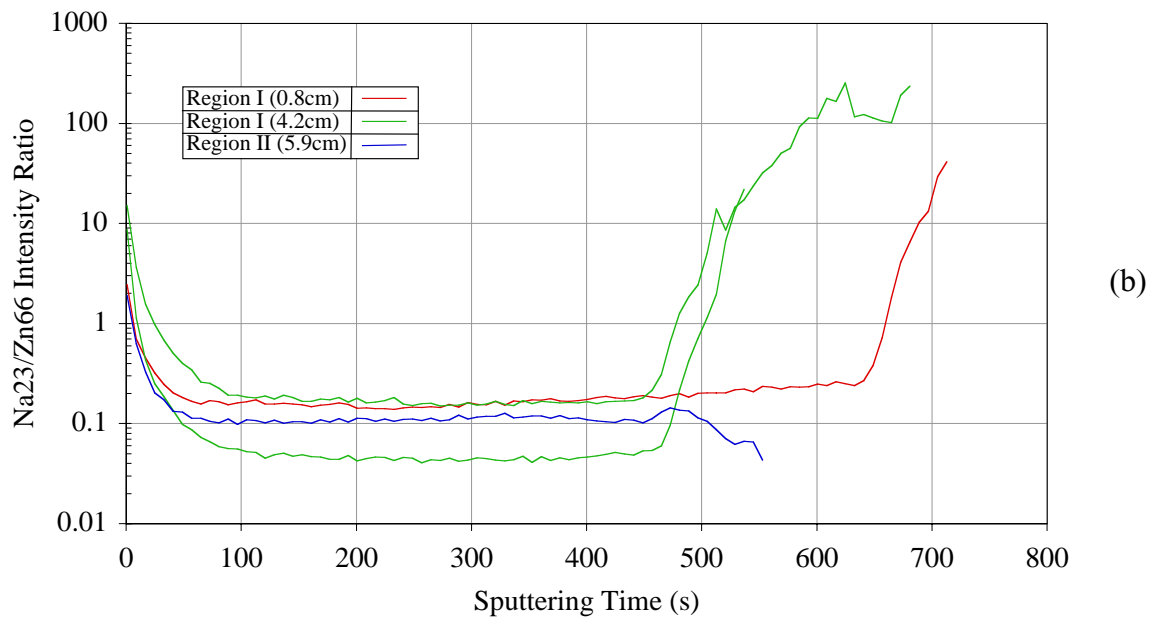
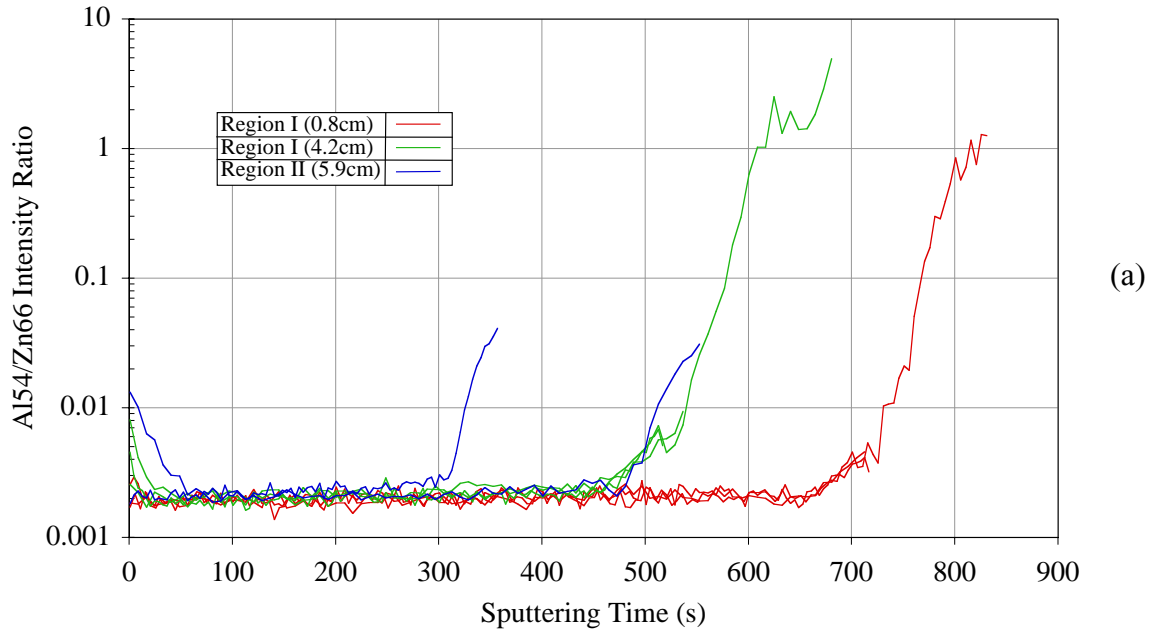
6.2.3 Secondary Ion Mass Spectrometry Results

The composition of the deposited ZnO:Al thin films is characterized by secondary ion mass spectrometry (SIMS). The SIMS data is collected from the Hall measurement sample, and the Al dot contacts used for Hall measurements are carefully avoided. Elements of interest include Zn, Al, and the alkali metals, which are electropositive elements; therefore results are collected with an oxygen primary beam using the conditions specified in section 3.4.6. The presented results are SIMS depth profiles taken using dynamic SIMS techniques. The plotted data are the intensity ratios of Al to Zn and Na to Zn as a function of sputtering time, with different positions indicated by the

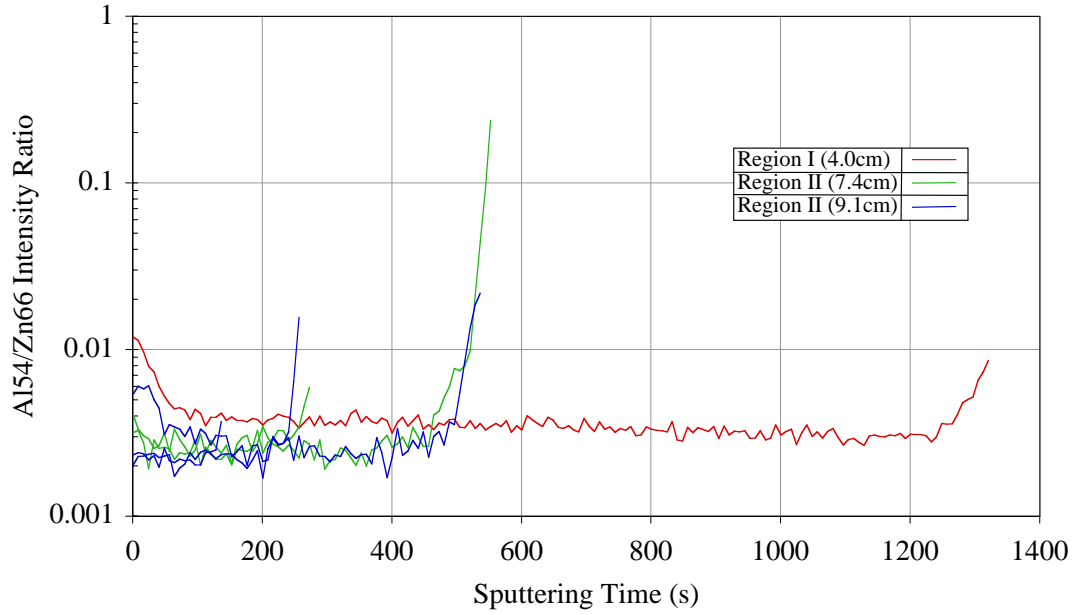
different colored lines. Multiple lines of the same color show replicate data, which is useful to evaluate the measurement error in the data. The Al to Zn and Na to Zn data for 250 W, 500 W, and 1000 W data are presented in Figures 6-11(a-b), 6-12(a-b), and 6-13(a-b), respectively. No standard compounds were available, therefore only qualitative analysis could be performed. The qualitative measurements are repeatable, which allows accurate comparison between data from different positions on the substrate.

The ratio of Al to Zn was found to be consistently between 0.015 and 0.045 for all samples from 250 W, 500 W, and 1000 W deposition powers when the large features at the beginning and/or end of the depth profile are neglected. This indicates that a factor of three is the maximum variation in the Al to Zn ratio that occurs. The consistent increase in the Al to Zn ratio at longer sputtering times likely results from the presence of alumina additive and lack of any zinc compounds in the float glass substrate. Data from samples deposited at 250 W show no change in the Al to Zn ratio as a function of position. For samples deposited at 500 W and 1000 W, the Al to Zn ratio is consistently higher in Region I compared to Region II, indicating areas receiving a negative ion flux had slightly higher Al concentrations. In all cases an almost direct overlap in data is found when more than one depth profile is collected from a sample.

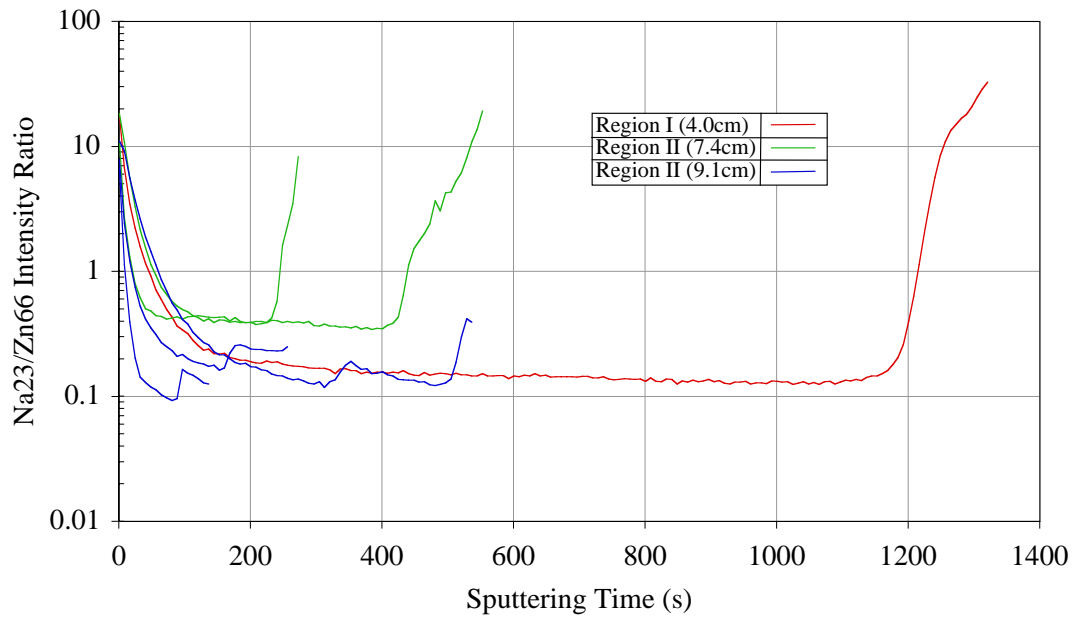
Values for the Na to Zn ratio range from 0.04 to 0.2 for 250 W data, 0.1 to 0.4 for 500 W data, and 0.035 to 0.1 for 1000 W data. There are also sharp increases at the beginnings and ends of the depth profiles, and result from Na contamination of the film's surface for the high ratios early in the profile, and presence of soda in the glass substrate for longer times in the depth profile. Though precise values for relative sensitivity factors (RSF) are not known due to the lack of standards, generally the RSF increases



Figures 6-11(a-b). SIMS depth profile data for ZnO:Al films deposited at 250 W for the ratio of (a) Al to Zn for the dopant concentration and (b) Na to Zn for concentration of compensating alkali metals.

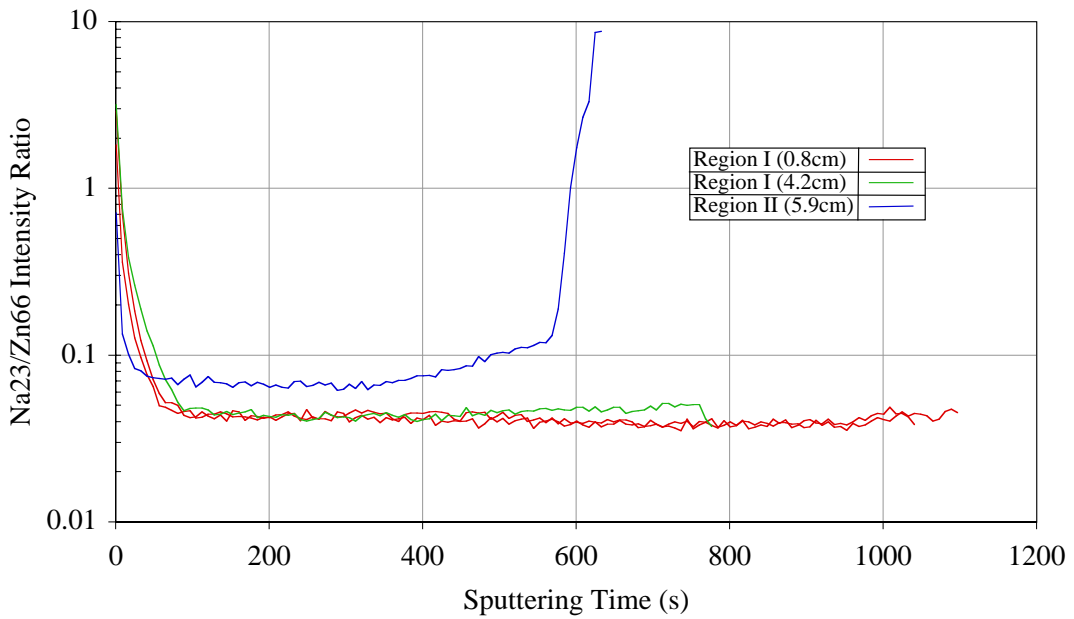
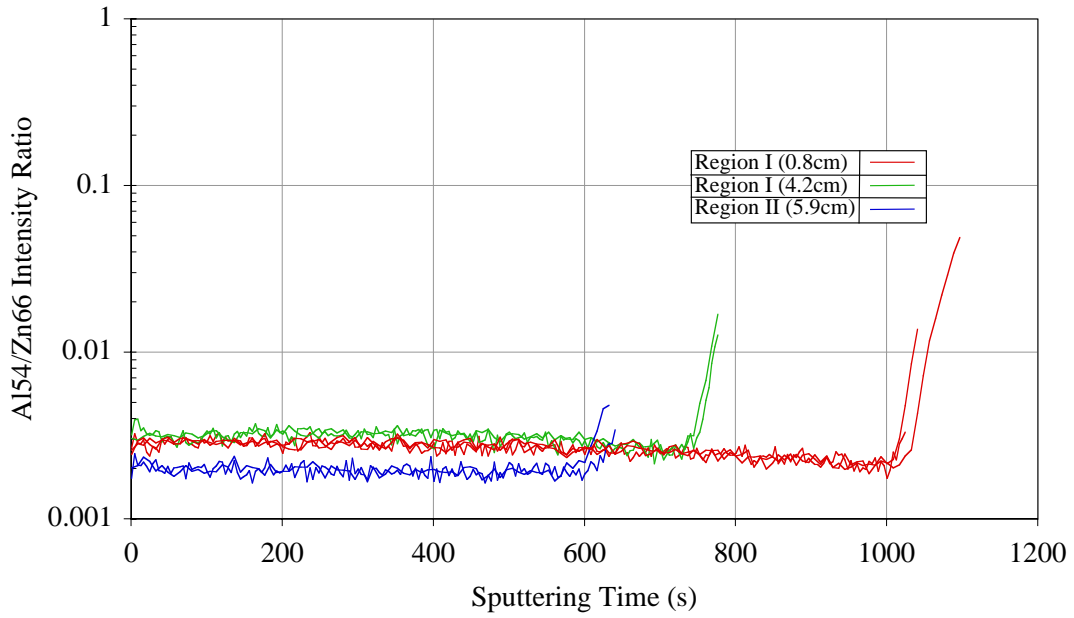


(a)



(b)

Figures 6-12(a-b). SIMS depth profile data for ZnO:Al films deposited at 500 W for the ratio of (a) Al to Zn for the dopant concentration and (b) Na to Zn for concentration of compensating alkali metals.



Figures 6-13(a-b). SIMS depth profile data for ZnO:Al films deposited at 1000 W for the ratio of (a) Al to Zn for the dopant concentration and (b) Na to Zn for concentration of compensating alkali metals.

for decreasing ionization potential for positive ions generated from an oxygen primary beam [138]. The ionization potential of Na is 5.1 eV compared to 9.4 eV for Zn and 6.0 eV for Al, therefore it is important to recall that the presented ratios are from raw data, and it is anticipated that SIMS is orders of magnitude more sensitive to Na compared to Zn and Al. More variation is found in the Na to Zn ratio data, where changes occur between duplicated depth profiles and as a function of power. Most duplicated depth profiles have similar Na to Zn ratio values, with the exception of data from the 4.2 cm sample deposited at 250 W, where there is a factor of five between replicate data sets. The value of the average between the two 4.2 cm data sets is similar to those for the 0.8 cm and 5.2 cm data sets, which suggests little variation in Na concentration occurs with position. Similarly, only small variations in the Na to Zn ratio are found as a function of position on the substrate.

6.2.4 X-ray Photoelectron Spectroscopy Results

The surface of the deposited ZnO:Al thin films are characterized by X-ray photoelectron spectroscopy (XPS). The presented XPS data are taken only from a sample deposited at 500 W from Region I on the substrate, and similar results are found for other samples. The spectra are collected using the conditions specified in the section 3.4.5. Survey spectra for binding energies from 0 to 1100 eV are collected from both as deposited and sputter etched surfaces. The sputter etch was 6 minutes using the Ar ion source with conditions specified in section 3.4.5. Characteristic peaks for Zn, O, and C are found in spectra from the as deposited surface, while only peaks consistent with Zn and O are found in the sputter etched surfaces. Because the carbon only appears in as deposited spectra, it is likely adventitious carbon as a surface contaminant.

Multiplex scans of the Zn ($2p_{3/2}$), O (1s), and C (1s) peaks for the same as deposited and sputter etched samples are used in conjunction with relative sensitivity factors to determine the stoichiometry of the exposed surface, and to investigate chemical bonding. The numbers in parentheses are the quantum numbers that specify the particular core level from which the photoelectron is excited. Stoichiometry data from quantitative analysis performed by the acquisition computer is presented in Table 6-1. The stoichiometry is calculated from the quantified peak area in conjunction with relative sensitivity factors.

The decrease of 27% in the carbon concentration with sputter etching is consistent with adventitious surface carbon from the atmosphere. Another interesting feature can be appreciated in the raw multiplex data for the O (1s) peak. The as deposited and sputter etch plots are presented in Figures 6-14a and 6-14b, respectively. For the as deposited sample, an overlap of at least two peaks is clearly resolvable. The curve is deconvoluted by background subtraction and fitting with two component Gaussian-Lorentzian functions which can be seen graphically in Figure 6-14a. One peak is located at 530.7 eV and has a full width at half maximum of 1.6 eV with peak intensity of 9594 counts, and represents 67% of the peak area. The second peak is at 532.3 eV and has a full width at half maximum of 2.0 eV with a peak intensity of 14147 counts, and represents 33% of the

Table 6-1. Atomic concentrations from XPS multiplex data for as deposited and sputter etched samples.

Element	Atomic Concentration (%) As Deposited	Atomic Concentration Sputter Etched (6 minutes)
Zn ($2p_{3/2}$)	13%	45%
O (1s)	53%	48%
C (1s)	34%	7%

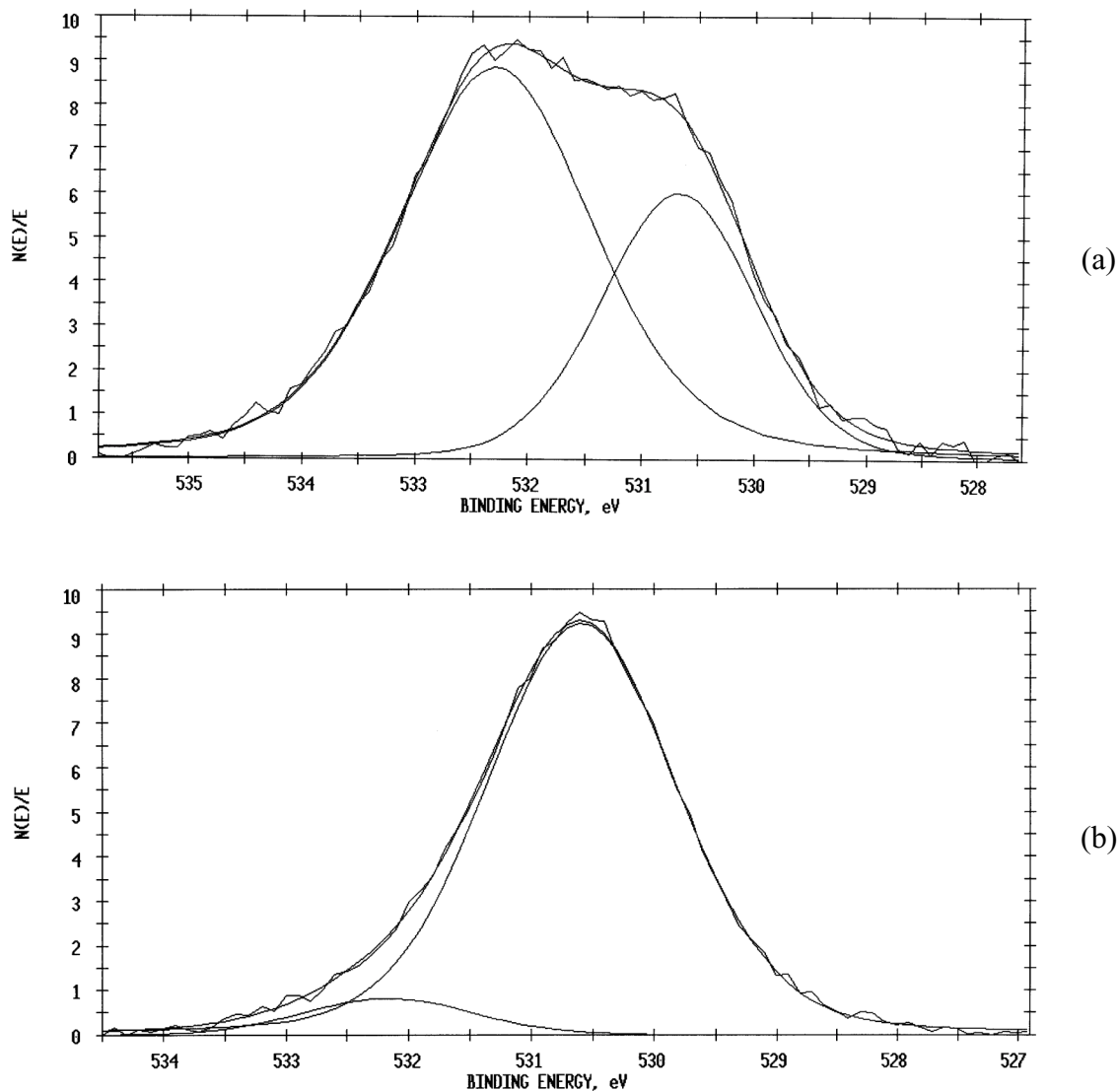


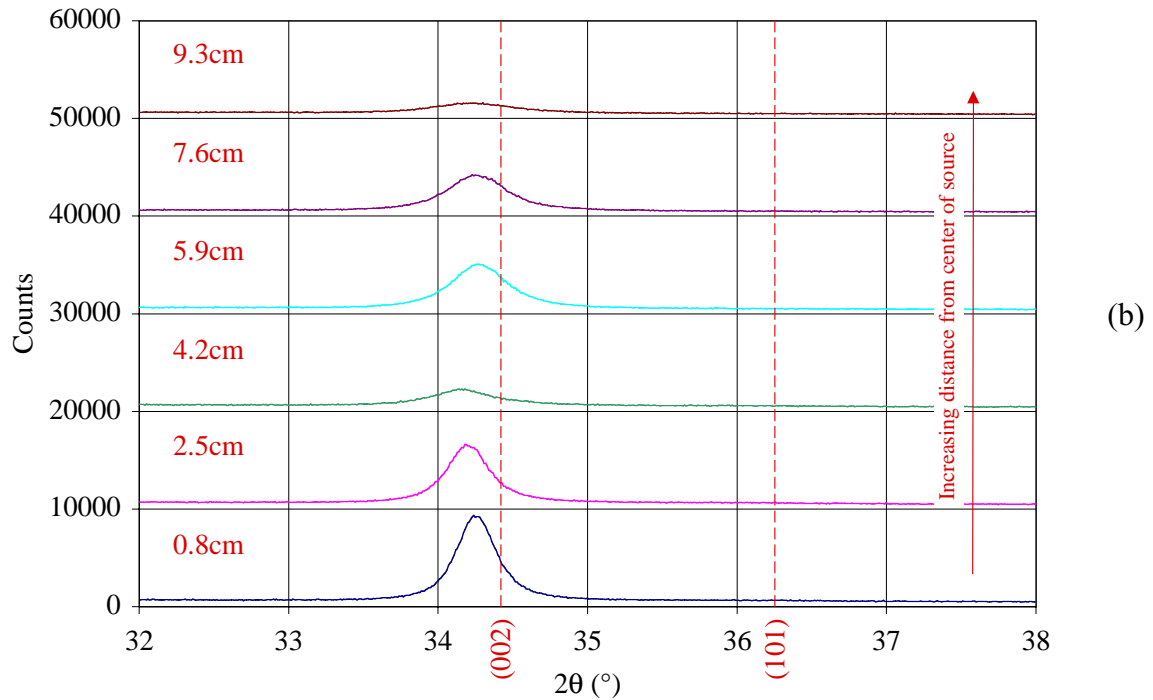
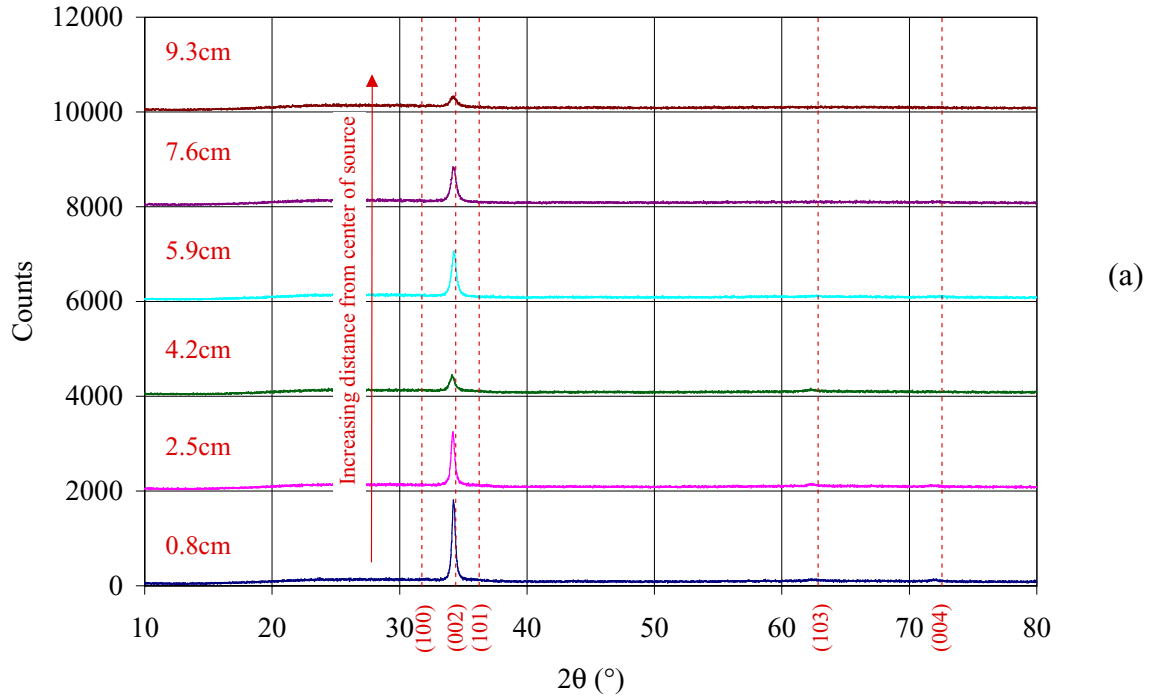
Figure 6-14(a-b). XPS multiplex spectra of the O (1s) peak showing two component peaks for (a) an as deposited film and (b) a sputter etched film.

peak area. For the O (1s) spectrum collected after sputter etching (Figure 6-14b), the higher energy 532.2 eV peak has sharply decreased in intensity relative to the 530.6 eV peak. The peak at 530.6 eV has a full width at half maximum of 1.8 eV, an intensity of 28,064 counts, and accounts for 93% of the peak area. The 532.2 eV peak has a full width at half maximum of 1.6 eV, an intensity of 2478 counts, and accounts for 7% of the

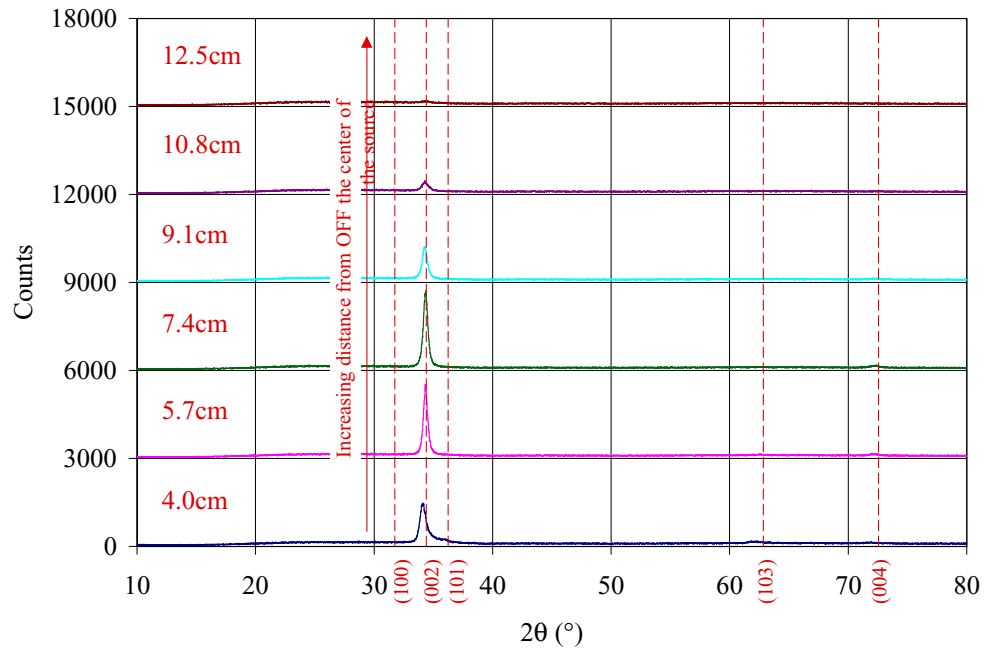
peak area. The 530.2 eV peak is consistent with bulk bonding between oxygen and zinc. The higher energy peak is consistent with a chemisorbed oxygen or hydroxide, which agrees with the fact that it is a strong presence on the as deposited surface, but is only a weak peak after sputter etching.

6.2.5 X-ray Diffraction Results

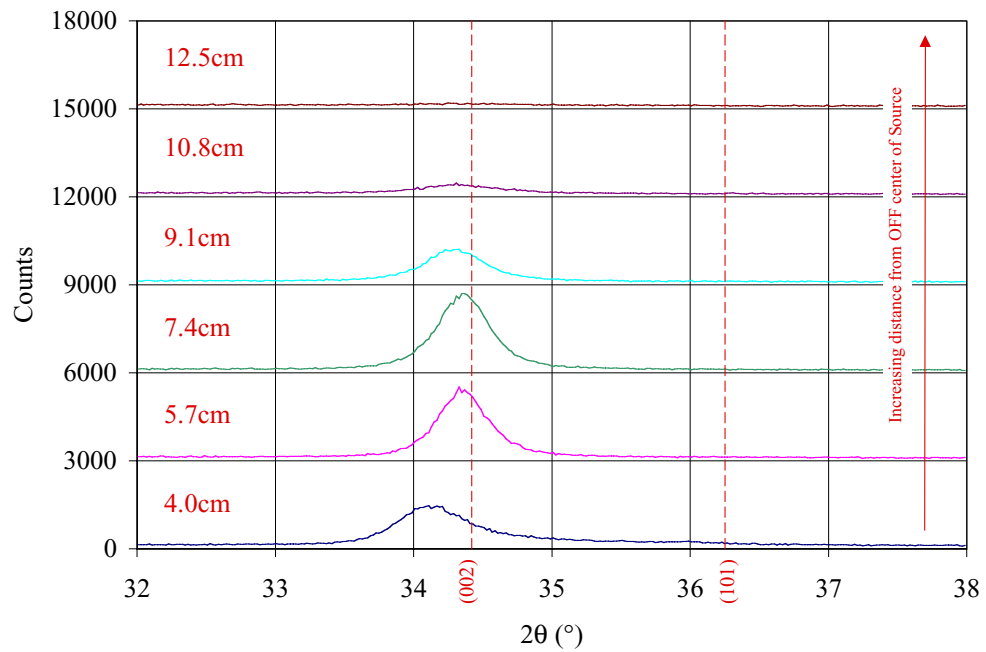
X-ray Diffraction (XRD) is used to characterize structural properties of the thin films. To obtain XRD data as a function of position, the 2.5 x 5.0 cm substrates are cleaved perpendicular to the long dimension into three 2.5 x 1.7 cm samples. No XRD data is taken from the third substrate (10 to 15 cm positions) because the very thin films at these large distances do not yield significant diffraction intensity. Survey scans ($10^\circ < 2\theta < 80^\circ$) and higher resolution line profile scans ($32^\circ < 2\theta < 38^\circ$) are shown in Figures 6-15(a-b) to 6-17(a-b) for each of the RF powers. Note that no line profile data were collected from the 500 W sample, so survey data are replotted on the same 2θ scale as line profile spectra. The zero for each spectra is offset on the y-axis by adding a constant to the ordinate values. The sensitivity for each row of a stacked set of spectra is constant and shown by the counts per division marker to the left of the spectra. The positional index for each row is given by the numbers in red arrayed vertically near the ordinate axis, with the value indicating the position for the center of the XRD sample presented in that row. Note that the spectra from the 2.5 cm position of the 1000 W condition are missing due to inadvertent breakage of this sample. The red numbers in parentheses below the abscissa refer to the Miller indices of the crystal planes whose 2θ values are marked by the vertical dashed red lines. The marked 2θ values are from the JCPDS



Figures 6-15(a-b). XRD spectra from ZnO:Al thin films deposited at 250 W as a function of position on the substrate with (a) survey spectrum and (b) high resolution spectrum.

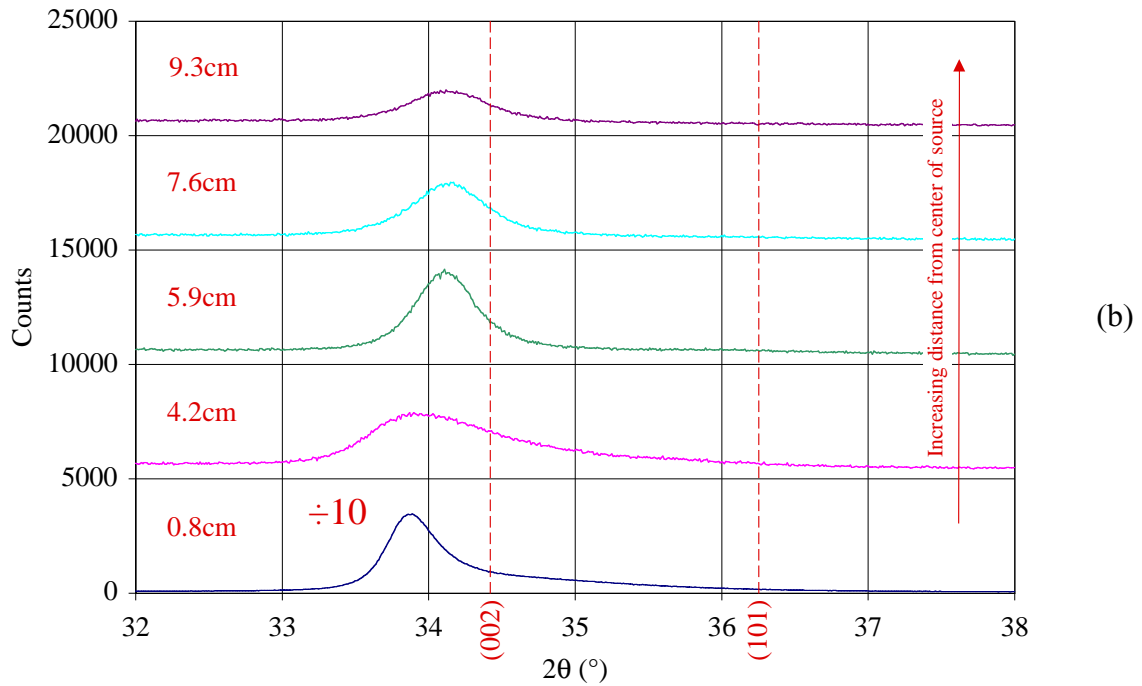
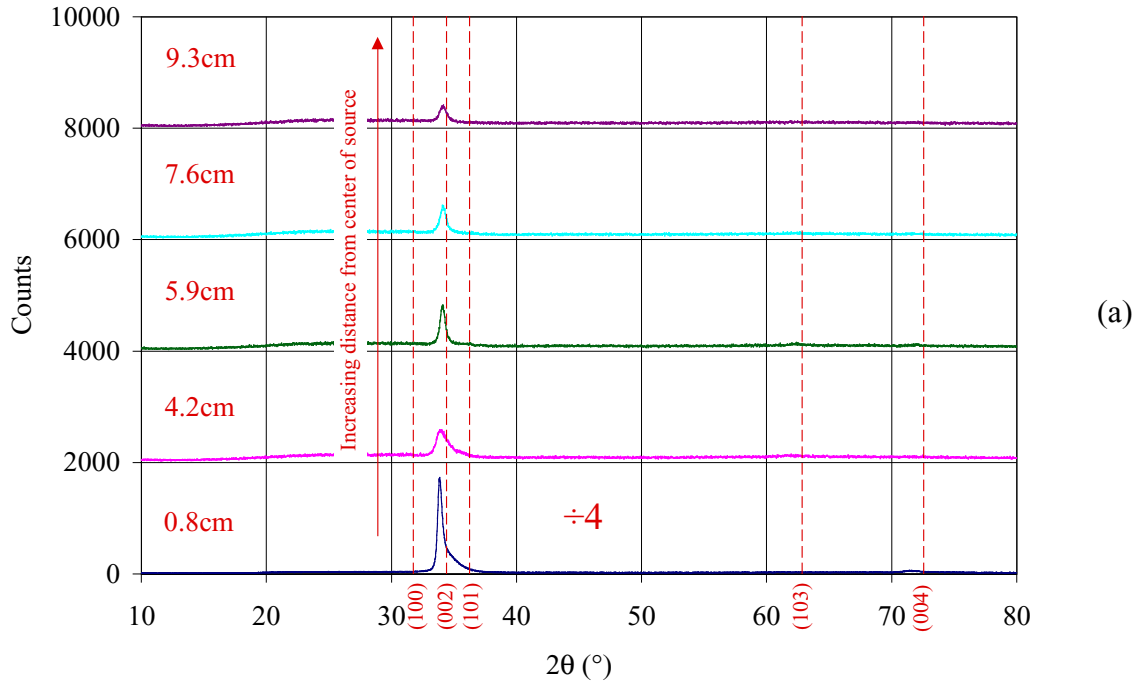


(a)



(b)

Figures 6-16(a-b). XRD spectra from ZnO:Al thin films deposited at 500 W as a function of position on the substrate with (a) survey spectrum and (b) high resolution spectrum.



Figures 6-17(a-b). XRD spectra from ZnO:Al thin films deposited at 1000 W as a function of position on the substrate with (a) survey spectrum and (b) high resolution spectrum.

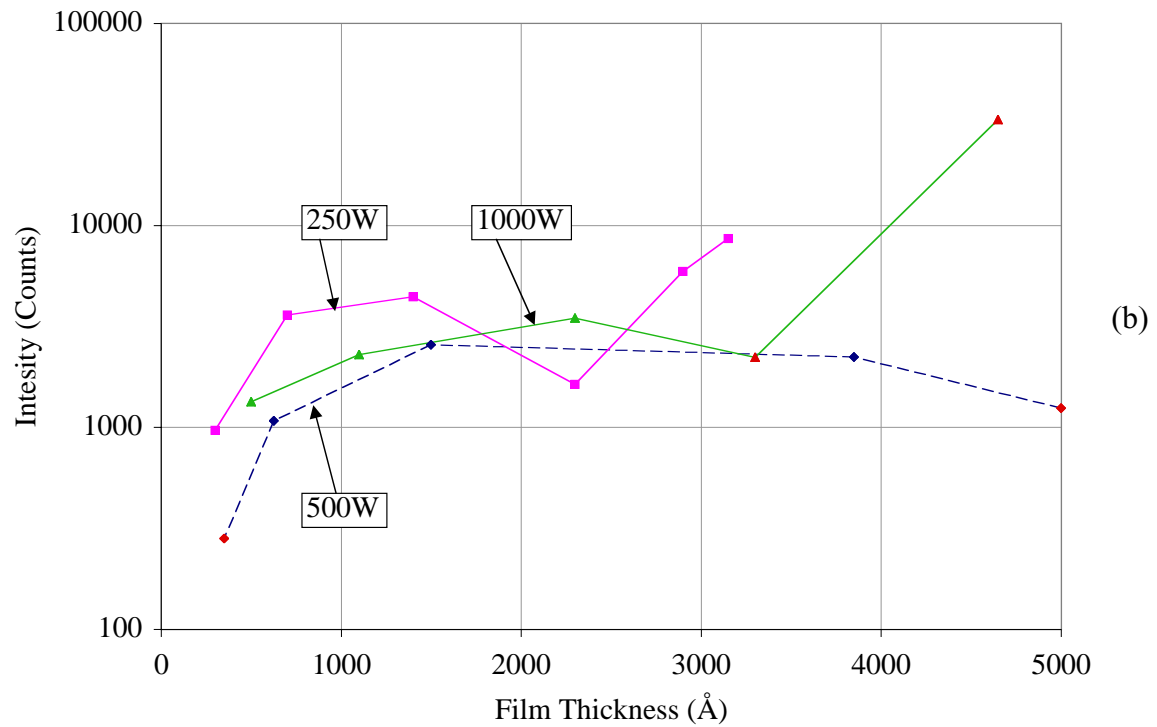
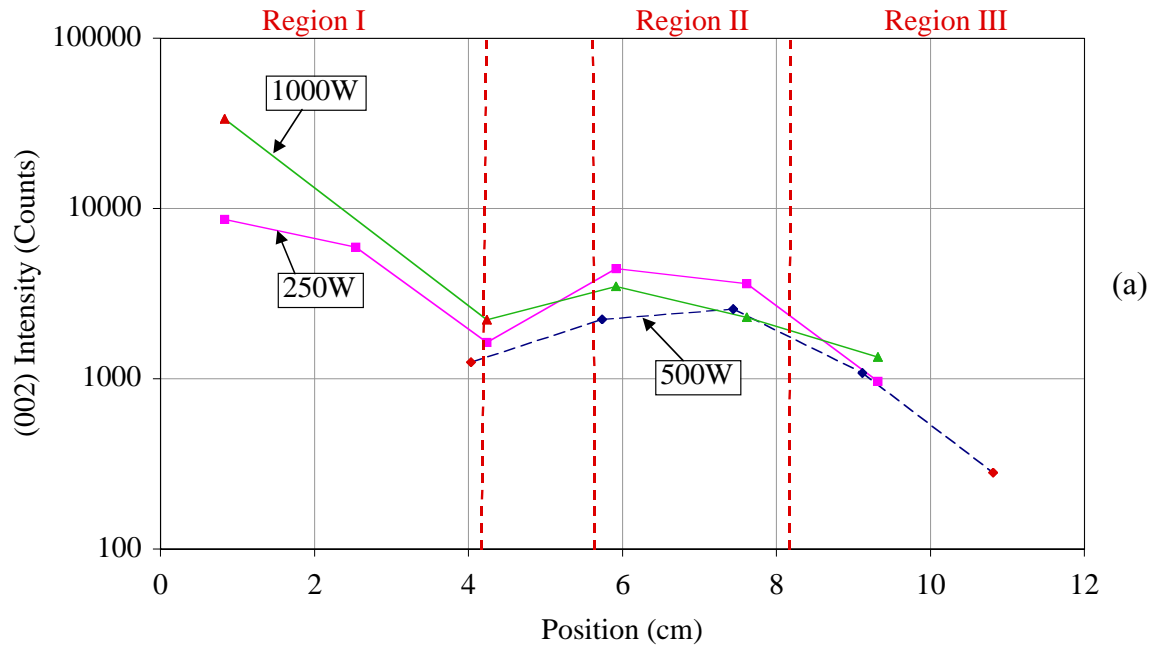
database entry for ZnO. Only crystal planes previously detected in sputter deposited films are labeled, not all of the diffraction peaks listed in the database.

In all XRD spectra, the 2θ peak consistent with the (002) basal plane of Wurtzite ZnO is the strongest peak. This peak from the present thin films is shifted to lower 2θ values and has a significant tail extending to higher 2θ values for some spectra from Region I. This is most easily seen in the line profile data. The changes in 2θ position and FWHM are quantified below. This tail extends into the 2θ region associated with the (101) reflection. There are also some minor perturbations from the baseline near the 2θ positions for the (103) and (004) peaks in some of the spectra. The dominance of the (002) peak, and lack of other peaks listed in the JCPDS database indicates that all of the deposited films have a strong basal plane crystallographic texture. Also note that the 1000 W data for position 0.8 cm was attenuated by dividing the value by 4 or 10 for the survey and line profile data, respectively. The (002) peak for these samples is exceedingly intense, and therefore the intensity needs to be scaled lower so that all 1000 W XRD spectra can be plotted with a constant sensitivity that also allows observation of less intense diffraction peaks for other 1000 W samples.

Focusing on the (002) reflection, significant variations in the 2θ position, intensity (I), and breadth (Δ) as a function of position on the substrate are seen in the spectra. This information is quantified from the line profile spectra for the 250 W and 1000 W samples, because these spectra had long count times yielding a good signal to noise ratio. Values are quantified from survey data for the 500 W sample, therefore the intensities are not comparable with the 250 W and 1000 W cases. Note that several data points below positions of 6 cm for 500 W and 1000 W data are marked with red markers. These data

points are taken from (002) peaks that have extended tails to higher 2θ values. The last data point on the 500 W curve also uses a red marker, and indicates that the quantified (002) peak was very weak. The red markers are used consistently in this section presenting quantified XRD results.

Intensity data is plotted as a function of position and thickness in Figures 6-18a and 6-18b, respectively, and is displayed on semi-logarithmic axes. It is quantified using *MacDiff* software after subtracting the background. To quantify the weak (002) peak for the 500 W sample at 10.8 cm, it is fitted with an approximated Voight function, because the signal to noise is significant relative to the peak intensity. The highest intensities for 250 W, 500 W, and 1000 W cases are 8600, 2600, and 33,000 counts, respectively, from positions of 0.8, 7.4, and 0.8 cm, respectively. Intensity from the (002) peak for 250 W and 1000 W samples decreases sharply across Region I to a local minimum at 4.2 cm position with values of 1900 and 2200, respectively. For 500 W samples, intensity is 1245 counts at a position of 4.0 cm, and is the only datum point from Region I. For Region II (5.7 to ~8.0 cm), intensities are ~1.5 to 2 times higher relative to the local minimum near 4.0 cm (Region I), with values of 4400, 2200, and 3500 counts for 250 W, 500 W, and 1000 W samples, respectively. Peak intensity decreases across Region II to 3600, 1100, 2300 counts for 250 W, 500 W and 1000 W samples, respectively. There is only one data point each in Region III for 250 W and 1000 W samples, and are 5 and 3 times lower than maximum intensities from Region II, with values of 970 and 1300 counts, respectively. Both data points from Region III for the 500 W case show a steadily decaying intensity, with the lowest being almost an order of magnitude lower than the highest from Region II with a value of 280 counts above baseline.

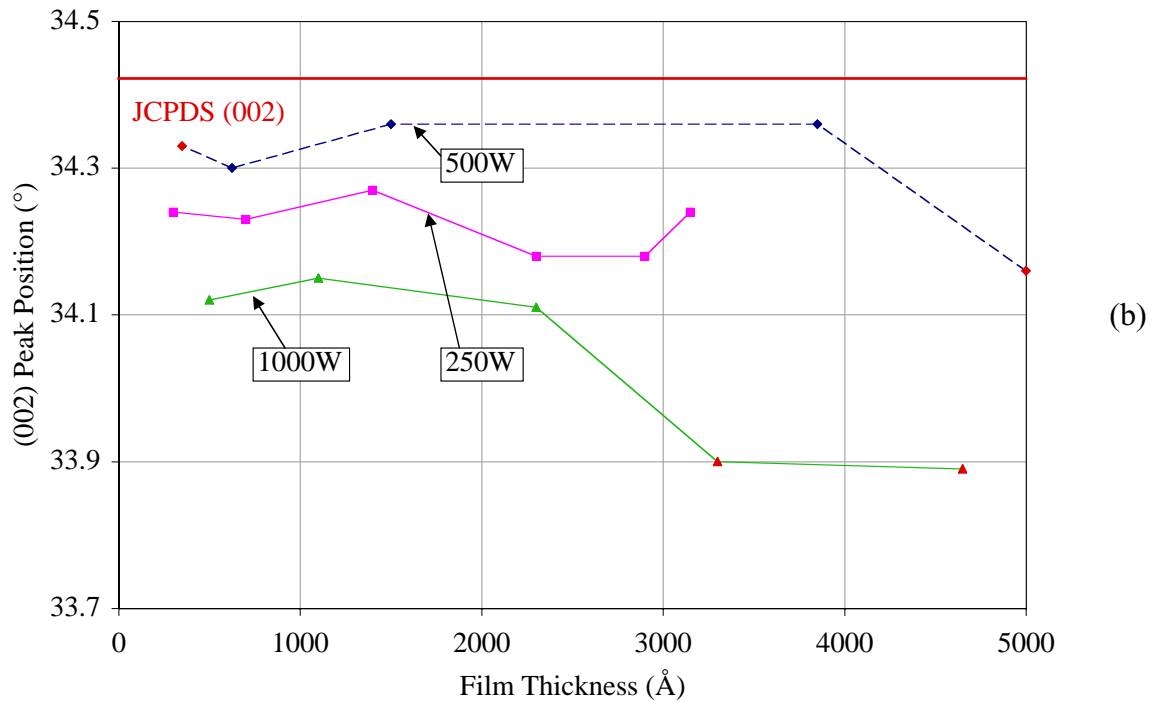
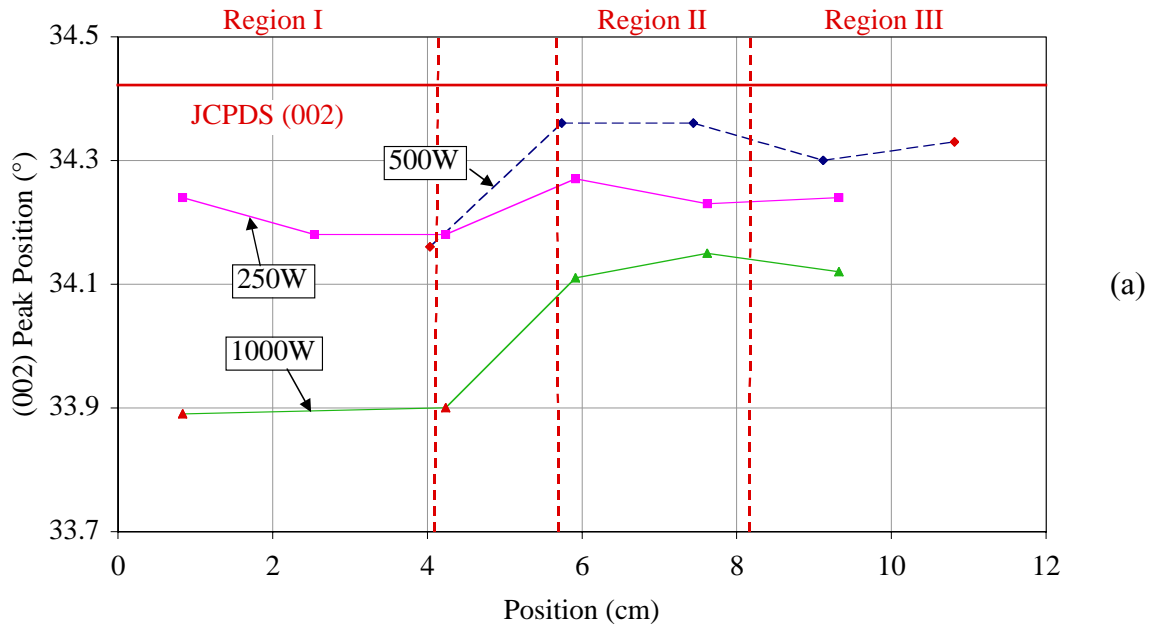


Figures 6-18(a-b). Maximum XRD peak intensity of the (002) peak for ZnO:Al thin films plotted versus (a) position on the substrate and (b) film thickness.

There is a good agreement in trends for the (002) peak intensity and thickness for films thinner than 1000 Å at all RF power conditions. Both the 250 W and 500 W data decrease sharply with similar trends between the thinnest and second thinnest samples, which occurs in the thickness range of ~300Å to 700Å. This trend does not appear in 1000 W data, but there is only the 500Å sample in this thickness range, and therefore trends in this region cannot be determined.

The 2θ angle of the (002) diffraction peak is plotted as a function of position and thickness in Figures 6-19a and 6-19b, respectively. Peak position is quantified by recording 2θ positions for the highest count intensity after subtracting the background, unless otherwise noted. All (002) peak positions are significantly lower than the JCPDS 2θ value of 34.422° . The JCPDS value is indicated with a red horizontal line on plots versus position and film thickness. Peak position from RF powers are offset from each other generally with $2\theta_{1000\text{ W}} < 2\theta_{250\text{ W}} < 2\theta_{500\text{ W}}$. Also, for each RF power the lowest 2θ peak position, which is furthest from the JCPDS value, occurred in Region I. The overall variation of the 250 W data is less than 0.1° , which is significantly less than the variations for the 500 W and 1000 W conditions. This is a small shift, but is discernable in the 250 W line profile spectra shown in Figure 6-11b. The lowest 2θ value of 34.18° translates to a 0.7% increase in d-spacing for the c-axis compared to the JCPDS value.

The 500 W data shows a range of 0.20° , with a lowest value of 34.16° at 4.0 cm, near the edge of Region I. A 2θ value of 34.16° translates to a 0.7% increase in d-spacing for the c-axis compared to the JCPDS value. The 2θ values in Region II increase to 34.36° for positions 5.7 and 7.4 cm. In Region III, the 2θ values decrease slightly to 34.30° at 9.1 cm before coming back up to 34.33° at 10.8 cm. The 1000 W sample also

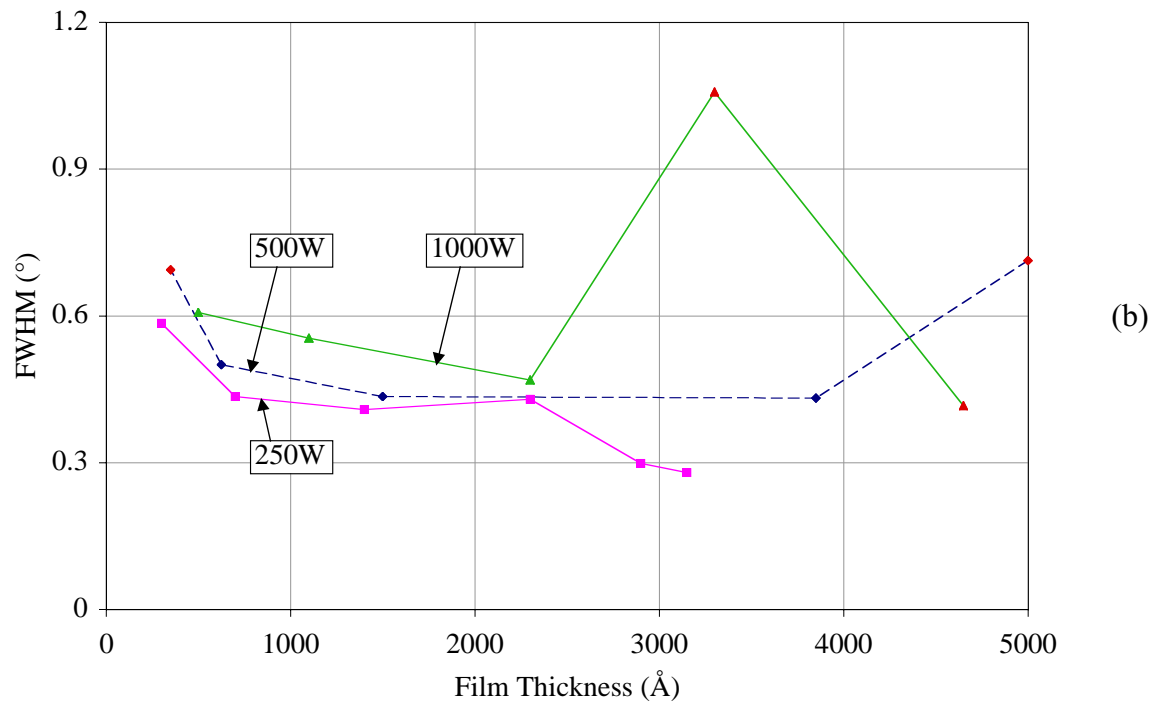
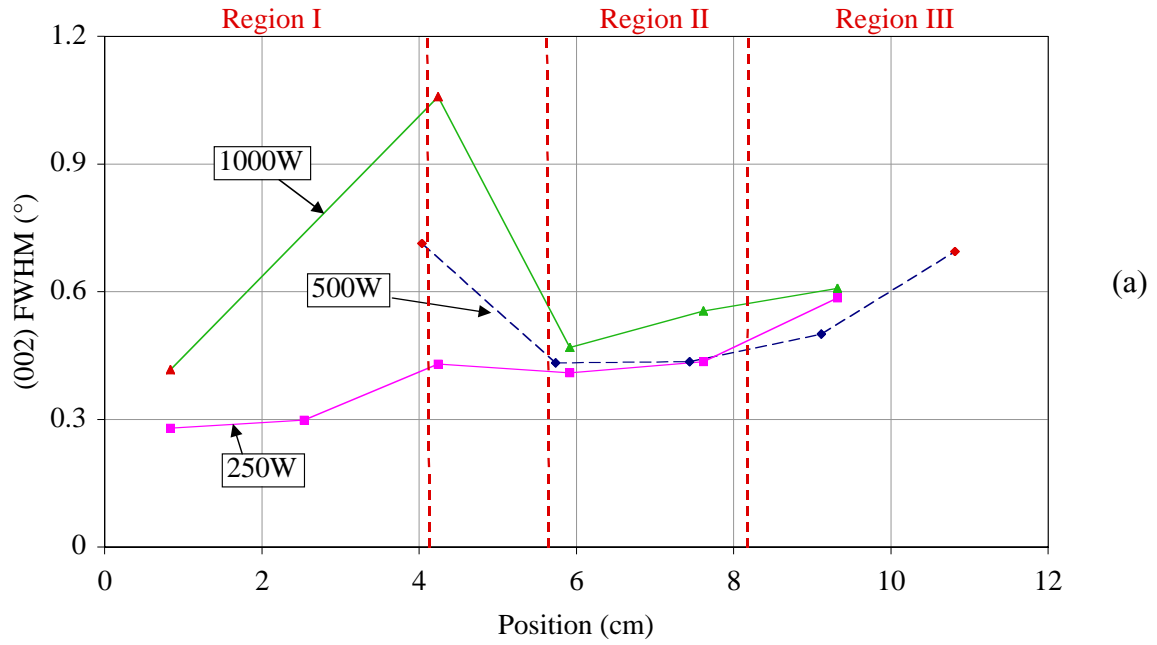


Figures 6-19(a-b). Position of the ZnO:Al (002) peak in 2θ (degrees) plotted versus (a) position on the substrate and (b) film thickness.

has an overall variation of 0.26° , and has similar trends with 500 W data for positions near 4, 6, and 7.5 cm, but 1000 W samples are consistently 0.2° lower in 2θ position. For 1000 W samples in Region I, 2θ values are 33.89° and 33.9° for positions near 1 cm and 4 cm, respectively, which is more than 0.5° lower than the JCPDS value, and represents a 1.5% increase in d-spacing. There is no significant variation between the remaining data points at 5.9, 7.6, and 9.3 cm, with values near 34.12° .

The Full Width at Half Maximum (FWHM) of the (002) peak as a function of position and thickness is presented in Figures 6-20a and 6-20b, respectively. The FWHM for the 500 W case is quantified with *MacDiff* by the finding the difference in 2θ position for the two sides of the peak at half the peak's intensity. All intensities are measured after subtraction of the background. For the 250 W and 1000 W cases, spectra from the samples and data from a quartz standard are input into the *Line Profile Analysis* package, and approximate analysis is performed. The software uses the quartz data to compensate for instrument broadening, and generates a FWHM value. All RF powers have a local maximum in FWHM at the position ~ 4 cm, and increase in FWHM monotonically across Regions II and III. For 250 W samples, the FWHM is smallest at 0.28° for the position 0.8 cm, and increases across Region I to 0.43° at 4.2 cm. The FWHM then decreases a small amount to 0.41° at 5.9 cm, which is the beginning of Region II, and monotonically increases across Regions II and III to the maximum value of 0.59° at 9.2 cm.

The only 500 W datum point in Region I has a large FWHM of 0.71° at a position of 4.0 cm. The data marker for this position is red, and indicates that the tail feature to higher 2θ values is present for the (002) peak from this position. The tail contributes to the large FWHM because the main (002) peak is weak enough the broadening due to the



Figures 6-20(a-b). FWHM of the (002) ZnO:Al XRD peak plotted as a function of (a) position on the substrate and (b) film thickness.

tail feature is included in the measurement. The FWHM decreases sharply to 0.43° at 5.7 cm in Region II, and steadily increases across Regions II and III to 0.69° at a position of 10.8 cm. The data marker at 10.8 cm is red indicating that the quantified peak is very weak, and is therefore fit with an approximated Voight function to improve accuracy mitigate signal to noise errors.

For 1000 W samples, the FWHM increases sharply across Region I from 0.416° to 1.06° for the positions 0.8 and 4.2 cm, respectively, with 1.06° being the highest FWHM measured for that sample. Both data markers for 1000 W samples in Region I are red, indicating the tail feature is present in both. The FWHM at 4.2 cm is much larger because the (002) peak is weaker, and therefore FWHM is measured across the tail feature and it contributes significantly to FWHM. For the sample at 0.8 cm, the (002) peak is of sufficient intensity that the tail does not contribute significantly to FWHM. In a similar trend to 500 W data, 1000 W samples decrease sharply in FWHM between Regions I and II, to 0.469° at 5.9 cm, followed by a steadily increasing with position to 0.607° at 9.3 cm.

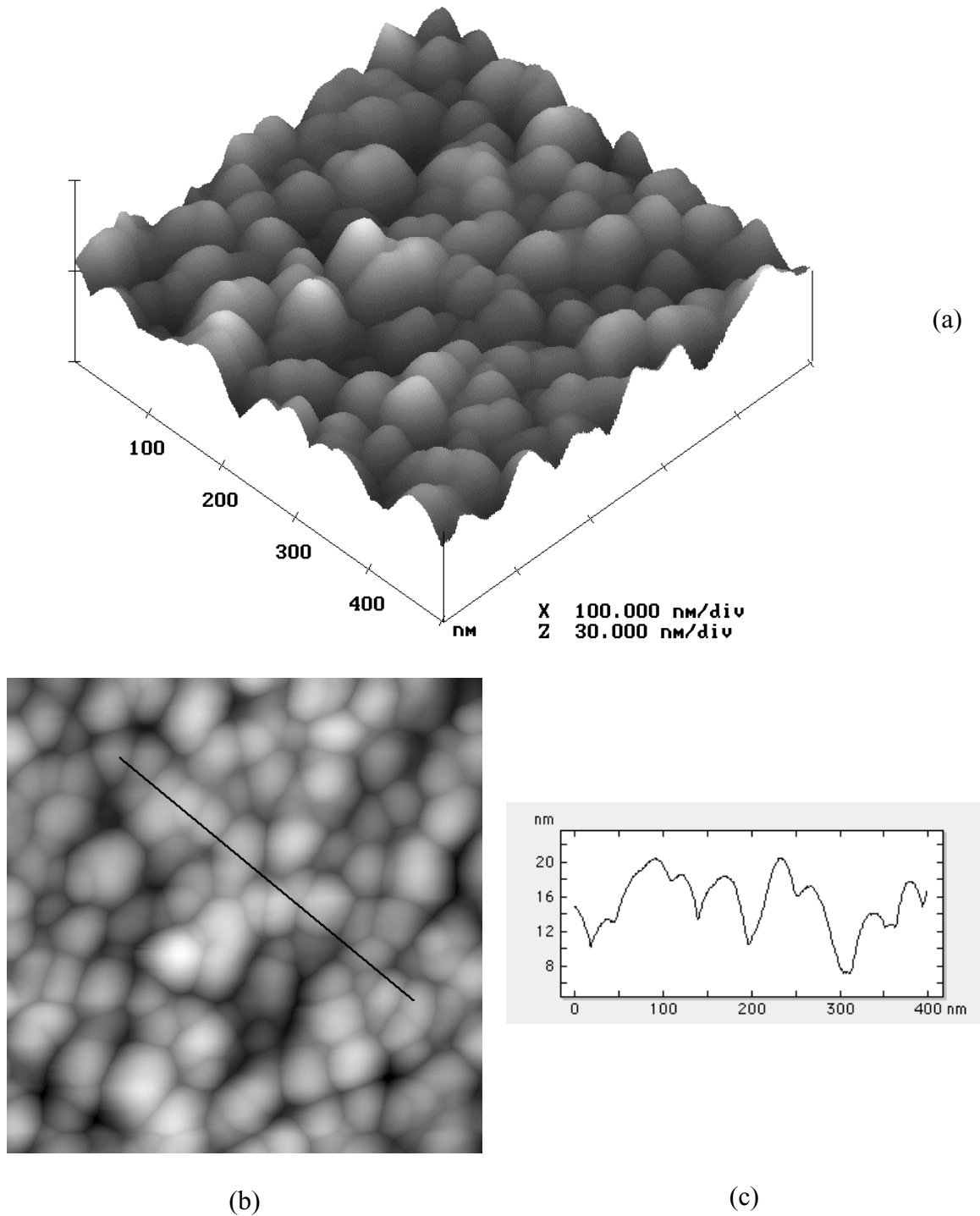
For the FWHM of the (002) peak versus film thickness, there is a large degree of variation in the data as a function of RF power for a film thickness greater than 2500 Å. Thus no correlation between the FWHM and the film thickness is found in this region. For films less than 2000 Å in thickness, which covers Regions II and III, the FWHM shows much less scatter, and below 1500 Å, the FWHM steadily increases with decreasing film thickness for all RF powers. Both the 250 W and 500 W data are relatively constant between 2000 Å and 700 Å, before increasing sharply to the data points for the thinnest films at ~ 300 Å. The 500 W trace in this region is offset slightly

higher in FWHM values. For 1000 W samples less than 2500 Å in thickness, 1000 W FWHM increases nearly linearly with decreasing film thickness.

6.2.4 Atomic Force Microscopy Results

Tapping mode atomic force microscopy (AFM) was used to characterize the surface morphology of the deposited thin films. Measurements are made on a roughly 7 x 7 mm square sample cleaved from the previously characterized XRD specimens. Recall from Chapter 3 that the exact positions for the cleaved samples are not known, therefore the data points are assumed to come from the sample's center. Six samples are measured for each RF power, totaling eighteen samples. A 0.5 x 0.5 µm area is measured on each sample. Generally more than one measurement is made for each sample to ensure that the micrographs are representative of the surface. Using stereological techniques described in the experimental methods (section 3.4.3), sizes of the surface morphological features in the micrograph are interpreted as "grain size". As previously discussed, the "grain size" is really the average size of distinctive granular surface features. This method is illustrated in Figures 6-21(a-c), with the first figure (a) showing a three-dimensional rendering of the sample's surface with shades of gray conveying height information. The second image (b) is a two-dimensional plot of the same information. An analysis line corresponding to 400 nm on the image appears as a black line from the 11 o'clock to 5 o'clock positions on Figure 6-20b. The output of the analysis line is presented in Figure 6-21c as a profile of height information from under the line, and is presented in the inset in the lower left corner of the AFM micrograph.

The "grain size" as a function of position and thickness is presented in Figures 6-22a and 6-22b, respectively. The "grain size" of the samples is larger for Region I where the film is thickest, with maximum grain sizes of 440 Å, 800 Å, and 670 Å for the

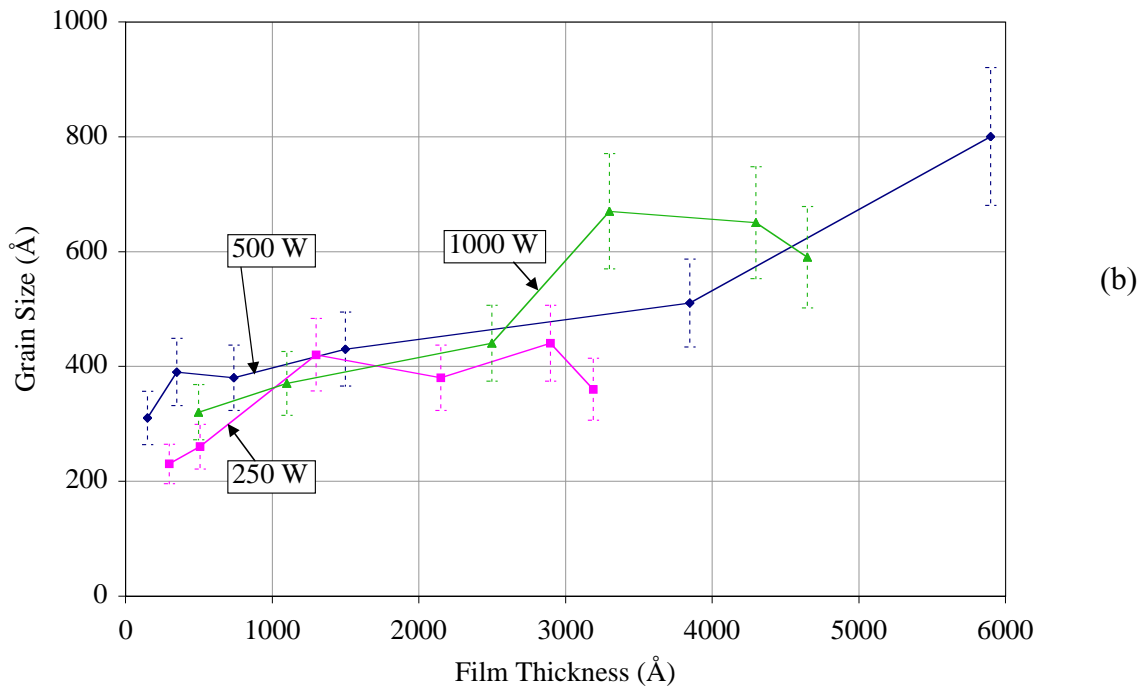
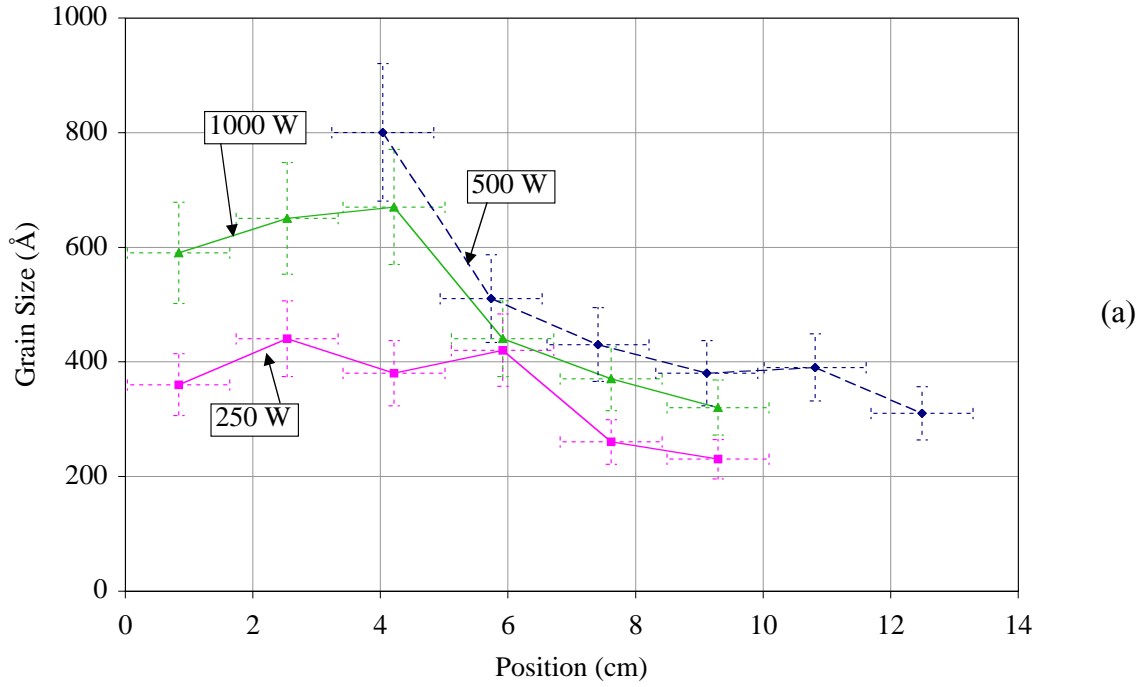


Figures 6-21(a-c). Process used to quantify “grain size” from AFM micrographs with (a) 3-D rendering of the surface morphology, (b) plane view of the surface with the position of a line scan shown a line scan showing the topography of the surface in cross-section, and (c) cross section of the topography from the line scan.

250 W, 500 W, and 1000 W conditions, respectively. Grain sizes are smallest in Region III, where the film thickness is thin, with minimum grain sizes of 230 Å, 310 Å, and 320 Å for the 250 W, 500 W, and 1000 W conditions, respectively. Even with the more than an order of magnitude change in film thickness along the substrate's length, grain size varies by less than a factor four along the same length. Less variation was found with position for each RF power condition, with variations of two times for 250 W and 1000 W conditions, and 2.5 times for 500 W.

For the 250 W sample, grain size fluctuates around a value of $400 \text{ Å} \pm 40 \text{ Å}$ for samples between the positions of 0.8 and 5.9 cm. The final two data points at positions of 7.6 and 9.3 cm show a decrease in grain size to values close to 250 Å. For 500 W samples, the first datum point at a position of 4.0 cm has the largest grain size, which is 800 Å. The value decreases significantly to 500 Å for the next datum point at 5.7 cm, and then trends to smaller sizes with decreasing thickness, reaching a minimum of 310 Å at 12.5 cm. For the 1000 W condition, grain size initially increases for the first three data points from 590 to 680 Å for 0.8 to 4.2 cm. At 5.9 cm, in Region II, the grain size decreases significantly to 450 Å, and continues to decrease in Region III to a value of 320 Å at 9.3 cm.

For the plot of “grain size” versus film thickness, there is a general trend to larger grain sizes with increasing thickness independent of RF power. For films with a thickness less than 1500 Å, the grain size trends to smaller grain sizes for thinner films for the different powers. The traces for the different power conditions are offset, and have different slopes, indicating more than film thickness is influencing “grain size” in Regions II and III.



Figures 6-22(a-b). “Grain size” of the ZnO:Al thin films estimated from AFM micrographs and plotted versus (a) position on the substrate and (b) film thickness.

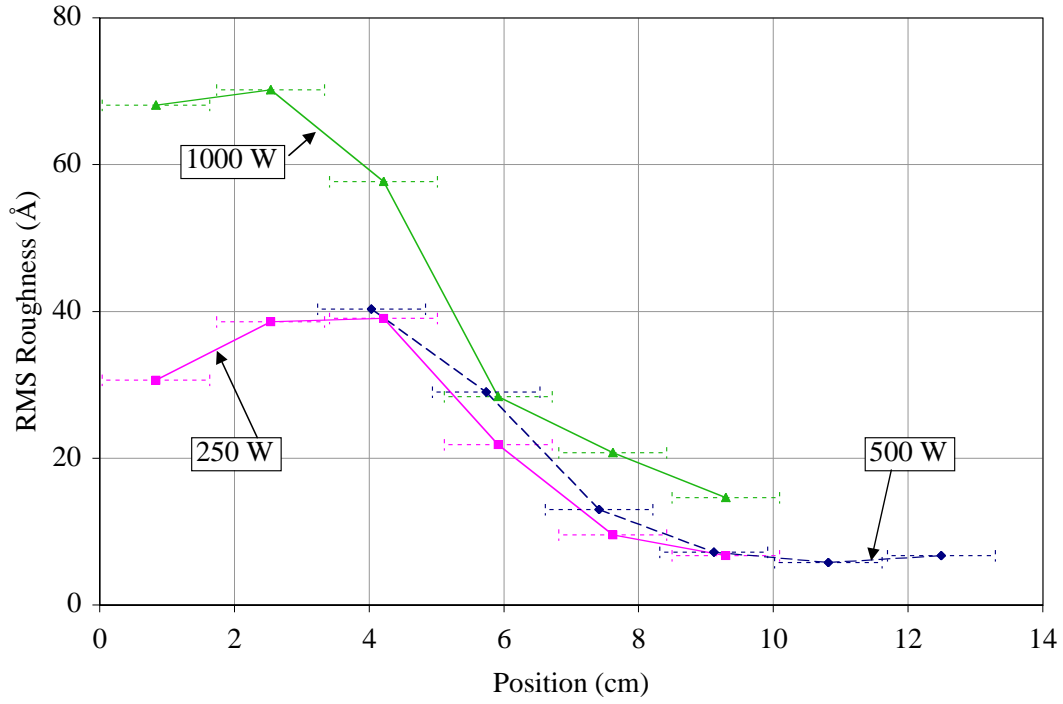
The RMS roughness is plotted as a function of position and film thickness in Figures 6-23a and 6-23b, respectively. The trends in RMS roughness versus position are similar to those of grain size versus position. The RMS roughness varies by more than an order of magnitude, with maximum values of 39 Å, 40 Å, and 70 Å for the 250 W, 500 W, and 1000 W conditions, respectively, all of which occur in Region I. The minimum values occur in Region III, and are 5.8, 6.7, and 14.6 Å for the 250 W, 500 W, and 1000 W conditions, respectively. The RMS roughness measured for a bare glass substrate is 2.0 Å. The RMS roughness decreases monotonically with increasing position across Regions II and III for all RF powers. Roughness for both 250 W and 1000 W samples tend to be constant or increase slightly across Region I (positions less than 4.2 cm).

For the RMS roughness plotted versus the film thickness, no consistent trends for the different power conditions are observed for films thicker than 2000 Å. Below 2000 Å, the RMS roughness monotonically decreases as the thickness decreases for all the power conditions, but the lines are offset and the slopes are different. This indicates that in general the RMS roughness decreases as the films become thinner, but that other factors also influence the roughness in this thickness range.

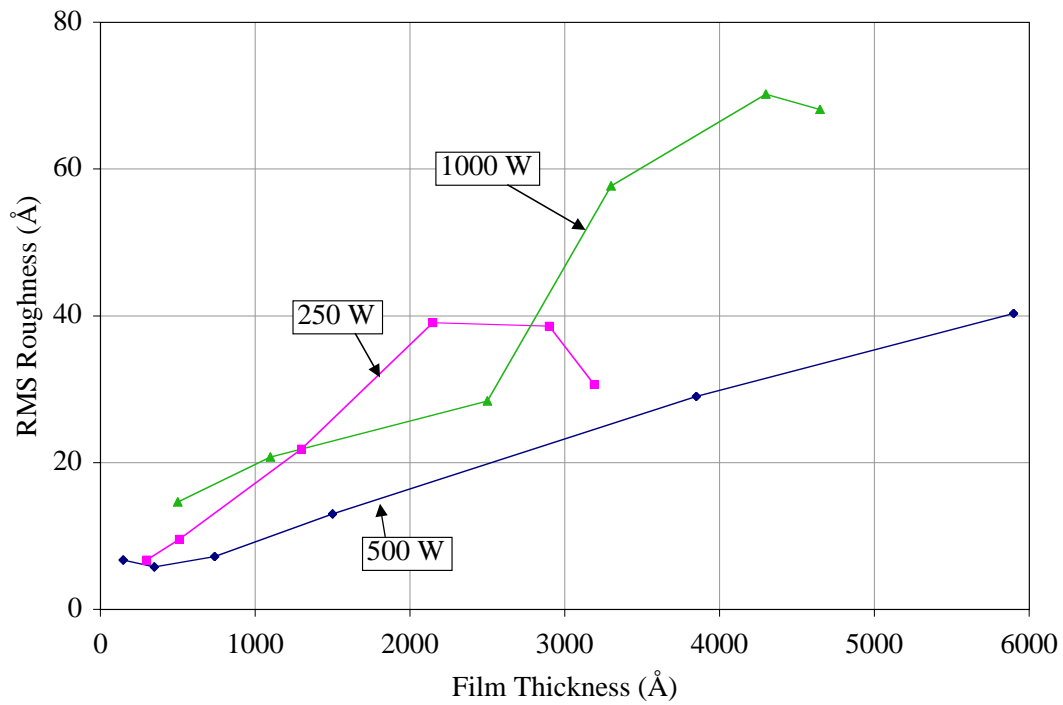
6.3 Discussion of RF Power Experiment

6.3.1 Model of the Effects of Negative Ion Resputtering on Electrical Properties

Discussion of the results is facilitated by first presenting a model proposed to explain them. In this model there are three separate regions at different positions on the substrate. These regions are designated Region I, II, and III, and are equivalent to those used to organize the results. The structure and properties are distinct for each of these regions, and result from differences in the sputtered flux. Therefore, the discussion is



(a)



(b)

Figures 6-23(a-b). RMS roughness of the ZnO:Al thin films measured by AFM as a function of (a) position on the substrate and (b) film thickness.

organized by Region, with experimental results discussed in terms of the proposed model. For these experiments, a position of 0 cm is directly below the source's center, and increasing values indicate increasing distance from this point. The substrate is also positioned such that it is perpendicular to the uniformity shield, as shown in the cross-sectional illustration of the proposed model in Figure 6-1. For 500 W samples, offset data will be used during discussion to maintain this consistent reference to deposition geometry.

Region I occupies areas with a direct vertical line of sight between source and substrate, and is therefore exposed to the negative ion flux, and occurs consistently between position 0 and 4.2 cm for this experiment. A direct vertical line of sight means there are no obstructions between positions on substrate and target along a vertical path. Negative ions are accelerated away from the target with a perpendicular trajectory because the self bias electric field is perpendicular to the cathode. Negative ions are reported to relax to neutrals during transport through the plasma, and therefore impinge on the substrate as energetic neutrals [115]. Though they impinge on the substrate as energetic neutrals, they will continue to be referred to as negative ions to distinguish their source, and avoid confusion with other energetic neutrals that impinge on the target i.e. reflected high energy Ar neutrals. The film's structure and properties in this region are strongly influenced by relationships between negative ion flux and deposited low energy neutral flux [94,101,117].

Ion bombardment during thin film deposition was discussed in Section 2.4.3 of the literature review. Again, though negative ions are neutralized before impinging on the substrate, they will continue to be referred to as negative ions. Two important terms

describing ion bombardment are flux and energy. For negative ions, the flux is equivalent to the negative ion current density (before the ions relax), and energy is kinetic energy of the ion, which is controlled by the target self bias (voltage). Multiplication of the target voltage and ion current density equals power density ($P_d=V \cdot J$). The flux ratio of negative ions to deposited neutrals is reported to critically control the magnitude of the Negative Ion Resputtering effect [117]. Because this ratio is used extensively during the discussion, it will be represented by the term $J(j_i/j_n)$ with j_i representing “negative ion” and j_n representing “deposited neutrals”, and J designates flux from the deposition source. It is assumed for that increasing $J(j_i/j_n)$ will result in increased damage due to ion bombardment.

Changes in ion energy influence results of ion impingement in a complex way, as is covered in the literature review. Ion-surface interactions include reflection, atom displacement, implantation, and resputtering [101], with the magnitude of these processes per incident ion being a function of the ion energy. Reflection of ions is not germane, as this will not affect film properties. Resputtering will decrease deposition rates, and is associated with atomic displacement in the film. Atom displacement at a surface can improve or degrade film properties depending on the property and the energy of ions. Low energy ions are utilized in Ion Beam Assisted Deposition (IBAD) and bias sputtering to improve some film properties. IBAD involves using an ion source, typically with He or Ar, focused on the substrate, and using the ion flux to improve film density or optical properties. Bias sputtering typically involves negatively biasing the substrate such that Ar ion in the plasma are attracted to the substrate [101]. Typically, ion energies between ~10 and 100 eV can improve some film properties, while higher energies

typically degrade film properties. Higher ion energies are reported to result in subsurface atomic displacement often generating Frenkel pair defects [101]. Implantation can also influence the stoichiometry of the deposited material. For example implantation of oxygen could change the stoichiometry of ZnO for areas exposed to oxygen ion bombardment.

It is proposed that negative ion resputtering influences the electrical properties of thin films by two mechanisms for compensation of conduction band carriers. One mechanism is consumption of conduction band electrons by oxygen interstitials [78]. The oxygen interstitial is ionized by trapping a conduction band electron, which maintains charge neutrality. Oxygen interstitials are generated by subsurface damage due to negative oxygen ions impinging on the film. Oxygen interstitials can form by negative oxygen ions being implanted and spontaneously coming to rest in an interstitialcy, or Frenkel pair generation involving knocking oxygen from lattice site to an interstitialcy. It is postulated that oxygen forms Frenkel pairs more commonly than zinc due to more efficient binary collision energy transfer for oxygen because both atoms have the same mass. Bonding in ZnO is between Zn and O, so to a first approximation interstitial formation energy should be similar, but O is smaller, and is therefore anticipated to have a smaller interstitial formation energy. This would help contribute to a higher concentration of oxygen interstitials resulting from Frenkel pairs. It is postulated that the resulting oxygen vacancy is often annihilated due to recombination with an oxygen atom from the growth surface or implantation. It is important to consider if it is reasonable for the large concentrations of oxygen interstitials needed to compensate degenerately doped ZnO:Al to be present. The calculated size of the octahedral interstitialcy suggests that

oxygen can be accommodated. Additionally, one of the proposed models for native defect doping for *n*-type ZnO transparent conductors is zinc interstitials. This supports the case that large interstitial concentration can occur in ZnO. The larger size of the oxygen ion ($O^{2-}=1.32 \text{ \AA}$ and $O^{-1}=1.76 \text{ \AA}$) compared to the zinc ion (0.74 \AA) suggests that more tensile strain in the ZnO matrix might result from oxygen interstitials.

The second mechanism is compensation by deviations in stoichiometry. Incorporation of excess oxygen is accommodated by formation of zinc vacancies. This defect consumes two conduction band electrons normally supplied by an ionized zinc atom to satisfy ionic bonding. The driving force for high oxygen incorporation into the deposited film is the reactive character of energetic negative oxygen ions. Thus films exposed to the negative ion flux grow in the presence of highly reactive energetic atomic oxygen.

There is a transition between Regions I and II, which results from $J(j_i/j_n)$ decreasing and approaching zero across this area. This transition is consistently between positions 4.2 and 5.7 cm on the substrate. Resistivities in this region are between those of Region I and Region II, and improve as Region II is approached because $J(j_i/j_n)$ is decreasing.

Region II occupies areas not in direct vertical line of sight with the target, and therefore receives no negative ion flux. Therefore one boundary is the uniformity shield, which blocks the negative ion flux for areas below it. The boundary between Region II and III occurs at higher position values, and is defined as where resistivity increases roughly by a factor of two over the Region II resistivity. Region II is not exposed to negative ions due to shadowing, but does receive a neutral flux because of the power

cosine distribution for the angular dependence of material ejected from the target [101]. Film properties in this region are independent of RF power, but are influenced by the more traditional process parameters of pressure and substrate temperature. The film properties in Region II are the best achievable with the process conditions used because degradation by negative ion bombardment does not occur. The width of Region II depends on deposition conditions including RF power and deposition time, because Region III is defined in terms of thickness. It occurs for areas where the film thickness is less than 500 Å and that receive no negative ion flux. For example, if film thickness is less than 500 Å for all the areas shadowed from negative ion resputtering, in which case there is no Region II at all.

In Region III, thickness dominates the electrical properties. Deposition of films in Region II and III depend on flux which is not parallel to the targets normal, i.e. flux resulting from a power cosine distribution of ejected material from a sputtering target. The power cosine distribution specifies that flux decreases as the angle relative to the target's normal direction increases [94,99]. Thus, the flux that reaches the substrate is the integrated amount of flux received from all unobstructed points on the target. At larger positions on the substrate, the uniformity shield increasingly obstructs the target, decreasing the flux. At some position, the integrated flux is too low and the film is so thin that it dominates the film's resistivity.

There are three possible mechanisms for increased resistivity with decreasing film thickness in Region III. The agreement between these mechanisms and the data will be discussed in sections 6.3.4.2 to 6.3.4.4 below, which are concerned with the resistivity, carrier concentration, and Hall mobility in Region III. Chemisorption of oxygen species

is proposed to be the dominant mechanism for increased ZnO:Al thin film resistivity with decreasing film thickness. Chemisorbed oxygen species on the free surface and grain boundaries are known to reduce carrier concentration in ZnO film solid state gas sensors [9], and are therefore proposed to cause the decreasing carrier concentration, which is the dominant source of the increased resistivity in Region III. This mechanism was previously proposed to explain the decreasing carrier concentration with decreasing film thickness found in data presented in section 5.3.2. Another possible mechanism for the increased resistivity is based on the Fuchs and Sondheimer model, which applies to very thin metallic films [133,134]. The Fuchs and Sondheimer model was also presented in Chapter 5, and postulates that as thickness decreases, interfacial scattering may reduce the electron carrier's mean free path, which reduces carrier mobility and increases resistivity. A decrease in Hall mobility is observed (Figure 6-10), but only by a factor of ~2. Instead, the carrier concentration is strongly reduced by up to an order of magnitude in Region III compared to Region II, which suggests interface scattering is not the dominant mechanism for increasing resistivity. A third mechanism to explain Region III resistivity data is an increased concentration of interface states, which is predominantly a function of grain size until film thickness approaches the grain size. Interface states act as electron carrier traps, and therefore decrease carrier concentration [87]. When this occurs, grain size in the vertical dimension will be constrained by film thickness. As the film becomes thinner, vertical grain size will decrease, and the free concentration of interface states will increase, decreasing the carrier concentration.

Turning attention to the RF power used to deposit the films, this varied parameter is important in this model by its influence on the magnitude of the negative ion

resputtering. Its primary influence is on the self bias of the target, which increases with RF power. A higher target potential will increase the energy of negative ions, which affects negative ion resputtering in ways previously discussed. The factor $J(j_i/j_n)$, which cannot be measured or derived easily, is assumed to depend only weakly on the RF power used to deposit the film.

6.3.2 Region I

In Region I, the model predicts that substrate is in direct line of sight with the target, and therefore receives a strong negative ion and deposited neutral flux.

Investigation of negative ion resputtering involves comparing differences between areas which are and are not resputtered, and differences between positions where $J(j_i/j_n)$ changes. Comparison between Regions I and II corresponds to the negative ion flux versus no negative ion flux comparison. Comparisons within Region I and for the transition between Regions I and II correspond to comparisons for changing negative ion flux, which affects the flux ratio of negative ions to deposited neutrals ($J(j_i/j_n)$).

6.3.2.1 Profilometry (Region I)

Deposition rate (Figure 6-3), and therefore film thickness (Figure 6-2) versus position on the substrate are predicted to depend on the target edge effects, and amount of negative ion resputtering, and RF power used to deposit the film for Region I. The deposition rate decreases between positions 0.6 and 4.2 cm by 30% and 35% for 250 W and 1000 W data, respectively. The smoothly decreasing deposition rate is consistent with target edge effects, or the decreasing deposition rate as the edge of the RF diode sputtering source is approached [117], with the target's edge effectively defined by the uniformity shield. Negligible sputtered flux is generated for areas of the target under the

electrically grounded uniformity shield, as the shield interrupts the plasma in this region, and obstructs the negative ion flux from reaching the substrate.

The relative effect of negative ion resputtering versus the sputter deposition rate depends on $J(j_i/j_n)$. To investigate the influence of negative ion resputtering on deposition rate, comparisons between areas that do and do not receive negative ion flux must be made. Deposition rate decreases smoothly with increasing position across Regions I and II for all RF powers. This suggests that growth rate in Region I is not dominated by negative ion resputtering effects. As discussed in Chapter 2, a strong negative ion resputtering effect can result in dramatically decreased growth rates, and possible even etching of the substrate.

The ratio of the deposition rate between 250 W and 1000 W samples, and 500 W and 1000 W samples as a function of position is presented in Figure 6-5. For 250 W data, the ratio is consistently near 22% in Region I, which agrees with the ratio of RF powers (25%) between the two conditions. For 500 W data, the two data point in Region I are consistently 57%, which is a small degree above the ratio of RF powers between the two conditions (50%). The 500 W/1000 W ratio data is expected to have poor accuracy resulting from two sources of error, the first of which is small inaccuracies in the positional offset applied to the 500 W data. A small inaccuracy in position offset can have a significant effect on the relative deposition rate data because of steep slopes of the deposition rate data versus position. The second source of error also results from the offset position, and results from misalignment of the positions for data points. Therefore linear interpolation between the data points was required to get 500 W and 1000 W deposition rate data for the same positions. These sources of error occur for all Regions.

The molecular deposited flux was calculated from deposition rate data and plotted in Figure 6-4. The molecular flux decreases with increasing position, with a trend similar to half of a bell-curve. Values of the molecular flux are taken to be approximately equal to the deposited neutral flux (j_n). The ratio of the negative ion to deposited neutral flux is an important factor in controlling the magnitude of the NIR effect on materials properties, and it is therefore useful to estimate the negative ion flux. The estimation is based on changes in the carrier concentration because it will be shown below to be sensitive to NIR. In Region I, the carrier concentration is decreased by as much as 90% compared to Region II. If the entire decrease in carrier concentration is attributed to NIR, and it is assumed that one negative ion generates an average of one compensating state, then the negative ion flux must be such that it can generate $\sim 5 \times 10^{20} \text{ cm}^{-3}$. The negative ion flux calculated based on $\sim 5 \times 10^{20} \text{ cm}^{-3}$ compensating states indicates that $J(j_i/j_n)$ is approximately 0.01 or 1%. The low negative ion flux is consistent with the lack of sharp changes in deposition rate between Region I and II, as a large negative ion flux causes decreased deposition rates for areas subjected to NIR. The value of one compensating state per incident negative oxygen ion is reasonable considering the sputter yields for oxygen are typically on the order of one atom sputtered per incident oxygen. For higher negative ion kinetic energies, some ions will be implanted. The impinging ion can generate compensating states through an initiation of a collision cascade in the deposited film, when the ion comes to rest on an interstitial site, and when a zinc vacancy is generated. It is therefore reasonable that each implanted ion generates on average of one compensating state.

6.3.2.2 Resistivity effects (Region I)

For 250 W samples in Region I, curvature is found with resistivities ranges from 3.3×10^{-3} to $7.0 \times 10^{-3} \Omega \cdot \text{cm}$ between 0.6 and 4.5 cm, respectively, as seen in Figure 6-7. Thus, the resistivity is slowly increasing with distance from the source's center. The increase in resistivity results from an increase in negative ion resputtering. More resputtering results from a larger $J(j_i/j_n)$ as positions approach the uniformity shield's edge (which effectively defines the edge of the deposition source). For higher positions in Region I, $J(j_i/j_n)$ decreases, i.e. the flux of deposited material decreases as the edge of the target is approached, while the negative ion flux remains constant for all areas exposed by a direct line of sight to RF diode source. Negative ion flux remains constant because it has a narrow distribution of departure angles centered on the targets normal axis. The changes in flux rates with position are schematically illustrated in Figure 6-1. Resistivities of 250 W samples are always lower than 1000 W samples in this region, and from the plot of resistivity versus film thickness in Figure 6-8, there is no correlation between resistivity for different RF powers with film thickness. More RF power correlates with increased resistivity. XRD evidence discussed below suggests increasing resistivity with RF power results from differences in the target's negative bias which increases from -300 V to -1000 V with increasing RF power from 250 W to 1000 W, respectively. Negative ion energy increases with target bias, while the generation rate of negative ions per Ar^+ incident on the target is not expected to change significantly across this range of target potentials. Lower negative ion kinetic energy will result in less resputtering and damage for the film. Thus, lower resistivities for 250 W versus 1000 W samples is consistent with a decrease in negative ion kinetic energy.

For 1000 W samples, resistivity is consistently $1.25 \times 10^{-2} \Omega \cdot \text{cm}$ for positions between 0.6 and 4.5 cm, as seen in Figure 6-7. The value of $J(j_i/j_n)$ is expected to vary with position in the same manner as 250 W samples. The lack of variation is attributed to a saturation of the effects of damage on resistivity, whereby increasing $J(j_i/j_n)$ has little influence on resistivity. A possible mechanism for higher RF powers is that the target bias is increased, yielding a larger fraction of implanted oxygen and more Frenkel pairs of oxygen on a lattice and interstitial sites due to ion bombardment. This effectively drives stoichiometry to oxygen rich. The sticking coefficient for normal oxygen decreases with excess oxygen, which moderates film composition. In turn film composition is critically important to doping due to intrinsic doping and compensation mechanisms.

For 500 W samples, there are only two data points in Region I. Resistivities at these points were 2.5×10^{-2} and $1.1 \times 10^{-2} \Omega \cdot \text{cm}$ for 3.8 and 4.5 cm, respectively, with the former being a small degree higher than 1000 W samples. Again, changes in resistivity with RF power are attributed to variation in negative ion energy due to target self bias. Negative ion energy is not expected to influence electrical properties linearly because the energy influences relative quantities of all four primary ion-surface interactions. It is speculated that for 500 W, which has a target bias of ~ 500 V will result in less implantation of O, but more damage to the growth surface.

The sharp decrease in resistivity for the transition between Regions I and II occurs at the same position for all three RF powers, with the decrease occurring between 4.2 and 5.7 cm. Some variation in slope occurs due to differences in resistivity on the Region I side. This strong drop in resistivity to the Region II minima of $1.5 \times 10^{-3} \Omega \cdot \text{cm}$ results

from a large decrease in $J(j_i/j_n)$. Both fluxes are decreasing due to shadowing from the uniformity shield, but narrow angular distribution for negative ions causes this flux to decrease more rapidly than the deposited neutral flux. This region is roughly 1.2 cm in width, and is at a distance of 9 cm from the target, suggesting the negative ion flux has an angular distribution confined to less than 10° off perpendicular.

6.3.2.3 Hall carrier concentration (Region I)

For all three Regions, Hall data are presented with 0.8 cm errors bars to indicate the uncertainty of the position where the samples are cleaved. To help mitigate this positional uncertainty, Hall resistivity is brought into agreement with four point resistivity by adjusting the film thickness and position. Four point probe and profilometry data are taken within 1 mm of the marked positions, and therefore have high positional accuracy. Resistivities derived by the Hall systems software depends on the film thickness entered into the software. If the actual film is thicker than the value entered, then the actual resistivity is higher and carrier concentration is lower than the values derived by the computer, and visa versa if the actual film thickness is thinner than the entered value. Calculation of Hall mobility derived by the van der Pauw method [121] does not depend on the film thickness, and therefore adjusting the film thickness does not influence Hall mobility. Film thickness is a function of position, and therefore as the film thickness for the Hall sample is adjusted, the position of the sample must be adjusted to maintain consistency with the thickness to position relationship. The thickness adjustments made are within the range of thicknesses defined by the positional uncertainty. This procedure is only done for samples with more than a 20% deviation between the Hall and four point probe resistivities. The improved relationship between Hall and four point probe resistivity can be appreciated in the plot shown in Figure 6-24.

This is a plot of resistivity as a function of position, and shows that good correlation can be achieved by adjusting the film thickness and position within their known boundaries. Data points that have changed are shown in orange. Corrected carrier concentrations are plotted as a function of both position and thickness in Figures 6-25a and 6-25b. The discussion of Hall data will be based on plots from corrected data.

In Region I all samples have lower carrier concentrations than in Region II. The carrier concentration for 250 W samples varies in Region I, and the variations are consistent with the previously described changes in resistivity. Resistivity increases and carrier concentration decreases by factors of 2.1 and 1.9 for 250 W samples across Region I, respectively. This indicates carrier concentration is responsible for most if not all of the changes in resistivity. Variations in carrier concentration are postulated to

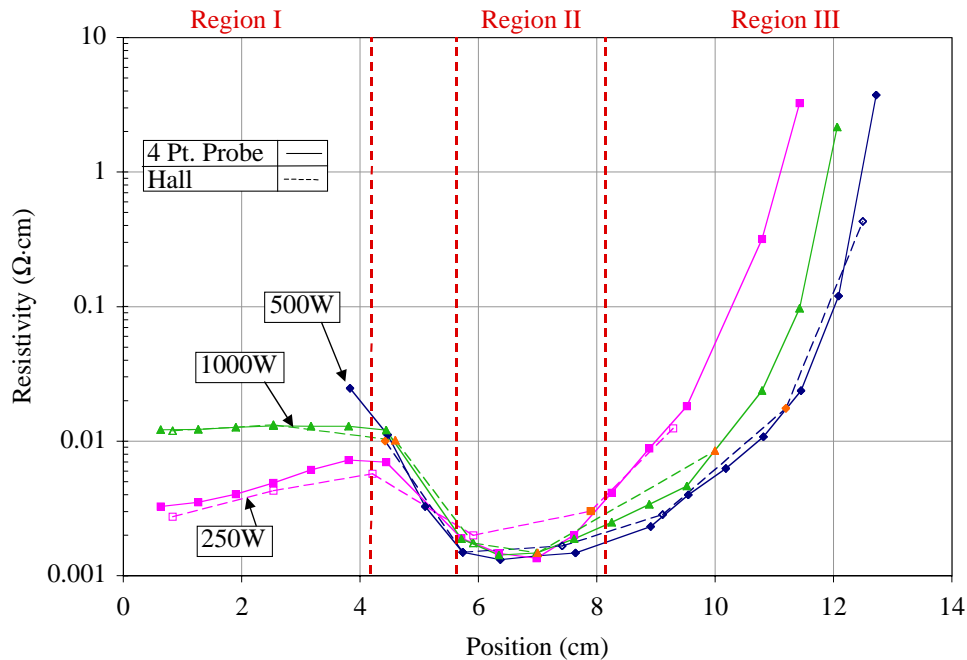
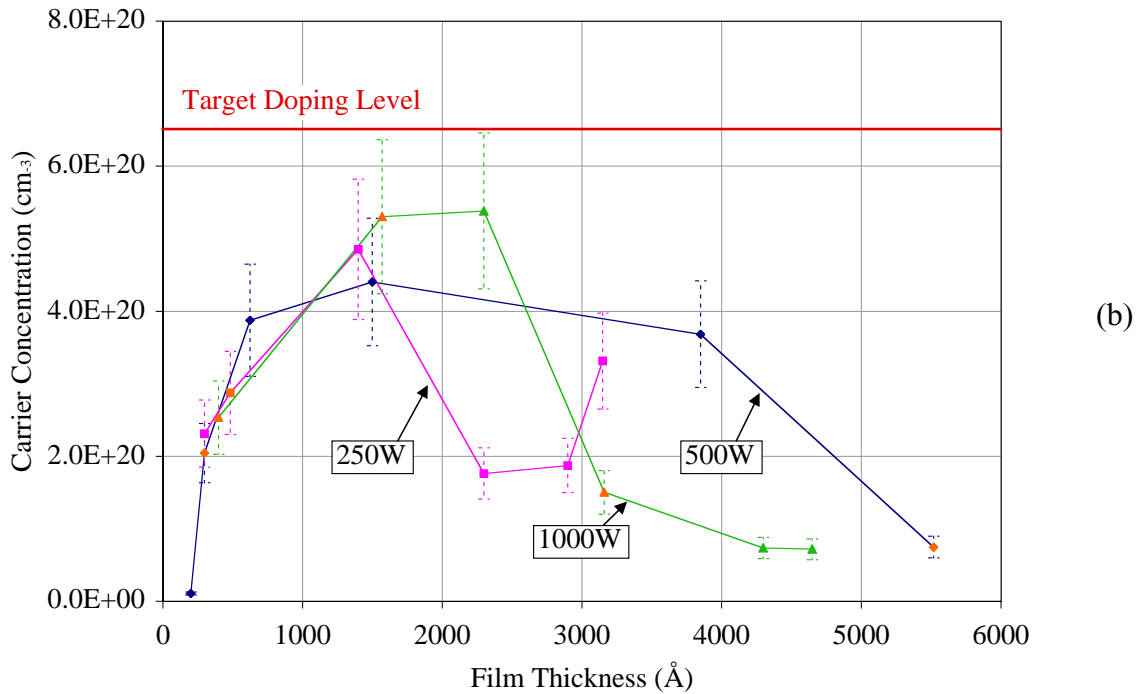
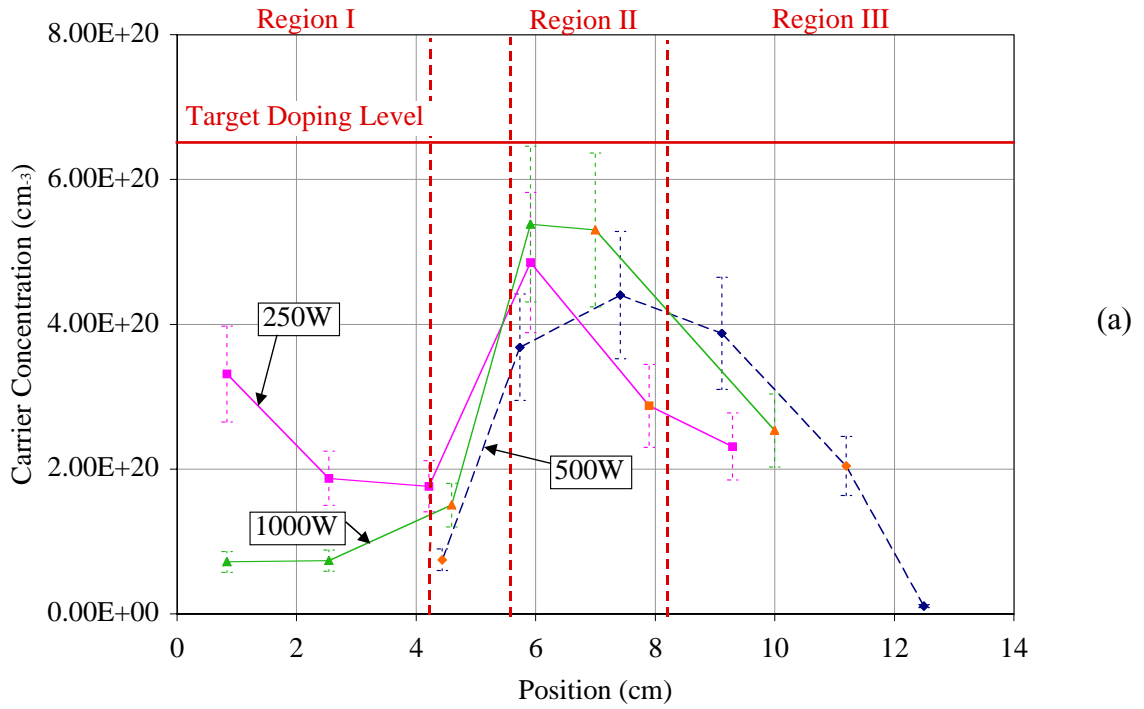


Figure 6-24. Resistivity of the ZnO:Al thin film with the Hall resistivity (dashed) corrected to agree with the four point probe resistivity (solid) versus position.



Figures 6-25(a-b). Corrected carrier concentration from Hall measurements for ZnO:Al thin films as a function of (a) position on the substrate and (b) film thickness.

result from changes in $J(j_i/j_n)$ as a function of position, with variations in $J(j_i/j_n)$ resulting from the same mechanisms presented during discussion of resistivity for this sample (Figure 6-1). Without changes in mobility, it is clear that negative ion resputtering influences resistivity by changes in carrier concentration. This is consistent with the postulate in the model that negative ion resputtering causes compensation of electron carriers by increasing interstitial oxygen concentration and/or higher than stoichiometric oxygen incorporation resulting in zinc vacancies.

There is only one 500 W datum point in Region I for carrier concentration, which is at 4.0 cm with a value of $7.5 \times 10^{19} \text{ cm}^{-3}$. Note that from quantified XRD data, this point is labeled with a red marker to indicate a significant tail to higher 2θ values for the (002) peak. The 500 W sample is ~ 2.4 times lower in carrier concentration than the 250 W sample for the same position, while the 500 W sample is ~ 1.8 times higher in resistivity than the 250 W sample. This is consistent with decreased carrier concentration by increased damage from negative ion resputtering. Data from SIMS measurements discussed below indicates that the changes in carrier concentration do not result from changes in the Al dopant concentration or compensation by alkali metals, which is consistent with the proposed native defect mechanisms.

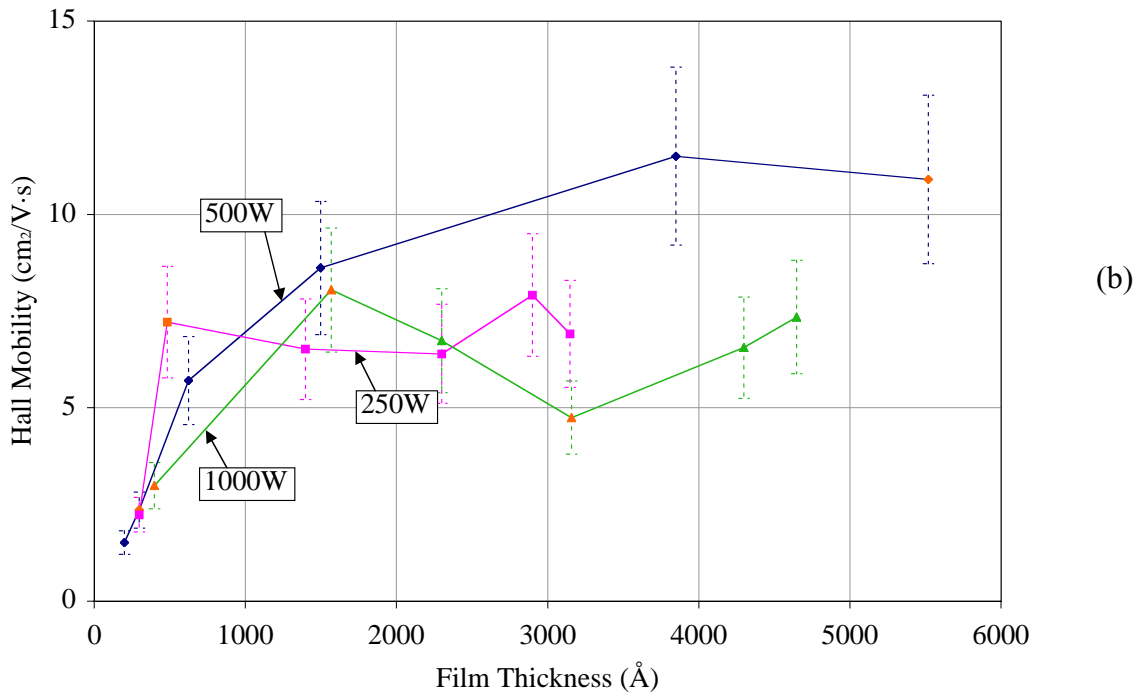
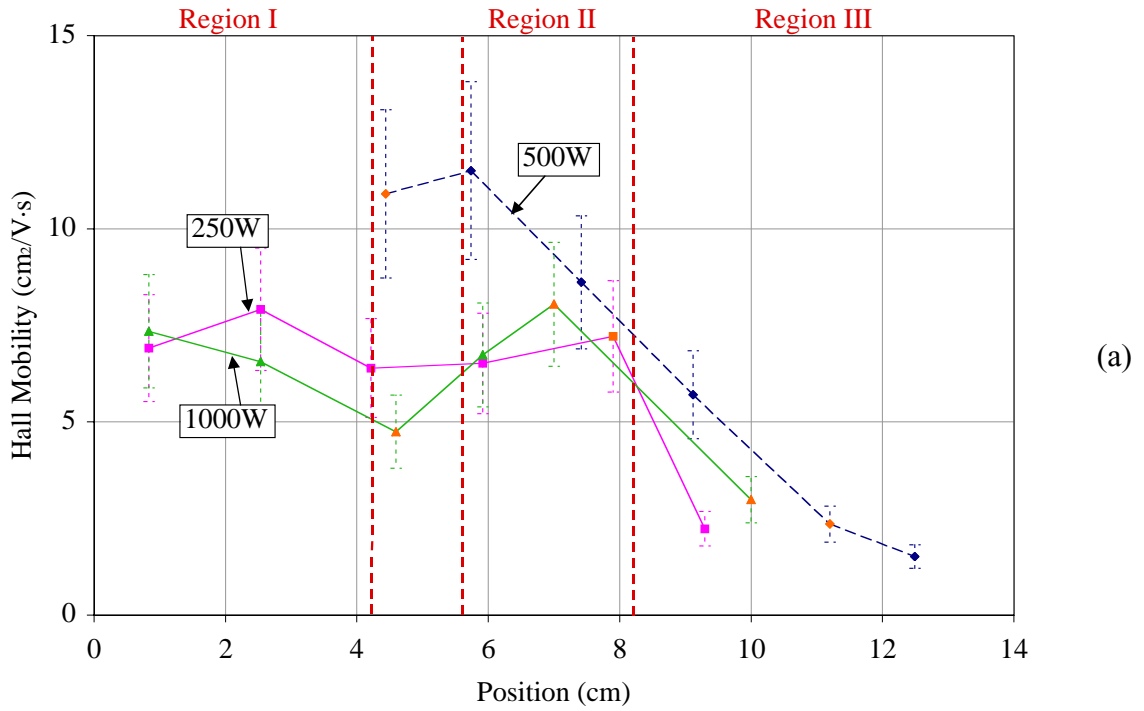
For 1000 W samples, red markers are also used in XRD data for the two positions (0.8 and 4.2 cm) from Region I. As a reminder, no data were collected for the position of 2.5 cm because the sample was inadvertently broken before XRD could be collected. Carrier concentrations for these positions have very low carrier concentrations with values of 7.1×10^{19} , 7.3×10^{19} , and $1.5 \times 10^{20} \text{ cm}^{-3}$ for positions 0.8, 2.5, and 4.6 cm, respectively. Increased carrier concentration for position 4.6 cm suggests this sample is

in the transition between Regions I and II, and therefore is partially shadowed from negative ions, which decreases $J(j_i/j_n)$. Lack of variation in carrier concentration is consistent with the lack of variation in resistivity found for 1000 W samples in Region I. Thus, for 500 W and 1000 W samples, Region I has low carrier concentration consistently near $7.4 \times 10^{19} \text{ cm}^{-3}$. The constant low carrier concentrations and lack of variation in electrical properties for 1000 W samples in Region I despite expected changes in $J(j_i/j_n)$ versus power or position are consistent with saturation. The saturation effect was postulated to explain the constant resistivities in Region I for 1000 W samples. The sources and implications of the XRD tail and its relationship to low carrier concentrations will be discussed further below.

For the transition between Regions I and II, resistivity decreases sharply from 4.2 and 5.7 cm for all three RF powers, and correlates well with a strong increase in carrier concentration. Between Region I and II, resistivities decrease by factors of 2.9, 6.0, and 7.6 for 250 W, 500 W, and 1000 W samples, respectively. Carrier concentrations increase by factors of 2.8, 4.5, and 7.3, respectively, indicating changes in carrier concentration are responsible for approximately 100%, 75%, and 95% of decrease in resistivity between Regions I and II. These data are consistent with the postulated relationship between negative ion resputtering and carrier concentration.

6.3.2.4 Hall mobility (Region I)

Corrected Hall mobility data are replotted in Figures 6-26(a-b) as functions of position and thickness, respectively. As previously described, it is the position and thickness that changes with the correction, not Hall mobility values. Within each RF power for Region I little variation in Hall mobility is found, which is consistent with small variations in resistivity and carrier concentration. Hall mobility for 250 W samples



Figures 6-26(a-b). Corrected Hall mobility for ZnO:Al thin films as a function of (a) position on the substrate and (b) film thickness.

is within $\pm 1 \text{ cm}^2/\text{V}\cdot\text{s}$ of the average value $7.1 \text{ cm}^2/\text{V}\cdot\text{s}$, which is less than experimental error. For 1000 W samples, the average Hall mobility is Region I is $7 \text{ cm}^2/\text{V}\cdot\text{s}$, and there is no significant variations outside of experimental error. For samples deposited at 500 W there only datum point from Region I (with a position of 4.4 cm) and has a mobility of $11 \text{ cm}^2/\text{V}\cdot\text{s}$, which is substantially higher than for 250 W and 1000 W samples. Low carrier concentration for this sample suggests that it is more compensated by oxygen interstitials and/or zinc vacancies than the 250 W sample. The higher concentration of point defects in the 500 W sample should decrease carrier concentration if point defects are dominating carrier mobility. This suggests there is another unknown parameter influencing mobility.

There is not sufficient data from the transition between Regions I and II to evaluate trends in Hall mobility. For 250 W and 500 W data, no changes outside experimental error occur between 4 cm (Region I) and 6 cm (Region II). For 1000 W samples, the mobility increase by a factor of 1.4 from Region I to II, but this is small compared to the change in resistivity and carrier concentration. In terms of the model, carrier concentration and resistivity have changed significantly between Regions I and II due to changes in negative ion flux reaching the substrate, while little or no change occurs in Hall mobility. This supports the postulate that negative ion resputtering primarily affects carrier concentration. The lack of influence from the proposed changes in point defect concentrations between Regions I and II on the mobility suggests another scattering mechanism is dominating the mobility.

Ionized impurity scattering is often reported in the literature as the dominant scattering mechanism in degenerately doped ZnO:Al thin films [60,89], but other reports

refute this claim [96]. In this study, large changes in carrier concentration occur between Regions I and II, with no correlation to changes in mobility. This suggests that ionized impurity scattering is not the dominant scattering mechanism limiting mobility. As reported above and discussed below, XRD and AFM data varies significantly across Region I and II, yet Hall mobility shows little change. This suggests that some factors not being detected or measured precisely by XRD or AFM are influencing the mobility. Point defects and line defects are not detected by these structural characterization techniques, but can affect scattering. Because point defects are known to be very important to electrical properties [85,89,139], it seems likely that they are controlling the mobility. Also, as will be shown below, carrier mean free path is calculated to be $\sim 5 \text{ \AA}$, a dimension similar to unit cell size. The calculated carrier mean free path seems unrealistically short, but is in agreement with reported values [82]. Point defects or a combination of point defects and other defect scattering mechanisms are only scattering mechanisms that might be possible in the concentrations indicated by the small carrier mean free path.

6.3.2.5 Secondary ion mass spectrometry

The SIMS data are used to evaluate changes in Al and Na concentrations in the film. Aluminum is the extrinsic dopant, and alkali metals can compensate electron carriers, therefore changes in the concentrations of these elements are potentially responsible for the changes in carrier concentration that are found between Regions I and II. From the plots of the Al to Zn ratio, it is clear that the concentration of Al does not change for the 250 W case, and is slightly higher in Region I compared to Region II for the 500 W and 1000 W cases. This suggests that there is actually a small increase in the dopant concentration in Region I, which is where the carrier concentration is drastically

lower relative to Region II. Thus, the changes in Al dopant concentration do not agree with changes in the carrier concentration, which suggests that decreased Al concentration is not responsible for lower carrier concentration in Region I.

The ratio of Na to Zn makes only small changes between Regions I and II, with a slightly lower ratio of Na in Region I being typical. This reveals that the concentration of Na is lower in Region I compared to Region II. Because Na acts to compensate electron carriers, the trend in Na concentration is opposite of what would cause lower carrier concentrations in Region I compared to Region II. Additionally, the Na to Zn ratio was found to be at most one order of magnitude larger than the Al to Zn ratio. Recall that the sensitivity of SIMS to Na is anticipated to be several orders of magnitude larger than for Al, which suggests that the Na concentration is not large enough to cause the up to 90% lower carrier concentration in Region I compared to Region II.

The SIMS data indicates that the two most likely extrinsic sources for decreased carrier concentration, which include loss of the Al dopant due to preferential resputtering and incorporation of Na from the soda-lime glass substrate, are not occurring in the deposited films. The lack of extrinsic causes for the change in carrier concentration suggests that an intrinsic mechanism involving native defects is responsible. This is consistent with the mechanism for compensation proposed in the model which involves formation of oxygen interstitials and/or zinc vacancies due to bombardment by negative ions.

6.3.2.6 X-ray photoelectron spectroscopy

Data from XPS measurements are used to evaluate composition and atomic bonding for the surface of the deposited ZnO:Al thin films. Only Zn, O, and C characteristic peaks are found for the as deposited state suggesting that carbon is the only

contaminant. A carbon peak is no longer detected after sputter etching for 6 minutes, indicating that carbon is a surface contaminant, which is consistent with adventitious carbon from the atmosphere.

Atomic concentrations of elements at the surface and shifts in peak energy associated with chemical bonding are evaluated using higher resolution multiplex data. The qualitative atomic concentration data presented in Table 6-1 indicate that the as deposited film's surface is 34% C, 53% O, and only 13% Zn. The much higher concentration of O compared to Zn indicates oxygen is present on the surface significantly in excess stoichiometry. After sputter etching for 6 minutes, the concentration of Zn has increased to 45%, while the oxygen and carbon concentrations decreased to 48% and 7%, respectively. The Zn and O concentrations are within experimental error of being stoichiometric, which indicates that the excess oxygen is also a surface feature.

A significant change in peak shape and area occur between as deposited and sputter etched spectra. A well-defined double peak is observed in the oxygen multiplex data (Figure 6-14a), with a higher binding energy (532.2 eV) and a lower binding energy (530.7 eV) peak. The high and low energy peaks account for 67% and 33% of the peak area, respectively. After sputter etching for six minutes, the areas of the high and low energy peaks change markedly, and comprise 7% and 93% of the peak area, respectively. The [140] and reports in the literature suggest that the chemically shifted higher energy (532.2 eV) peak is consistent with a surface oxide species. The chemical shift cannot explicitly identify if the surface species is oxygen, hydroxide, or a combination of both. These results are consistent with chemisorbed oxygen, and therefore offer physical

evidence which supports the hypothesis that chemisorbed oxygen is the source for compensation of electron carriers for the less than 500 Å films in Region III.

6.3.2.7 X-ray diffraction (Region I)

Quantification of XRD results focused on peak intensity (counts), 2θ peak position (degrees), and full width half maximum (FWHM) (degrees). Diffracted intensity is a function of the fraction of sampled volume that satisfies the Bragg condition for a given 2θ angle. All films are thinner than the X-ray beam's sampling depth ($\sim 5 \mu\text{m}$), therefore intensity is expected to be a function film thickness, with thinner films yielding less intensity at the peak maximum if all else is equal [110]. The 2θ peak positions depend on lattice d-spacings between crystal planes. This is not expected to be a function of thickness, but is sensitive to shifts in d-spacing resulting from out-of-plane strain [110]. The FWHM characterizes the diffracted peak's breadth. The breadth is influenced by instrument broadening, which is assumed to be constant. Breadth can also be increased by variations in d-spacings, and changes in domain size over which coherent scattering occurs. Larger domain or crystallite sizes result in larger volumes of coherent scattering, which results in a smaller FWHM. As domain size decreases, FWHM increases. Thus, because the vertical domain size in very thin films becomes dependent on the film thickness, the FWHM is expected to increase as the film thickness decreases. Thus, both film thickness and crystal quality must be considered during interpretation of XRD [110].

All data are quantified from the (002) or basal plane 2θ peak of wurtzite phase of ZnO. Line profile spectra are used for quantification of 250 W and 1000 W data, and survey spectra are used for quantification of 500 W data, as discussed in Chapter 3. The

(002) peak is consistently the most intense, which indicates the film has a strong basal plane texture. This suggests that adatoms have sufficient surface mobility that they can migrate over large distances to facilitate growth of low free energy (002) crystal planes. This occurs despite water cooling of the substrate support and changes in impingement angle, negative ion flux, and deposited neutral flux. The JCPDS database indicates the (002) peak occurs at 34.422° 2θ for pure ZnO and Cu K_α X-rays. Discussion of XRD data will be broken down into sections based on data type, and will cover variations in intensity, 2θ peak position, and FWHM, so that positional effects and film thickness effects can be evaluated together.

Maximum peak intensity data are plotted as functions of position and film thickness in Figures 6-18a and 6-18b, respectively. Intensities from 500 W samples are consistently lower because shorter count times are used in the XRD survey spectra. Both 250 W and 1000 W samples show a monotonic decrease in intensity across Region I. The fact that intensity increases in Region II despite thinner films, suggests that decreasing film thickness accounts for only part of the decreased intensity in Region I. The proposed model postulates that $J(j_i/j_n)$ increases with position across Region I due to target edge effects and the narrow angular distribution of negative ions leaving the target. It is postulated that as $J(j_i/j_n)$ increases, structural damage to the film is also increasing. Structural damage would act to reduce domain size, which would broaden the peak. A broader peak will have a lower peak intensity. This suggests that increased FWHM and decreased film thickness across this region are both responsible for decreased peak intensity in 250 W and 1000 W samples across Region I. This is supported by increases in FWHM with increasing position across Region I for 250 W and 1000 W data.

Before 2θ peak positions are discussed, recall that red data markers are used in quantified XRD results to signify a highly anisotropic peak shape. The anisotropy is best appreciated by examining those spectra presented in Figures 6-16b and 6-17b. Also note that red data markers in Region I are associated with 2θ peak positions that are roughly 0.2° lower than Region II values. Four points marked in red include 1000 W samples from 0.8 and 4.2 cm, and 500 W samples from 4.0 and 10.8 cm. The three data points from Region I are marked due to a significant tail on the peak, which extends to larger 2θ values. The 500 W sample at 10.8 cm is marked because the peak is very weak and therefore might have significant error due to noise. Also notice that no red markers are used for 250 W data. This fact suggests that the tail feature is a function of deposition power. Red data markers in Region I are also associated with positions where carrier concentrations are significantly lower and resistivities are significantly higher than Region II.

All 500 W and 1000 W data points have red data markers, indicating the presence of the tail to higher 2θ values for the basal peak. Presence of the tail is also associated with a large (0.2°) increase in 2θ position between Regions I and II. If spectra for these points are examined, the tail is found to extend roughly 2° higher in 2θ than the peak. Significant diffraction for 2θ values larger than the JCPDS value indicates both contraction and expansion of the c-axis occur in the surface normal direction. The out-of-plane expansion is attributed to high interstitial concentrations, and is discussed in the following paragraph. One possible mechanism for out-of-plane lattice contraction is mismatch between the thermal expansion coefficients of the glass substrate and the ZnO film. The coefficients of thermal expansion (α with units of K^{-1}) are 8.8×10^{-6} , 4.75×10^{-6} ,

and $2.92 \times 10^{-6} \text{ K}^{-1}$ for soda lime float glass, a-axis ZnO, and c-axis ZnO, respectively. Thus, for a film and substrate cooling after unintentional heating during deposition, the substrate will contract more than the film, yielding in-plane compressive strain. To maintain constant unit cell volume, out-of-plane lattice expansion may occur [101]. Thus, strain induced due to the mismatch of thermal expansion coefficients is not consistent with out-of-plane contraction. Ion peening can generate compressive strain in the out-of-plane axis. This process involves film bombardment by energetic particles, which cause deformation of chemical bonds to force atoms closer together. At low growth temperatures the deformation does not relax, freezing damage into the lattice. The tails has significant intensity only for 500 W and 1000 W samples where the 2θ peak position is shifted to significantly lower values. At these powers, negative oxygen ions have approximately 500 eV and 1000 eV kinetic energy, respectively. This suggests that ion peening is intensified by higher ion kinetic energies.

Another possible contribution to out-of-plane compressive strain is a non-uniform distribution of interstitials within the ZnO grains. If grain boundaries act to deplete interstitials by a gettering and desorption mechanism, then constant grain volume could be maintained by expansion in the grain's center to accommodate interstitials in balance with contraction in outer portions of the grain where interstitial concentrations are depleted. Gettering is postulated to increase at higher temperatures, and higher substrate temperatures are expected with higher deposition powers [94,99,101]. Also, interstitial concentrations are postulated to increase with increasing ion energies. Both of these effects would yield increased out-of-plane expansion and contraction for higher ion energies. Because it seems plausible that collision cascades from negative ions would

subsequently disturb strain induced by ion peening, the postulate of non-uniform interstitial concentrations is considered more likely.

The 2θ peak position for 250 W samples has significantly less variation than 500 W and 1000 W samples. The peak position for 1000 W samples in Region I is more than 0.5° lower in 2θ than the value for pure ZnO, which translates to a 1.6% larger d-spacing in the out-of-plane direction (i.e. the [0001] direction). In terms of residual stress, the film has tensile out-of-plane stress. For sputtering, this typically results from lattice expansion due to a high concentration of interstitials [101]. These interstitials are either implanted Ar atoms reflected from the source, or Frenkel pairs from impingement of the high energy reflected Ar atoms. In-plane expansion is constrained by bonding to the substrate, and therefore results in bi-axial in-plane compressive stress [94,101]. If this stress is sufficiently large, film delamination can result. The out-of-plane dimension is not constrained, and therefore expands to accommodate the high interstitial concentration. Because the 2θ peak position moves towards the pure ZnO value in Region II, the increased interstitial concentration suggested by out-of-plane lattice expansion is postulated to result from negative oxygen ions. The negative ions impinge on the film, in which some are implanted and come to rest in interstitial positions. Other negative ions form Frenkel pairs during the collision cascade within the film. As mentioned in the model first postulated in Section 6.3.1, Frenkel pairs with oxygen as the interstitial should be more common due to efficient binary collision energy transfer with other oxygen atoms. The 500 W sample at 4 cm also has a significantly lower 2θ peak position than the pure peak, suggesting it also has a high concentration of interstitial oxygen. The 500 W and 1000 W samples are both shifted $\sim 0.2^\circ$ lower in 2θ in Region I,

compared to Region II. For 250 W samples, the peak position is 0.09° lower in Region I than Region II. If Regions II and III are considered to have minimal interstitial concentrations, then the smaller change in 2θ peak position 250 W is consistent with higher carrier concentration due to less compensation by oxygen interstitials, which was found in Hall data. There are both octahedral and tetrahedral interstitial sites available in ZnO. Comparing the equilibrium size of the interstitial site to the size of single and doubly ionized oxygen ions, the oxygen ions are 4% and 38% larger than the tetrahedral site for single ionized and double ionized oxygen, respectively. For an octahedral site, the oxygen ion is 30% and 6.4% smaller for the singly and doubly ionized oxygen, respectively. Because the interstitial sites are bounded by oxygen ions in the ZnO lattice, strong repulsive coulombic forces are anticipated between the interstitial and the lattice. This suggests that oxygen ions smaller than the interstitial sites can cause tensile strain in crystals that are free to expand. Both the singly and doubly ionized oxygen ions are larger than the tetrahedral sites, which indicates that this configuration would generate a large amount of strain, and is therefore likely to be energetically unfavorable. The offset to lower 2θ peak positions for Regions II and III will be discussed subsequently.

For the transition between Regions I and II, the 2θ peak positions for all RF powers move to higher values, which are closer to the JCPDS value for basal plane diffraction. The high 2θ tail is not observed for the (002) peak. Low negative ion resputtering in Region II is supported by the correlation between electrical properties and position. The changes in peak position and loss of the high 2θ tail correlate well with the decrease in resistivity between Regions I and II.

For FWHM, 250 W and 1000 W data was quantified by the *Line Profile Analysis* [122] software from Philips, and 500 W data was quantified using the *MacDiff* [128] software package using procedures reported in Chapter 3. In Region I, large variations are found for the 1000 W data. The large increase in FWHM for samples from positions 0.8 and 4.2 cm results from the previously mentioned tail. The well-defined basal peak is sufficiently intense from the 0.8 cm sample that the tail is below half the maximum intensity, and therefore contribute little to the FWHM. At 4.2 cm, the basal peak and tail intensities are similar, therefore the tail contributes to a much larger FWHM at this position. This is similar to 500 W data at 4.0 cm, whose large breadth also includes a significant contribution from the tail. Again, the tail is postulated to result from a combination of a non-uniform distribution of oxygen interstitials and ion peening.

For 250 W data, no significant tail can be detected for any sample in Region I. Thus, the tail is only associated with higher target biases from higher RF powers. The FWHM does increase across Region I for 250 W samples. The increase in FWHM is consistent with thinner films, but the subsequent decrease in FWHM with thinner films between Regions I and II suggests another factor besides film thickness is influencing FWHM. Changes in FWHM for 250 W data are postulated to result from a combination of decreasing film thickness and degraded crystallinity in the films. Changes in peak position are small (0.06°), which suggests change in strain is small. This suggests that little of the broadening in 250 W FWHM data results from changed peak asymmetry induced by strain. For 500 W and 1000 W samples, peak asymmetry cannot be evaluated due to the presence of the tail. Increased FWHM associated with higher positions (i.e. ~ 4

cm) in Region I is consistent with degraded crystallinity caused by an increase in $J(j_i/j_n)$ with higher positions.

6.3.2.8 Atomic force microscopy (Region I)

Analysis of atomic force microscopy (AFM) images is used to quantify “grain size” and surface roughness. Recall that the technique used to quantify grain size is based on interpretation of granular surface features as distinct grains of the polycrystalline thin film. No variation in grain size outside of experimental error is found for 250 W and 1000 W samples in Region I. At 4 cm, grain size from highest to lowest occur for 500 W, 1000 W, and 250 W samples, which correlates with film thickness. Thus, differences in grain size correlate with film thickness, with larger grain sizes associated with thicker films. Thus thickness influences grain size, but the lack of consistent correlation suggests other factors are also involved. For 500 W and 1000 W samples, there is a significant decrease in grain size between Regions I and II, while no significant changes are found for 250 W samples. Also, ion bombardment is reported in the literature to enhance grain size by enhancing surface mobility of adatoms [101]. This suggests that changes in grain size induced by ion bombardment depends on kinetic energy of the ion, and that the ion energies for the 250 W case are low enough that bombardment does not induce a significant change in grain size.

The significant decrease in grain size from Region I to II for 500 W and 1000 W samples and the lack of change for Hall mobility data suggests that Hall mobility is not strongly influenced by grain size in Regions I and II. This is consistent with the estimated mean free path of $\sim 5 \text{ \AA}$ being much smaller than the grain size, and reports in the literature which also suggest that mobility is not dominated by grain boundary scattering.

For Region I, changes in RMS roughness for 250 W and 1000 W samples are similar to experimental error, and therefore within each RF power are considered constant. From RMS roughness versus thickness, RMS roughness is observed to generally increase with film thickness, but this trend is interrupted in Region I. This suggests another parameter is influencing RMS roughness in Region I. The maximum RMS roughness of the 1000 W sample is nearly two times the maximum roughness of the 250 W samples. Some of this difference is attributed to differences in thickness for between 1000 W and 250 W samples, but the deviation from thickness to roughness relationship in Region I suggests a second factor is involved. Also, RMS roughness for all three powers decreases sharply from Region I to Region II. This change correlates with changes in negative ion resputtering, which suggests negative ion resputtering is the second factor, which increases RMS roughness. If this is true then the higher energy ions formed for the 1000 W condition should contribute to the higher roughness in Region I relative to 250 W condition. While the RMS roughness is not expected to influence electrical properties in Region I, the changes in this property do support the model proposed in Section 6.3.1.

6.3.3 Region II

Region II is shadowed from negative ion resputtering by the uniformity shield, and the film thickness is greater than 500 Å.

6.3.3.1 Profilometry (Region II)

Deposition rate decreases by more than 50% across Region II. In Region II, the uniformity shield shadows the direct vertical flux from the deposition source to the substrate. Therefore, all the deposited flux impinging on the substrate results from sputter material that leaves with the target with some angle relative to the deposition

source's normal axis. Flux decreases as angle increases, which is consistent with the decaying deposition rate with higher positions for Regions II and III.

In Figure 6-5, changes are observed in the ratio of deposition rates between both 250 W and 1000 W samples, and 500 W and 1000 W samples. In both cases the ratio is lower in Region II than Region I, indicating a relatively high deposition rate at 1000 W in Region II compared to Region I. This is speculated to result from changes in the value of the power cosine distribution (Section 2.4.1) [94]. Higher target biases generate a higher exponent [99], which has the result of narrowing the angular distribution of the sputtered flux [94]. Thus, for positions just past the uniformity shield's edge, the sputtered flux can leave the source with relatively acute angles, therefore receiving relatively high flux from the higher exponential power cosine distribution associated with higher target biases at 1000 W compared to 250 W and 500 W.

6.3.3.2 Resistivity effects (Region II)

Region II receives no negative ion flux, but because of the cosine distribution for deposited neutrals film thicker than $\sim 500 \text{ \AA}$ can be achieved with deposition times of less than an hour. Resistivities in this region are consistently near $1.5 \times 10^{-3} \text{ } \Omega \cdot \text{cm}$, and are independent of RF power. This independence of resistivity from power and position is true despite a range of film thicknesses between 510 \AA to 3870 \AA , and deposition rates from 0.14 \AA/s to 2.25 \AA/s . Despite the large differences in film thickness, the "grain size" from AFM only changed from $\sim 250 \text{ \AA}$ to 500 \AA . Thus thickness is not a primary factor in the resistivity value if it is greater than $\sim 500 \text{ \AA}$. Low deposition rates are typically more influenced by contamination of the film from the gas phase, with higher deposition rates allowing less time for contamination of the growth surface by residual

gas fluxes [101]. The constant resistivity in Region II suggests that gas phase contamination is not an issue.

Region II is defined to end when the resistivity increases from above $1.5 \times 10^{-3} \Omega \cdot \text{cm}$ (Region II value) by an amount larger than the experimental error, which is $2.0 \times 10^{-3} \Omega \cdot \text{cm}$. Region III begins when thickness effects dominate the resistivity, which occurs for films less than 500 \AA thick. In the plot of resistivity versus film thickness, there are significant differences between resistivities of 250 W samples and 500 W and 1000 W samples. These differences do not correlate with film thickness for films $< 500 \text{ \AA}$, but some factors are increasing resistivity to above the $1.5 \times 10^{-3} \Omega \cdot \text{cm}$ value. It is postulated that 500 W and 1000 W samples have higher resistivity than 250 W samples for thicknesses between 1000 \AA and 500 \AA because films with this thickness occurs at significantly higher positions. These higher positions translate to a longer path length for deposited materials through the gas ambient. The mean free path of a room temperature Ar atom at the pressure of 5mTorr used in this experiment is $\sim 1 \text{ cm}$ [141]. Data for an 800 \AA thick film shows a higher resistivity for 500 W and 1000 W samples ($2.5 \times 10^{-3} \Omega \cdot \text{cm}$) than 250 W sample ($1.4 \times 10^{-3} \Omega \cdot \text{cm}$). For 500 W and 1000 W samples, a film thickness of 800 \AA occurs at approximately 8.5 cm, and indicates that both are equal distances from the uniformity shield edge. This consistency in location suggests a geometric factor is responsible for increasing resistivity at high positions (i.e. $\sim 8 \text{ cm}$). At 8.5 cm, the path length from source to substrate is $\sim 12 \text{ cm}$, a 33% increase over the vertical substrate to target distance. Gas phase scattering of sputter deposited flux is commonly believed to degrade the properties of sputter deposited films [94,101]. The mechanism is that the sputter deposited flux is formed of atoms with energy greater than

thermal energy (hyperthermal) when they leave the source. This extra energy is generally believed to improve the properties of the deposited films. Loss of this energy from gas phase scattering results in degraded film properties. Lower deposition rates for 250 W samples result in a film thickness of 450 Å at 8.2 cm, which is already in Region III. Thus the film must be thick enough that resistivity is not dominated by film thickness effects for small changes in resistivity from gas phase scattering to be significant.

6.3.3.3 Hall carrier concentration (Region II)

Carrier concentration is highest for all RF powers conditions in Region II, with carrier concentrations close to the Al dopant content of the target. Corrected data indicates maximum dopant activation levels are 75%, 68%, and 83% for 250 W, 500 W, and 1000 W samples, respectively. The differences between these values are within experimental error, which suggests that there is either a weak or no dependence of carrier concentration on power in Region II. There is only one datum point in Region II for the 250 W sample (5.9 cm), therefore trends in carrier concentration cannot be evaluated. For 500 W and 1000 W samples, carrier concentrations are within 10% of the average values of 4.0×10^{20} and $5.3 \times 10^{20} \text{ cm}^{-3}$, respectively.

The low variation of resistivities and carrier concentration suggests that electrical properties are uniform in Region II. In terms of the model, films are thick enough that thickness does not influence electrical properties. Region II is also close enough to the uniformity shutter that a less than 30% increase in path length through the ambient occurs. The substantial improvement in electrical properties results from shadowing of negative ions. The transition between Regions II and III is small compared to the distance between Hall samples. Therefore, there is not enough data available to determine if carrier concentration changes over Region II.

6.3.3.4 Hall mobility (Region II)

For 250 W samples, there is only one data point in Region II at 5.9 cm. The value is $6.5 \text{ cm}^2/\text{V}\cdot\text{s}$, which is within experimental error of the values from Region I. There is no variation outside experimental error for Hall mobility of 1000 W samples in this region. The 500 W sample has the largest variation, and decreases by a factor of 1.3 between 5.7 and 7.4 cm. The steady decrease in Hall mobility for 500 W samples versus both position and thickness suggests the decrease might be related to thickness. The lack of correlation between Hall mobility and thickness for different powers in Figure 6-26b indicates that another factor is important. The trend for decreasing mobility in Region II and the transition from Regions II to III has a reasonable correlation with position. This correlation is similar to the correlation between increasing resistivity and position found between Regions II and III. Therefore decreasing mobility with higher positions in Region II and between Regions II and III is also attributed to gas phase scattering by the same increasing path length argument previously used for resistivity. Thus degradation of film quality at higher positions resulting from gas phase scattering [101] leads to a slow decrease in Hall mobility.

6.3.3.5 X-ray diffraction (Region II)

Peak intensity increases between 4 and 6 cm for all samples, which corresponds to the transition from Regions I to II. This occurs despite decreasing film thickness, which decreases the volume fraction of ZnO in the probed volume, and therefore should decrease intensity. The increased intensity corresponds with a decrease in FWHM, also shown below.

For Region II, there is less than a 0.1° variation in the 2θ peak position within each RF power, but there are substantial differences between different RF power

conditions. Also, all 2θ peak positions are lower than the JCPDS values, suggesting constant out-of-plane expansion or tensile strain for each RF power. Thermal expansion mismatch between ZnO and glass also yields an out-of-plane tensile strain, which should increase with increasing substrate temperature. Based on differences in thermal expansion coefficients for a-axis ZnO and glass, this mismatch would only result in 0.04% strain per 100°C of temperature change. The substrate temperature is estimated to be between 50° and 100°C at completion of the deposition. A tensile strain of 0.04% corresponds to a decrease of $\sim 0.01^\circ 2\theta$ for the peak, which is significantly smaller than the measured deviations. The Poisson's ratio for ZnO is 0.23, indicating that out-of-plane tensile strain will be less than in-plane compressive strain which generates it. Thus, thermal expansion mismatch is not anticipated to generate strains of the magnitude observed. Another mechanism for generation of residual stress is subsurface recrystallization. Recrystallization reduces disorder within the grain, and therefore is expected to decrease grain size. Bonding with other grains prevents this change in volume, resulting in development of tensile strain within the grain to maintain its size. Though substrate temperatures are low, recrystallization is known to occur in some thin film materials at temperatures as low as room temperature.

For Region II, the FWHM increases monotonically. In the plot of FWHM as a function of film thickness, all powers show an increased FWHM with decreasing film thickness for samples in Region II. This is consistent with the fact that the FWHM increases with decreasing film thickness even for single crystal films [110]. Higher FWHM for 1000 W samples compared to 250 W and 500 W samples results from increased asymmetrical peak broadening. This type of broadening results from strain.

1000 W samples exhibit relatively low 2θ peak positions in Region II indicating higher tensile strain, which is consistent with the broadened peak.

6.3.3.6 Atomic force microscopy (Region II)

Grain size steadily decreases with increasing position in Region II. Data from all RF powers are the same within experimental error, which suggests that grain size is influenced by film thickness in Regions II. But the small magnitude of the changes in grain size indicate the influence of film thickness is weak. Again, changes in grain size across Regions II do not correlate well with changes in electrical properties, which suggests that grain size does not have a dominant influence on electrical properties. This is consistent with most reports in the literature, and conclusions based on the data from Region I.

For Region II, a good correlation in RMS roughness trends occurs with different RF powers, and suggests both film thickness and RF power influence roughness. Roughness that approaches the 2 Å RMS roughness of the bare glass surface agrees with results from Chapter 5 that indicate RMS roughness decreases with decreasing film thickness for continuous layers ($t > 100$ Å).

6.3.4 Region III

Region III occurs for samples less than 500 Å in thickness, which are not subjected to negative ion resputtering. Because this Region III is defined in terms of film thickness, the positions where it occurs depend on the deposition parameters.

6.3.4.1 Profilometry (Region III)

In Region III deposition rates are very low, and slowly trending towards zero with higher positions. Similar to Region II, decreasing deposition rate is consistent with decreasing flux with increasing exit angle relative to the deposition source's normal axis

resulting from the power cosine distribution. From Figure 6-5, changes are again observed in deposition rate ratios between both 250 W and 1000 W samples, and 500 W and 1000 W samples as a function of position. The 250 W to 1000 W ratio increases for positions greater than 8 cm (Region III) compared to Region II. Again this results from different power for the cosine distribution associated with target bias. The higher power values associated with 1000 W results in relative high flux compared to 250 W for small off-normal angles. But for higher angles, the higher power value for the cosine distribution (1000 W) decays more quickly than for the lower power value (250 W). This would suggest a similar trend should be observed for the deposition rate ratio between 500 W and 1000 W samples, but this ratio continues to decrease in Region III. It is speculated that this deviation from the predicted trend results from inaccuracies in the data. Errors were discussed in Section 6.3.2.2 above.

6.3.4.2 Resistivity effects (Region III)

In Region III resistivity is dominated by film thickness, which is consistently true for films thinner than 500 Å. In this thickness range, resistivities increase exponentially with decreasing thickness as is seen in Figure 6-8. Also, resistivity versus film thickness for different RF powers overlap one another, suggesting resistivity is independent of power in Region III. The exponential increase in resistivity associated with Region III occurs at different positions and deposition rates for different RF powers, indicating no significant influence of these parameters on resistivity in Region III. This is consistent with postulate that resistivity in Region III is dominated by film thickness.

6.3.4.3 Hall carrier concentration (Region III)

Data used in discussion of Region III are presented in the plot of corrected carrier concentration as a function of film thickness in Figure 6-25b. These data show a strong

correlation between carrier concentrations and thickness with different RF powers for films less than 500 Å thick. This strongly suggests that decreased carrier concentrations for films less than 500 Å thick are at least partly responsible for increased resistivity. Hall mobility data discussed below also decreases significantly in Region III for all RF power conditions, and therefore also contribute to increasing resistivity in Region III. The decrease in carrier concentration is similar to those reported from thin films in Chapter 5. Data from Chapter 5 also shows an increase in resistivity for very thin films resulting from a strong decrease in carrier concentration for films with a thickness less than ~800 Å. Though the trends are similar, the thickness at which they occur is different.

The sharply decreasing carrier concentration in Region III is consistent with compensation of free carriers by chemisorption of oxygen on ZnO surfaces. For 500 W samples, the carrier concentration is 97% lower for the 200 Å film than the 625 Å film. This suggests that the quantity of chemisorbed species is similar to the quantity of dopants for the film. If dopant activation is assumed to be constant across Regions II and III, then the uncompensated carrier concentration for 500 W samples in Region III would be $\sim 5 \times 10^{20} \text{ cm}^{-3}$. Similar to the calculation performed in Chapter 5 with Equations 5.2 and 5.3, for an idealized single crystal film, the carrier quantity per square centimeter is the product of carrier concentration and film thickness. If the density of surface sites available for chemisorption is taken as the typical value of $10^{15} \text{ atoms/cm}^2$, then the quantity of surface sites suitable for chemisorption would equal the quantity of carriers when the film thickness is ~200 Å. This rough calculation suggests that if the films surface is saturated with chemisorbed oxygen, it would fully deplete the electron carriers

in a 200 Å film. This is in reasonable agreement with the 97% depletion that is observed for the 200 Å sample deposited at 500 W. Additionally, high carrier concentrations are achieved for films greater than 500 Å in thickness despite a very fine grain size. A fine grain size suggests the possibility of a large grain boundary surface area available as chemisorption sites. Instead, the large carrier concentrations observed in Region II despite only marginally larger grain size suggest chemisorption at grain boundaries is a small effect. Therefore carrier compensation results mainly from chemisorbed oxygen at the film's free surface.

6.3.4.4 Hall mobility (Region III)

Hall mobilities in Region III are significantly lower than Regions I or II, and a good correlation between Hall mobility values for all RF powers is observed for films less than 500 Å in thickness, as seen in Figure 6-26b. This suggests that film thickness influences mobility, with the mobility decreasing as the film thickness decreases. This is somewhat different than the data presented in Chapter 5, which showed no discernable trend in mobility with film thickness. However, the average Hall mobility in Chapter 5 is $4.1 \text{ cm}^2/\text{V}\cdot\text{s}$, and all values are lower than $6 \text{ cm}^2/\text{V}\cdot\text{s}$. This is lower than most Region I and II Hall mobilities, and makes trends in decreasing mobility difficult to observe as the films become too resistive to measure in the instrument.

Assuming electrons are free to move in the solid and using Equation 2.10 from Chapter 2, a thermal velocity for electrons of 10^7 cm/s [83], and a mobility of $10 \text{ cm}^2/\text{V}\cdot\text{s}$ translates to a mean relaxation time of $5 \times 10^{-15} \text{ s}$, which agrees with value calculated by Coutts *et al.* [82]. Thus using Equation 2.7 from the literature review, the mean free path (l) is approximately $5 \times 10^{-8} \text{ cm}$, or 5 Å. This dimension is on the order of the unit cell, and is significantly smaller than the film thickness or “grain size” for Region III samples

where the decrease in Hall mobility is found. For the Fuchs and Sondheimer model presented in Chapter 5, increased scattering from the interfaces becomes significant when film thickness approaches the carriers mean free path. For this experiment, thickness influences mobility for films less than 500 Å in thickness, which is much thicker than where interfacial scattering is anticipated to be significant. Grain sizes also much larger than carrier mean free path, suggesting grain boundary scattering is not the source for decreased carrier concentration. This suggests increased concentrations of point defects are the most likely mechanism for decreased Hall mobility. If the concentration of Al in the film is assumed to equal the concentration of $6.5 \times 10^{20} \text{ cm}^{-3}$ from the target, then the average distance between Al atoms is $\sim 13 \text{ Å}$. Thus, the mean free path of carriers is similar to the distance between point defects, which indicates the results are consistent with scattering by point defects. It is speculated that increased point defects results from increased gas phase scattering, and therefore continues the trend previously discussed in the section on Hall mobility for high positions in Region II and the transition from Region II to III.

6.3.4.5 X-ray diffraction (Region III)

In Region III, intensity of the (002) peak drops significantly for all RF powers. Different RF powers are observed to have similar trends for decreasing intensity with film thicknesses less than 1500 Å in Figure 6-18b. Recall that low 500 W intensities result from use of survey spectra parameters. If the intensity for the 500 W samples are compensated for shorter count times, a good correlation is found for decreasing intensity with decreasing film thickness. This suggests that film thickness contributes to decreased peak intensity, and therefore makes evaluation of changes in crystallinity difficult for Region III.

The 2θ peak position data in Region III shows the same lack of variation within the RF powers found in Region II. Also, peak position is the same amount lower than the JCPDS value as in Region II, and therefore the same interpretations of the data for Region II and the transition from Region II to III also apply for Region III. The FWHM data is also similar to Region II data, with values increasing monotonically with decreasing film thickness. Changes in FWHM induced by film thickness make evaluations of changes in crystallinity impossible for Region III.

6.3.4.6 Atomic force microscopy (Region III)

For both grain size and RMS roughness, there is only one datum point in Region III for both 250 W and 1000 W samples. For both 250 W and 1000 W samples, grain size and RMS roughness in Region III are the lowest values measured, which is consistent with the previously reported trend of decreasing grain size and roughness with decreasing film thickness. For 500 W samples, there are two data points for both grain size and RMS roughness in Region III. A small decrease in grain size and a small increase in RMS roughness with decreasing film thickness are observed, but both are less than experimental error.

6.4 Summary

A model concerning variations in electrical and structural properties of sputter deposited ZnO:Al thin films has been developed. This model incorporates changes in negative ion resputtering with deposition geometry and very thin film effects, and relates these to electrical properties of deposited films. The model also incorporates mechanisms for the influence of negative ion resputtering and film thickness effects on the electrical properties of the deposited films. Negative ion resputtering is proposed to

increase film resistivity through compensation of conduction band carriers.

Compensation results from high concentrations of oxygen interstitials resulting from impingement of high energy oxygen atoms and/or an oxygen rich stoichiometry promoting the formation of zinc vacancies. Film thickness effects dominate resistivity for film less than 500 Å thick. The proposed mechanism involves strong compensation of conduction band electrons by consumption during chemisorption of oxygen species. Hall mobility also decreases for films less than 500 Å thick. It is speculated that Hall mobility decreases due to higher point defect concentrations.

CHAPTER 7 CONCLUSIONS

7.1 Negative Ion Resputtering

The research presented in this work has investigated the relationships between the properties of ZnO:Al thin films and the sputter deposition process used to deposit them. This investigation was performed by depositing ZnO:Al followed by characterization of their structural, electrical, and optical properties. The negative ion resputtering (NIR) effect was found to be one of the most influential factors in controlling the properties of sputter deposited ZnO:Al thin films. For the case of depositing ZnO films, this effect involves generation of negative oxygen ions in close proximity to the deposition source, which are then accelerated away from the source by the negative bias developed on the target. The accelerated negative ions can impinge on the substrate and cause significant damage to the deposited film. Negative ion resputtering is a pervasive and difficult to alleviate problem for sputter deposition of ZnO, and has also been reported to be an important factor in controlling properties of thin films for many ionically bonded materials including halides and oxides [101,114,142]. Therefore understanding and controlling NIR is critical for sputter deposition of these materials. The effect of negative ion resputtering was systematically investigated in Chapter 6, but its influence was also evident from variations in electrical properties found in Chapter 4 and the subsequent improvement in the electrical properties from use of the off-axis geometry reported in Chapter 5. The samples for the experiment reported in Chapter 6 were deposited in 20

cm diameter planar diode sputter deposition source. Electrical characterization results from Chapter 6 revealed that higher resistivities (3.3×10^{-3} to $1.5 \times 10^{-2} \Omega \cdot \text{cm}$) occurred for areas that receive a negative ion flux compared to a lower resistivity ($1.5 \times 10^{-3} \Omega \cdot \text{cm}$) for areas of the substrate that do not receive a negative ion flux. Hall data indicated that NIR increased the resistivity primarily by decreasing the carrier concentration from $\sim 5 \times 10^{20} \text{ cm}^{-3}$ for areas with no NIR to from 7.2×10^{19} to $3.3 \times 10^{20} \text{ cm}^{-3}$ for areas where NIR occurs. Hall mobility ranged between 4.7 and $12 \text{ cm}^2/\text{V} \cdot \text{s}$ and showed no significant changes with NIR. This supported the conclusion that NIR primarily degrades the resistivity of ZnO:Al thin films by decreasing carrier concentration through compensating free electrons. Compensation was proposed to occur by formation of native defects including oxygen interstitials and/or zinc vacancies due to implantation of oxygen and/or an oxygen rich stoichiometry due to the reactive character of the atomic negative oxygen ions.

Results from secondary ion mass spectrometry (SIMS) indicated that no change in the Al dopant concentration occurs as a function of NIR. The concentrations of alkali metals, which could compensate electron carriers, were found to be too low to account for the levels of carrier compensation found by Hall measurements, and also did not vary as a function of NIR. The lack of compensating impurities or changes in doping concentration supported the case for compensation occurring through the previously mentioned native defect mechanisms. From X-ray diffraction, a 0.2° decrease in 2θ position for the (002) or basal peak for 500 W and 1000 W samples was measured for areas with NIR compared to areas without NIR. This peak shift represented 0.6% tensile lattice strain, which is consistent with lattice expansion due to a large concentration of interstitials expanding the lattice for areas with NIR. Larger interstitial concentrations for

higher powers were consistent with interstitial formation by ion implantation, and zinc vacancies are consistent with an oxygen rich stoichiometry due to the reactive character of the negative oxygen ion flux. The activation energies for the compensating defects were unknown but the lack of native *p*-type ZnO suggested the levels were deep.

A model was developed to explain the changes in properties as a function of negative ion resputtering. The ratio of negative ion to deposited neutral flux ($J(j_i/j_n)$) after Kester *et al.* and the kinetic energy of the oxygen ions were concluded to be two critical parameters controlling the amount of damage generated by negative ion resputtering [117]. A value on the order of 0.01 is empirically derived for $J(j_i/j_n)$ for areas where NIR occurs, while the kinetic energy of negative ions measured from the target bias was between -300 and -1000 V. Higher target biases for 500 W and 1000 W deposition conditions were found to result in more damage to the deposited films, as indicated by higher measured resistivities. It was therefore concluded that deposition power is an important parameter in controlling the degree of negative ion resputtering.

Evidence supporting the influence of NIR on the electrical properties of thin films was also observed in results presented in Chapter 4. The experiment presented in Chapter 4 was designed to investigate the variations in electrical properties, and the influence of the ambient used during heat treatment of the deposited films. The samples were deposited using a 5 cm diameter planar magnetron sputter deposition source. Resistivity data reported in Chapter 4 revealed more than four orders of magnitude variation in resistivity (1.4×10^{-2} to $>500 \Omega \cdot \text{cm}$) occurred with position on the surface of the substrate for as deposited films. A pattern in the resistivity of higher resistivities for the center and areas directly opposed to the source's *racetrack* region, and lower

resistivities for the edges of the deposited films was observed. This is consistent with $J(j_i/j_n)$ increasing for areas opposed to the source's *racetrack* and therefore agrees with the proposed model. The influence of annealing ambient on the structural, electrical, and optical properties of heat treated ZnO:Al thin films was then investigated. The heat treatment was conducted at a temperature of 400°C for one hour using flowing nitrogen, forming gas, stagnant air, or oxygen, and compared to a control sample (no anneal). Resistivity decreased by between 8.3 and 330 times for anneals in non-oxidizing (nitrogen) or reducing ambients (forming gas). The sample annealed in forming gas had up to an order of magnitude lower resistivity than samples annealed in other ambients with a minimum resistivity of $1.7 \times 10^{-3} \Omega \cdot \text{cm}$. Spectrophotometry measurements indicated that the deposited films have an optical band gap of 3.2 eV in the as deposited state. All band gaps increased by 0.08 eV with annealing except the sample annealed in forming gas, which increased by 0.31 eV. The increased optical band gap with annealing was consistent with the Burstein-Moss shift, which indicates that improvements in resistivity with annealing result in part from increased carrier concentration. Fourier transform infrared (FT-IR) spectra exhibited only silica phonon modes consistent with the glass substrate for spectra taken both before and after annealing. By the Drude free electron theory, this is consistent with low carrier concentrations ($n < 10^{19} \text{ cm}^{-3}$) in the ZnO:Al film. The one exception was the sample annealed in forming gas for which high reflectivity was observed across the FT-IR spectra, indicating a carrier concentration greater than 10^{20} cm^{-3} for that sample. This agreed with the larger Burstein-Moss shift for this sample in demonstrating that a large increase in carrier concentration occurred. Thus, results from Chapter 4 also indicated that NIR increases resistivity by decreasing

carrier concentration, and is therefore consistent with results from Chapter 6.

Additionally, the much larger improvement in carrier concentration for samples annealed in reducing ambients was consistent with compensation occurring due to excess oxygen in the form of oxygen interstitials and zinc vacancies.

7.2 Chemisorbed Oxygen

The influence of chemisorbed oxygen at free surfaces and grain boundaries was also found to be a critical factor in the electrical properties of ZnO:Al thin films. This was particularly important as the film thickness decreased and the quantity of carriers became similar to the quantity of chemisorption sites available to oxygen. Though there are many literature reports of chemisorbed oxygen on ZnO and its influence on electrical properties in references regarding solid state gas sensors, this effect is largely neglected in literature pertaining to ZnO as a transparent conductor. The influence of this effect is observed in results from Chapter 5 and results from very thin films ($< 500 \text{ \AA}$) presented in Chapter 6. In both cases, resistivity increased with decreasing film thickness. Resistivity data from Chapter 5 increased from 4.3×10^{-3} to $3.3 \times 10^{-2} \text{ \Omega}\cdot\text{cm}$ for decreasing film thickness from 1575 \AA to 315 \AA , respectively, before becoming too high to measure by the Hall system. Carrier concentration at these thicknesses was found to decrease from 2.7×10^{20} to $6.5 \times 10^{19} \text{ cm}^{-3}$, respectively, while the Hall mobility was constant within experimental error. The average Hall mobility was found to be $4.4 \text{ cm}^2/\text{V}\cdot\text{s}$. This suggested that increasing resistivity with decreasing thickness results from decreasing carrier concentration.

A similar relationship was found between resistivity and carrier concentration for results from films less than 500 \AA reported in Chapter 6. Resistivity increased from

$\sim 5 \times 10^{-3}$ to $\sim 3 \text{ } \Omega \cdot \text{cm}$, as film thickness decreased from 500 Å to 150 Å for all films independent of the RF power used to deposit the films. Hall data indicated that a majority of the increased resistivity resulted from decreased carrier concentration, though a decrease in Hall mobility for thinner films also occurred. A simple model was developed and used to evaluate the degree of compensation that could result from chemisorbed oxygen at the free surface. The model predicted that oxygen chemisorption could fully deplete films with a carrier concentration similar to the Al doping level of the target ($6.5 \times 10^{20} \text{ cm}^{-3}$) for thicknesses less than $\sim 200 \text{ Å}$. This agrees with the estimated 90% compensation measured for a 150 Å films from Chapter 6 and $\sim 75\%$ compensation for a 315 Å film from Chapters 5. Therefore it was concluded that chemisorption can increase the resistivity of deposited films, and the magnitude of the effect depends on the thickness and carrier concentration of the film.

7.3 Property Development in Thin ZnO:Al Thin Films

The experiment in Chapter 5 was designed to investigate the development of structural properties in sputter deposited ZnO:Al thin films. The ZnO:Al thin films were deposited by a 5 cm planar magnetron source, and deposition time was controlled to generate films with thickness ranging from 18 Å to 1575 Å in thickness. Even with films calculated to be 18 Å thick, the surface morphology observed in Atomic Force Microscopy (AFM) micrographs changed significantly from a low irregular hillock morphology of the bare glass substrate, to a large, more distinct, and regular hillock morphology. Auger electron spectroscopy results indicated the films were free of contamination and that the bare glass substrate is exposed for films less than $\sim 100 \text{ Å}$ in thickness. The fraction of exposed substrate decreased from 40% to 0% as film thickness

increased from 18 Å to 100 Å, respectively. The large RMS roughness of 18 Å and 11 Å, and the fact that 40% and 30% of the substrate was exposed for 18 Å and 36 Å thick films, respectively, indicates the films were nucleating in the island (Volmer-Webber) mode. For films less than 36 Å, feature height on the surface was larger than the calculated film thickness, and had two different feature sizes. The smaller size features, which have a height range of 70 Å and 50 Å for 18 Å and 36 Å thick films, respectively, were found to be realistic and agreed with island nucleation. The agreement with island nucleation was determined by applying a simple model for a constant volume transformation from a smooth film to one with an island morphology. The larger features, which had a height up to 112 Å and 97 Å for 18 Å and 36 Å thick films, respectively, were attributed to the effects of static electricity on the AFM tip. Electrical properties for films between 18 Å and 105 Å could not be measured because their resistance was too high for the instrumentation, which was consistent with poor electrical properties typical of uncoalesced thin films.

By a thickness of 54 Å, film RMS roughness had decreased to a minimum value of 1.9 Å (which was near the roughness of 2 Å for the bare glass surface) before it began steadily increasing with increasing film thickness. As film thickness increased beyond 100 Å, where AES results indicate the films were continuous, nucleation was complete and thin film growth occurred. With film growth, the Z range, RMS roughness, and “grain size” were all observed to slowly increase with increasing film thickness. Similar trends of increasing Z range, RMS roughness, and “grain size” were found in data from Chapter 6. It was concluded that a slow grain coarsening occurred with film growth.

7.4 Future Work

The NIR effect was found to have a strong influence on the electrical and structural properties of deposited ZnO:Al films justifying further investigation into this effect. The influence of Ar sputtering pressure on NIR from an RF diode source is interesting because the pressure influences the current to voltage relationship of the plasma, and also influences gas phase scattering. Kester *et al.* have investigated the influence of gas phase scattering on NIR for BaTiO₃, and found a strong effect [117], and their work provides a good background for interpreting results.

Heat treatments in oxidizing and reducing ambients would be useful for investigation of native doping and compensation mechanisms. The postulated mechanism was based on point defects, which could be strongly influenced by modest heat treatments. Additionally, there is evidence in the literature that electron paramagnetic resonance (EPR) is sensitive to some point defects in ZnO, one of the defects being O_i. If EPR is sensitive to oxygen interstitials, it could be used to investigate the validity of the proposed model of carrier compensation by O_i from implanted oxygen due to NIR. A combination of heat treatments, electrical measurements, structural characterization, and EPR measurements could provide some insights into the influence of native defects on electrical properties. This experiment could also lead to improvements in quantifying the relationships between process parameters and the NIR effect, and is therefore of both fundamental and practical importance.

There was some evidence presented in Chapter 6 that geometry influences the resistivity of the deposited films for positions far away (>8 cm) from the deposition source. This effect could be investigated simply by varying the length of the sputter deposition, while keeping other process parameters constant. Recall that with increasing

position on the substrate, the distance the deposited flux travels through the vacuum and the incident angle of the arriving flux relative to the substrates normal are both increasing. For longer deposition times, films with thickness greater than 500 Å will occur at higher positions. Thus, any influence from deposition geometry could be investigated by evaluating the resistivity for constant film thicknesses at different deposition times.

Optical properties of ZnO:Al films are another area that could benefit from further investigation, as transmittance of the transparent conducting electrode is a critical factor in solar cell efficiency. Optical data reported in Chapter 4 were used to characterize the band gap and carrier concentration, and could also be used to determine film thickness. Thus, optical characterization could be used to rapidly characterize a series of properties. Additionally, a better understanding of relationships between defects and optical properties could make optical measurements a useful tool for investigating defects. Improved transparency of the ZnO film might results from quantifying defects and their relationships to process parameters. Improved transparency of the ZnO:Al TCE would help improve the efficiency of CIS based solar cells.

Research into electrical properties of single crystal films implanted with dopants could improve understanding of electrical properties for ZnO films and provide a useful stoichiometric standard for SIMS and EPMA analysis. Varying the dose and energy of the implant generates various doping levels, which can be used to evaluate acoustic phonon and ionized impurity scattering as well as the maximum achievable electron mobility. The lack of grain boundaries would also facilitate investigation of chemisorbed oxygen species on electrical properties by restricting chemisorption to the free surface of

the ZnO film. X-ray photoelectron spectroscopy has been found to be sensitive to the chemisorbed oxygen species based on results in Chapter 6 and in the literature.

Investigating the influence of chemisorbed oxygen at grain boundaries and the free surfaces might discover techniques to reduce chemisorbed oxygen, which would decrease levels of carrier compensation. Lower compensation would increase doping efficiency and result in the need for less dopant, and thereby possibly improving carrier mobility by decreasing ionized impurity scattering. Investigation of chemisorbed oxygen is also useful for applications of ZnO as a gas sensor.

LIST OF REFERENCES

1. 1999, Department of Energy, Webpage, (<http://www.eia.doe.gov/emeu/aer/contents.html>), Accessed: 12/2001.
2. M. A. Contreras, B. Egaas, K. Ramanathan, J. Hiltner, A. Swartzlander, F. Hasoon, and R. Noufi, *Progress in Photovoltaics: Research and Applications* **7** (4), 311-316 (1999).
3. K. L. Chopra and S. R. Das, *Thin Film Solar Cells* (Plenum Press, New York, NY, 1983).
4. H. J. Möller, *Semiconductors for Solar Cells* (Artech House, Inc., Norwood, MA, 1993).
5. K. Ramanathan, M. A. Contreras, J. R. Tuttle, J. Keane, J. Webb, S. Asher, D. Niles, R. Dhere, A. L. Tennant, F. S. Hasoon, and R. Noufi, Proceedings of Twenty Fifth IEEE Photovoltaic Specialists Conference, Washington, DC, USA, 1996.
6. P. Mitra, A. P. Chatterjee, and H. S. Maiti, *Materials Letters* **35**, 33-38 (1998).
7. J. J. Osborne, G. T. Roberts, A. R. Chambers, and S. B. Gabriel, *Sensors and Actuators B* **63**, 55-62 (2000).
8. G. Sberveglieri, P. Nelli, S. Groppelli, F. Quaranta, A. Valentini, and L. Vasanelli, *Materials Science & Engineering B* **B7** (1-2), 63-8 (1990).
9. Y. Shimizu and M. Egashira, *Materials Research Society Bulletin* **24** (6), 18-24 (1999).
10. S. J. Chang, Y. K. Su, and Y. P. Shei, *Journal of Vacuum science and Technology A - Vacuum, Surfaces, and Films* **13** (2), 385-8 (1995 Mar/Apr).
11. K. L. Chopra, S. Major, and D. K. Pandya, *Thin Solid Films* **102**, 1-46 (1983).
12. H. Hartnagel, *Semiconducting Transparent Thin Films* (Institute of Physics Publications, Philadelphia, PA, 1995).
13. H. Kawazoe, H. Yanagi, K. Ueda, and H. Hosono, *MRS Bulletin* **25** (8), 28-36 (2000).

14. *The Random House College Dictionary* (Random House, Inc., New York, 1988).
15. D. M. Chapin, C. S. Fuller, and G. L. Pearson, *Journal of Applied Physics* **25**, 676 (1954).
16. H. S. Ullal, K. Zweibel, and B. G. von Roedern, *Proceedings of the 28th IEEE Photovoltaic Specialists Conference*, Anchorage, AK, 2000.
17. S. S. Li, *Semiconductor Physical Electronics* (Plenum Press, New York, 1993).
18. M. B. Prince, *Journal of Applied Physics* **26**, 534 (1955).
19. C. H. Huang, S. S. Li, L. Rieth, A. Halani, M. L. Fisher, J. Song, T. J. Anderson, and P. H. Holloway, *Proceedings of the 28th IEEE Photovoltaic Specialists Conference*, Anchorage, AK, 2000.
20. C.-H. Chang, "Processing and Characterization of Copper Indium Selenide for Photovoltaic Applications," PhD Dissertation, University of Florida, 1999.
21. B. J. Stanbery, "Heteroepitaxy and Nucleation Control for the Growth of Metal Chalcogenides Using Activated Reactant Sources," PhD Dissertation, University of Florida, 2000.
22. L. C. Olsen, F. W. Addis, W. Lei, and J. Li, *Proceedings of the 13th NREL Photovoltaics Program Review*, Lakewood, CO, USA, 1996.
23. R. Noufi, P. Souza, and C. Osterwald, *Solar Cells* **15** (1), 87-91 (1985).
24. R. G. Gordon, *MRS Bulletin* **25** (8), 52-57 (2000).
25. D. Schmid, M. Ruckh, and H. W. Schock, *Solar Energy Materials and Solar Cells* **41/42**, 281-294 (1996).
26. A. Rothwarf and A. M. Barnett, *IEEE Transactions on Electron Devices* **24** (4), 381-387 (1977).
27. D. S. Ginley and C. Bright, *MRS Bulletin* **25** (8), 15-18 (2000).
28. K. Ellmer, *Journal of Physics D: Applied Physics* **33** (4), R17-32 (2000).
29. S. E. Demian, *Journal of Materials Science: Materials in Electronics* **5** (1), 360-363 (1994).
30. J. S. Kim, H. A. Marzouk, P. J. Reucroft, and C. E. Hamrin Jr, *Thin Solid Films* **217** (1), 133-137 (1992).

31. V. Srikant, V. Sergo, and D. Clarke, *Journal of the American Ceramic Society* **78** (7), 1931-4 (1995).
32. V. Craciun, J. Elders, J. G. E. Gardeniers, J. Geretovsky, and I. W. Boyd, *Thin Solid Films* **259** (1), 1-4 (1995).
33. K. Badeker, *Annals of Physics* **22**, 749 (1907).
34. B. G. Lewis and D. C. Paine, *MRS Bulletin* **25** (8), 22-27 (2000).
35. J. M. Mochel, Patent# 2,564,706, USA (1947).
36. H. A. McMaster, Patent# 2,429,420, USA (1947).
37. W. O. Lytle, Patent# 2,566,346, USA (1951).
38. J. M. Mochel, Patent# 2,564,707, USA (1951).
39. L. Holland and G. Siddall, *Vacuum III* (1955).
40. H. F. Dates and J. K. Davis, Patent# 3,331,702, USA (1967).
41. A. J. Nozik, Patent# 3,811,953, USA (1974).
42. A. J. Nokik and G. Haacke, Patent# 3,957,029, USA (1976).
43. R. G. Gordon, Patent# 4,146,657, USA (1979).
44. S. R. Kurtz and R. G. Gordon, *Thin Solid Films* **139**, 277 (1986).
45. S. Major, A. Banerjee, and K. L. Chopra, *Thin Solid Films* **122**, 31 (1984).
46. T. Minami, H. Nanto, and S. Takata, *Japanese Journal of Applied Physics, Part 2: Letters* **23**, L280 (1984).
47. S. N. Qiu, C. X. Qiu, and I. Shih, *Solar Energy Materials* **15**, 261-267 (1987).
48. P. S. Vijayakumar, K. A. Blaker, R. D. Weiting, B. Wong, A. T. Halani, and C. Park, Patent# 4,751,149, USA (1988).
49. B. H. Choi, H. B. Im, J. S. Song, and K. H. Yoon, *Thin Solid Films* **193/194**, 712-720 (1990).
50. J. Hu and R. G. Gordon, *Solar Cells* **30** (1-4), 437-450 (1990).

51. J. Hu and R. G. Gordon, *Journal of Applied Physics* **71** (2), 880-890 (1992).
52. J. Hu and R. G. Glordon, *Journal of Applied Physics* **72** (11), 5381-5392 (1992).
53. J. Hu and R. G. Gordon, *Proceedings of Fall Materials Research Society: Microcrystalline Semiconductors: Materials Science and Devices Symposium*, Boston, MA, 1993.
54. H. Enoki, T. Nakayama, and J. Echigoya, *Physica Status Solidi A* **129** (1), 181-191 (1992).
55. T. Minami, H. Sonohara, S. Takata, and H. Sato, *Japanese Journal of Applied Physics, Part 2: Letters* **33**, L1693 (1994).
56. J. M. McGraw, P. A. Parilla, D. L. Schulz, J. Alleman, X. Wu, W. P. Mulligan, D. S. Ginley, and T. J. Coutts, *Proceedings of Spring Materials Research Society Conference: Film Synthesis and Growth Using Energetic Beams Symposium*, San Francisco, CA, 1995.
57. S. Maniv, C. J. Miner, and W. D. Westwood, *Journal of Vacuum Science and Technology A* **1** (3), 1370-1375 (1983).
58. T. Minami, H. Nanto, and S. Takata, *Applied Physics Letters* **40** (10), 961-3 (1982).
59. T. Minami, H. Nanto, S. Shooji, and S. Takata, *Thin Solid Films* **111** (2), 167-174 (1984).
60. T. Minami, *MRS Bulletin* **25** (8), 38-44 (2000).
61. S. Jäger, B. Szyszka, J. Szczyrbowski, and G. Bräuer, *Surface and Coatings Technology* **98** (1-3), 1304-1314 (1998).
62. R. Menner, R. Schäffler, B. Sprecher, and B. Dimmler, *Proceedings of the 2nd World Conference Exhibition on Photovoltaic Solar Energy Conference*, 1998.
63. R. Cebulla, R. Wendt, and K. Ellmer, *Journal of Applied Physics* **83** (2), 1087-1095 (1998).
64. O. Kluth, B. Rech, L. Houben, S. Wieder, G. Schöpe, C. Beneking, H. Wagner, A. Löffl, and H. W. Schock, *Proceedings of the 2nd International Conference Coating Glass*, Saarbücken, Germany, 1998.
65. K. Tominaga, N. Umezumi, I. Mori, T. Ushiro, T. Moriga, and I. Nakabayashi, *Thin Solid Films* **334**, 35-39 (1998).

66. K. C. Park, D. Y. Ma, and Kim, *Thin Solid Films* **305**, 201-209 (1997).
67. A. Löffl, S. Wieder, B. Rech, O. Kluth, C. Beneking, and H. Wagner, *Proceedings of the 14th European Photovoltaic Solar Energy Conference*, Barcelona, Spain, 1997.
68. K. Ellmer, F. Kudella, R. Mientus, R. Schiek, and S. Fiechter, *Thin Solid Films* **247**, 15-23 (1994).
69. T. Nakada, N. Murakami, and A. Kunioka, *Proceedings of the 12th European Photovoltaic Solar Energy Conference*, Amsterdam, Netherlands, 1994.
70. R. Schäffler and H. W. Schock, *Proceedings of the 23rd IEEE Photovoltaic Specialists Conference*, Louisville, KY, 1993.
71. R. Konishi, K. Noda, H. Harada, and H. Sasakura, *Journal of Crystal Growth* **117**, 939-942 (1992).
72. R. H. Mauch and H. W. Schock, *Proceedings of the Tenth E.C. Photovoltaic Solar Energy Conference*, Lisbon, Portugal, 1991.
73. Y. Igasaki and H. Saito, *Journal of Applied Physics* **70** (7), 3613-3619 (1991).
74. Z.-C. Jin, I. Hamberg, and C. G. Granqvist, *Journal of Applied Physics* **64**, 5117-31 (1988).
75. T. Minami, H. Sato, T. Sonoda, H. Nanto, and S. Takata, *Thin Solid Films* **171**, 307-311 (1989).
76. T. Minami, H. Sato, H. Nanto, and S. Takata, *Japanese Journal of Applied Physics* **24** (10), L781-L784 (1985).
77. J. B. Webb, D. F. Williams, and M. Buchanan, *Applied Physics Letters* **39**, 640-642 (1981).
78. D. H. Zhang and H. L. Ma, *Applied Physics A* **62** (5), 487-92 (1996).
79. N. F. Mott, *Metal-insulator Transitions*, 2nd ed. (Taylor & Francis, New York, 1990).
80. R. E. Hummel, *Electronic Properties of Materials*, Second ed. (Springer-Verlag, Berlin, 1993).
81. C. Kittel, *Introduction to Solid State Physics* (John Wiley & Sons, Inc., New York, 1986).

82. T. J. Coutts, D. L. Young, and X. Li, *MRS Bulletin* **25** (8), 58-65 (2000).
83. J. W. Mayer and S. S. Lau, *Electronic Materials Science: For Integrated Circuits in Si and GaAs* (Macmillan Publishing Company, New York, 1990).
84. D. L. Young, T. J. Coutts, and V. I. Kaydanov, *Review of Scientific Instruments* **71** (2), 462-6 (2000).
85. S. B. Zhang, S.-H. Wei, and A. Zunger, *Physical Review B* **63** (7), 63-69 (2001).
86. L. H. van Vlack, *Elements of Materials Science and Engineering*, 6th ed. (Addison-Wesley, New York, 1990).
87. R. L. Petritz, *Physical Review* **104** (6), 1508-16 (1956).
88. G. Bogner, *The Physics and Chemistry of Solids* **16**, 235 (1961).
89. D. L. Young, T. J. Coutts, V. I. Kaydanov, A. S. Gilmore, and W. P. Mulligan, *Journal of Vacuum Science & Technology A* **18** (6), 2978-85 (2000).
90. H. Brooks, *Theory of the Electrical Properties of Germanium and Silicon* (Academic Press, New York, 1955).
91. S. Major, A. Banerjee, and K. L. Chopra, *Thin Solid Films* **122** (1), 31-34 (1984).
92. S. Bose, S. Ray, and A. K. Barua, *Journal of Physics D: Applied Physics* **29** (7), 1873-77 (1996).
93. L. Burstein, *Physical Review* **93**, 632 (1954).
94. M. Ohring, *The Materials Science of Thin Films* (Academic Press, Inc., London, 1992).
95. H. Sato, T. Minami, Y. Tamura, S. Takata, T. Mouri, and N. Ogawa, *Thin Solid Films* **246** (1-2), 86-91 (1994).
96. A. Sarkar, S. Ghosh, S. Chadhuri, and A. K. Pal, *Thin Solid Films* **204** (1), 255-264 (1991).
97. K. Ellmer, F. Kudella, R. Mientus, R. Schieck, and S. Fiechter, *Applied Surface Science* **70/71**, 707-11 (1993).
98. W. R. Grove, *Philosophical Transaction of the Royal Society* **142** (78) (1852).
99. B. Chapman, *Glow Discharge Processes* (John Wiley & Sons, New York, 1980).

100. P. Sigmund, *Physical Review* **184**, 383 (1969).
101. D. M. Smith, *Thin-Film Deposition* (McGraw-Hill, Inc., New York, 1995).
102. H. K. Pulker, *Coatings on Glass* (Elsevier, New York, 1984).
103. H. S. Butler and G. S. Kino, *The Physics of Fluids* **6**, 1346 (1963).
104. J. A. Thornton, *Journal of Vacuum Science and Technology* **11** (4), 666-670 (1974).
105. D. Bloss, *Crystallography and Crystal Chemistry* (Holt, Rinehart and Winston, New York, 1989).
106. G. J. Exarhos and S. K. Sharma, *Thin Solid Films* **270** (1-2), 27-32 (1995).
107. Y. F. Lu, H. Q. Ni, Z. H. Mai, and Z. M. Ren, *Journal of Applied Physics* **88** (1), 498-502 (2000).
108. L.-J. Meng and M. P. dos Santos, *Thin Solid Films* **250**, 26-32 (1994).
109. T. Minami, K. Oohashi, S. Takata, T. Mouri, and N. Ogawa, *Thin Solid Films* **193/194**, 721-729 (1990).
110. B. Cullity, *Elements of X-ray Diffraction*, 2nd ed. (Addison-Wesley Publishing Company, 1978).
111. S. Zafar, C. S. Ferekides, and D. L. Morel, *Proceedings of 1994 IEEE 1st World Conference on Photovoltaic Energy Conversion*, Waikoloa, HI, USA, 1994.
112. K. Tominaga, K. Kuroda, and O. Tada, *Japanese Journal of Applied Physics* **27** (7), 1176-1180 (1988).
113. K. Tominaga, T. Murayama, Y. Sato, and I. Mori, *Thin Solid Films* **343-344**, 81-84 (1999).
114. J. J. Cuomo, R. J. Gambino, J. M. E. Harper, and J. D. Kuptsis, *IBM Journal of Research and Development* **21**, 580-583 (1977).
115. J. M. E. Harper, J. J. Cuomo, R. J. Gambino, H. R. Kaufman, and R. S. Robinson, *Journal of Vacuum Science and Technology* **15** (4), 1597-1600 (1978).
116. K. Tominaga, T. Yuasa, M. Kume, and O. Tada, *Japanese Journal of Applied Physics, Part 1* **23** (7), 936-937 (1984).

117. D. J. Kester and R. Messier, *Journal of Materials Research* **8** (8), 1928-1937 (1993).
118. D. J. Kester and R. Messier, *Journal of Materials Research* **8** (8), 1938-1957 (1993).
119. H. Sato, T. Minami, S. Takata, T. Mouri, and N. Ogawa, *Thin Solid Films* **220**, 327-332 (1992).
120. J. Caughman, "Basics of Radiofrequency Technology," (The Short Course Executive Committee American Vacuum Society, 2000), pp. 162.
121. L. J. van der Pauw, *Philips Research Reports* **13** (1) (1958).
122. Software: *Line Profile*, (Philips Corporation, 1995).
123. B. R. Morris, A. M. Gokhale, and G. F. V. Voort, *Mettallurgical and Materials Transactions A* **29A**, 237-244 (1998).
124. D. Briggs and M. P. Seah, "Practical Surface Analysis: Second Edition," (John Wiley & Sons Ltd, West Sussex, England, 1990), Vol. 1 - Auger and X-ray Photoelectron Spectroscopy.
125. J. C. Vickerman, "Surface Analysis-- The Principle Techniques," (John Wiley & Sons, Inc., New York, 1997), pp. 457.
126. J. I. Pankove, *Optical Processes in Semiconductors*, Second ed. (Dover Publications, New York, 1976).
127. S. Ghosh, A. Sarkar, S. Bhattacharya, S. Chaudhuri, and A. K. Pal, *Journal of Crystal Growth* **108** (3-4), 534-40 (1991).
128. R. Petschick, Software: *MacDiff*, (2000).
129. R. Anthony, 2000, British Glass Ltd., Webpage, (<http://www.britglass.co.uk/publications/mglass/making8.html>), Accessed: 11/2001.
130. L. E. Davis, N. C. MacDonald, P. W. Palmberg, and G. Riach, *Handbook of Auger Electron Spectroscopy : A Reference Book of Standard Data for Identification and Interpretation of Auger Electron Spectroscopy Data* (Physical Electronics Industries, Eden Prairie, 1976).
131. Software: *MathCAD*, (MathSoft, Inc, 1996).

132. F. Ohuchi and P. H. Holloway, *Journal of Vacuum Science and Technology* **20** (3), 863-867 (1982).
133. K. Fuchs, *Proceedings of the Cambridge Philosophical Society* **34**, 100 (1938).
134. E. H. Sondheimer, *Advances in Physics* **1**, 1 (1951).
135. A. F. Mayadas and M. Shatzkes, *Physical Review B (Solid State)* **1** (4), 1382-1389 (1970).
136. L. I. Maissel and R. Glang, "Handbook of Thin Film Technology," (McGraw-Hill, New York, 1970), Vol. 1.
137. K. L. Chopra, *Thin Film Phenomena* (McGraw-Hill, Inc., New York, 1969).
138. R. Fleming, 2000, Charles Evans and Associates, Webpage, (<http://www.cea.com/cai/simstheo/caistheo.htm>), Accessed: 11/2001.
139. V. Srikant, V. Sergo, and D. Clarke, *Journal of the American Ceramic Society* **78** (71), 1935-9 (1995).
140. C. D. Wagner, W. M. Riggs, L. E. Davis, J. F. Moulder, and M. G.E., *Handbook of X Ray Photoelectron Spectroscopy : A Reference Book of Standard Spectra for Identification and Interpretation of Xps Data* (Physical Electronics Industries, Eden Prarie, 1979).
141. J. F. O'Hanlon, *A User's Guide to Vacuum Technology*, 2nd ed. (John Wiley & Sons, New York, 1989).
142. D. J. Kester and R. Messier, *Journal of Vacuum Science & Technology A* **4** (3), 496-9 (1986).

BIOGRAPHICAL SKETCH

Loren Wellington Rieth was born in Lawrence, Kansas April 29, 1972, younger brother to Herbert III, and son to Herbert and Sheri Rieth. He moved with his family to Bloomington, Indiana in 1976, and there attended elementary school. In 1985 he moved to Nashville, Tennessee, and there graduated from Hillsboro High School in 1990. He attended The Johns-Hopkins University from August of 1990 to his graduation with a BS in Materials Science and Engineering in May of 1994. A variety of interests were developed during his tenure at this institution, the most lasting of which has been a love of outdoor recreation and photography. His education continued with graduate studies at the University of Florida in the Department of Materials Science and Engineering. He received his MS in Materials Science under Paul Holloway in 1997.

He has participated in research concerning ultrasonic characterization of polymer welds and optical rotation by the Faraday effect in the Department of Materials Science at Johns-Hopkins. He was also a summer research intern at the National Renewable Energy Laboratory in Golden, Colorado in 1995. His duties focused on deposition and characterization of CuInSe_2 thin films for solar cell applications.